UNIVERSITÀ DEGLI STUDI DI TRIESTE

XXXV CICLO DEL DOTTORATO DI RICERCA IN NANOTECNOLOGIE

NANOSTRUCTURED CATALYSTS FOR SUSTAINABLE CO_2 CONVERSION

Settore scientifico-disciplinare: **CHIM/03**

DOTTORANDO
MATTEO BISETTO

COORDINATORE
Chiar.mo PROF. ALBERTO MORGANTE

SUPERVISORE DI TESI
Chiar.mo PROF. PAOLO FORNASIERO

CO-SUPERVISORE DI TESI
PROF. TIZIANO MONTINI

ANNO ACCADEMICO 2021/2022

\

Abstract

In the recent years, different strategies have been studied to mitigate the impact of CO_2 emissions on the global environment. In particular, CO_2 reduction has emerged as a promising approach for recycling this gas and the direct conversion to fuels or chemicals. Despite great improvements in the last decades, the recycling of CO_2 still suffers a mismatch between the lab and the industrial scales due to the high costs of the entire process and the lifetime of the catalysts. Catalysts play a pivotal role in CO_2 reduction applications, and their characteristics, such as catalytic activity, selectivity, and long-term stability, are crucial for enabling the feasibility of this process at an industrial scale. Nanostructuration has been identified as a key factor in tailoring the morphology at the nanoscale and enhancing the overall performance of catalyst materials. The presented work focuses on the development and characterization of nanostructured catalysts for CO_2 reduction. The use of advanced synthetic techniques as well as morphological, textural and (electro)chemical characterizations allowed to optimize various catalysts for different applications at the forefront of research. Cu-based catalysts were explored toward the eCO_2RR. Firstly, well-defined nanoparticles of Cu_2O were synthetized and widely characterized toward eCO_2RR, revealing different catalytic behavior and a low selectivity toward a particular product. Moreover, operando XAS characterization confirmed a rapid reduction to metal Cu. To overcome these limitations, the study explores the formation of heterostructures and the utilization of 2D materials like g-C_3N_4, RGO and MoS_2, leading to an improved catalytic selectivity and productivity. On the other hand, the preparation of bimetallic CuSn alloys via an easy and scalable urea glass route can open new perspectives for the affordability of this process at an industrial-scale level. Another approach to exploit nanostructuration for the reduction of CO_2 investigated the employing of TiN nanotubes decorated with metal nanoparticles as catalyst for gas-phase photothermal reduction of CO_2. Further considerations regarding optimization and environmental impact are fundamental to enable large-scale CO_2 reduction processes. Continued research and development in these areas are essential to bridge the gap between laboratory-scale advancements and industrial-scale implementation of CO_2 recycling technologies.

Negli ultimi anni, diverse strategie sono state studiate al fine di mitigare l'impatto delle emissioni di CO_2 sull'atmosfera. In particolare, la riduzione di CO_2 risulta essere un promettente approccio per il riuso di questo gas e la sua diretta conversione in combustibili o prodotti chimici. Nonostante i grandi miglioramenti degli ultimi decenni, questi metodi presentano ancora una differenza tra l'utilizzo ai fini di ricerca e l'applicabilità a livello industriale a causa degli alti costi dell'intero processo e della durata dei catalizzatori. I catalizzatori svolgono un ruolo fondamentale in questa tipologia di applicazioni e le loro caratteristiche, come l'attività catalitica, la selettività e la stabilità nel tempo, sono aspetti cruciali per permettere l'utilizzo di questi processi a livello industriale. La nanostrutturazione è un fattore chiave per ottimizzare la morfologia del catalizzatore su scala nanometrica e migliorarne le prestazioni complessive.

Il lavoro presentato verte sullo sviluppo e la caratterizzazione di catalizzatori nanostrutturati per la riduzione di CO_2. L'uso di tecniche sintetiche avanzate e caratterizzazioni morfologiche, tessiturali e (elettro)chimiche, ha permesso di ottimizzare vari catalizzatori per diverse applicazioni. In particolare, catalizzatori a base di Cu sono stati studiati per il processo di riduzione elettrochimica della CO_2 (eCO_2RR). In primo luogo, nanoparticelle di Cu_2O dalla forma specifica sono state sintetizzate e studiate come catalizzatori nel processo di eCO_2RR, mostrando un diverso comportamento catalitico e una bassa selettività verso un particolare prodotto della riduzione. Inoltre, la caratterizzazione XAS in operando ha confermato una rapida riduzione del materiale a Cu metallico. Per superare questi limiti, lo studio esplora la formazione di eterostrutture e l'utilizzo di materiali 2D come g-C_3N_4, RGO e MoS_2, mostrando una migliore selettività catalitica e produttività nei confronti di determinati prodotti. Inoltre, la sintesi di leghe di CuSn bimetalliche attraverso un metodo facile e scalabile come il cosiddetto "Urea Glass Route" può aprire nuove prospettive per l'utilizzo di questo processo a livello industriale.

Nanotubi di TiN decorati con nanoparticelle metalliche sono infine stati utilizzati come catalizzatori per la riduzione fototermica di CO_2.

Ulteriori considerazioni relative all'ottimizzazione e all'impatto ambientale sono fondamentali per consentire processi di riduzione di CO_2 su larga scala. Il continuo sviluppo in queste aree è essenziale per colmare il divario tra i progressi nella ricerca e l'implementazione su scala industriale delle tecnologie di riciclaggio della CO_2.

Table of contents

Chapter 1

Introduction

1.1 Global warming and increasing of CO_2 concentration

In the last centuries, the world's population has observed a general improvement in living conditions and expectations thanks to the development of new technologies and the higher availability of goods or services. In addition to this, other problems have risen in parallel, in particular linked to the increased demand of natural resources for industrial applications, to the greater quantity of residual waste and to a constant and rapid increase of polluting emissions. Several phenomena are linked to the average increasing of global temperatures due to the so-called global warming. Also referred as climate change, global warming refers to the long-term increase in average earth temperatures linked to anthropogenic factors and the consequent increase of the concentration in the atmosphere of poisonous gases such methane and carbon dioxide [1]. Under normal conditions, greenhouse gases can trap heat within the atmosphere, creating a natural "greenhouse effect" that keeps the earth's temperature stable to support biological life. However, if the concentrations of these gases increases rapidly due to anthropogenic reasons, the greenhouse effect enhances, causing a general increase in global temperatures and leading to a variety of impacts including sea level rise, more frequent and severe weather events and ecological upheavals [2–4]. According to recently available data from the National Oceanic and Atmospheric Administration (NOAA), the global average atmospheric CO_2 concentration in 2021 was 414.7±0.1 parts per million (ppm), which is the highest concentration of CO_2 in the atmosphere in millions of years (Figure 1.1 A) [5]. Although the concentration of greenhouse gases has always fluctuated in different eras, the main cause of global warming is certainly linked to human beings and their impact on the earth's ecosystem. Indeed, the NOAA report claims that a large fraction of these emissions is related to developed or developing nations such as USA, Europe, China and India (Figures 1.1 B).

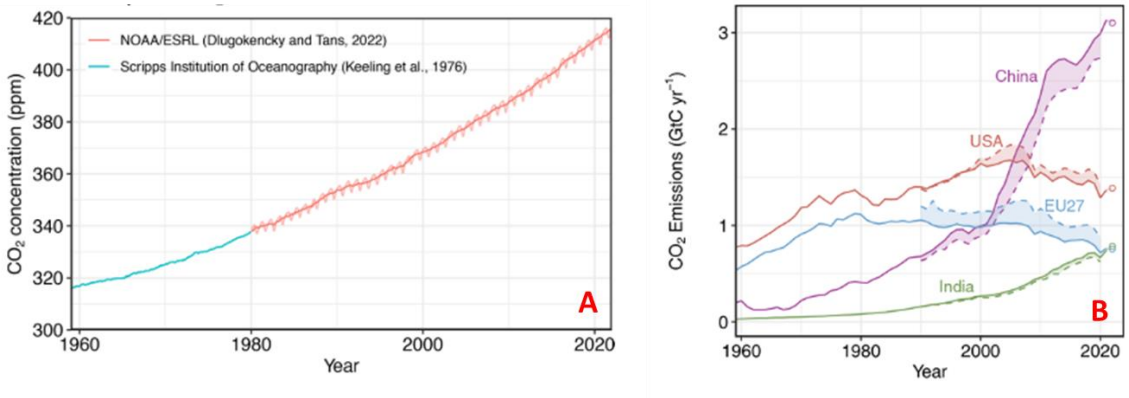

***Figure 1.1**: A) CO_2 concentration in the atmosphere over the years. B) Territorial (solid lines) and consumption (dashed lines) emissions for Europe, USA, India and China over the years. From [5].*

Several causes of CO_2 increase had been identified, mainly related to the combustion of fossil fuels, industries and agriculture. In particular, the large quantities of fossil fuels such as coal, oil or natural gas that are burnt for producing electricity, heating or industrial purposes release large amounts of carbon dioxide into the atmosphere, as shown in Figure 1.2.

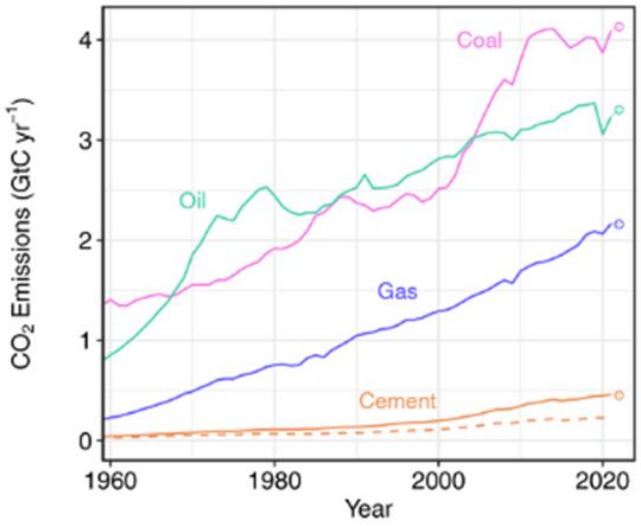

***Figure 1.2**: Global CO_2 emissions over years from the different fuels. From [5].*

These human activities have caused a significant increase in the concentration of CO_2 (and other gases) in the atmosphere since the industrial revolution, with huge impacts on global temperatures and natural disasters, but also on the economy and geopolitics [6]. In

the absence of serious and urgent global warming mitigation strategy for the coming years, leading to a step drop in greenhouse gas emissions by 2030, the global temperature increase will exceed 1.5°C in the coming decades, leading to irreversible loss of the most fragile ecosystems, and crisis after crisis for the most vulnerable people and societies [7]. Governments and international institutions are considering addressing these challenges through a transition to renewable energy sources, the electrification of transport and investments in policies or research. But to drastically limits the impact of the global warming on our planet, it is essential to reduce greenhouse gas emissions and minimize the effects of our activities through a change in economic models and the way we manage the wastes. The first step in tackling the problems related to global warming is to consider the overall environmental impact of a particular activity in terms of natural resources, pollution and costs thanks to the Life-Cycle Assessment (LCA) [8]. LCA is a common method for understanding the effects on environment of a particular process (or product) during its entire life cycle, including the extraction of raw materials, their industrial processing, transportation and end-of-life management (such as recycling or disposal). This is an essential tool for assessing the impact of a process or product, while understanding which steps need to be optimized in order to improve sustainability and limit the negative effects of industrial processes on the global atmosphere [9]. A typical LCA can be divided into four distinct phases, all of which are essentials for defining the overall impact of a product / process (Figure 1.3): Definition of goal and scope, analysis of the inventory, evaluation of the impact and interpretations of the data collected [10].

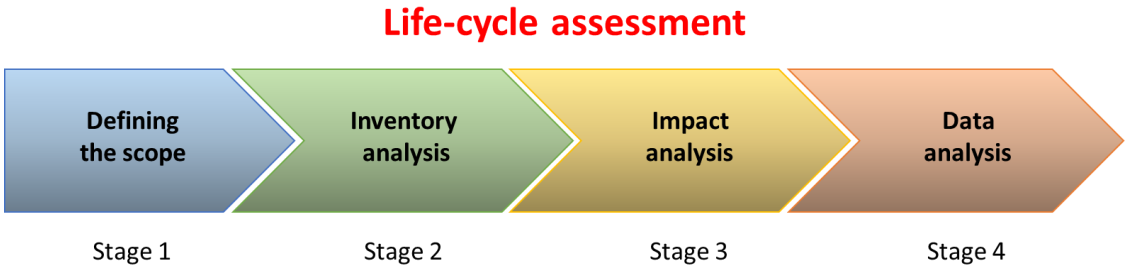

***Figure 1.3**: Different steps of a Life Cycle Assessment.*

Evaluating of overall impact of a process is certainly important to deal with the increasing of CO_2 concentration but it is not enough without a complete change of the economical way to conceive an industrial process. Indeed, the take-make-dispose model (or the so-

called linear economy), with the production and direct consumption of goods and services without waste treatments, is a significant driver of the increased release of greenhouse gases. This model is no longer accepted by international institutions, and it is necessary to consider a change in the economic system, which provides for the complete waste treatment and recycling during the entire productive process. The circular economy model can offer an effective way to improve all these aspects through an appropriate reduction of waste and the promotion of recycling and regeneration of materials (Figure 1.4) [11]. Furthermore, the circular economy can contribute to mitigate the climate change effects through the rational use of renewable energy sources and a contemporaneous limitation of fossil fuels [12].

***Figure 1.4**: Scheme of a circular economy. From* [13].

In general, several actions are required to achieve a fully circular economy, including a totally renewed way of designing and producing a given good, optimized supply chain management and improved consumer behavior [14]. What this cycle currently does not account is the use of the CO_2 already emitted as a source for the chemical industry. It is therefore possible to imagine one smaller cycle in which common molecules, such as CO_2, are used as starting building blocks for the synthesis of products with high added value (i.e. hydrocarbons or alcohols). To fully understand which processes we can exploit to convert CO_2 into other products, a brief overview regarding the chemistry and reactivity of CO_2 is presented in the followings.

1.2 The chemistry and the reactivity of CO_2

Carbon dioxide (CO_2) is a colorless and odorless gas that occurs naturally in nature and in which two atoms of oxygen are bonded with a central atom of carbon through covalent bond. Figure 1.5 shows the 3d linear structure of the CO_2 molecule, a non-polar molecule characterized by a high rate of symmetry.

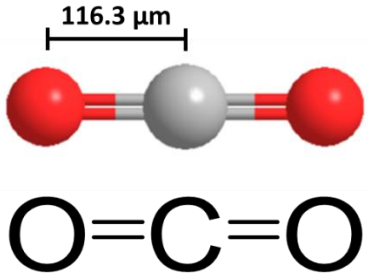

***Figure 1.5**: Molecule of CO_2.*

The characterization of CO_2 is not trivial due to its stable and symmetric structure and the most common way to characterize it is by vibrational spectroscopies such as Infrared (IR) or Raman spectroscopy [15]. CO_2 has three normal vibrational modes (Figure 1.6): the symmetric and antisymmetric modes and the bending mode [16]. The three modes are different, and they show different activity toward the two aforementioned techniques: while the first mode is Raman active, the other two vibrations are IR active. In particular, the symmetric linear molecular geometry of CO_2 results in unique vibrational features, characterized by two intense peaks, referred as $\nu_1$and ν_3 bands, which correspond to symmetric and antisymmetric stretching vibrations respectively. The ν_1 band occurs at around 1388 cm^{-1} and this intense peak is sensitive to changes in the bond length of the C-O bonds in CO_2 and can be used to determine the concentration of CO_2 in a sample. In addition to these two intense peaks, the vibrational feature of CO_2 also contains weaker peaks corresponding to bending vibrations and combination bands.

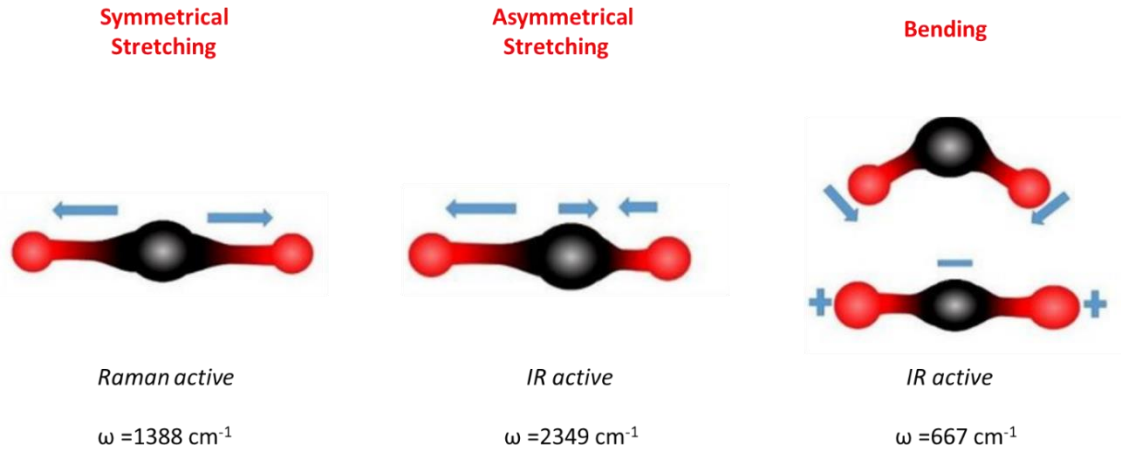

Figure 1.6: *Characteristic vibrations of CO_2 molecule.*

The chemistry of CO_2 is complex and has huge environmental implications. Indeed, its relative chemical stability inhibits reactivity under normal conditions, so that CO_2 is able to chemically react under specific conditions. For instance, in aqueous solutions, carbon dioxide dissolves and reacts with water to form H_2CO_3 which can further dissociate to HCO_3^- and CO_3^{2-} as shown in equation 1.1.

$$CO_{2(g)} + H_2O_{(l)} \rightleftharpoons H_2CO_{3(aq)} \rightleftharpoons H^+_{(aq)} + HCO^-_{3(aq)} \rightleftharpoons 2\ H^+_{(aq)} + CO^{2-}_{3(aq)} \qquad (1.1)$$

This reaction is fundamental to drive and control the acidity of natural waters such as oceans or lakes [17]. Carbon dioxide can also react with some metals to form metal carbonates. For example, when CO_2 reacts with calcium oxide (CaO), it forms calcium carbonate ($CaCO_3$), which is the primary component of limestone and other sedimentary rocks, having important implications on the formation of geological structures such as caves and coral reefs (equation 1.2).

$$CaO_{(s)} + CO_{2(g)} \rightarrow CaCO_{3(s)} \qquad (1.2)$$

While the solubility in non-aqueous media is considerably higher, the concentration of CO_2 dissolved in H_2O is quite low. For example, in $KHCO_3$ solutions at concentrations from 0.1 to 1.5 M, the concentration of dissolved CO_2 is only about 33 mM to 45 mM at room temperature [18]. CO_2 can be liquefied under high pressure and find applications in a wide range of industries such as [19,20]:

- Refrigeration;

- Food and beverage industries;
- Methanol and other chemical syntheses;
- Medical applications;
- Oil and gas industry.

Reducing CO_2 emissions and recycling it can be efficient ways to contrast the general increasing of CO_2 concentration in the air and mitigate the negative effects of climate change. Different strategies can be implemented to reduce CO_2 emissions, such as improving of the energy efficiency of industrial plants, equipment or domestic building by optimizing the facilities and limiting transport [21,22]. On the other hand, Carbon Capture and Storage (CCS) technologies are also investigated to capture the concentrated CO_2 emissions from industrial processes and store them in long-term storage locations [23,24]. Another way to reduce CO_2 emissions is to increase the use of renewable energy (such as solar, wind or hydropower) in order to maximize the use of green energies, limiting the emissions of CO_2 related to the use of electricity produced from fossil fuels [25].

A promising approach to limit the negative effects of the increasing of CO_2 emissions is recycling and the subsequent conversion to higher value-added chemical compounds such as hydrocarbons or alcohols [26]. These processes firstly involve the capture of the emitted CO_2 and its reduction to form building blocks for other chemical processes. Recycling of CO_2 has the potential to significantly limit the concentrations of this gas on earth's atmosphere and create new economic opportunities, but it is essential to understand that the development of technologies devoted to recycling of CO_2 is still primordial and requires significant investments and improvements. In the next section, typical processes for CO_2 recycling and conversion are presented, with particular attention to the electrochemical CO_2 Reduction Reaction (eCO_2RR) and the synthesis of e-Fuels.

1.3 Different ways to perform CO_2 Reduction: the case of electrochemical CO_2 Reduction Reaction

A large variety of methods can be exploited to perform the reduction of CO_2 (Figure 1.7); They are promising and under study, but at the same time they all have weaknesses that limit their use in industrial applications.

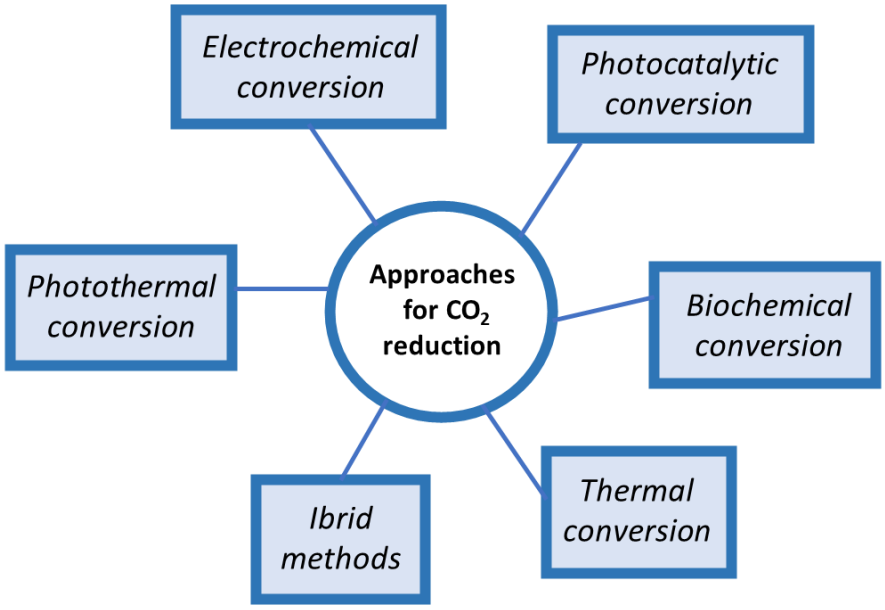

Figure 1.7: *Typical methods for reduction of CO_2.*

One of the most common ways to convert CO_2 is thermal reduction. With this process CO_2 is converted into other carbon-based compounds (such as CO or C) by exploiting high temperatures or pressures on a particular reactor vessel [27,28]. In particular, one common process is the so-called reverse Water Gas Shift reaction (rWGS), in which CO_2 and H_2 react, under studied conditions, to form a mixture of CO and H_2O, a typical starting point for other catalytic processes such as Fischer-Tropsch [29]. Due to its intrinsic endothermic behavior, rWGS is favored with the increasing of the overall temperature of the process; other factors that help to improve the efficiency of the reaction are the H_2:CO ratio and a lower contact times [30]. rWGS can be studied as a stand-alone process to form syngas, but also as a starting point for other important catalytic reactions, such as in example the CO_2 methanation reactions (or Sabatier reaction) [31]. However, the relatively high temperature of the processes introduces some important limitations, mostly related to the low life expectancy of reactors or catalysts, as well as a higher cost

in terms of dissipated energy and capital costs. One of the most important tasks of research is to achieve high conversion rates and selectivity using thermal processes but maintaining at the same time a good level of energy efficiency. Researchers are studying different experimental conditions (such as gas composition or temperature of the process) in order to improve the overall catalytic rate [32,33]. Methanol synthesis is another relevant industrial process that utilize enormous quantities of CO_2 in combination with CO and hydrogen to form this essential building block for chemical processes [34]. Conventionally, methanol is produced from syngas via hydrogenation of CO and CO_2, following the chemical reaction presented in equation 1.3.

$$CO_2 + 3H_2 \leftrightharpoons CH_3OH + H_2O \quad (1.3)$$

Due to the massive demand of methanol (more than 200 kTons per day), the recycling of CO_2 from atmosphere or industrial processes has significant potential for growth as a commodity chemical or fuel toward methanol production [35].

Another promising method is the biochemical conversion of CO_2, a process able to exploits the capability of some microorganisms or enzymes to exploit CO_2 as carbon source for the synthesis of other chemicals via biological processes. In example, certain bacteria are able to convert CO_2 into methane through a process called methanogenesis [36]. The idea behind this family of processes is to mime the natural photosynthesis where photosynthetic organisms (such as bacteria, algae or plants) convert CO_2 into different organic compounds, referred as biofuels or bio-based chemicals [37]. Even if in general biological processes have several advantages mainly related to the low environmental impact, the methods still suffer of a low efficiency and limited scalability (requirement of long operational times and large space). Therefore research is currently exploring a number of innovative strategies, such as synthetic biology or genetic engineering to address these problems [38,39].

Homogeneous and heterogeneous photocatalytic reduction of carbon dioxide is a challenging and deeply investigated process that involves light instead of thermal energy and the use of a particular photocatalyst to convert CO_2 into other molecules such as CO, methane, formic acid or alcohols. In particular, heterogeneous photocatalytic CO_2 reduction exploit the capability of a semiconductor that is able to absorb light of an

opportune wavelength and to promote electrons from valence band to the conduction band leaving a hole in the valence band (Figure 1.8).

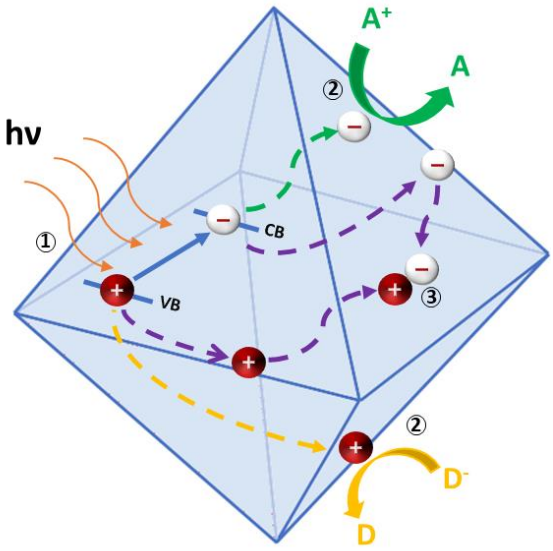

***Figure 1.8**: Photoinduced generation of electron-hole pairs: 1) A radiation with an opportune wavelength promotes the generation of an electron in the conduction band (CB) and a hole in the valence band (VB). 2) These carriers can migrate to the surface of the catalyst to catalyze the half reactions. 3) Process of recombination of the carriers.*

The exciton couple that is formed through the absorption of a photon is able to catalyze the semi reactions of the process, in particular the reduction of carbon dioxide [40]. Photocatalysis has several advantages over traditional chemical processes, including its potential for green and sustainable chemistry, as well as its ability to operate at room temperature and atmospheric pressure [41]. However, this process suffers of different drawbacks including the low activity or stability of photocatalysts, the low lifetime of the exciton couple and the presence of contaminants that can easily poison the catalytic centers [42,43]. In addition to these problems, research is focusing on the optimization of photocatalysts, exploring a range of materials including metal oxides, metal sulfides and carbon-based materials or finding new synthetic strategies such as nanostructuration, doping with heteroatoms or formation of heterostructures [44–46]. Many researchers are investigating new hybrid synthetic methods where photocatalysis is coupled with other material functionalities [47,48]. For example, photothermal processes combine photocatalysis and thermal effects [49]. Localized Surface Plasmon Resonance (LSPR)

has been proved to be able to efficiently convert light into local heat, driving the thermocatalytic CO_2 reduction along with or promoting the photocatalytic conversion of CO_2 [50].

Compare to the aforementioned processes, the electrochemical CO_2 Reduction Reaction (CO_2RR or eCO_2RR), often coupled with the utilization of renewable energy sources (such as solar or wind), is able to operate under mild conditions (less demanding with respect to thermal catalysis) or without the need of complex additional operations such as in the case of enzyme or microorganisms management [51]. Furthermore, the possibility of exploiting different technologies and electrochemical configurations, allows to use these processes even on an industrial scale, with easy implementation on existing infrastructures. The compounds that are produces from eCO_2RR are referred as E-fuels (or electrofuels) if the products are produced using renewable sources of energy [52]. eCO_2RR is performed in an electrochemical cell, a particular device where electrical energy is converted into chemical energy, performing a non-spontaneous process. A general explanation of different electrochemical setups is presented in chapter 1.5 focused on the study of electrocatalytic devices for CO_2RR.

As already observed for photocatalytic process, also for the eCO_2RR the catalyst plays a key role. The material must have some common features in order to be used efficiently as working electrode toward the CO_2 reduction such as a low overpotential, high selectivity toward a particular CO_2RR product and high stability over time [53]. In particular, the selectivity is a very important parameter to describe an electrocatalysts due to the different reduction processes that can occur during CO_2 reduction. Many reaction products can take place during CO_2RR even if, depending on the working conditions, only part of them are easily formed [54]. The main half reactions and the relevant concurring hydrogen evolution reaction are summarized in Table 1.1:

Electrode	Half Cell Reaction	Potential (V Vs SHE)
Cathode	$CO_2 + 2H^+ + 2e^- \rightarrow CO + H_2O$	-0.106
	$CO_2 + 2H^+ + 2e^- \rightarrow HCOOH$	-0.250
	$2CO_2 + 2H^+ + 2e^- \rightarrow H_2C_2O_4$	-0.500
	$CO_2 + 4H^+ + 4e^- \rightarrow HCOH + H_2O$	-0.070
	$CO_2 + 6H^+ + 6e^- \rightarrow CH_3OH + H_2O$	0.016
	$CO_2 + 8H^+ + 8e^- \rightarrow CH_4 + 2H_2O$	0.169
	$CO_2 + 12H^+ + 12e^- \rightarrow C_2H_4 + 4H_2O$	0.064
	$2H^+ + 2e^- \rightarrow H_2$	0.000
Anode	$2H_2O \rightarrow O_2 + 4H^+ + 4e^-$	1.230

***Table 1.1**: Main half reactions involved on eCO_2RR.*

The mechanism of eCO_2RR is complex and depends on several factors such as the material, the applied voltage, the cell configuration or the local CO_2 concentration. Different intermediate species have been proposed to be involved in the reaction mechanism. The reaction pathway can be schematically summarized in four main steps (Figure 1.9): 1) adsorption of a CO_2 molecule on the surface of the active material; 2) diffusion of electrons and/or protons to form a particular CO_2 intermediate; 3) other further electronation that happen in order to form the final product; 4) desorption of the final product from the surface of the electrode [55]. The number of involved electrons or protons transfer during these steps depends mostly by the adsorption capability of the involved intermediates, affecting the catalytic pathway of the process and leading to the formation of different products.

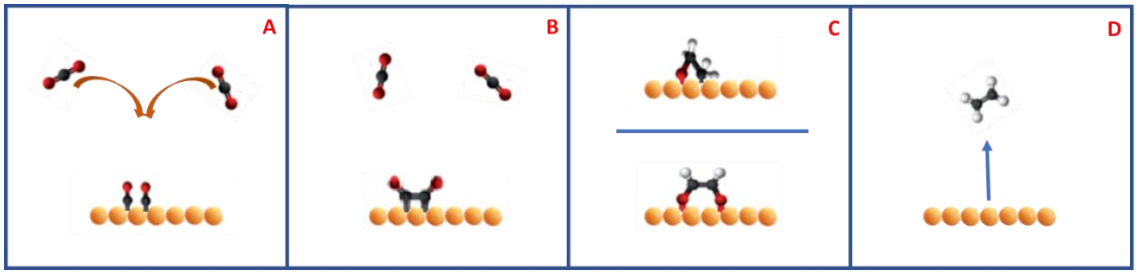

***Figure 1.9**: Steps of eCO_2RR on the surface of a catalyst: A) adsorption of CO_2 molecule on the surface of the catalyst; B) and C) flow of the charge carriers and rearrangement of the product; D) desorption of the product from the surface of the catalyst.*

In particular, the catalytic pathway of CO_2RR on Cu-based catalysts (the aim of this thesis) have been previously investigated by Schouten et al, proposing that it starts from the formation of a negatively charged carboxyl radical CO_2^-(Figure 1.10) followed by its adsorption on the surface of the electrocatalysts [56]. At this point the reaction can proceed via two different pathways: the carboxyl radical can be reduced to form formate, that is easily desorbed in solution, or to form CO. Carbon monoxide can be also protonated to carbonyl and then to methane; or, if the concentration of adsorbed CO on the surface is particularly high, can dimerize, forming ethylene or other C_n products.

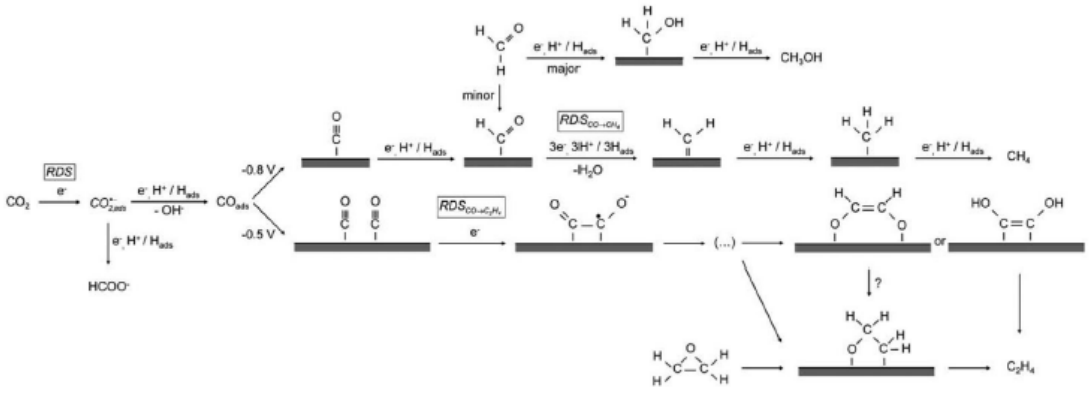

***Figure 1.10**: Proposed mechanism for the eCO₂RR on a Cu surface. From* [56].

Great efforts had been done to optimize the cell setup, the cathodic material and the overall catalytic process, but the present systems still are not able to fulfill the industrial requirements for large scale applications. First, major efforts must be made to synthetize a catalyst capable to selectively drive the process toward the desired product. The control of the selectivity is fundamental to minimize undesirable effect of catalyst poisoning or subsequent problem of products separation. Moreover, despite enormous research efforts towards CO_2 conversion in C_{2+} products, this process is still not economically feasible as a proper balance of overall costs (including costs related to the electrical source and separation of the different products) need to be done [57–59].

Summarizing, e-fuels have the potential to be a promising solution to reduce greenhouse gas emission by using renewable energy sources and recycling CO_2 emitted from those industrial sectors where decarbonization is difficult to achieve but much more research in material and devices design is still needed.

1.4 The role of nanostructuration on the catalytic process

The heterogeneous reduction of CO_2 has the potential to produce valuable chemicals and fuels while simultaneously reducing greenhouse gas emissions. The different methods presented in chapter 1.3 are characterized by promising advantages with still significant drawbacks that limit or preclude their use on real industrial applications. The scalability and economic viability of these approaches is still under debate, mainly due to the significant required energy inputs and the need of sophisticated and dedicated equipment that affect the overall cost of the processes. Moreover, the high stability of CO_2 molecule reduces the overall conversion efficiency. The difficulties in fully understand the particular catalytic pathways for emerging materials is still an important limitation on their optimization. The large variety of parameters that can affect the reaction mechanism often results in low selectivity, with subsequent increased costs related to the separation of the different products [60].

From this point of view the catalyst play a fundamental role in guiding the CO_2 reduction toward a particular product. The ability to tune the structure and morphology of a heterogeneous catalyst at nanoscale level is a powerful tool to modulate catalytic properties in general and therefore, also in the case of CO_2 reduction. Improved catalytic performances upon fine control of size, exposed facets or composition have been shown to occur in metal-based oxides, metals, carbon-based materials or molecular compounds [61,62]. Different strategies have been exploited to tailor materials at the nanoscale, including top-down (i.e., ball milling or nanofabrication) and bottom-up (through chemical synthesis or self-assembly approaches) methods. By rational modification of a catalyst, the coordination of atoms can change and the number of under coordinate atoms can increase, promoting the adsorption of molecules and favoring the overall reactivity (Figure 1.11) [63]. For example, one promising strategy to improve the catalytic behavior of a system is the selection of the exposed facets through facet engineering [64]. Other approaches can be useful for the optimization of a catalyst activity such as the obtainment of porous or 2D morphologies. Porosity can be either intrinsic to the chemical structure or been created through post-synthetic modification, for instance by etching of alloyed NPs [65,66]; the result is a catalyst characterized with an extremely high surface area and an intrinsically enhanced activity. The obtainment of an active nanostructure is important for enhancing reactivity, but to guarantee stability it is necessary that the nanostructure

do not undergoes structural modifications such as sintering or coarsening. Therefore, nanomaterials are often supported on inert or active supports/co catalysts [67]. These supports can be also nanostructured such as 2D flat g-C_3N_4, graphene and derivates or MoS_2. When these supports are used in electrochemical applications, they must be able to compensate the low charge mobility typical of metal oxides. This is achieved by making high and homogeneous dispersion of the nanoparticles onto conductive supports [68]. The close contact between catalyst and support implies an efficient electron and mass transfer.

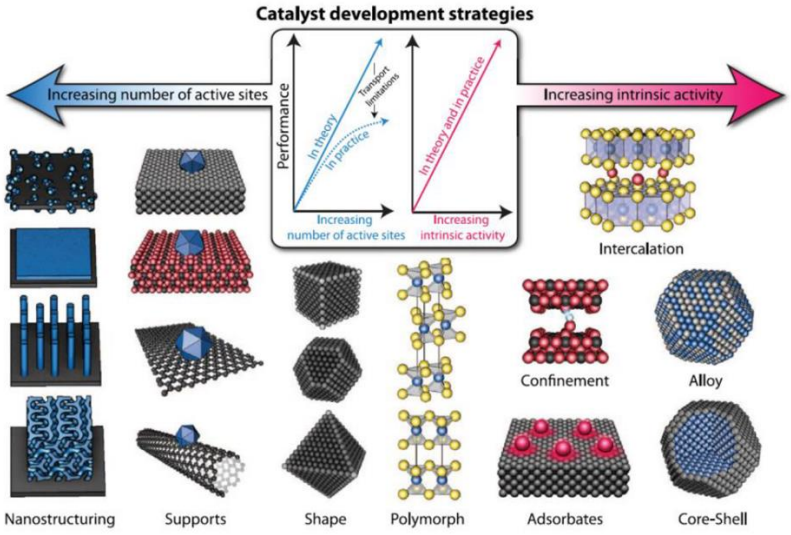

***Figure 1.11**: Different approaches for the improvement of catalytic behavior of a material through increasing of the number of active sites or increasing of intrinsic activity. From* [69].

1.5 Different electrochemical setups for CO_2 Reduction Reaction

Electrochemistry is a branch of chemistry where the interactions that occurs between a material and an electrical voltage are studied and rationalized. Electrocatalysis interprets the effects of an applied potential on the interface between an electrode and an electrolyte. This allows to study redox reactions that occurs at the electrode surface and to obtain indications of the catalytic behavior of the material toward a particular faradaic process. Beside a general behavior, where the reagents of the semi reactions are consumed to form products through flowing of electrons, there are different phenomena that could introduce deviations from the ideality. For example, an unavoidable consequence of an applied potential is the "charging" of the electrode – electrolyte interface: free charges (holes or

electrons) accumulate on the electrode surface, while in the electrolyte there is a buildup of the opposite ions. This result in the formation of a double layer (i.e., a capacitor), and a subsequent capacitive current readable by a potentiostat. Moreover, diffusion of the involved species from bulk solution to the surface of the electrode (where the semi-reaction occurs) can limit the mechanism of the process and affects the overall behavior [70].

To perform electrochemical processes and understand the chemistry involved in the reaction, it is necessary to have at least a second electrode to close the circuit and isolate the entire setup from external interferences. Among different electrochemical cells, three-electrode configuration is the most used setup and the choice for the electrochemical characterization performed throughout this Ph.D. thesis. In this particular configuration, a working electrode (WE), at which the reaction of interest takes place, is faced with a reference electrode (RE) and a counter electrode (CE), where the counter-reaction occurs to close the electric circuit. In the case of CO_2RR performed in aqueous electrolytes, the WE is a negatively charged cathode where CO_2 and protons are reduced, while on the counter electrode H_2O is oxidized to O_2 through Oxygen Evolution Reaction (OER) process. The RE is fundamental in those measurements because it is used as a reference for the applied voltages, thanks to its non-polarizability and the stability of its potential over the time [71]. Different reference electrodes are commonly used for these measurements (in our case Ag/AgCl or Saturated Calomel Electrode, SCE). Generally, potentials are referred/converted to the Reversible Hydrogen Electrode (RHE), a RE that takes in account the variation of the voltage due to a different pH [72]. In order to well compare the results obtained along this work with respect to the state-of-the art, the voltage values recorded vs. Ag/AgCl sat. had been converted to RHE.

From a theoretical point of view, the working potential of an electrochemical cell (V) is directly related to the thermodynamic potentials of the considered reactions (E). Beside this, different parameters can affect the effective voltage of the cell: for this reason, other terms need to be added in the typical expression of voltage (Equation 1.4). These factors are mostly related to the electrode material or the composition of the electrolyte and are describe as: the overpotential that need to be applied in order to have detect reasonable currents (η), the Ohmic loss due to the intrinsic resistance of an electrochemical setup

(V_Ω) and the stabilization voltage (V_t), corresponding to the potential variation due to the degradation of the material during the measure [73].

$$V = E + \eta + V_\Omega + V_t \tag{1.4}$$

All these contributions result in higher operative voltages and resistive heating that could affect the overall efficiency of the electrochemical process and the stability of the entire setup. From this point of view, the minimization of all the different contributions is essential to drive the entire process in an efficient and sustainable way. Overpotentials can be limited by the optimization of the material constituting the electrode, while ohmic losses can be drastically mitigated by optimizing the design of the electrochemical device [74].

In order to study the catalytic properties of a new material devoted for a particular electrochemical process, usually it is appropriate to first use a basic electrochemical device, without membranes to avoid multiple interfaces. For this reason, the electrochemical characterization is usually performed preliminarily in a single chamber cell where the working electrode is typically separated from the other two electrodes, RE and CE, each confined in a bridge and separated from the electrolyte solution by glass frits. Moreover, the possibility to use a Rotating Disk Electrode (RDE) with a fixed geometrical area allows to neglect the issues related to a low diffusion of the involved species and perform hydrodynamic studies (Figure 1.12). More in dept studying of a particular material can be done in more sophisticated setups varying the electrodes or with the addition of a membrane.

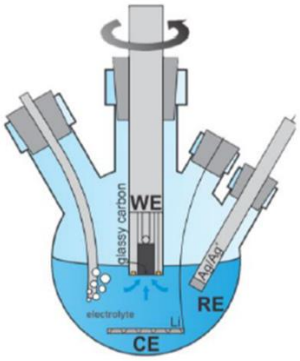

***Figure 1.12**: Schematic representation of a typical 3-electrode electrochemical cell with a Rotating Disk Electrode.*

A more complex electrochemical device respects the single-chamber cell is the so-called H-cell (Figure 1.13). In this kind of electrochemical setup, working electrode and counter electrode are located in two different reaction chambers, separated by a membrane and filled with the chosen electrolyte [75].

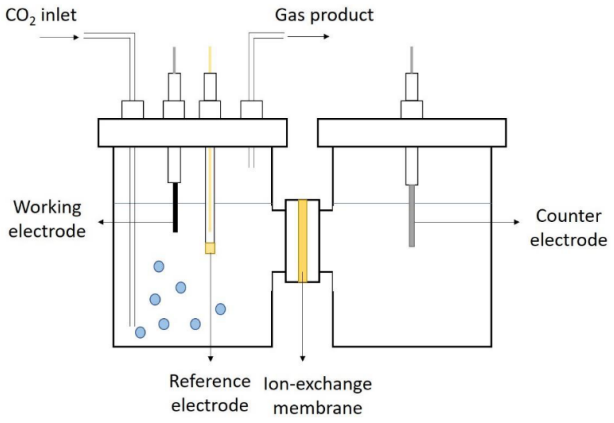

***Figure 1.13**: Schematic representation of a H-cell. From* [75].

The reference electrode is generally introduced in the same chamber of the working electrode, in order to easily control the voltage on the side of the interested process. The catalyst can be a powder deposited on conductive supports like carbon paper, glassy carbon or metal plates. During the catalytic experiment, CO_2 flows on both sides of the device and the gas phase products are collected from the headspace and sent to online Gas Chromatography analysis. The membrane is a fundamental part for the correct functioning of the device, due to its ability to face the hydrostatic pressure from one or both sides of the cell, avoiding at the same time the crossover of different products and their re-oxidation on the counter electrode [76]. Membranes must be permeable to charge carriers to maintain the charge neutrality in the system during operation. Polymer membranes are rated for their charge conductivity and their permeability to other chemicals. While their backbone is based on inert and resistant polymers, the different chemical and structural features of the commercial-available membranes are tailormade in order to fit the desired working conditions (pH of media, minimal permeability to reactants and products). For example, the permeability of the charge carriers on the two sides of a H-cell is guaranteed by the different terminal groups of the chosen membrane. Even the different electrolyte (and so even the choice of the operative pH) affects the selection of the membrane: in case of CO_2RR performed under acidic conditions, the use

of Nafion® membranes is suggested, thanks to their capability to transport protons; On the other hand, the use of Sustainion® membranes is particularly appropriate for electrocatalytic processes performed in alkaline environments. The main advantages of the H-cells are the compact dimensions, ease of use and clean and ability to rapid screen of catalysts. On the other hand, besides many successful works on the lab-scale, H-cells suffers of difficulties on the scaling up, in particular in terms of exposed surface area of the catalyst and the difficulties to reach industrial current densities [77].

A more sophisticated device useful for CO_2RR characterization is the liquid phase electrolyzer (or flow cell), an implementation of H-cell where the two compartments are separated using a particular membrane (Figure 1.14). The main difference with a H-cell is the direct contact of feeding gas (CO_2), electrolyte and electrode, forming an interface called Triple Phase Boundary (TPD). This is possible thanks to the presence of a Gas Diffusion Electrode (GDE) composed of a conductive hydrophilic surface on one side (in contact with the electrolyte), and a hydrophobic and porous structure where the gas can flow. The GDE is able to improve the intimate contact between the catalyst, the gaseous reactant and the electrolyte, minimizing at the same time the resistance due to the insulating gas bubbles of products formed during the electrochemical process [78]. Compared to the typical H-cell, a flow cell with a GDE is able to improve the mass transportations and shorter the diffusion path of CO_2, limiting at the same time the activity of HER process [79]. As a result of these advantages, a nanostructured material, tested in a flow cell, can showed improved activity toward the considered process, allowing to use higher industrial-scaled current densities [80,81]. As reported for other configurations, also Polymer Electrolyte Membrane (PEM) cells show some disadvantages that limits their use in CO_2RR applications. First the high ohmic losses on these particular devices can be significant. due to the presence of many different interfaces and the typical high applied current densities [78]. Moreover, different issues are reported regarding the management of H_2O, the geometrical limitations of these devices and the low stability of the GDL under operative conditions [82].

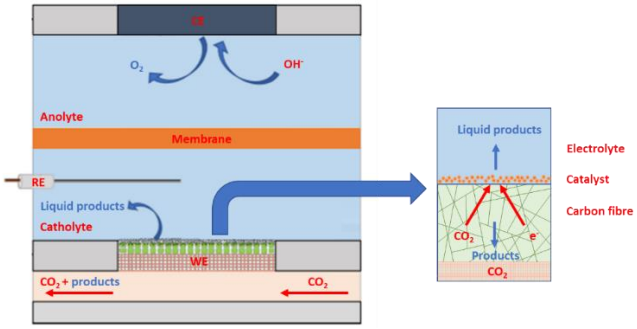

***Figure 1.14**: Schematic representation of a Liquid electrolyzer. Insert: cross section of a GDL (gas diffusion layer).*

One of the main goals of electrocatalysis is the fully understanding of the mechanisms that control the competition between different possible reactions that can occur on the catalysts surface, rationalizing at the same time which catalytic pathways are favored. The ultimate goal is to drive both the activity and the selectivity of the process toward a selected product, especially in multi-steps processes. This is the case of CO_2RR, where carbon dioxide can be converted to a large range of products[83]. To summarize, it is important to consider that real industrial conditions are different from those of lab-scale tests. This implies that the indications obtained in preliminary investigations on simplified electrochemical cells might not be directly or easily transfer to or compared with more realistic industrial cases. In the specific case of CO_2RR process, typical experiments are conducted under pure CO_2 feeding, a condition totally different than the industrial context where the CO_2 supplied is less pure and where the purification increase the overall costs of the process. Working under real conditions means also that the CO_2 feedstock could have some contaminants that can poison the catalysts and make them less efficient toward the CO_2 conversion.

1.6 Aim and outline of the thesis

CO_2 recycling is an essential and promising class of processes where CO_2 is reused and converted in useful fuels or chemicals; however, it still suffers of poor selectivity of the products, low efficiencies and stability of the catalysts. Among the different way to catalyze CO_2 reduction, electrocatalytic CO_2RR processes can be able to face the increased demand and industrial scaling-up productivities. The present Ph.D. thesis was

focused on the development of a synthetic route to prepare Cu-based catalysts for electrochemical CO_2RR, analyzing the activity, the selectivity and stability, with attention to the evaluation of the catalyst nanostructure.

In the first chapter background introduction is reported, focusing on the most important ways to convert CO_2 into other high-value added compounds. After a short overview on the role of CO_2 as greenhouse gas and circular economy, the key features of the different processes of CO_2 reduction are presented, focusing on the electrocatalytic CO_2RR and the role of nanostructure to prepare efficient catalysts.

In chapter 2 an overview of the different synthetic methods and characterization techniques is presented, focusing on structural (XRD), morphological (TEM and SEM) and electrochemical techniques.

In chapter 3, synthesis and characterization of Cu_2O nanoparticles with two different morphologies (cubic and rhombo dodecahedral) are presented. These nanoparticles have been used as electrocatalysts toward the formation of E-fuels through eCO_2RR, highlighting the different behavior of the two shapes in terms of current and selectivity. Moreover, the effects of the electrochemical catalytic process on the obtained nanoparticles have been studied by *operando* or post-characterizations such as EXAFS or SEM. Chapter 4 discusses the formation of Cu_2O-based heterostructures based on different supports such as g-C_3N_4, RGO or MoS_2. This is part of the strategy to increase stability and selectivity of the original unsupported Cu_2O nanoparticles. In particular, syntheses of different composites are presented with a deep characterization of the features of the materials, focusing the attention on the study of CO_2RR activity.

In chapter 5, the problem of stability is further tackled by making bimetallic alloys and structures based on Cu and Sn through a facile and scalable urea glass route. The XRD characterization revealed the intrinsic relationships between the two metal of the materials and the electrochemical CO_2RR studies confirmed an improved catalytic activity toward the reduction of CO_2 respect of the monometallic catalysts.

In chapter 6, a promising TiN nanotube array for gas phase photothermal catalytic CO_2 reduction is briefly presented. The focus was on optimizing the cell configuration/working conditions to obtain decent and promising catalytic performances.

A summary of the work and some future perspectives are presented in chapter 7.

1.7 References

[1] J. Houghton, *Reports Prog. Phys.* 68 (**2005**) 1343–1403.

[2] K.Z. (Canada) Myles Allen (UK), Mustafa Babiker (Sudan), Yang Chen (China), Heleen de Coninck (Netherlands), Sarah Connors (UK), Renée van Diemen (Netherlands), Opha Pauline Dube (Botswana), Kris Ebi (USA), Francois Engelbrecht (South Africa), Marion Ferrat (UK/France), *Ipcc* (**2018**).

[3] C.W. Landsea, *Nature* 438 (**2005**) 1571–1576.

[4] A.A. Khasnis, M.D. Nettleman, *Arch. Med. Res.* 36 (**2005**) 689–696.

[5] P. Friedlingstein, M. O'sullivan, M.W. Jones, R.M. Andrew, L. Gregor, J. Hauck, C. Le Quéré, I.T. Luijkx, A. Olsen, G.P. Peters, W. Peters, J. Pongratz, C. Schwingshackl, S. Sitch, J.G. Canadell, P. Ciais, R.B. Jackson, S.R. Alin, R. Alkama, A. Arneth, V.K. Arora, N.R. Bates, M. Becker, N. Bellouin, H.C. Bittig, L. Bopp, F. Chevallier, L.P. Chini, M. Cronin, W. Evans, S. Falk, R.A. Feely, T. Gasser, M. Gehlen, T. Gkritzalis, L. Gloege, G. Grassi, N. Gruber, Ö. Gürses, I. Harris, M. Hefner, R.A. Houghton, G.C. Hurtt, Y. Iida, T. Ilyina, A.K. Jain, A. Jersild, K. Kadono, E. Kato, D. Kennedy, K. Klein Goldewijk, J. Knauer, J.I. Korsbakken, P. Landschützer, N. Lefèvre, K. Lindsay, J. Liu, Z. Liu, G. Marland, N. Mayot, M.J. Mcgrath, N. Metzl, N.M. Monacci, D.R. Munro, S.I. Nakaoka, Y. Niwa, K. O'brien, T. Ono, P.I. Palmer, N. Pan, D. Pierrot, K. Pocock, B. Poulter, L. Resplandy, E. Robertson, C. Rödenbeck, C. Rodriguez, T.M. Rosan, J. Schwinger, R. Séférian, J.D. Shutler, I. Skjelvan, T. Steinhoff, Q. Sun, A.J. Sutton, C. Sweeney, S. Takao, T. Tanhua, P.P. Tans, X. Tian, H. Tian, B. Tilbrook, H. Tsujino, F. Tubiello, G.R. Van Der Werf, A.P. Walker, R. Wanninkhof, C. Whitehead, A. Willstrand Wranne, R. Wright, W. Yuan, C. Yue, X. Yue, S. Zaehle, J. Zeng, B. Zheng, *Earth Syst. Sci. Data* 14 (**2022**) 4811–4900.

[6] R. Revesz, K. Arrow, L. Goulder, R.E. Kopp, M. Livermore, M. Oppenheimer, T. Sterner, *Nature* 508 (**2014**) 173–175.

[7] R.A. Kerr, *Science.* 316 (**2007**) 188–190.

[8] B. Godskesen, N. Meron, M. Rygaard, Life Cycle Assessment: Theory and Practice, Springer, **2017**.

[9] G. Finnveden, M.Z. Hauschild, T. Ekvall, J. Guinée, R. Heijungs, S. Hellweg, A. Koehler, D. Pennington, S. Suh, *J. Environ. Manage.* 91 (**2009**) 1–21.

[10] S. Hellweg, L.M.I. Canals, *Science.* 344 (**2014**) 1109–1113.

[11] W.R. Stahel, *Nature* 531 (**2016**) 435–438.

[12] S. Geisendorf, F. Pietrulla, *Thunderbird Int. Bus. Rev.* 60 (**2018**) 771–782.

[13] Https://www.Europarl.Europa.Eu/News/En/Headlines/Economy/20151201STO05603/Circular-Economy-Definition-importance-and-Benefits.

[14] J. Camacho-Otero, C. Boks, I.N. Pettersen, *Sustain.* 10 (**2018**) 2758.

[15] A.R. Davis, B.G. Oliver, *J. Solution Chem.* 1 (**1972**) 329–339.

[16] D.A. Palmer, R. Van Eldik, *Chem. Informationsd.* 15 (**1984**) 651–731.

[17] F.J. Millero, *Chem. Rev.* 107 (**2007**) 308–341.

[18] H. Zhong, K. Fujii, Y. Nakano, F. Jin, *J. Phys. Chem. C* 119 (**2015**) 55–61.

[19] M.J. Li, H.H. Zhu, J.Q. Guo, K. Wang, W.Q. Tao, *Appl. Therm. Eng.* 126 (**2017**) 255–275.

[20] M. Raventós, S. Duarte, R. Alarcón, *Food Sci. Technol. Int.* 8 (**2002**) 269–284.

[21] S.Y.W. Chai, L.H. Ngu, B.S. How, M.Y. Chin, K. Abdouka, M.J.B.A. Adini, A.M. Kassim, *Int. J. Greenh. Gas Control* 119 (**2022**) 103727.

[22] L. Holappa, *Metals (Basel).* 10 (**2020**) 1117.

[23] R. Steeneveldt, B. Berger, T.A. Torp, *Chem. Eng. Res. Des.* 84 (**2006**) 739–763.

[24] E.S. Rubin, J.E. Davison, H.J. Herzog, *Int. J. Greenh. Gas Control* 40 (**2015**) 378–400.

[25] T. Qi, X. Zhang, V.J. Karplus, *Energy Policy* 68 (**2014**) 60–69.

[26] S. Perathoner, G. Centi, *ChemSusChem* 7 (**2014**) 1274–1282.

[27] Z. jun Wang, H. Song, H. Liu, J. Ye, *Angew. Chemie - Int. Ed.* 59 (**2020**) 8016–8035.

[28] D. Mateo, P. Maity, G. Shterk, O.F. Mohammed, J. Gascon, *ChemSusChem* 14 (**2021**) 5525–5533.

[29] M. González-Castaño, B. Dorneanu, H. Arellano-García, *React. Chem. Eng.* 6 (**2021**) 954–976.

[30] J.E. Whitlow, *Am. Inst. Phys.* (**2003**) 1116–1123.

[31] T. Sakakura, J.C. Choi, H. Yasuda, *Chem. Rev.* 107 (**2007**) 2365–2387.

[32] C. Ampelli, S. Perathoner, G. Centi, *Philos. Trans. R. Soc. A Math. Phys. Eng. Sci.* 373 (**2015**).

[33] A. Wolf, A. Jess, C. Kern, *Chem. Eng. Technol.* 39 (**2016**) 1040–1048.

[34] P. Borisut, A. Nuchitprasittichai, *Front. Energy Res.* 7 (**2019**) 1–10.

[35] D.S. Marlin, E. Sarron, Ó. Sigurbjörnsson, *Front. Chem.* 6 (**2018**) 446.

[36] R.L. Tyne, P.H. Barry, M. Lawson, D.J. Byrne, O. Warr, H. Xie, D.J. Hillegonds, M. Formolo, Z.M. Summers, B. Skinner, J.M. Eiler, C.J. Ballentine, *Nature* 600 (**2021**) 670–674.

[37] Ö. Biçen Ünlüer, R. Say, A. Ersöz, *Biotechnol. Appl. Biochem.* 68 (**2021**) 392–403.

[38] P. Savakis, K.J. Hellingwerf, *Curr. Opin. Biotechnol.* 33 (**2015**) 8–14.

[39] H. Salehizadeh, N. Yan, R. Farnood, *Chem. Eng. J.* 390 (**2020**) 124584.

[40] J. Wu, Y. Huang, W. Ye, Y. Li, *Adv. Sci.* 4 (**2017**) 1700194.

[41] J. Ran, M. Jaroniec, S.Z. Qiao, *Adv. Mater.* 30 (**2018**) 1704649.

[42] P. Liu, X. Peng, Y.-L. Men, Y.-X. Pan, *Green Chem. Eng.* 1 (**2020**) 33–39.

[43] S. Zeng, P. Kar, U.K. Thakur, K. Shankar, *Nanotechnology* 29 (**2018**) 052001.

[44] S.R. Lingampalli, M.M. Ayyub, C.N.R. Rao, *ACS Omega* 2 (**2017**) 2740–2748.

[45] S. Nahar, M.F.M. Zain, A.A.H. Kadhum, H.A. Hasan, M.R. Hasan, *Materials (Basel).* 10 (**2017**).

[46] Z. Wang, S. Akter Monny, L. Wang, *ChemNanoMat* 6 (**2020**) 881–888.

[47] M. Liu, Y. Yi, L. Wang, H. Guo, A. Bogaerts, *Catalysts* 9 (**2019**) 275.

[48] X. Chang, T. Wang, J. Gong, *Energy Environ. Sci.* 9 (**2016**) 2177–2196.

[49] X. Meng, T. Wang, L. Liu, S. Ouyang, P. Li, H. Hu, T. Kako, H. Iwai, A. Tanaka, J. Ye, *Angew. Chemie - Int. Ed.* 53 (**2014**) 11478–11482.

[50] J. Ren, S. Ouyang, H. Xu, X. Meng, T. Wang, D. Wang, J. Ye, *Adv. Energy Mater.* 7 (**2017**) 1601657.

[51] Y. Quan, J. Zhu, G. Zheng, *Small Science* (**2021**) 1, 2100043.

[52] F. Ausfelder, K. Wagemann, *Chemie-Ingenieur-Technik* 92 (**2020**) 21–30.

[53] Q. Lu, F. Jiao, *Nano Energy* 29 (**2016**) 439–456.

[54] P. Saha, S. Amanullah, A. Dey, *Acc. Chem. Res.* 55 (**2022**) 134–144.

[55] L. Zhang, Z.J. Zhao, J. Gong, *Angew. Chemie - Int. Ed.* 56 (**2017**) 11326–11353.

[56] K.J.P. Schouten, Y. Kwon, C.J.M. Van Der Ham, Z. Qin, M.T.M. Koper, *Chem. Sci.* 2 (**2011**) 1902–1909.

[57] A. Badgett, M. Ruth, A. Crow, G. Grim, Y. Chen, L. Hu, L. Tao, W. Smith, K.C. Neyerlin, R. Cortright, *J. Clean. Prod.* 351 (**2022**) 131564.

[58] J.M. Spurgeon, B. Kumar, *Energy Environ. Sci.* 11 (**2018**) 1536–1551.

[59] S. Garg, M. Li, A.Z. Weber, L. Ge, L. Li, V. Rudolph, G. Wang, T.E. Rufford, *J. Mater. Chem. A* 8 (**2020**) 1511–1544.

[60] X. She, Y. Wang, H. Xu, S. Chi Edman Tsang, S. Ping Lau, *Angew. Chemie - Int. Ed.* 61 (**2022**) e202211396.

[61] J. Rosen, G.S. Hutchings, Q. Lu, S. Rivera, Y. Zhou, D.G. Vlachos, F. Jiao, *ACS Catal.* 5 (**2015**) 4293–4299.

[62] U.O. Nwabara, E.R. Cofell, S. Verma, E. Negro, P.J.A. Kenis, *ChemSusChem*

13 (**2020**) 855–875.

[63] W. Zhu, R. Michalsky, Ö. Metin, H. Lv, S. Guo, C.J. Wright, X. Sun, A.A. Peterson, S. Sun, *J. Am. Chem. Soc.* 135 (**2013**) 16833–16836.

[64] R. Bin Song, W. Zhu, J. Fu, Y. Chen, L. Liu, J.R. Zhang, Y. Lin, J.J. Zhu, *Adv. Mater.* 32 (**2020**) 1903796.

[65] M.I. Gonzalez, E.D. Bloch, J.A. Mason, S.J. Teat, J.R. Long, *Inorg. Chem.* 54 (**2015**) 2995–3005.

[66] Q. Lu, J. Rosen, Y. Zhou, G.S. Hutchings, Y.C. Kimmel, J.G. Chen, F. Jiao, *Nat. Commun.* 5 (**2014**) 3242.

[67] B. Zhang, Y. Jiang, M. Gao, T. Ma, W. Sun, H. Pan, *Nano Energy* 80 (**2021**) 105504.

[68] X. Hu, J. Hu, S. Zheng, Y. Fan, H. Li, S. Zhang, W. Liu, B. Zha, F. Huo, F. Saleem, *Chem. - An Asian J.* 17 (**2022**).

[69] Z.W. She, J. Kibsgaard, C.F. Dickens, I. Chorkendorff, J.K. Nørskov, T.F. Jaramillo, *Science* 355 (**2017**).

[70] L.H. Hess, N. Fulik, J. Röhner, E. Zhang, S. Kaskel, E. Brunner, A. Balducci, *Energy Storage Mater.* 37 (**2021**) 501–508.

[71] S. Papavinasam, *Tech. Corros. Monit.* (**2008**) 49–85.

[72] Y. Gao, Q. Wu, X. Liang, Z. Wang, Z. Zheng, P. Wang, Y. Liu, Y. Dai, M.H. Whangbo, B. Huang, *Adv. Sci.* 7 (**2020**) 1902820.

[73] S. Trasatti, *Int. J. Hydrogen Energy* 20 (**1995**) 835–844.

[74] H.J. Gores, H. Schweiger, Encyclopedia of Applied Electrochemistry, **2014**.

[75] R. Lin, J. Guo, X. Li, P. Patel, A. Seifitokaldani, *Catalysts* (**2020) 473**.

[76] D.R. Dekel, *J. Power Sources* 375 (**2018**) 158–169.

[77] T. Burdyny, W.A. Smith, *Energy Environ. Sci.* 12 (**2019**) 1442–1453.

[78] K. Liu, W.A. Smith, T. Burdyny, *ACS Energy Lett.* 4 (**2019**) 639–643.

[79] A. Seifitokaldani, C.M. Gabardo, T. Burdyny, C.T. Dinh, J.P. Edwards, M.G. Kibria, O.S. Bushuyev, S.O. Kelley, D. Sinton, E.H. Sargent, *J. Am. Chem. Soc.* 140 (**2018**) 3833–3837.

[80] T.N. Nguyen, C.T. Dinh, *Chem. Soc. Rev.* 49 (**2020**) 7488–7504.

[81] S. Hernandez-Aldave, E. Andreoli, *Catalysts* 10 (**2020**) 713.

[82] D.M. Weekes, D.A. Salvatore, A. Reyes, A. Huang, C.P. Berlinguette, *Acc. Chem. Res.* 51 (**2018**) 910–918.

[83] T. Chatterjee, E. Boutin, M. Robert, *Dalt. Trans.* 49 (**2020**) 4257–4265.

Chapter 2

Characterization techniques

2.1 Introduction

Materials can exhibit unique new properties or behaviors when synthesized at the nanoscale [1,2]. Therefore, adequate structure and morphology characterization of nanomaterials is of paramount importance to understand the relationship between nanostructure and performances. Consistently, a brief description of the experimental techniques used in this Ph.D. thesis is reported. Several characterizations have been used to study the structure, morphology and texture of the investigated nanomaterials. In particular, X-ray Diffraction and Raman spectroscopies are widely used techniques to unravel the structure of the synthetized materials and, in the case of carbon-based structures, to investigate the nature of organic species adsorbed on the surface of the catalysts. On the other hand, X-Ray Photoelectron Microscopy and X-ray Absorption Spectroscopy are useful tools to study the chemical state and composition of the catalyst surface and of the bulk, respectively. Microscopy characterization is used to investigate morphological features of a material.

Many efforts have been dedicated to study the different synthetized materials from an electrochemical point of view. Therefore, in the following subchapters it will be presented also a rapidly overview of the most common electrochemical techniques and characterizations, both under Direct Current (DC) and Alternate Current (AC) fields. To conclude, a short overview of the different experimental procedures is presented.

2.2 Powder X-Ray Diffraction

X-Ray Diffraction (XRD) is a widely-used technique to investigate the structure of materials [3]. XRD is based on the diffraction phenomenon that occurs when x-ray photons are scattered by crystallographic lattice planes. The diffracted photons are characterized on a maximum of the intensity when a constructive interference occur between the waves, as described by the Bragg's law (equation 2.1):

$$n\lambda = 2dsen\theta \qquad (2.1)$$

where n correspond to the diffraction order, λ the wavelength of the incident x-ray, d is the interplanar spacing and θ is the incident angle of the beam.

The analysis of the diffraction pattern gives information regarding the different lattice planes of the material, the typical features of the unit cell and the crystallite size. In particular, the crystallite size is directly extrapolated from the width of considered reflections on the XRD diffractogram, by applying the Scherrer's equation (equation 2.2):

$$\tau = \frac{K\lambda}{\beta \cos\theta} \qquad (2.2)$$

where τ is the crystallite mean size, K is a constant related to the peak shape, λ is the x-ray wavelength, β is the full width at half maximum (FWHM) and θ is the Bragg angle.

From the analysis of equation 2.2, it is possible to observe that materials with small crystallite size are directly related to broad reflections with higher FWHM. Based on the same principle, amorphous materials display no sharp reflections but only broad bands due to the absence of long-range order. Beside these considerations, Scherrer's law is not always reliable due to the dependency of the broadening to other factors such as the presence of grain boundaries or dislocations, crystalline mismatch and intrinsic stress or impurities in the crystalline lattice. In addition, the β value may be affected by instrumental factors. In this Ph.D. thesis, the crystalline structure of the different materials was investigated by X-ray diffraction (XRD) using a high-resolution X-ray powder diffractometer (PANalytical X'Pert Pro MPD) with Cu Kα radiation (λ = 0.1541 nm). The measurements were performed in Bragg−Brentano geometry in a 2θ range of 10−100° with a step size of 0.033°.

2.3 Raman Spectroscopy

Raman spectroscopy is a technique used to characterize the chemical phase of a sample by studying the vibrations of modes related to the scattering of light [3]. In this technique, a laser is used to irradiate a sample, and the scattered light is collected and analyzed. The particular light source can be either at the same wavelength as the incident laser light (Rayleigh scattering) or at a different wavelength due to the vibrational energy of the

sample molecules (Raman scattering). The Raman scattering occurs due to the inelastic scattering of the incident photons by the molecular vibrations of the sample. By measuring the Raman scattering, information about the vibrational modes of the sample can be obtained. The different information can be used to identify the molecular structure of the sample or to study its physical properties. In particular, Raman is exploited to understand the vibrational modes for crystalline materials through the analysis of the characteristic vibrations of a probe atom in the sample crystalline cell.

There are two types of Raman spectroscopy: spontaneous and stimulated. In spontaneous Raman spectroscopy, the sample is irradiated with a laser and the scattered light is collected and analyzed. In stimulated Raman spectroscopy, two laser beams are used: one to excite the sample and a second to probe the Raman scattering. This technique can provide higher sensitivity and faster acquisition times compared to spontaneous Raman spectroscopy.

In Raman spectroscopy, the scattered light at a different frequency (Raman scattering) is due to the interaction between the incident laser light and the vibrational modes of the molecules in the sample. Vibrational modes are the specific ways in which the atoms in a molecule, or in a crystalline cell, can vibrate relative to each other. Each vibrational mode has a specific energy associated with it, and this energy can be probed by Raman spectroscopy. When the incident laser light interacts with the sample, it excites the vibrational modes of the molecules causing them the transition to higher vibrational states. Some of the scattered light from the sample has a frequency that corresponds to the difference in energy between the initial and final vibrational states of the molecules. This Raman scattered light carries information about the vibrational modes of the molecule or of the atoms in the crystalline lattice and can be used to identify the molecular / crystalline structure of the sample or to study its physical properties. Different types of vibrational modes can be excited in Raman spectroscopy, including stretching modes (related to the stretching of chemical bonds), bending modes (related to the bending of chemical bonds), and torsional modes. Torsional modes involve the twisting of chemical bonds. The frequencies and intensities of the Raman scattered light depend on the types of vibrational modes that are excited and the molecular or crystalline structure of the sample. Overall, Raman spectroscopy provides a powerful tool for studying the vibrational modes of molecules or crystalline materials and has a wide range of

applications in many scientific fields [4]. Raman spectra have been acquired using a Renishaw InVia™ confocal Raman microscope coupled with three lasers with respectively 533, 632 and 785 nm as wavelength.

2.4 X-Ray Photoelectron Spectroscopy

X-ray Photoelectron Spectroscopy (XPS) is a technique that exploit the photoelectric effect to evaluate the binding energy of electrons and their kinetic energy and to have information regarding the chemical state of the first layers of a sample. Indeed, due to the short inelastic mean free path of the photoelectrons in matter, photoemission spectroscopies give reliable composition information only at the surface and nearby (1-10 nm thickness). Thanks to this interesting feature, XPS is a very useful tool to evaluate phenomena that occurs on the surface of catalysts and their effects on its chemical state [5,6]. Moreover, XPS gives much information about the chemical nature of the nearest neighbours and the hybridization state of different species with a large variety of materials such as metals, semiconductors, polymers and, in general, nanostructured materials [7,8]. Besides the interesting information gives by this technique, XPS shows even limitations, mostly related to the experimental setups used to these characterizations. In fact, generally XPS require high vacuum or ultra-high vacuum conditions ($<10^{-9}$ millibar), that limits the uses of this techniques for ex-situ experiments. Moreover, ultra-high vacuum or x-ray could affect the texture of the sample, modifying its structure during the analysis.

As the energy of the x-ray is known (i.e. 1486.7 eV for Al Kα sources) and the kinetic energies of emitted electrons are measured during the analysis, the electron binding energy can be obtained by applying the energy conservation equation (equation 2.3):

$$BE = E_p - (E_k + \Phi) \qquad (2.3)$$

with *BE* being the electron binding energy, E_p is the x-ray photon energy, E_k the photoelectron kinetic energy (measured during analysis) and Φ is the work function.

An XPS spectrum shows the detected photoelectrons as counts toward their Binding Energy and each element has its own characteristic spectrum, where the different oxidation states are referred and related to its electronic configuration. Even if the counts are proportional to the amount of the particular element in a small sampling volume, the

quantitative accuracy of the technique is affected by different parameters such as the intensity of the obtained signal, the homogeneity and uniformity of the sample or the signal to noise ratio. To improve the overall quality of the acquired spectra, it is possible to perform these measurements exploiting synchrotron radiation. A typical instrument for XPS analysis is made with characteristic parts that includes a x-ray source, different chambers where sample is placed and ultra-high vacuum is maintained and a series of electromagnetic lenses that allows to focalize the photoemitted electrons. The analytical part is based on an electron energy analyser (Figure 2.1), composed by two hemispherical conductive magnets, and a detector.

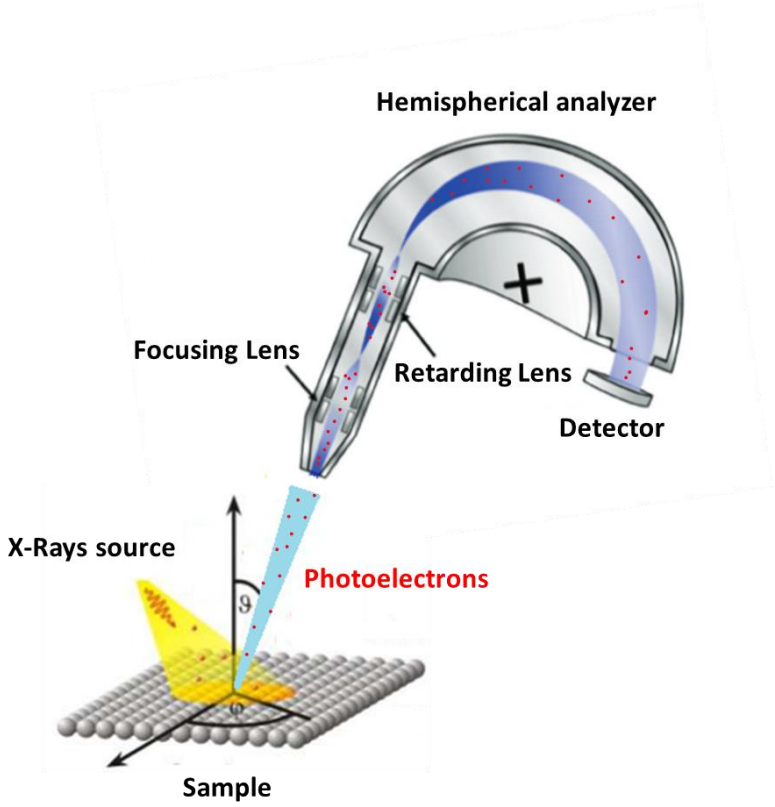

***Figure 2.1**: Scheme of a typical XPS instrument.*

2.5 X-ray Absorption Spectroscopy

X-ray Absorption Spectroscopy (XAS) is a useful technique employed for the study of local geometric and electronic structure of matter [9]. In particular, XAS measures the dependency of the variation of x-ray absorption coefficient on varying the energy of the x-ray near the absorption edge of a particular element. The definition of the absorption

coefficient μ(E) rise directly from the Lambert Beer's law, when x-rays pass through a body of *l* as length. This law allows to understand the relationship between the energy of the transmitted radiation $I_t(l)$ and the incident radiation I_0 by the equation 2.4:

$$I_l(l) = I_0 e^{-\mu(E)l} \qquad (2.4)$$

Where I_l is the transmitted intensity and $\mu(E)$ is the energy-dependent x-ray absorption coefficient. At larger energy regions, $\mu(E)$ varies approximately as (equation 2.5):

$$\mu(E) \approx \frac{dZ^4}{mE^3} \qquad (2.5)$$

Where *d* is the target density, *Z* the atomic number and *m* the atomic mass. Accordingly with equation 2.5, the absorption coefficient $\mu(E)$ is directly proportional to the atomic number of the elements and it decreases with increasing of the radiation energy. At the smallest x-ray energies for which the photon can be absorbed, the photoelectron will be excited to unoccupied bound states of the absorbing atom. This can lead to a strong increase of the absorption coefficient at particular x-ray energies corresponding to the energy difference between the core level and the unoccupied states (pre-edge absorption bands). When photon energy increases, transitions to continuum states are promoted and the obtained wave can scatter at the neighbouring atoms, causing an interference between the emitted and scattered waves that could induce a variation of the $\mu(E)$. This interference, that depends even on the geometry of the system, the distribution of the atoms that bound the central atom or the wavelength of the photoelectron, can be constructive or destructive, causing an energy-dependent final state and a dependency of absorption coefficient from the energy of the radiation [10]. Three main regions can be distinguished from the analysis of an XAS spectra (Figure 2.2) such as the pre-edge region, the X-Ray Absorption Near Edge Structure (XANES) and the Extended Absorption Fine Structure (EXAFS).

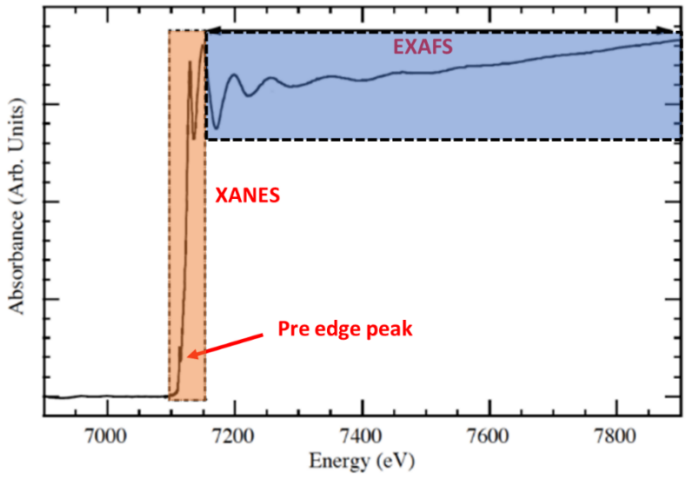

***Figure 2.2**: Characteristic regions of a typical XAS spectrum.*

XANES spectra are dependent on the different chemical bonding of the considered species, and it can exhibit different features based on the chemical oxidation states of the involved species. These features are affected by multiple scattering phenomena, and they could depend on the local geometry of the absorbing atom. The analysis of XANES region can gives useful information related to the coordination chemistry of the absorbing atom, the possible hybridizations of the orbitals and, more in general, the chemical state of the different crystal phases [11,12]. Besides improvements in recent years, theoretical simulations of XANES spectra are still demanding. Therefore, XANES spectra are generally compared with those of pure standards and in many cases, the XANES analysis is empirically based on linear combinations of spectra of "reference compounds". In the EXAFS region (photon energies above 30 eV after the edge), the core electron is promoted to the continuum state and the signal depends on the neighbouring environment of the absorbing atom. EXAFS spectra give much information related to the coordination chemistry of the system, in particular in terms of type and number of neighbour atoms, and interatomic distances [13].

XAS experiments are typically performed at synchrotron facilities since there is the need of the variation of the incident radiation energy. In a typical XAS beamline, x-rays are firstly separated and selected based on the different wavelength trough a double crystal monochromator and send to the sample by appropriate mirrors. During these experiments, the energy of the radiation is tunned, and the absorption coefficient is measured. In this

configuration, the measure of $\mu(E)$ can be obtained by direct measure of the incident and transmitted intensities of the radiation (so-called transmission mode) or by the measure of the incident radiation and the decay ones such as fluorescent radiation of Auger electrons (Fluorescence or electron yield mode) (Figure 2.3).

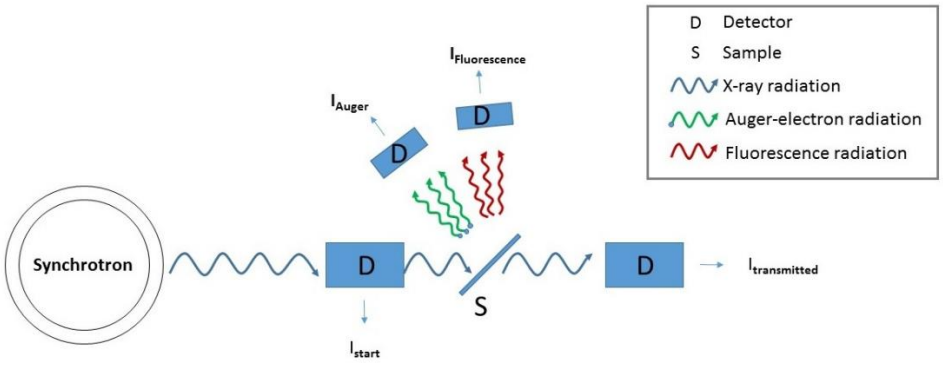

***Figure 2.3**: Schematic representation of a typical XAS experimental facility.*

In general, the two regions of the spectrum are analysed separately due to the different information that can be extracted. Data analysis is characterized by different characteristic steps where the first is the so-called normalization of the spectrum, where the contribution of sample thickness is removed prior to the fitting process. The normalization of XANES spectra is performed by subtracting the pre-edge line from the measured spectrum over the whole energy range and division by $\Delta\mu_0$ prior to levelling the spectrum after the threshold.

The elaboration of EXAFS region is generally more difficult, and more processing steps are required. First, the fine structure *X(E)* is obtained from the absorption background by fitting the pre- and post-edge lines. The pre-edge is subtracted from the experimental spectrum at every energy value and the background $\mu_0(E)$ is approximated by a spline function that approaches the post-edge line at energies over the absorption edge. The difference between absorption coefficient $\mu(E)$ and the background $\mu_0(E)$ is normalized toward $\Delta\mu_0$, resulting in the fine structure *X(E)*. To find *X(k)* the threshold energy E_0 is needed: this is typically considered as the maximum of the derivative of $\mu(E)$ toward *E* or as the energy value determined at half height of the step. Following, a Fourier transform (FT) into R-space is applied, giving useful information regarding all the contributions related with the scattering process. Due to the difficulties of interpretations of FT

functions, both real and imaginary part need to be considered in the processing steps to achieve a complete interpretation of the experimental measure.

2.6 Microscopy techniques

Acquisition of accurate and representative images of nanomaterials, approaching atomic resolution is mandatory in the field of nanotechnology. In this respect, electron microscopies are pivotal for the investigation of nanostructured materials. Modern electron microscopes are suitable for the morphological structural study of many different materials such as nanoparticles, clusters or heterostructures.

The first fundamental parameter of a microscope (in particular for electron microscopy) is its resolution, defined as the minimum distance where two different objects can be distinguished. In a Transmission Electron Microscopy (TEM), the limitations of a typical optical microscope are easily overcome thanks to its high resolution [14]. The resolution of a microscope depends on several parameters, but it is mainly related to aberration and diffraction. Aberration is explained by geometrical optics and is limited by enhancing the optical quality of the instrument. Diffraction, on the other hand, is tangled to the nature of the wave used for the observation. If considering diffraction only, the maximum theoretical resolution that a microscope can achieve is related to the radiation wavelength, according to the Rayleigh criterion, that puts the resolution limit of any imaging process to the order of the wavelength used. From this concept it is possible to understand that normal optical microscopes are not suitable for the characterization of nanomaterials due to their low maximum theoretical resolution. On the other hand, the resolution of an electron microscope allows to achieve nanoscale magnifications.

In a typical TEM instrument, the electrons are accelerated by a voltage *V*, acquiring a potential energy *eV* that is converted to kinetic energy of the electrons at the end of the accelerating section. Equating the two energies, the momentum as a function of the potential can be defined (equation 2.6 and 2.7):

$$eV = \frac{1}{2} m_0 V^2 \qquad (2.6)$$

$$p = \sqrt{2 m_0 eV} \qquad (2.7)$$

The value of λ of an electron can be obtained by substituting equation 2.7 in the typical De Broglie's relationship. For instance, an electron accelerated to 100 keV has a wavelength of about 0.004 nm, that is 100 times smaller than the diameter of an atom. In addition, increasing the accelerating voltage, the electron's wavelength will decrease. However, it must be highlighted that equations 2.6 and 2.7 do not consider the relativistic effect that cannot be neglected for energies above 100 keV. Moreover, there are even some practical limitations related to the microscopes to take in account (such as the homogeneity of the magnetic lenses or some aberrations effects), limiting the resolution of this technique [15]. Nevertheless, atomic scale resolution is achievable by the use of modern instruments like aberration corrected TEM (AC-TEM) in which spatial and spectral resolution is significantly improved, even when using low accelerating voltages (Figure 2.4) [16]. The possibility to have great resolutions without using high accelerating voltages is definitely advantageous in case of unstable materials, where a strong electron beam could affect the nanostructuration or the stability of the sample [17].

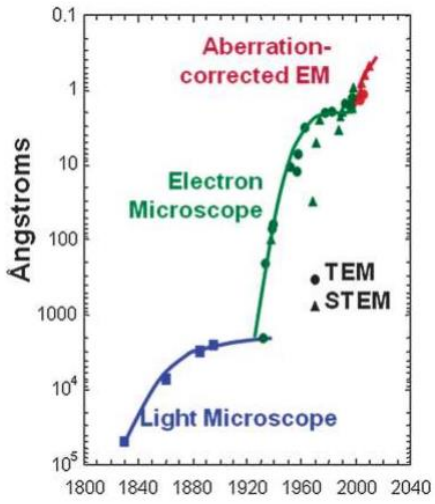

***Figure 2.4**: Spatial resolution of different microscopy instruments over the years.*

In a typical TEM instrument, an electron beam is generated on the top of a vertical column and directed to pass through a sample positioned in a holder aligned with the beam (Figure 2.5). Two common types of electron sources are used in a TEM instrument that are thermionic emission source and Field Emission Gun (FEG) and they are characterized by the way electrons are generated. After that the electrons are generated from the source, these particles are accelerated by an electrostatic field before entering the column; the

strength of the field control the kinetic energy of the electrons. The column is kept under ultra-high vacuum in order to drastically reduce the scattering of electron beams due to the presence of gaseous atoms. Some electron lenses are positioned along the column and helps to maintain the beam focused and aligned to the sample. When the beam reaches the specimen, the electrons pass through the sample, interacting with its crystal structure and generating diffracted and non-diffracted electrons. These electrons are focused by another lens to the back focal plane (BFP), where a diffraction pattern is formed and in which every spot is related to the reflection of crystal planes in one particular orientation. Images and diffraction patterns are visualized on a fluorescent screen and may be digitally recorded using a camera positioned below this screen.

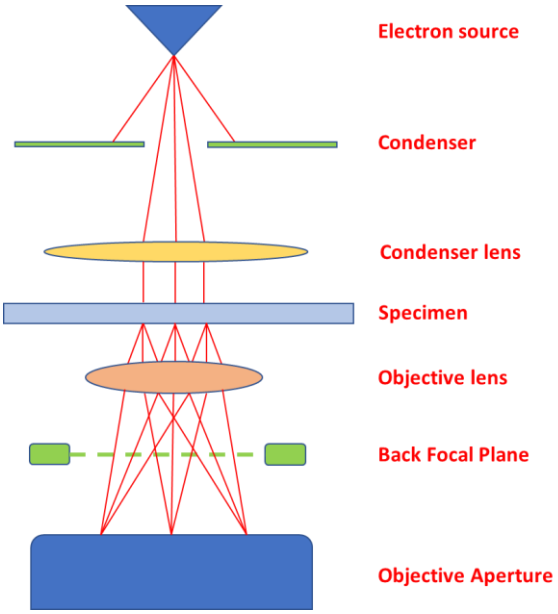

Figure 2.5: *Schematic representation of a TEM column.*

Generally, the diffraction pattern is obtained by selecting a specific area with particular lenses, in order to avoid the saturation of the camera sensor. This operation generates the so-called Selected Area Electron Diffraction images (SAED) [18]. After this selection of the diffraction pattern area, different detections systems could be used (Figure 2.6). The direct diffracted electrons could form the so-called Bright Field (BF) mode, while those collected from scattered electrons result in Dark Field (DF) mode. The BF detector is aligned to the transmitted electrons while the DF detector is annular and surrounds the BF detector. Another detector, positioned at very high angles with respect to the

transmitted beam, can be mounted on the TEM instrument (High Angle Annular Dark-Field detector, HAADF). The images obtained by this detector have a high z-contrast and this technique is particularly advantageous for detecting heavy metal nanostructures. High Resolution TEM (HR-TEM) consists in the use of high voltages to increase the resolution of the typical measurements and it is very useful to characterize crystalline lattices, planar distances or eventual defects on the crystalline structure [19]. On the other hand, the use of high voltages could induce some modifications or damages to the structure of the sample and there are still issues related to the representation of a crystalline 3D structure in a 2D image.

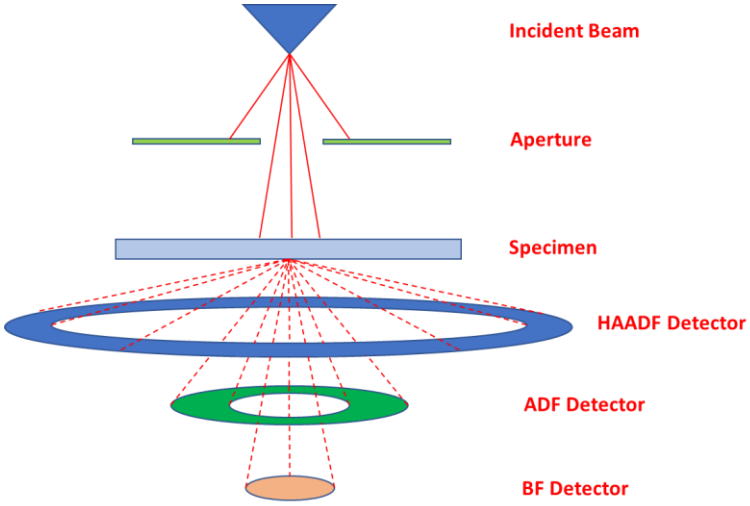

***Figure 2.6**: Schematic representation of the various detectors in a TEM.*

From the inelastic interactions of the electrons with the sample, in which energy is transferred, it is possible to obtain information regarding the composition of a sample. Energy transfer from an incoming high energy electron to core electrons of the atoms sample may result in the ionization of the atom itself forming a hole that can recombine with higher energy level electrons releasing the excess under x-ray photons. These photons are characteristic of the atoms nature from which it was emitted and they can collected and analysed using x-ray Energy Dispersive Spectroscopy (EDS), building a spectrum of the elemental composition of the sample [20].

Scanning Electron Microscopy (SEM) is another common microscopy technique where an electronic beam is focalized on a specimen and used to create an imagine that shows

the morphology of the sample. In particular, SEM exploit the secondary electrons (SE) emitted from the sample to form the image allowing the morphological characterization even to thick samples. Secondary electrons are the most common electrons used for imaging due to high abundance and they are arbitrarily defined as electron with less than 50 eV of energy after the exit from the sample. A SEM instrument is made of different main components such as the electron source, electron lenses, the specimen and the detectors (Figure 2.7).

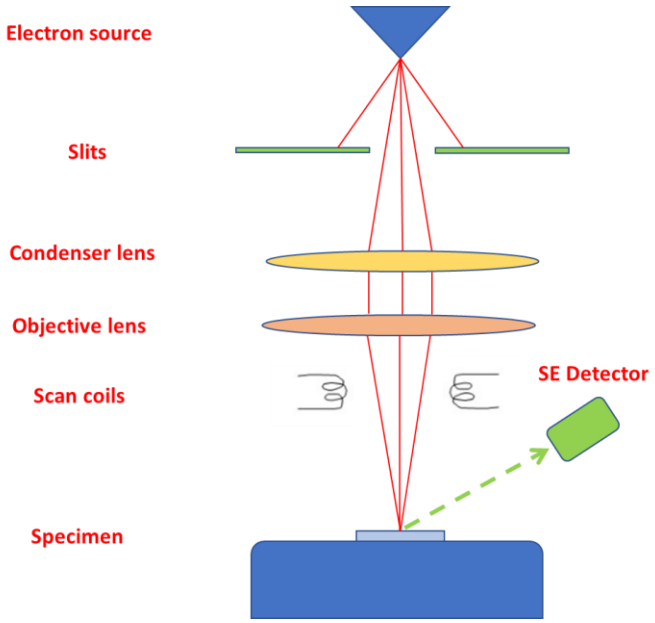

***Figure 2.7**: Schematic representation of a typical SEM instrument.*

The secondary electron detector (SED) is the main tool to form the image on a SEM due to the high amount of emitted secondary electrons. These electrons form images of the morphology of the sample, but they cannot give information regarding its composition. To do this, SEM can be equipped with a BackScatter Electron Detector (BSED) that is able to detect the backscattered electrons that are more energetic and very sensitive to the atomic number, giving information regarding which atoms are present in the specimen.

In this Ph.D. thesis, the morphology of fabricated nanostructures was investigated using a Hitachi FE-SEM 4800 scanning electron microscope (SEM) and TEM JEOL 2010 with a LaB_6 emission gun operating at 160 kV for TEM images. For EDX measurements, the samples were diluted in EtOH, sonicated for 3 min and were drop-casted on grids.

Samples were then examined under Jeol-7900F SEM microscope with accelerating voltage of 5 kV.

2.7 Electrochemical methods and apparatus

2.7.1 Theoretical Bases of Electrocatalytic processes and techniques

The importance of electrochemistry rises from the ability to drive the energy of an electron on an electrode surface by applying a voltage difference. In particular, in a reductive process, the electron could transfer from the electrode to the considered molecule if the potential energy is higher than the Lowest Unoccupied Molecular Orbital of the species (Figure 2.8).

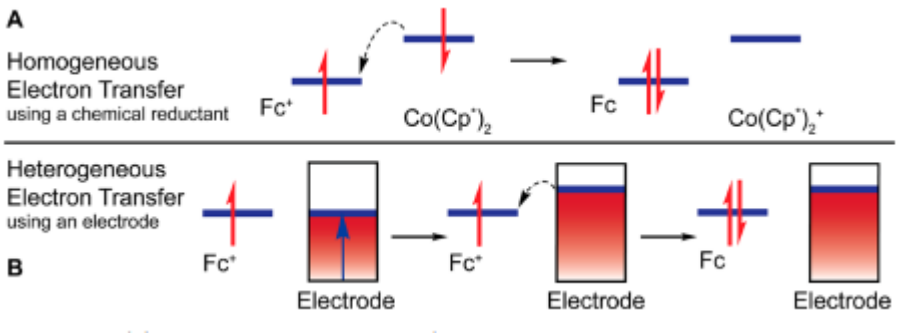

***Figure 2.8**: Representation of electron transfer in an electrode. From Reference [19].*

Moreover, the applied bias is an external parameter controlled by the operator and that means that it can be exploited for the calculation of the thermodynamic (through evaluation of E_0 or ΔG) and kinetic (i_0, k_0) that rule the process.

Electrochemical techniques can be divided in two main groups: the Direct Current (DC) techniques such as Cyclic Voltammetries (CVs), Linear Sweep Voltammetries (LSVs), ChronoAmperometries (CAs) or ChronoPotentiometries (CPs) and the Alternating Current (AC) methods, i.e. Electrochemical Impedance Spectroscopy (EIS). Cyclic Voltammetry is a potential sweep technique, where the voltage is scanned in a fixed window in a reversible way, by using a triangular pulse (Figure 2.9) [21].

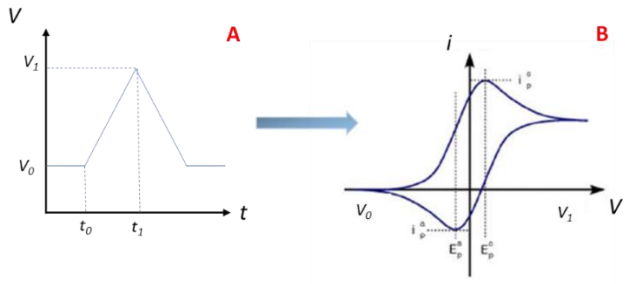

***Figure 2.9**: Shape of the pulse (A) and the signal (B) in a Cyclic Voltammetry.*

During the first part of the CV (the anodic sweep), the potential changes at a fixed rate from V_0 to V_1. If a peak in the voltammogram (Figure 2.8 B) is registered, an oxidation is taking place. The height of the peak is affected by different parameters such as the reactant concentration, the scan rate of the process and the diffusional properties of the electroactive species. The relationship between the current of the peak and the electrochemical features of the process in a solution is described by the Randles-Sevcik equation (equation 2.8):

$$i_P = 0.4463\, n\, F\, A\, C \left(\frac{n\, F\, v\, D}{RT}\right)^{1/2} \qquad (2.8)$$

Where i_P is the current maximum, *n* is the number of electrons transferred, *A* the electrode surface area, *F* the Faraday Constant, *D* is the diffusion coefficient, *C* is the concentration of the reactant, *v* is the scan rate, *R* is the Gas constant and *T* is the temperature.

The particular shape of the CV curve is due to the diffusion of the species to the electrode. Indeed, the peak current potential (E_p) is the potential at which the rate of reaction on the interface between the electrode and the electrolyte is equal to the diffusion rate of the reactant from the solution to the interface. The same considerations can be done for the second part of the CV (the cathodic sweep), where a reduction can take place. The analysis of the position, the shape and the area of the peaks is fundamental to rationalize the electrochemical processes that occurs in the system.

Similarly to CVs, LSVs are potential sweep techniques where a single electrochemical process is monitored due the application of a particular voltage difference (Figure 2.10).

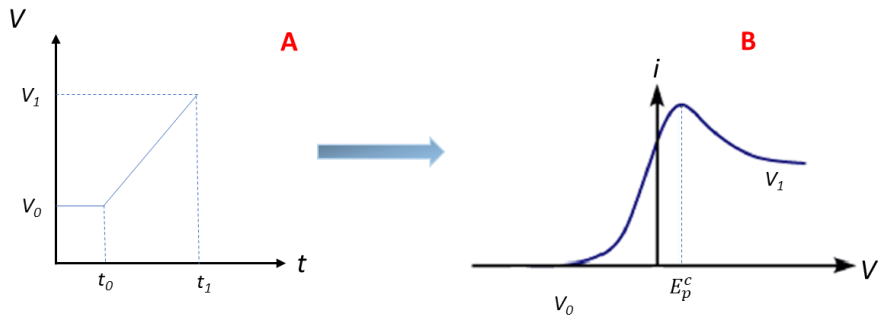

***Figure 2.10**: Shape of the pulse (A) and the signal (B) in a Linear Sweep Voltammetry.*

Chrono-dependent methods (CA and CP) are techniques where current (CA) or potential (CP) is measured over the time, while the other parameter is fixed at a chosen value [22]. The typical form of a CA (Figure 2.11) follows the Cottrell equation (equation 2.9):

$$i = \frac{n\,F\,A\,c_j^0 D_j{}^{1/2}}{(\pi t)^{1/2}} \qquad (2.9)$$

Where c_j^0 is the initial concentration of the analyte *j*. The shape of the CA curve depends on the diffusion of the analyte to the surface of the electrode. Indeed, as the analyte reacts at the electrode interface, its local concentration is depleted, and the current will decay over time until either the analyte is completely consumed ($i = 0$) or an equilibrium with diffusion is reached ($i = i_{eq}$).

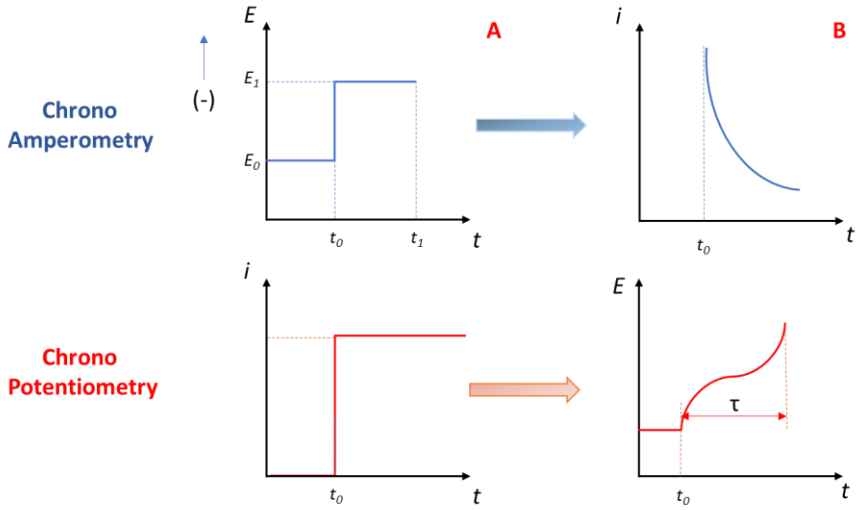

***Figure 2.11**: Excitation (A) and Response (B) waves for Chrono Amperometry (blue) and Chrono Potentiometry (red).*

It is important to underline that all the discussed techniques fits well when reversible systems (Redox couples with very fast kinetics) are considered. In the case of nanostructured electrocatalysts, that represent the main subject of this study, the behavior will deviate from ideal due to the presence of other processes such as change in structure and morphology, leading a different electrode kinetics.

Electrochemical Impedance Spectroscopy (EIS) provides information about the phenomena that occur at the electrode-electrolyte interface by evaluating the resistive or capacitive properties of a system [23]. As previously noted, EIS uses an AC sinusoidal excitation signal as a probe collecting the impedance value at varying AC frequencies. Impedance is defined as expression of the opposition that an electronic component, circuit, or system offers to alternating and/or direct electric current. EIS response can be studied with an equivalent circuit, in which every component (such as resistors, capacitors and inductors) corresponds to a particular phenomenon in the cell. The simplest case is represented by a pure resistance R across which a sinusoidal voltage is applied. The current can be calculated by the Ohm's law ($i = V/R$) and its onset is instantaneous, leading to a sinusoidal current wavefunction in phase with the bias. However, if we consider a capacitor in the same situation, the potential and current wavefunctions will be out of phase. Indeed, when the capacitor starts charging the current is maximized, while when the potential is at its peak, the capacitor is fully charged and no current passes (the capacitor acts as a brake). This difference in phases can be expressed more easily with complex notation, as the real and imaginary parts can facilitate calculations.

The simplest model for a cell, the Randles circuit, presents a resistor coupled with a capacitor and a resistor in parallel and the corresponding EIS gives a semicircle in a Nyquist plot (real impedance values vs imaginary impedance values) (Figure 2.12).

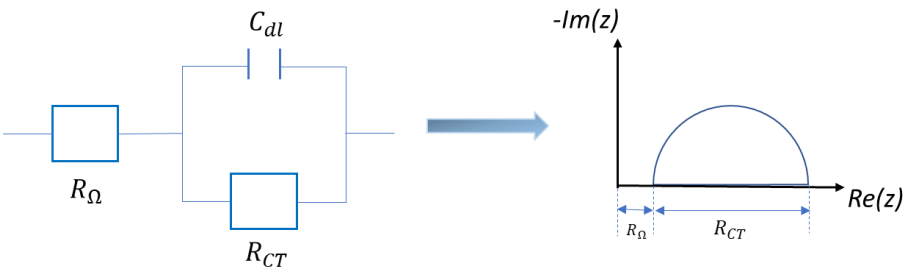

Figure 2.12: *Randles equivalent circuit for a typical electrode and relative Nyquist plot.*

To understand the connection between Randles circuit and an electrochemical cell, we can evaluate each component at a time. The first resistance (R_Ω) and the capacitance (C_{dl}) depend on the nature of the electrode-electrolyte interface. R_Ω, also called uncompensated resistance (R_u), is the resistance of the electrolyte between the Working Electrode (WE) and the Reference Electrode (RE) (Figure 2.12). The C_{dl} capacitance is instead caused by the accumulation of ions in solution on the electrode surface when a bias is imposed. C_{dl} is mainly dependent on the electrode and can be used to calculate the Electrochemical Surface Area (ECSA) of different catalytic materials. The Charge Transfer Resistance (R_{ct}) can be derived from the Butler-Volmer equation (equation 2.10):

$$R_{ct} = \frac{RT}{nFi_0} \qquad (2.10)$$

From this relation, it can be seen that R_{ct} and i_0 (exchange current) are inversely proportional: this means that faster kinetics have lower charge transfer resistance values. As previously noted, a normal Randles circuit will give a semicircle-shaped response in the R(Z) vs -Im(Z) space (i.e. Nyquist plot). The real response of an electrochemical system affects the non–ideal shape of Nyquist response by varying the typical figure of the plot. Two differences are particularly important to properly fit an EIS Nyquist plot. First, the semicircle can appear depressed (not perfectly spherical). This deviation from the model is due to the roughness of the electrode surface [24]. To fit properly this shape, a Constant Phase Element (CPE) can be used. The admittance (Y, the inverse of the impedance) of a CPE is:

$$Y_{CPE} = Q_0(wi)^n \qquad (2.11)$$

With $0 < n < 1$. When $n = 1$ the CPE behaves as a pure capacitor, while for $n = 0$ the CPE behaves as a pure resistor (equation 2.11). Usually, values of n near 0.8 are assumed for electrode surfaces, resulting in a slightly depressed semicircle. A second correction is at the end of the semicircle (low frequencies), where diffusion limitations can give rise to a linear response in the Nyquist plot. To fit this data, a Warburg element (W) can be used to model semi-infinite linear diffusion, in other words unrestricted diffusion to a large planar electrode. The presence of the Warburg element can be recognized from a straight line with a 45° slope.

2.7.2 Electrochemical setup

The electrochemical experiments were performed using a Metrohom Autolab PG302N electrochemical workstation, integrated with an EIS module and the full equipment for Rotating Disk Electrode (RDE) and Rotating-Ring Disk Electrode (RRDE) measurements. Purely electrochemical characterizations were carried out in a three electrode-setup, using a Saturated Calomel Electrode (SCE) as reference electrode, Pt wire as counter electrode and a Rotating disk electrode (RDE, Metrohm, with a geometric area of 0.196 cm^2) as working electrode. For simple electrochemical characterizations (LSVs, CVs or EIS) a single compartment cell was used (Figure 2.13), equipped with a bridge with a Vycor® frit to separate the catholyte (electrolyte in contact with the cathode) from the anolyte (electrolyte in contact with the anode). The reference electrode was connected through the electrolyte of the working electrode with a Luggin capillary. On the other hand, CAs and FEs measurements were performed in a single compartment gas tight electrochemical cell where a Pt filament (CE) was faced to an Ag/AgCl sat. Reference Electrode (RE) and the working electrode. Toray® Carbon paper was used as conductive support for the dropcasting of the investigated materials.

***Figure 2.13**: Setup for electrochemical characterization using RDE (A) and for CO_2RR tests (B).*

All measured potentials for CVs and LSVs were corrected for ohmic losses estimated through EIS analysis and converted to Reversible Hydrogen Electrode (RHE). Electrochemical active surface area ($ECSA$) and Roughness factor (R_F) values were calculated via the capacitive current near OCP at different scan speeds and using the capacitance of blank RDE electrode as reference (C_{br}) (equation 2.12 and 2.13) [25,26].

$$i_C = C_{DL} * v_{scan} \quad (2.12)$$

$$ECSA = R_F * A_{geom} = \frac{C_{DL}}{C_{br}} * A_{geom} \quad (2.13)$$

Electrochemical impedance spectroscopy (EIS) measurements were performed using a frequency response analyzer (FRA, AutoLab 302 N, Metrohm) at room temperature. EIS spectra were recorded at OCP under pure Ar atmosphere with a 10 mV amplitude voltage perturbation in the maximum frequency range from 100 kHz to 1 Hz.

Faradaic Efficiency (FE) was calculated from the concentration of the different products during the time. The following equation 2.14 is valid for any product either in solution or in the gas phase:

$$FE = \frac{n_e * n * F}{Q} \quad (2.14)$$

Where:

- n_e is the number of electrons involved in the particular reaction.
- n is the moles of product.
- F is the Faraday constant (96 485 C mol^{-1}).
- Q is the charge obtained from integration of the CA (as an absolute value).

Other typical PEM (Polymer Electrolyte)-based electrochemical setups had been used such as Flow cell electrolyzer and H-cell (Figure 2.14). This cell is a 5cm x 5 cm x 5 cm cube of poly carbonate, with a 4 mL volume for the single compartment and where a glassy carbon act as support and a Pt foil as counter electrode.

***Figure 2.14**: Homemade H-cell.*

2.8 Experimental procedures

Preparation of the ink for electrochemical experiments

In a typical procedure, 3.0 mg of catalyst had been dissolved in a solution of 0.9 mL of high pure milliQ H_2O, 0.100 mL of i-propanol and 50 µL of Nafion. The obtained ink had been sonicated for one hour in order to disperse the catalyst and the following Working Electrodes (WE) had been prepared by dropcasting of a fixed amount of the solution on an opportune electrochemical support.

Electrochemical characterization of materials using RDE

The working electrode was prepared by dropcasting 10 µL of the ink (in two different depositions of 5 µL) on a polished Rotating Disk Electrode (RDE) with an area of 0.196 cm^2. All the electrochemical characterization had been performed by rotating the RDE at 1600 RPM in a 0.1 M $KHCO_3$ solution and connecting the entire setup to a Autolab PGSTAT302N as potentiostat workstation. The determination of ElectroChemical Surface Area (ECSA) had been performed by collecting chrono voltammetry in Ar atmosphere had in a range where no faradaic processes occur (from -0.2 V to -0.3 V vs SCE). The measure was repeated at different scan rates in order to analyze the trend of the capacitive current by varying the scan rate. The capacitance was obtained from the

linear regression of the experimental values and it was normalized using the capacitance of blank RDE as a background. The obtained ECSA was used to normalize all the performed measurements. Linear Sweep Voltammetries had been performed by choosing -1.3 V, -1.5 V and -1.7 V (vs SCE) as lower voltage limit and using a scan rate of 5 mV/s. Each LSV at a single voltage was repeated for three times to desorb all the gaseous species adsorbed on the surface of the electrode and have a clear indication of the electrochemical behavior of bare materials. Chrono Amperometries were collected by tracking the current at the same voltages of CVs during 90 minutes of experiment. All the experiments were done both in Ar and CO_2 atmosphere, correcting the voltage with iR compensation.

CO_2RR experiments

In a typical procedure for CO_2RR characterization, 100 µL of ink (two depositions of 50 µL) had been deposited on both sides of a Toray® carbon paper support, covering an area of 10 mm x 5 mm. The second side of the support was covered with the catalyst and not with insulating material; indeed, it was observed from preliminary experiments that the presence of the protective layer alters the results obtained from chromatographic measurements. This electrode is used as WE in a three electrodes cell, coupled with a platinum wire (1.00 mm thick, 99.9 % of purity, Sigma Aldrich) as CE and an Ag/AgCl sat. electrode as RE. The electrochemical tests were performed using 15 mL of $KHCO_3$ 0.1 M as electrolyte (purity > 99.95%, Sigma Aldrich) by purging 20 mL/min of CO_2 (Ar has been used for blank experiments).

The different materials have been tested by performing a CA for three hours and analyzing the gaseous composition through an on-line gas-cromatography (Agilent 7890) and the liquid products by ionic chromatography by taking 1 mL of electrolyte and replacing it with fresh electrolyte. A 5 cycle-CV with a scan rate of 100 mV/s had been performed before each electrocatalytic experiments in order to clean the surface of the catalyst from the adsorbed gaseous species. CAs had been studied at voltages of -1.3 V, -1.5 V and -1.7 V vs Ag/AgCl sat. (respectively -0.7 V, -0.9 V and -1.1 V vs RHE) and using the equation (2.15) it is possible to convert the voltages to RHE.

$$V_{RHE} = V_{Ag/AgCl} + 0.197\,V + 0.059 \times pH \qquad (2.15)$$

Each WE was substituted at the end of each complete electrochemical characterization.

Gas and ionic-chromatography measurements

The analysis of the gaseous products (CO, CH_4, CH_2CH_2, CH_3CH_3) was performed using a J&W Select Permanent Gases/CO_2 column connected to a methanizer and a FID detector. The analysis of H_2 amount was performed using a Molsieve 5A plot column (Restek, 30m, 0.53 mm ID, 30 μm film) connected to a TCD detector. Formate accumulated in the liquid phase has been determined by ion chromatography using a Metrohm 833 instrument, mounting a column Metrosep A Supp 19-250/4.0 with eluent $NaHCO_3$ 1.0 mM / Na_2CO_3 3.2 mM.

2.9 Conclusions

In this chapter, it has been presented a short overview of the main characterization techniques used in this thesis. The next chapters, will present and discuss the most relevant results obtained, starting from the synthesis and the electrochemical characterization of well-defined Cu_2O nanoparticles and their composites, to conclude with the studies of catalytic behavior of TiN nanotubes as solar absorber for gas-phase photocatalytic CO_2 reduction.

2.10 References

[1] S. Bashir, P. Hanumandla, H.Y. Huang, J.L. Liu, *Nanostructured Mater. Next-Generation Energy Storage Convers. Fuel Cells* 4 (**2018**) 517–542.

[2] K. Rossi, R. Buonsanti, *Acc. Chem. Res.* 55 (**2022**) 629–637.

[3] A. Townshen, Principles of Instrumental Analysis, **1983**.

[4] C. Jing, T. Yuan, L. Li, J. Li, Z. Qian, J. Zhou, Y. Wang, S. Xi, N. Zhang, H.J. Lin, C. Te Chen, Z. Hu, D.W. Li, L. Zhang, J.Q. Wang, *ACS Catal.* 12 (**2022**) 10276–10284.

[5] C.J. Corcoran, H. Tavassol, M.A. Rigsby, P.S. Bagus, A. Wieckowski, *J. Power Sources* 195 (**2010**) 7856–7879.

[6] K. Artyushkova, S. Levendosky, P. Atanassov, J. Fulghum, *Top. Catal.* 46 (**2007**) 263–275.

[7] E.P. Dillon, C.A. Crouse, A.R. Barron, *ACS Nano* 2 (**2008**) 156–164.

[8] F. Liang, J.M. Beach, P.K. Rai, W. Guo, R.H. Hauge, M. Pasquali, R.E. Smalley, W.E. Billups, *Chem. Mater.* 18 (**2006**) 1520–1524.

[9] J.J. Rehr, A.L. Ankudinov, *J. Electron Spectros. Relat. Phenomena* 114–116 (**2001**) 1115–1121.

[10] J.J. Rehr, *Radiat. Phys. Chem.* 75 (**2006**) 1547–1558.

[11] P.C. Angelomé, L. Andrini, M.E. Calvo, F.G. Requejo, S.A. Bilmes, G.J.A.A. Soler-Illia, *J. Phys. Chem. C* 111 (**2007**) 10886–10893.

[12] T.F. Hsu, T.L. Hsiung, J. Wang, C.H. Huang, H.P. Wang, *Nucl. Instruments Methods Phys. Res. Sect. A Accel. Spectrometers, Detect. Assoc. Equip.* 619 (**2010**) 98–101.

[13] L. Nagy, T. Yamaguchi, K. Yoshida, *Struct. Chem.* 14 (**2003**) 77–84.

[14] P.Y. Yu, M. Cardona, Graduate Texts in Physics Ch2, **2010**.

[15] F. Hosokawa, H. Sawada, Y. Kondo, K. Takayanagi, K. Suenaga, *J. Electron Microsc. (Tokyo).* 62 (**2013**) 23–41.

[16] K.W. Urban, *Science (80-.).* 321 (**2008**) 506–510.

[17] M.H. Gass, U. Bangert, A.L. Bleloch, P. Wang, R.R. Nair, A.K. Geim, *Nat. Nanotechnol.* 3 (**2008**) 676–681.

[18] J.L. Lábár, *Ultramicroscopy* 103 (**2005**) 237–249.

[19] R.L. Vander Wal, A.J. Tomasek, M.I. Pamphlet, C.D. Taylor, W.K. Thompson, *J. Nanoparticle Res.* 6 (**2004**) 555–568.

[20] V.D. Hodoroaba, C. Motzkus, T. Macé, S. Vaslin-Reimann, *Microsc. Microanal.* 20 (**2014**) 602–612.

[21] N. Elgrishi, K.J. Rountree, B.D. McCarthy, E.S. Rountree, T.T. Eisenhart, J.L. Dempsey, *J. Chem. Educ.* 95 (**2018**) 197–206.

[22] F. Scholz, D.A. Fiedler, G. Inzelt, H. Kahlert, H. Lohse, M. Lovric, F. Marken, A. Neudeck, U. Retter, F. Scholz, Z. Stojek, F. Scholz, *Springer* (**2007**).

[23] A.C. Lazanas, M.I. Prodromidis, *ACS Meas. Sci. Au* (**2022**).

[24] W.H. Mulder, J.H. Sluyters, T. Pajkossy, L. Nyikos, *J. Electroanal. Chem.* 285 (**1990**) 103–115.

[25] J.J. Velasco-Vélez, C.H. Chuang, D. Gao, Q. Zhu, D. Ivanov, H.S. Jeon, R. Arrigo, R.V. Mom, E. Stotz, H.L. Wu, T.E. Jones, B. Roldan Cuenya, A. Knop-Gericke, R. Schlögl, *ACS Catal.* 10 (**2020**) 11510–11518.

[26] R.K.F. Della Bella, B.M. Stühmeier, H.A. Gasteiger, *J. Electrochem. Soc.* 169 (**2022**) 044528.

Chapter 3

Well-defined Cu_2O nanoparticles as catalyst toward eCO_2RR

3.1 Introduction

Cuprous Oxide (Cu_2O) is a cheap and nontoxic p-type semiconductor widely used as catalyst in various applications [1]. In particular, in the recent years, well defined Cu_2O nanostructures have received attention due to their peculiar behavior [2]. Thanks to the rational choice of the exposed facets called facet engineering, several properties of the material can be tuned, affecting the overall catalytic activity [3].

Facet engineering is ruled by a large number of phenomena, mostly related to the nucleation process or the growth of the seeds into nanocrystals [4]. The growth of well-defined nanoparticles is controlled by the minimization of the surface energy and several parameters influence it from a thermodynamic and kinetic point of view. During this process, seeds of nucleation are selectively bounded with the molecules of surfactants, hindering the growth of some peculiar facets [5]. As result of the different growth rate for blocked and unblocked planes, characteristic exposed facets can disappear, shaping the crystals with the obtained final structure [6,7]. Shape-controlled Cu_2O nanoparticles exhibit facet-dependent properties such as optical behavior, adsorption of target molecules and selectivity toward particular catalytic processes [8,9].

Different wet chemical procedures are used for the synthesis of morphologically controlled Cu_2O nanocrystals. These methods are based on reducing agents able to convert Cu-based precursors to Cu_2O, providing a fixed structure to the final material [10]. The obtained final shape of the nanoparticles is affected by different parameters such as pH [11], concentration of surfactants or reducing agents [12,13] and the presence of specific inorganic ions [14,15]. Narrow sizes distributions have been obtained with these methods; however, further improvements of the synthesis are required to optimize the final dimensions. Moreover, stabilizers or surfactants typically form strong surface bonds with nanoparticles, requiring efforts to remove them, preventing collapse of the nanostructures [16].

Well-defined Cu_2O-based nanostructures are used as catalyst in a large variety of

applications such as photocatalytic processes [17–21], dye degradations [22,23], organocatalytic reactions [24] and electrocatalytic CO_2RR [25,26]. The tunable selectivity toward different products, optical properties and catalytic behavior through facet engineering plays a pivotal role on the diffuse uses of Cu_2O as electrocatalytic system [27]. In the last years, the capability of Cu to form C-C bonds has been exploited to catalyze the direct electrochemical transformation of CO_2 into more high value-added molecules [28,29]. The catalytic behavior of Cu_2O-based nanoparticles as electrocatalyst is direct correlated to the exposed facets of the material. For instance, DFT calculations revealed that {100} facet increases the C-C coupling while the {111} allows an easier desorption of ethylene [28]. Beside the promising performances of the material, metal Cu is able to catalyze the formation of more than 16 different CO_2RR products, introducing problems related to the low selectivity and high costs of separation [30].

Here, well-defined Cu_2O nanoparticles were synthetized through a wet-chemical method. Two different morphologies were chosen: Cubic (CU Cu_2O) and Rhombo-Dodecahedral (RD Cu_2O) (Figure 3.1). Cubic is the most stable structure of Cu_2O; it is full bounded with {100} facets and it can directly convert CO to C_2H_4 through a CO dimer pathway thanks to the strong affinity with the CO [31]. On the other hand, RD Cu_2O is bounded with twelve {110} facets and, besides the reported lower stability than CU Cu_2O, it is interesting for the wide number of higher-add values that catalyze such as acetate, formate or ethanol [32]. Different efforts have been dedicated to characterize the obtained nanoparticles from a chemical, structural and morphological points of view. The nature of crystalline structure and the chemical phase of Cu_2O nanocrystals were analyzed means of XRD and Raman, confirming the purity of obtained Cu_2O material. SEM and TEM characterization revealed that Cu_2O nanoparticles can be easily obtained with cubic and rhombo-dodecahedral morphology, showing averages diameters of 200 nm (with σ=20 nm) for CU Cu_2O and 280 nm (σ=30 nm) for RD Cu_2O. The facet dependent behavior of the two nanoparticles was confirmed by studying the formation of triazoles via click reaction using the materials as catalysts [33,34]. Furthermore, the electrocatalytic characterization of the two morphologies towards CO_2RR revealed an improved formation of ethylene for CU Cu_2O, highlighting however a poor selectivity towards the desired products and a partial reduction during the electrochemical process.

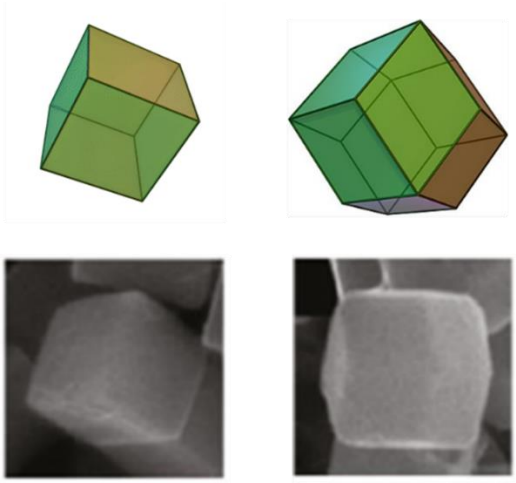

Figure 3.1*: Cubic (left) and rhombo-dodecahedral (right) nanoparticles.*

3.2 Experimental section

Preparation of Cu_2O nanoparticles with different morphology

All reagents were of analytical grade and used without further purifications. Sodium Dodecyl Sulfate (SDS), $CuCl_2$, NH_2OH*HCl and NaOH were used as precursor for the preparation of the Cu_2O nanoparticles.

CU and RD Cu_2O nanoparticles were prepared by a wet chemical method following a published procedure [35]. In a typical experiment, 0.348 g of SDS have been mixed with Milli-Q H_2O (35.65 mL for CU and 27.80 mL for RD) and stirred at 30°C for 10 minutes. 2 mL of a $CuCl_2$ 0.1 M solution were introduced dropwise under vigorous stirring. The formation of Cu_2O nanoparticles starts when 0.72 mL of NaOH 1M and a fixed volume of NH_2OH*HCl (1.6 mL for CU and 9.48 mL for RD) was added very quickly to the solution of $CuCl_2$. The different volume ratio of NH_2OH*HCl allowed the variation of the shape of the obtained Cu_2O. The mixture was aged for 60 min at 30°C, while the color of the solution changed from light blue to orange and confirming the formation of Cu_2O. The nanoparticles were washed three times with absolute ethanol, separate from the solution by filtration and dried for 12 hours at 45°C in order to remove the surfactants from the surface.

Click Reaction using Cu_2O nanoparticles

In a typical experiment, 0.25 mmol of benzyl bromide (Sigma Aldrich) and 0.40 mmol of NaN_3 (Sigma Aldrich) were mixed in a flask containing 5 mL of absolute ethanol. The flask was heated at 55° C under Ar atmosphere and stirred at 500 rpm and, after 10 minutes, 1.0 eq of phenyl acetate were added. At this point, Cu_2O nanoparticles were mixed with the reactive blend. For a correct comparison between the two shapes of nanoparticles, a fixed quantity of nanoparticles was weighted in order to have a similar exposed surface (0.87 m^2). The reaction had been performed for 8 hours, tracking the variation of the concentration of the reagents and products by using 1-decanol as internal standard. After that reaction was stopped, the mixture was separated via centrifugation and the nanoparticles were washed three times with absolute ethanol in order to perform recycling tests. The solvent was removed under vacuum to isolate the final product and the resulting crude was washed two times with H_2O and separated using an equal amount of ethyl acetate. The organic product was dried under vacuum and separated using a chromatographic column.

Electrochemical characterization of Cu_2O nanoparticles

The electrochemical experiments were performed in the typical 3-electrodes system, using the procedures mentioned in chapter 2.8. All the voltages were referred to RHE electrode and the measurements have been corrected toward the iR drop and the geometrical electrode area in order to neglect the effects of the surface and the ohmic resistance of the electrochemical setup.

3.3 Results and discussion

3.3.1 Characterization of Cu_2O nanoparticles

Well-defined Cu_2O nanocrystals were obtained at room temperature by mixing an aqueous solution of $CuCl_2$, sodium dodecyl sulphate (SDS) as surfactant, sodium hydroxide, and hydroxylamine hydrochloride as reducing agent (Figure 3.2). Moreover, by an easy cleaning protocol, it was possible remove all the surfactants from the surface of Cu_2O nanoparticles.

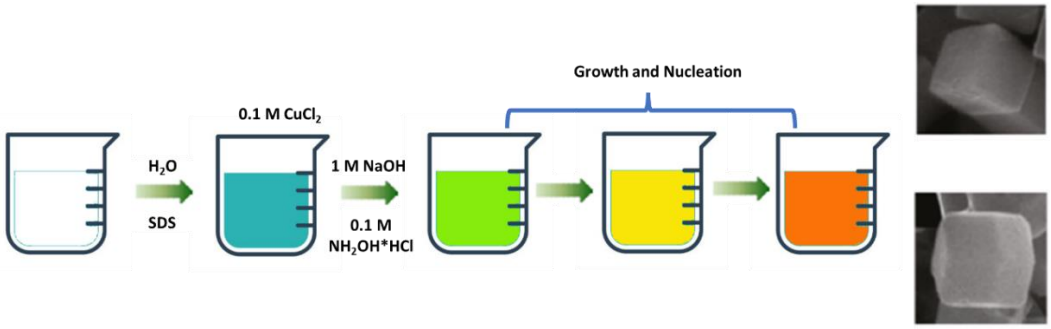

***Figure 3.2**: Synthetic route to obtain Cu_2O nanoparticles with a well-controlled shape.*

The obtained final morphology is correlated to the pH of the solution and the strength of the reductive environment [35]. Indeed, systematic shape evolution from Cubic (CU) to Rhombo-Dodecahedral (RD) nanocrystals was achieved by adjusting the volume of reducing agent. In particular, CU NPs are formed at a faster rate than RD NPs, confirming the dependency of the final morphology of the nanoparticles to the growth rates of the different facets [36].

The study of the chemical phase of the synthetized materials is fundamental to investigate the purity of the obtained copper oxide and its implications on the catalytic behavior of the material. Structural analysis of the pristine materials performed by XRD is shown in Figure 3.3.

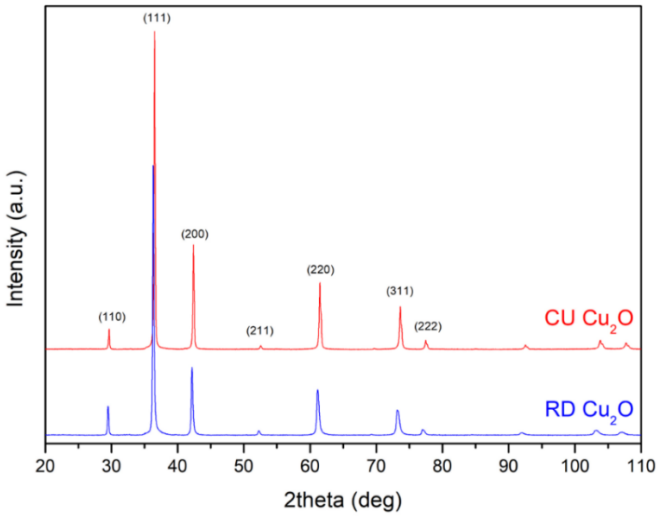

***Figure 3.3**: XRD diffractogram of CU (red) and RD (blue) Cu_2O nanoparticles.*

Raman spectroscopy allowed to confirm the purity of the chemical phase, even for amorphous materials. With this characterization, copper (I) oxide can be discriminate from copper (II) oxide through the determination of characteristic vibrations. The Raman spectrum of CU and RD Cu_2O is shown in Figure 3.4, where the characteristic peaks of Cu_2O phase are marked with numbers.

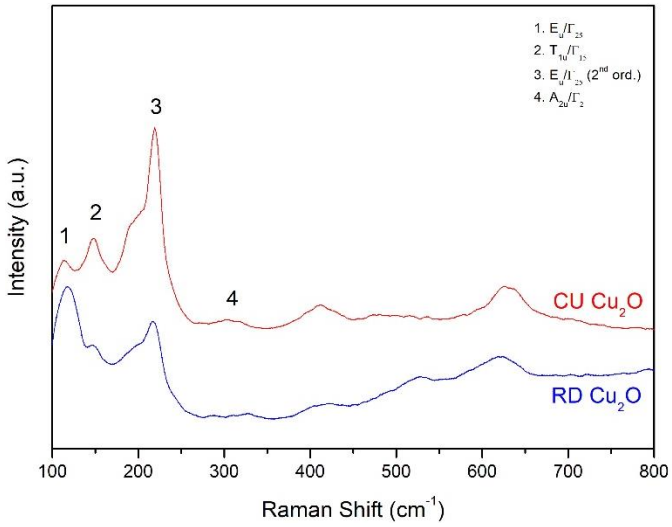

***Figure 3.4**: Raman spectra of well-defined Cu_2O nanoparticles collected using a 533 nm Laser.*

The spectrum shown in Figure 3.4 helps to identify the different characteristic vibrations and discriminate the different phase of copper. The peaks present at 630 cm^{-1} is common to both oxides, however, the region below than 200 cm^{-1} allows to discriminate the type of oxide due to the absence of peaks related to CuO. Table 3.1 reports the characteristics Cu_2O Raman peaks.

Raman shift values (cm^{-1})				
Commercial	CU	RD	Reference	Simmetry
115	114	118	72-110	E_u/Γ_{25}^-
146	148	148	146-153	$T_{1u}/\Gamma_{15}^{-(1)}$
217	219	218	220	E_u/Γ_{25}^- second order
312	309	328	307-338	A_{2u}/Γ_2^-

***Table 3.1**: Characteristic vibrations of Cu_2O and comparison with experimental values.*

The E_u mode at 115 cm^{-1} and the T_{1u} mode at 150 cm^{-1} are related to the rotation of the Cu tetrahedra around their centers and the A_{2u} mode at 330 cm^{-1} corresponds to the oscillations of the copper atoms along the diagonal axes of the cubic structure (Figure 3.5) [37,38]. On the other hand, the intense vibration observed at 220 cm^{-1} is related to the second order of the E_u mode [39].

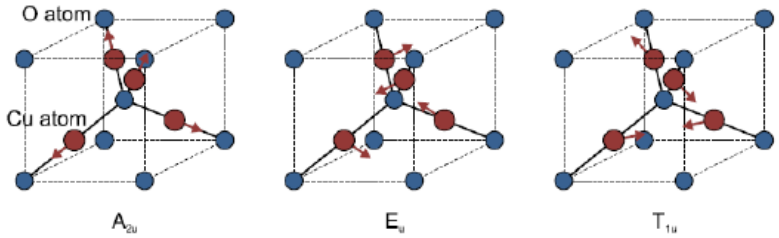

***Figure 3.5**: Vibrational modes of Cu_2O from [37].*

The determination of the reflectance spectrum allowed to have an estimation of the band gap of the material [40]. Tauc Plots of the two morphologies are shown in Figure 3.6. The energy gap of Cu_2O was calculated from the reflectance spectrum using the Kubelka-Munk transformation (Figure 3.6).

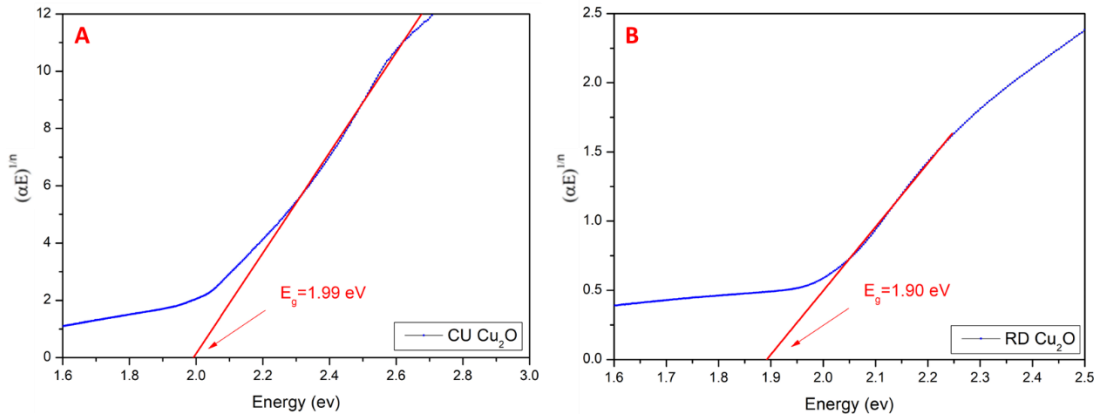

***Figure 3.6**: Calculated Tauc plot for CU Cu_2O (A) and RD Cu_2O (B).*

The values of band gap were extrapolated from Tauc plots, obtaining an E_g of 1.99 eV for CU Cu_2O and 1.90 eV for RD Cu_2O, comparable with reported values for similar nanostructures [41,42].

The chemical state of the Cu_2O undergo to oxidation due to the presence of oxygen. To evaluate the surface chemical state of the material, XPS analysis was performed in the

Cu_{2p} region, revealing the absence of the strong satellite peaks related to CuO and confirming the effective Cu_2O phase even on the surface of the nanoparticles (Figure 3.7) [43].

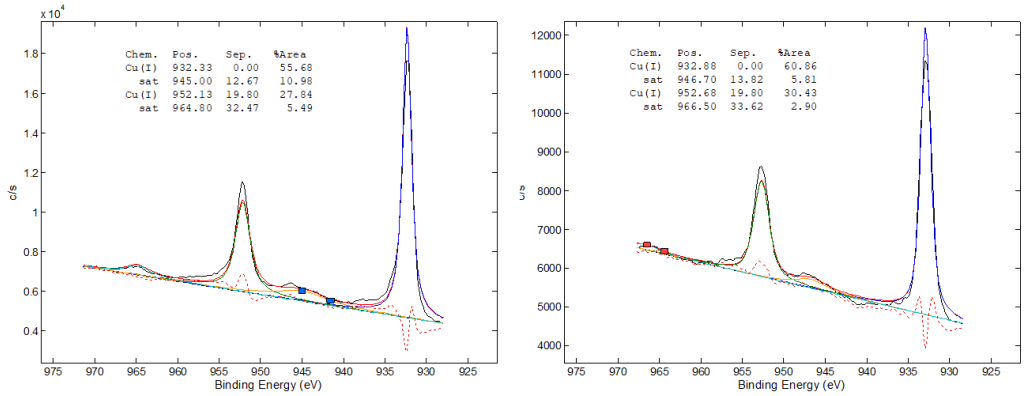

***Figure 3.7**: XPS analysis of Cu_{2p} region for CU Cu_2O (left) and RD Cu_2O (right).*

SEM and TEM characterizations show the formation of cubic and rhombo-dodecahedral Cu_2O nanoparticles, exposing respectively {100} and {110} facets (Figure 3.8). From the analysis of the obtained SEM and TEM images, it was possible to obtain a statistical distribution of the sizes of the Cu_2O nanoparticles, revealing averages diameters of 200 nm (with σ=20 nm) for CU Cu_2O and 280 nm (σ=30 nm) for RD Cu_2O (Figure 3.9).

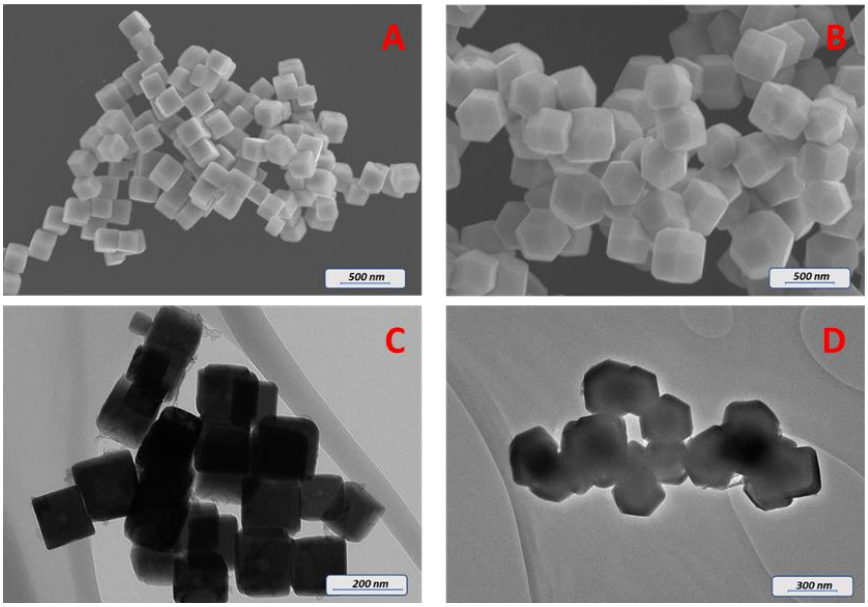

***Figure 3.8**: SEM and TEM images of CU Cu_2O (A and C) and RD Cu_2O (B and D).*

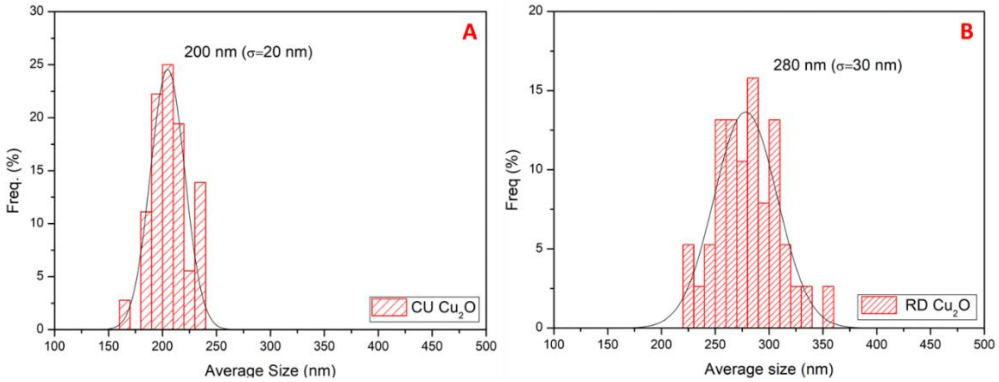

***Figure 3.9**: Analysis of average sizes of CU Cu_2O (A) and RD Cu_2O (B) nanoparticles. Counts 400 nanoparticles.*

3.3.2 Click reaction

Cu_2O nanoparticles with different shapes show a diverse catalytic behavior that depends on the surface concentration of metal atoms on the different crystal facets. Copper-catalyzed Azide-Alkyne Cycloaddition (CuAAC) can be a useful benchmark for the direct evaluation of the facet dependent properties and as proof of the dependency of the behavior on the exposed facets [44].

CuAACs are widely used reactions in organic chemistry, pharmaceutical synthesis and medical applications [45–47]. In this family of processes, a terminal or internal alkyne reacts with an organic azide to form a molecule with a triazole ring via a "click reaction". This reaction was firstly reported as a thermal process, but it was characterized of harsh conditions and low conversion rates. In the early years of the third millennium, the group of Meldal in Denmark and the group of Fokin and Sharpless in the United States, discovered independently that copper-based materials can efficiently catalyze these processes under mild conditions. The reaction can proceed with both electron-deficient or electron-rich azides, in both protic and aprotic solvents. CuAAC occurs with good conversion yields and without any particular byproducts obtaining 1,2,3-triazole heterocycle as a typical product [48]. Triazole ring is generally inert to most organic reactions (especially hydrolysis, oxidation and reduction) and it is stable at medium-high temperatures. Moreover, triazole ring own aromaticity and is also capable to form hydrogen bonds with other molecules, rising interesting properties of this molecule [49].

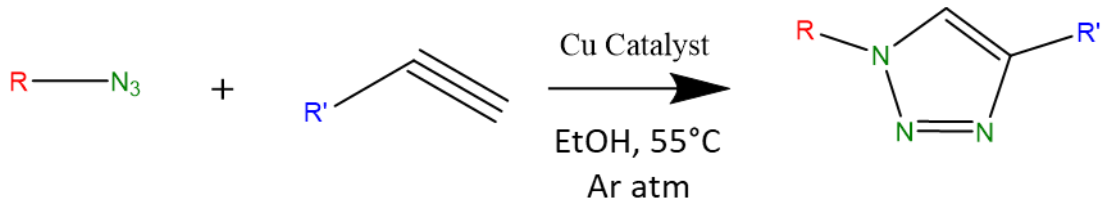

***Figure 3.10**: Formation of triazole through Cu-catalyzed Click reaction.*

Cu_2O nanoparticles were therefore used as catalysts towards the formation of 1-benzyl-4-phenyl-1H-1,2,3-triazole (BPT) in a single pot reactor where phenyl acetylene, benzyl bromide and sodium azide were mixed and heated at 50 °C for 8 hours (Figure 3.10). The trend of reagents and products was monitored during the reaction through GC-MS analysis, using 1-decanol as internal standard. The variation of concentration of the different species (such as phenyl acetylene) was tracked during the 8 hours of reaction, evidencing an increase of the concentration of BPT and a different behavior between the two chosen shapes (Figure 3.11).

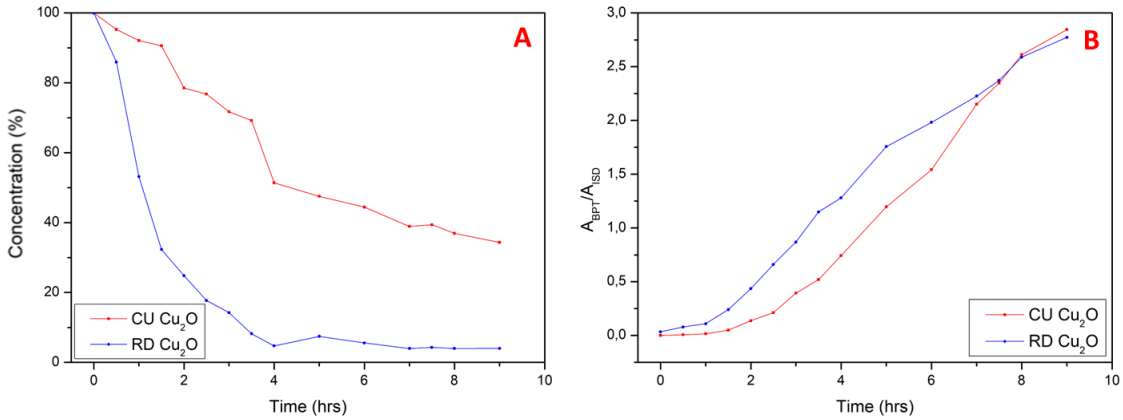

***Figure 3.11**: Evolution of the concentration of phenyl acetylene (A) and triazole (B) during 8 hours of experiments for the two morphologies of Cu_2O nanoparticles.*

The two morphologies of Cu_2O nanoparticles presented different behaviors towards the formation of the triazole. In particular, RD nanoparticles converted the reagents faster than CU, as already reported in literature [44]. Upon completion of the reaction, the NMR spectra of the obtained product indicate the formation of the desired BPT (Figure 3.12).

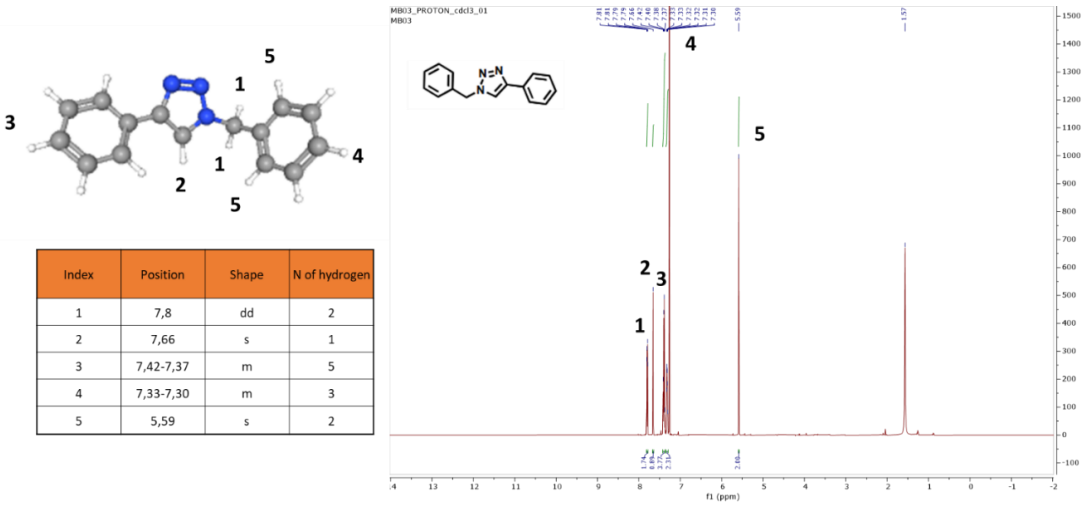

Index	Position	Shape	N of hydrogen
1	7,8	dd	2
2	7,66	s	1
3	7,42-7,37	m	5
4	7,33-7,30	m	3
5	5,59	s	2

Figure 3.12: *NMR assignation for isolated BPT.*

Recyclability tests were performed to investigate the stability of the two morphologies during the catalytic process (Figure 3.13). In a typical procedure, after the first reaction test, the nanoparticles were separated, washed with absolute ethanol and dried in order to use them in the following catalytic test. Each morphology was studied for several cycles, evidencing a decreasing of the comsumption of phenyl acetylene and a limited formation of BPT, suggesting low stability for the Cu_2O nanoparticles under these conditions.

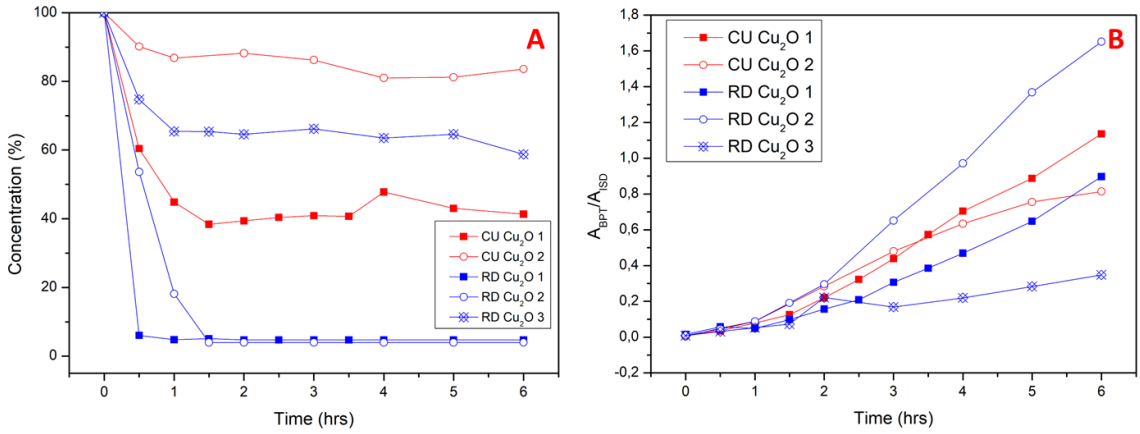

Figure 3.13*: Recyclability tests for CU and RD Cu_2O nanoparticles. A) Conversion % of phenyl acetylene during the experiments. B) Corresponding increasing of the relative amount of BPT.*

The low stability of the nanoparticles was confirmed by SEM characterization. SEM images of RD Cu_2O after each cycle are presented in Figure 3.14. The catalytic process

has dramatic influences on the morphology of the nanoparticles, leading to an increased rugosity of the nanoparticles and a subsequent disappearing of the exposed facets.

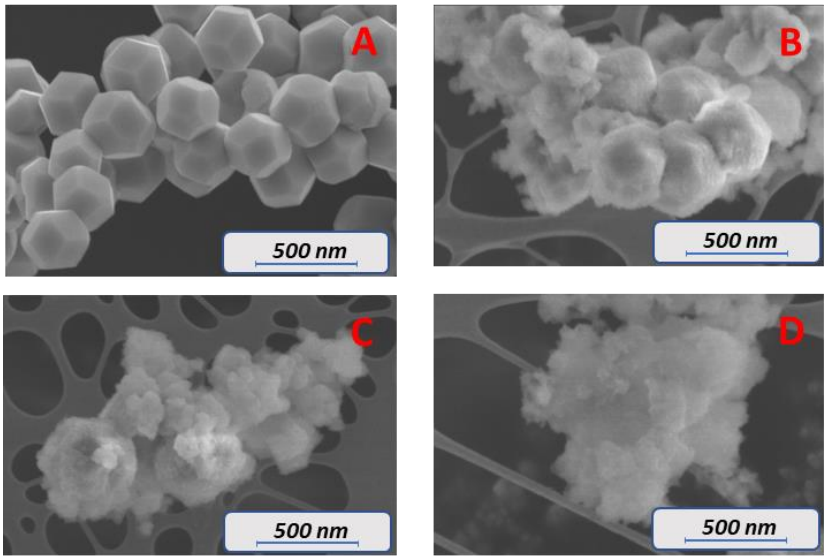

***Figure 3.14**: SEM images of RD Cu_2O nanoparticles after three consecutive catalytic of click reaction. A) Pristine material. B) After the first catalytic test. C) After the second catalytic test. D) After the third catalytic test.*

3.3.3 Electrochemical characterization of Cu_2O nanoparticles

CU and RD nanoparticles of Cu_2O were characterized from an electrochemical point of view. The Electro Chemical Surface Area (ECSA) was determined in order to evaluate the active area of the two morphologies and to normalize all the following analysis. Figure 3.15 presents the CVs obtained at different rates. The plot of the faradaic currents calculated from these curves towards the scan rates allowed to have an estimation of the capacitance, the Roughness Factor (R_f) and the desired ECSA of the two different shapes of Cu_2O nanoparticles [50] (Figure 3.16). From the analysis of the linear trends presented in Figure 3.16, it was possible to obtain an ECSA value of $(2.2\pm0.2)*10^{-1}$ cm^2 for CU Cu_2O and $(3.7\pm0.2)*10^{-1}$ cm^2 for RD Cu_2O. The ECSA values indicates a higher surface-active area for RD Cu_2O instead of CU Cu_2O. The analysis of ECSA is a very important tool to normalize all the performed measurements and to neglect the dependency from the area.

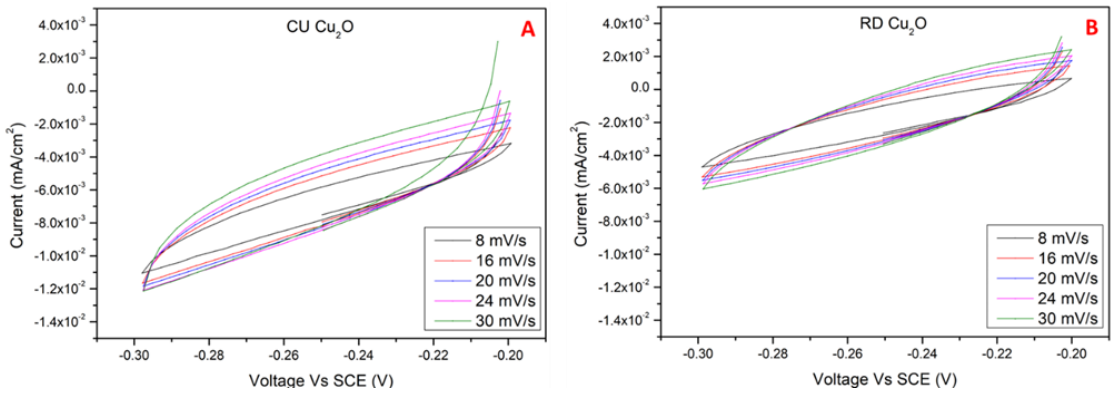

***Figure 3.15**: Cyclic voltammetries for CU Cu_2O (A) and RD Cu_2O (B) at different scan rates by varying the voltage between -0.3 V to -0.2 V vs SCE. Compensated toward the iR drop.*

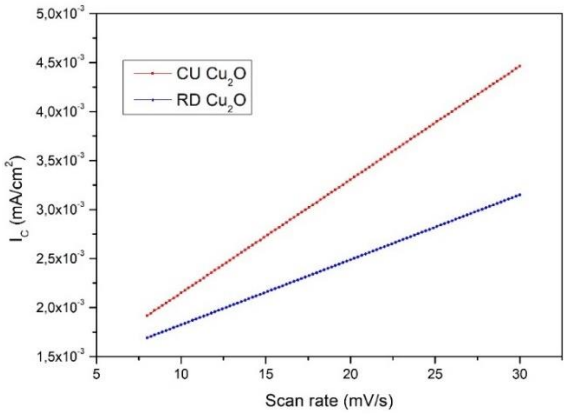

***Figure 3.16**: ECSA calculations for CU Cu_2O (red) and RD Cu_2O (blue).*

CVs (Figure 3.17 A, B and C) revealed the typical behavior of copper based-electrocatalysts [51]. In particular, the presence of a reduction peak around -1.0 V, corresponds to the reduction of Cu^+ to copper metal [52]. This reversible change is more relevant in RD nanoparticles instead of CU Cu_2O, suggesting an easier conversion of the material to Cu and a lower stability. Furthermore, both the structures showed a similar trend of the current and a general increase activity when the experiment are performed in CO_2 atmosphere, indicating a higher reactivity under CO_2RR flow.

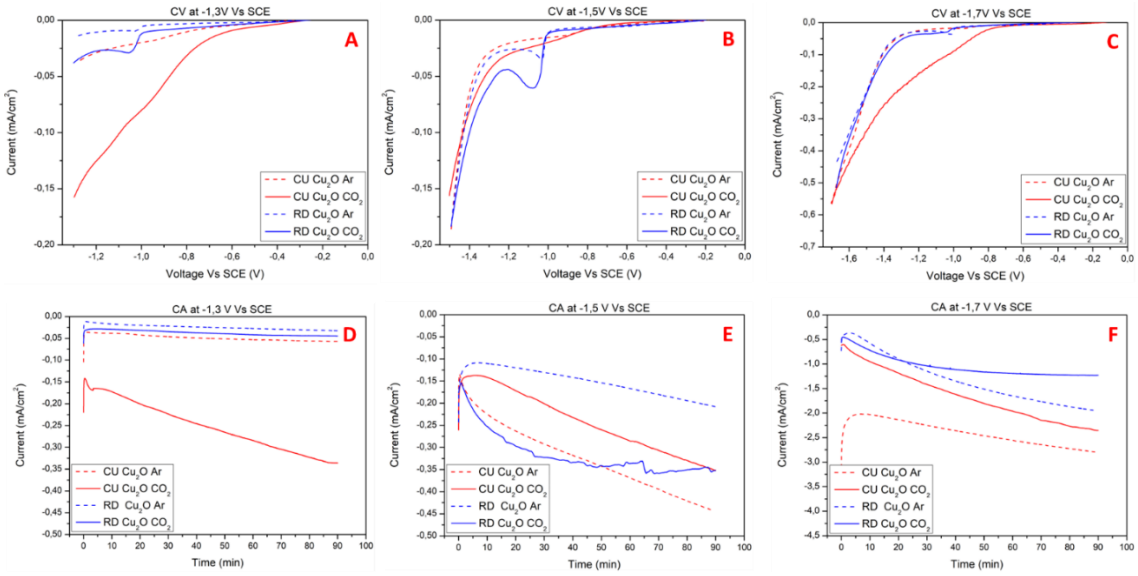

***Figure 3.17**: Linear Sweep voltammetries and Chrono Amperometries at -1.3 V (A and D), -1.5 V (B and E) and -1.7 V (C and F) for CU Cu_2O (red) and RD Cu_2O (blue). All the voltages are vs SCE and corrected with iR compensation. Dotted lines correspond to the experiment performed in Ar atmosphere while the full line in CO_2 atmosphere.*

Similar results were obtained from CA tests (Figure 3.17 D, E and F) where a higher current for the experiments under CO_2 atmosphere was observed, suggesting an improved activity of the catalyst with these experimental conditions.

The application of a voltage to Cu_2O-based WE during a CO_2RR experiment have implication on the chemical state of the material, causing a rapid reduction to metal copper that affect the catalytic behavior towards CO_2RR. Indeed, Oxide Derived Cu materials are widely exploited as catalysts for the formation of C_{2+} products even because they show improved catalytic behavior compared the pristine Cu materials [53,54]. The partial reduction of the catalysts to metal copper become a good strategy to drive the catalytic behavior toward the formation of desired products.

3.3.4 Electrocatalytic CO_2RR

CO_2RR experiments were performed in a gas tight electrochemical cell connected to a GC for the direct analysis of the gaseous products over the time (Figure 3.18).

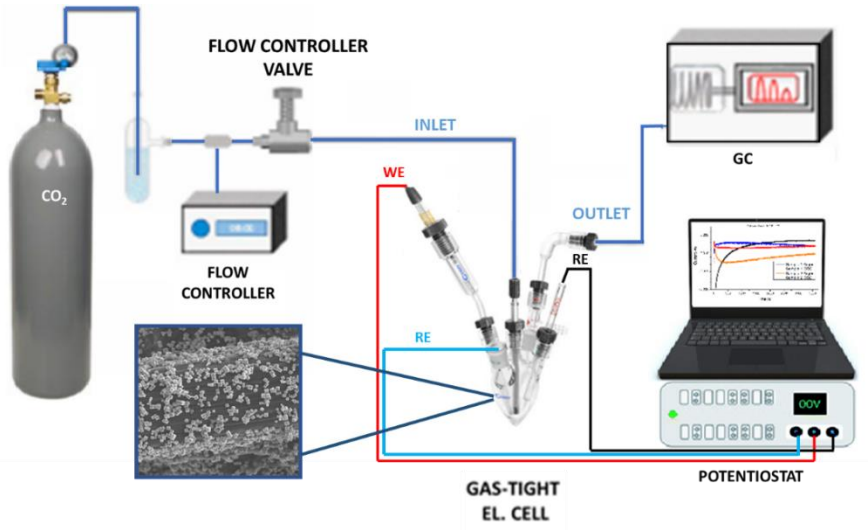

***Figure 3.18**: Schematic setup of CO_2RR experiments.*

As already explained in the paragraph 2.8, the working electrodes were prepared by dropcasting of the ink based on Cu_2O nanoparticles on both the sides of a Toray® carbon paper. The sonication of the ink did not affect the morphology or the roughness of the nanoparticles and the deposition allowed a good distribution of the catalyst on the carbon-based support (Figure 3.19). CO_2RR tests were done using both the shapes of pristine Cu_2O as catalyst, in order to investigate the role of exposed facets on selectivity toward CO_2RR. Chronoamperometries were performed for three hours at different voltages (-0.7 V, -0.9 V and -1.1 V vs RHE) and the different products were monitored through GC and IC.

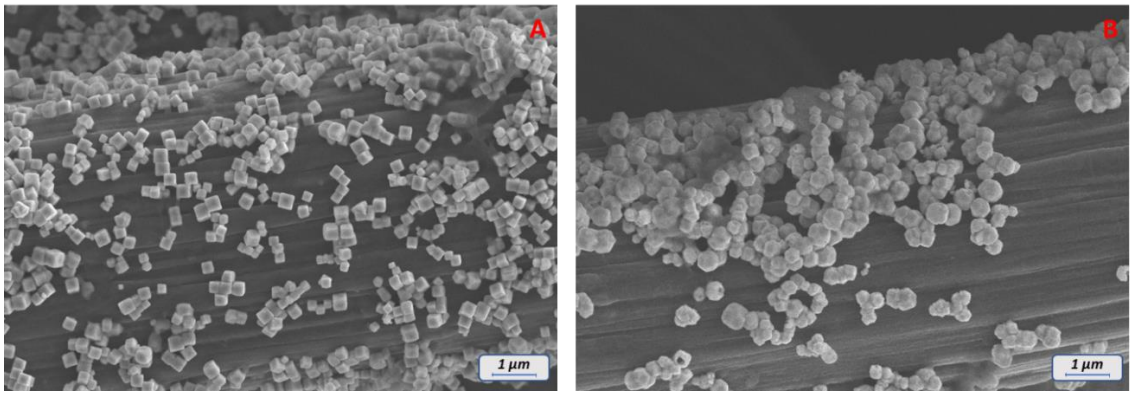

***Figure 3.19**: SEM images of pristine CU Cu_2O (A) and RD Cu_2O (B) dropcasted on Toray paper.*

The obtained current densities, moles of products and *FEs* for CU Cu_2O and RD Cu_2O at the different operative voltages of -0.7 V, -0.9 V and -1.1 V vs RHE are presented respectively in Figure 3.20, 3.21 and 3.22.

The current of RD Cu_2O is higher than CU Cu_2O in all the presented cases, reporting an overall increased production of all the products. Chromatography analysis showed that both materials can catalyze the formation of a wide spectrum of different products, especially at higher voltages. In particular, as it is possible to observe from the analysis of *FEs* presented in Figures 3.21 and 3.22, H_2, CO, HCOOH and ethylene were found at the voltage of -0.9 V and -1.1 V vs RHE; some traces of methane were detected for RD nanoparticles at -1.1 V vs RHE. CAs under Ar-saturated electrolyte showed no other than HER activity, confirming that the reduction is at the expense of dissolved CO_2 in solution (Figure 3.23). Indeed, when CO_2 was bubble on the electrolyte, HER was suppressed and the FE_{H_2} dropped to 20 % for CU Cu_2O and 25% for RD Cu_2O.

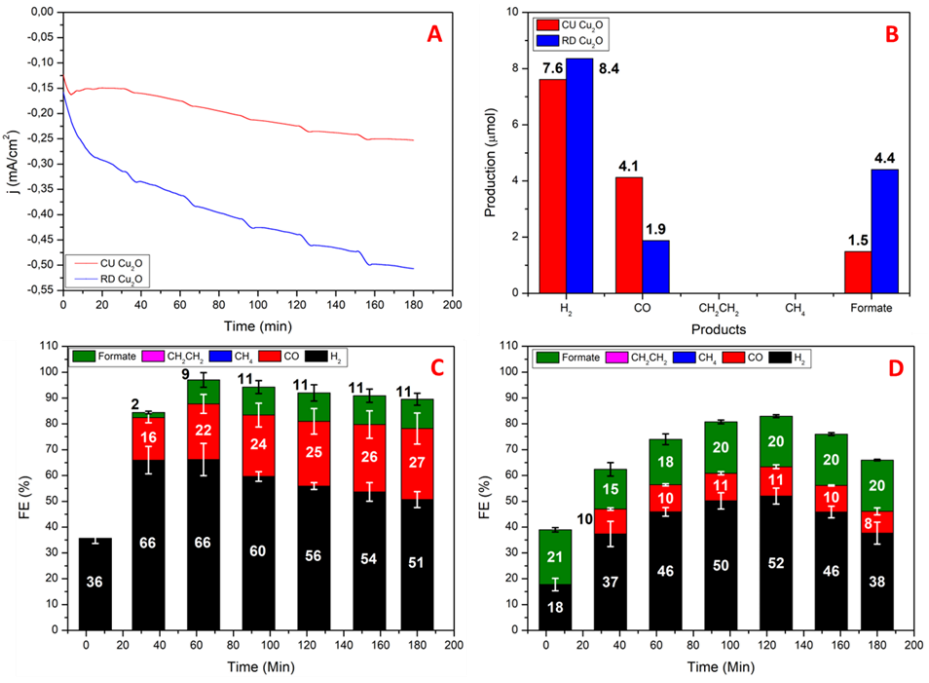

***Figure 3.20**: A) 3-hrs CA under CO_2 atmosphere at the voltage of -0.7 V vs RHE. B) mol of CO_2RR products after 3-hrs CA for CU Cu_2O (red) and RD Cu_2O (blue). FEs toward gaseous and liquid products at the voltage of -0.7 V vs RHE for CU Cu_2O (C) and RD Cu_2O (D).*

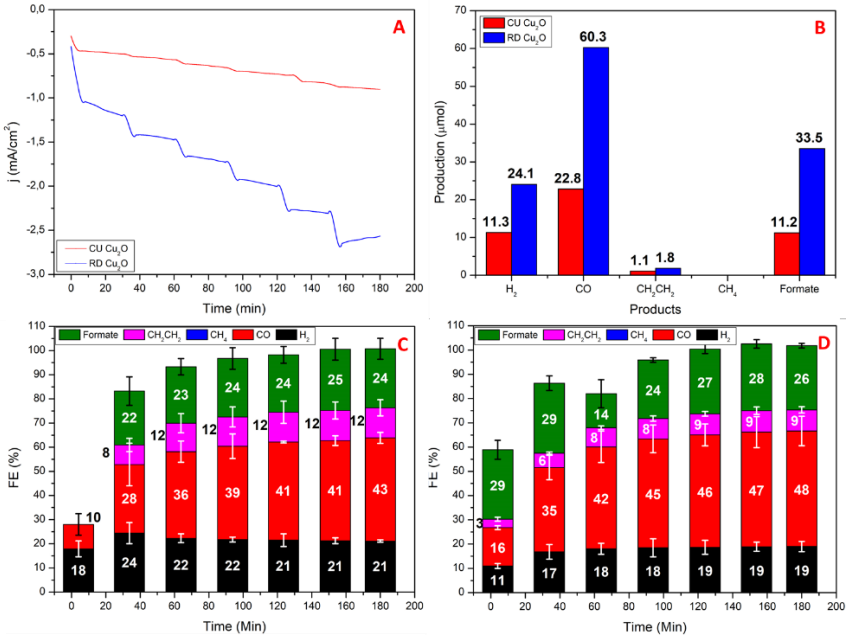

***Figure 3.21**: A) 3-hrs CA under CO_2 atmosphere at the voltage of -0.9 V vs RHE. B) mol of CO_2RR products after 3-hrs CA for CU Cu_2O (red) and RD Cu_2O (blue). FEs toward gaseous and liquid products at the voltage of -0.9 V vs RHE for CU Cu_2O (C) and RD Cu_2O (D).*

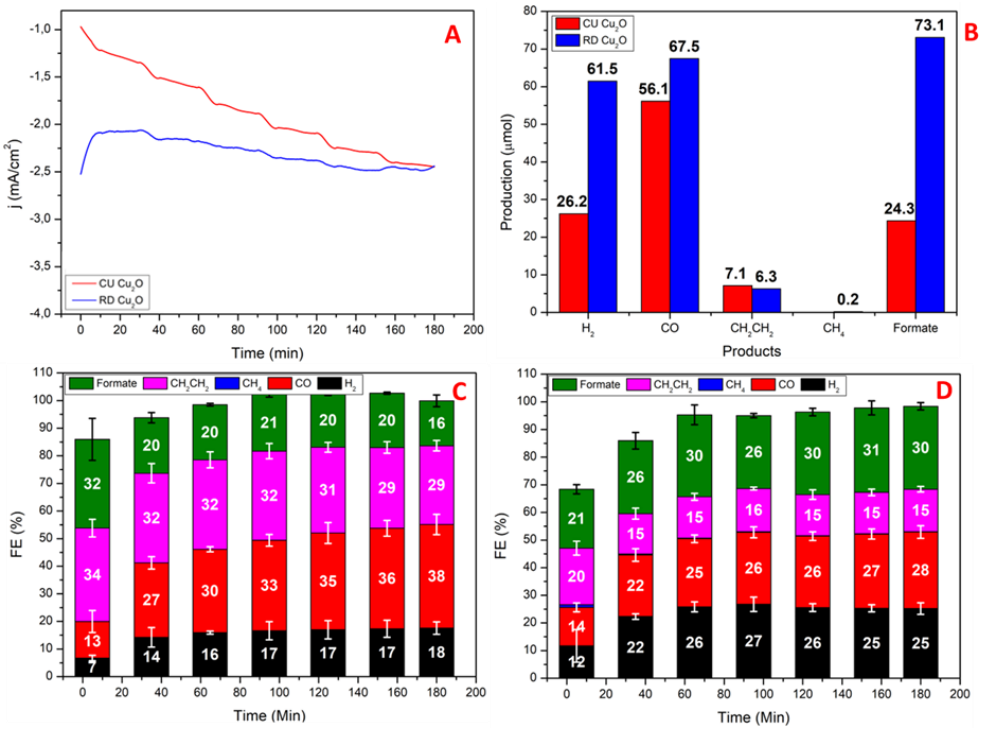

***Figure 3.22**: A) 3-hrs CA under CO_2 atmosphere at the voltage of -1.1 V vs RHE. B) mol of CO_2RR products after 3-hrs CA for CU Cu_2O (red) and RD Cu_2O (blue). FEs toward gaseous and liquid products at the voltage of -1.1 V vs RHE for CU Cu_2O (C) and RD Cu_2O (D).*

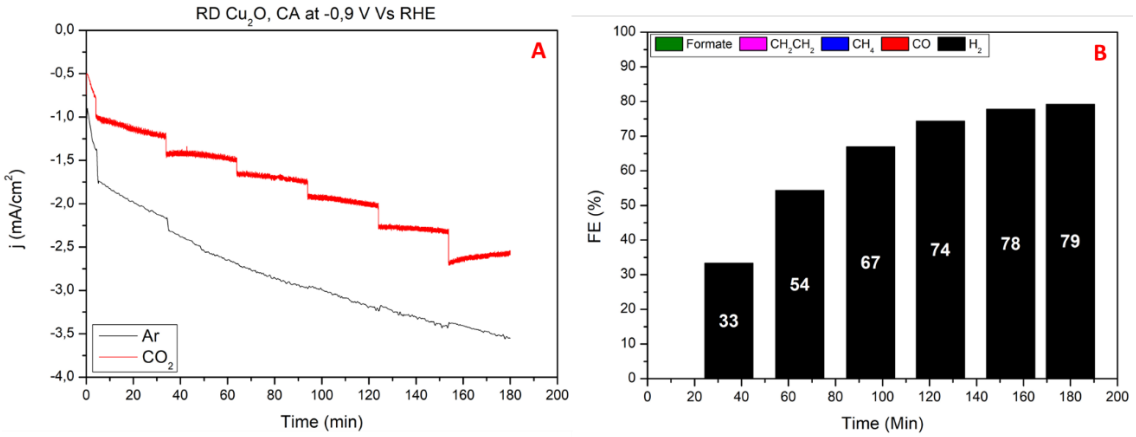

***Figure 3.23**: Representative Chrono amperometry at -0.9 V vs RHE performed under Ar atmosphere (A) and analysis of FE for different products for RD Cu_2O.*

At the same time, the reactivity toward CO_2RR products drastically increased, as it is possible to observe in Figures 3.24 where the ratios between CO_2RR products and H_2 at different voltages are presented. Cubic Cu_2O showed a heightened activity toward ethylene production, as result of the improve reactivity of {100} facets toward the formation of this molecule [55], with an average *FE* of about 30% over the time. On the other hand, RD boosts the formation of formic acid, and both materials show good CO production, especially at the voltage of -0.9 V vs RHE. Traces of CH_4 were detected during the electrochemical characterization but the contribute to the overall FE is negligible ($FE_{CH_4} < 1\ \%$), meaning that the investigated materials are not active toward the formation of Hydrocarbons. In general, some electrons are lost probably due to non-tracked products (i.e. methanol [56]) or side reactions at the electrode (such as reduction of copper oxide to metal copper), resulting in an overall *FE* lower than 100%, especially for first minutes of experiments.

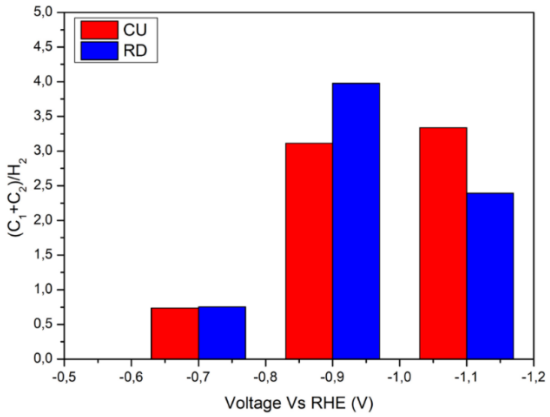

***Figure 3.24**: Ratio between the CO_2RR products and H_2 at different voltages for the two morphologies (CU Cu_2O red, RD Cu_2O blue).*

3.3.5 Scaling up of CO_2RR

Further analyses were performed in order to characterize the selectivity of pristine materials even using other electrochemical setups. This is relevant because the selectivity of a material depends on all the phenomena that occur in the interface electrode-electrolyte [57,58]. The different interaction between catalyst and the chosen support affects the porosity of the active layer and drastically affect the overall reactivity of the system. For these reasons, electrocatalytic CO_2RR had been performed in two others electrochemical devices particularly devoted for these applications: an H-cell and a flow cell electrolyzer. A H-cell is a two-chamber device commonly used for electrochemical screening of catalytic activity of a material, thanks to its small dimensions and volume of electrolytes (Figure 3.25) [59].

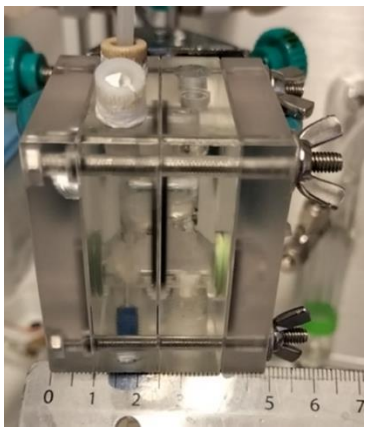

***Figure 3.25**: H-cell used for CO_2RR characterization.*

1 hr-chronoamperometries (at -1.1 V vs RHE) has been performed on the two pristine materials, revealing a different selectivity at the representative voltage respect the results obtained with gas-tight electrochemical cell (Figure 3.26). In particular, smaller FE_{CO} were obtained, with a subsequent increasing of the HER activity for both the morphologies. Even in this case an improved $FE_{CH_2CH_2}$ was observed for CU Cu_2O respect than RD Cu_2O.

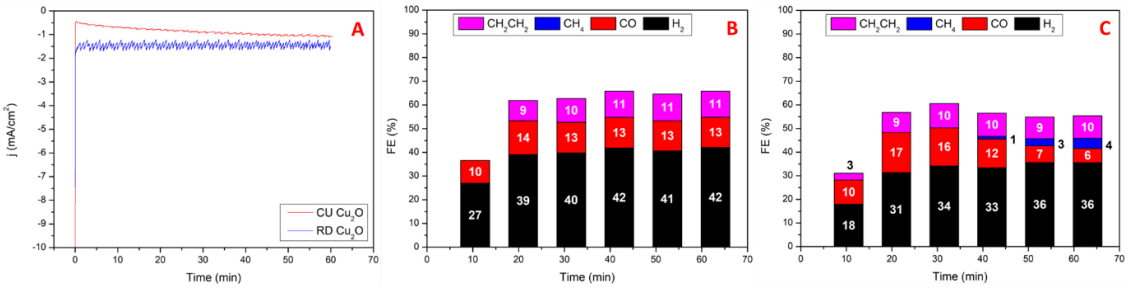

***Figure 3.26**: A) CA obtained for the two shapes of Cu_2O with H-cell at the voltage of -1.1 V vs RHE (Red: CU Cu_2O; Blue: RD Cu_2O). Analysis of Faradaic Efficiencies toward different products at the same voltage (B: CU Cu_2O; C: RD Cu_2O).*

As already introduced in the chapter 1.5, an electrolyzer is a complete electrochemical device where electricity is used to perform electrochemical processes such as CO_2RR [59]. Electrolyzers and flows cells help to fulfill the gap to the large-scale devices thanks to the possibility of use commercially-relevant current densities and to an easier control of the gaseous feeding [60,61]. The pristine materials were studied toward CO_2RR in a flow cell by performing 1 hr-chronopotentiometries (CP) at fixed applied current densities (50 mA/cm^2). The obtained CP and *FEs* for CU Cu_2O and RD Cu_2O are reported in Figure 3.27. The characteristic trend of the voltage on the presented CP is related to the formation of bubbles on the surface of GDL support, insulating the catalyst from the solution while the bubbles are growing. As it is possible to observe, CU Cu_2O showed a rapid change on the selectivity from CO to H_2, supporting a partial reduction of the catalyst (Figure 3.27 B). The observed variation of the selectivity is less evident on the RD Cu_2O, where the FE_{CO} reached almost 30% after one hour of catalytic test (Figure 3.27 C).

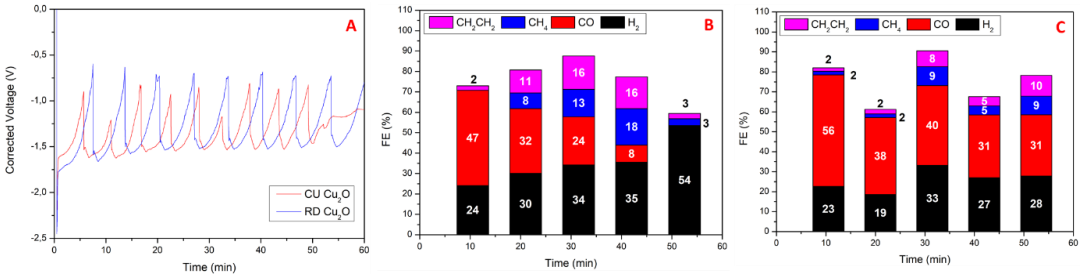

***Figure 3.27**: A) CP obtained for the two shapes of Cu_2O with electrolyzer by applying 50 mA/cm^2 (Red: CU Cu_2O; Blue: RD Cu_2O). Analysis of Faradaic Efficiencies toward different products (B: CU Cu_2O; C: RD Cu_2O).*

Despite these results, the average potentials obtained during a CP using flow cell are quite high (-1.3 V vs RHE for both the pristine materials) due to limitations of the diffusions and to overvoltage in the cell [62].

3.3.6 Effects of electrochemical characterization on Cu_2O

As it was clearly observed in the case of Click reaction (chapter 3.3.2), a catalytic reaction can have major effects on the morphology of Cu_2O, in particular in terms of roughness of the surface and/or exposed facets. Furthermore, the presence of the reductive peak of Cu_2O to metal copper during electrochemical CO_2RR confirmed the low stability of the material, especially for the case of rhombo-dodecahedral nanocrystals. To investigate the effects of CO_2RR experiments on the surface of the nanoparticles and mainly, the chemical state of the catalyst, post characterizations of the different electrodes had been performed. In particular, SEM images of CU and RD Cu_2O after electrochemical CP tests are shown in Figure 3.28 (to be compared with fresh materials presented in Figure 3.8).

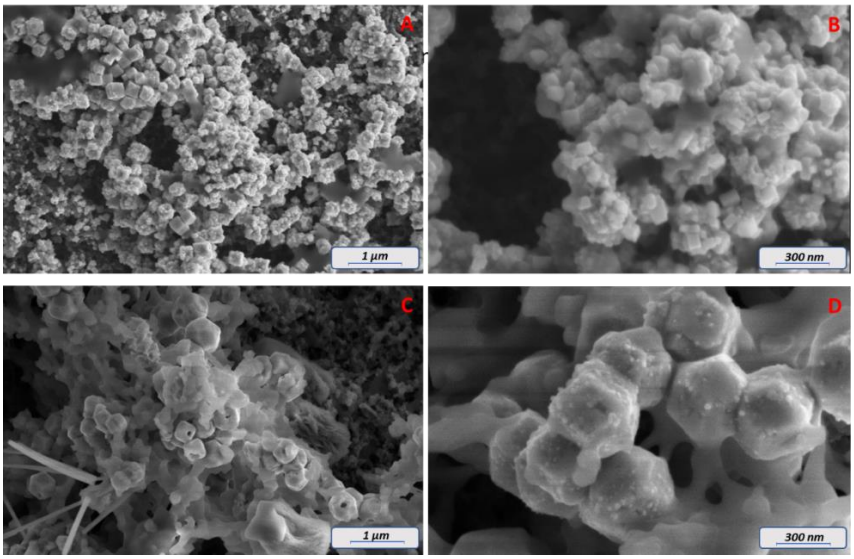

***Figure 3.28**: Electrochemical characterization on Cu_2O nanostructures after CP 50 mA/cm^2. A) and B) CU Cu_2O; C) and D) RD Cu_2O.*

CO_2RR experiments affected the surface of nanoparticles, making them rougher and with the edges less sharp and defined. These effects were dramatic especially for the rhombo-dodecahedral material (Figure 3.28 C and D), where several nanoparticles were collapsed and it is difficult to define a particular exposed facet, confirming again the lower stability of RD Cu_2O compared to CU Cu_2O.

The characterization of Cu-oxidation state during or after CO_2RR is not trivial due to low amount of material deposited on the electrode and fast re-oxidation occurring when reduced catalyst is exposed to air. Several attempts were done in order to get some structural and chemical information about the state of Cu_2O after the tests, but the amount of material was too low to find any important behavior. In particular, low angle XRD and XPS were used for this purpose, without any particular success (Figure 3.29). XRD after electrochemical characterization revealed only one intense peak related to the carbon-based support, as already reported in literature [63]. On the other hand, quantitative analysis of XPS spectra showed an oxidated copper phase, probably related to the subsequent exposition on the air after the CO_2RR.

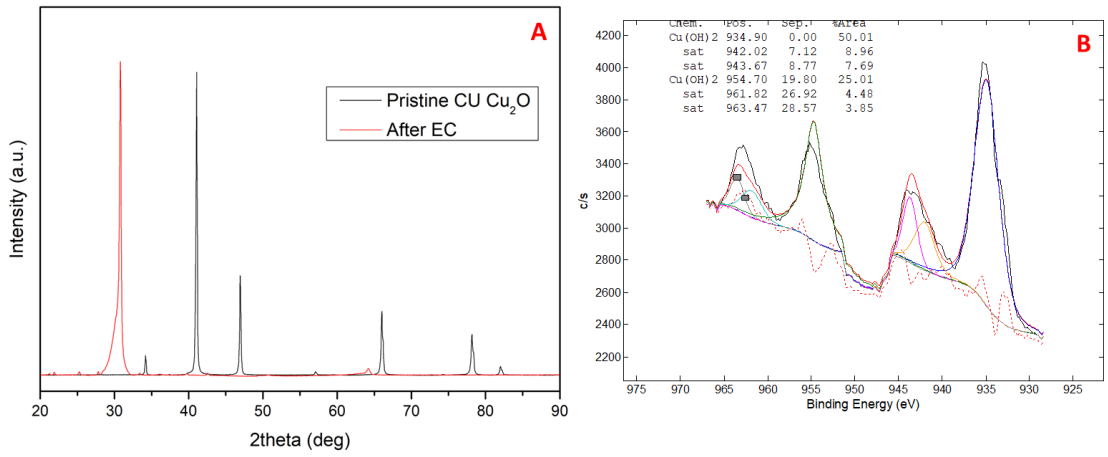

***Figure 3.29**: XRD (A) and XPS (B) of Cu_{2p} region after electrochemical characterization. Material: CU Cu_2O on Toray® carbon paper.*

To unveil the effects of the electrochemical characterization on the chemical state of the catalysts, *operando* XAS characterization during the CO_2RR process were performed on the SAMBA beamline of Soleil Synchrotron. Here, the electrochemical tests were performed in a home-made system where the catalyst was firstly dropcasted on a graphite foil (Figure 3.30).

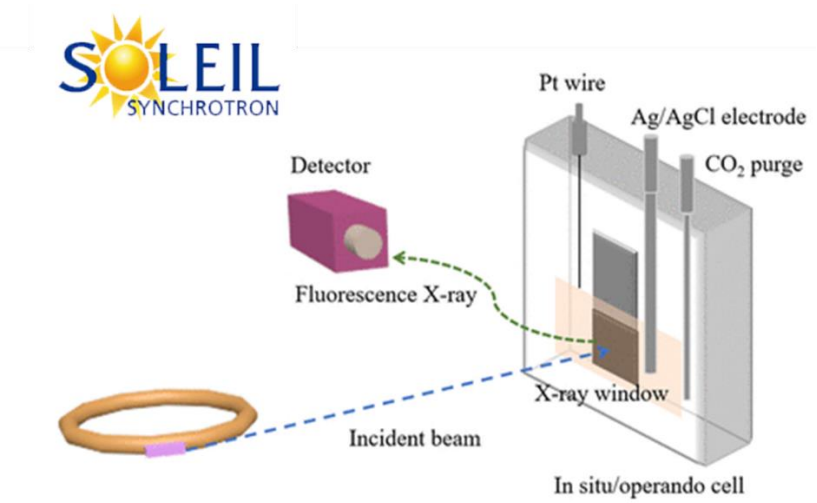

***Figure 3.30**: Experimental setup for operando XAS characterization during CO_2RR.*

With the experimental setup, it was possible to monitor the chemical state of copper by collecting XANES spectra during the electrochemical CO_2RR. The *operando* experiments at -0.7 V vs RHE (-1.3 V vs Ag/AgCl sat.) for CU and RD Cu_2O revealed a

rapid conversion of Cu_2O to metal copper, confirming the effects of reductive voltage on the working catalyst and explaining the lack of *FE* for the first minutes of chronoamperometry (Figure 3.31). In particular, with the application of a constant voltage, the pre-edge peak became less intense and broader, with a contemporaneous change of the characteristic features of Cu_2O above the edge to the usual peaks of metal copper [64].

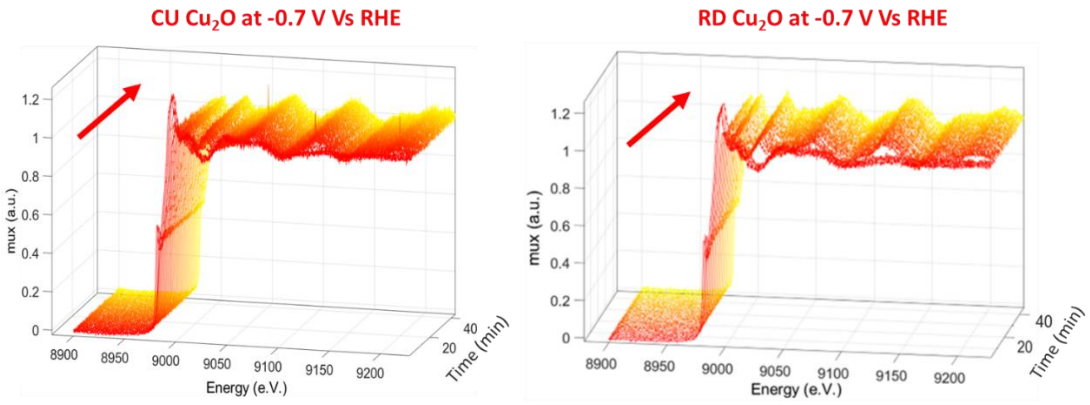

***Figure 3.31**: Trend of Cu reduction during electrochemical CO_2RR at -0.7 V vs RHE for CU Cu_2O (left) and RD Cu_2O (right).*

The experimental spectra are linear combinations of the references (metal Cu and Cu_2O) weighted for their fraction over the time. Thus, by comparing Figure 3.31 with those of the references, it was possible to investigate the variation of the composition of copper phase during the time (Figure 3.32 A and B). Interestingly, a significant fraction of Cu(I) species (about 21% for CU Cu_2O and 15% for RD Cu_2O) can still be observed even at the end of 1 hr-chrono amperometry (Figure 3.32). Further increase of the potential has implication just on the rate of the reduction from Cu_2O to Cu, without relevant modifications of the final fractions of Cu(0) and Cu(I) (Figure 3.32 C and D). Here, the lower stability of RD Cu_2O was suggested due to the faster conversion and the higher concentration of metal copper over the time. This low stability of the material and the rapid conversion to metal copper is a strong limitation and need to be faced in order to perform eCO_2RR process in an efficient way.

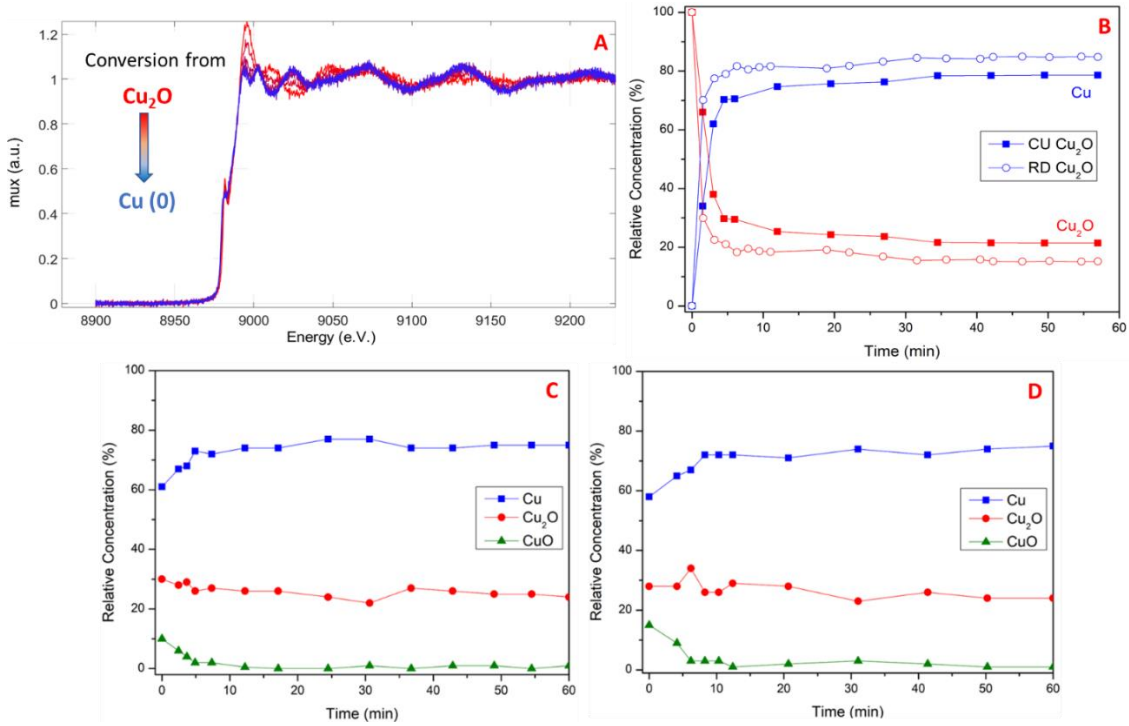

***Figure 3.32**: A) EXAFS spectra of CU Cu_2O (collected at -0.7 V vs RHE) compared to the references (metal Cu and Cu_2O). Analysis of the composition of the catalyst during the time for the two structures at the voltage of -0.7 V (B), -0.9 V (C) and -1.1 V vs RHE.*

3.4 Conclusions

In this chapter, a synthetic procedure to obtain well defined nanoparticles of Cu_2O was presented. The synthesis allows to directly obtain cubic (bounded with {100} facets) and rhombo-dodecahedral (bounded with twelve {110} facets) nanoparticles with a very sharp distribution of average sizes. The characterization of these nanoparticles confirmed the formation of surface and bulk pure Cu_2O. Electrochemical experiments revealed promising catalytic behavior under CO_2RR conditions but, at the same time, an easy reduction of Cu_2O to metal copper, especially in the case of RD Cu_2O.

Catalyst	Electrolyte	Conditions	Device	$FE_{CH_2CH_2}$	Ref.
Cu_2O (CU)	$KHCO_3$ 0.1 M	-1.1 V Vs RHE	Gas-tight cell	29 %	This work
Cu_2O (RD)	$KHCO_3$ 0.1 M	-1.1 V Vs RHE	Gas-tight cell	15 %	This work
Single Crystal Cu_2O (CU)	$KHCO_3$ 0.1 M	-1.4 V Vs SHE	Pyrex electrolysis cell	40 %	[32]
Cu_2O (CU)	$KHCO_3$ 0.1 M	-0.9 V Vs RHE	H-cell	25 %	[64]
Cu_2O (CU)	$KHCO_3$ 0.1 M	-100 mA/cm^2	Flow-cell	19 %	[64]
Cu_2O/C	$KHCO_3$ 0.5 M	-1.1 V Vs RHE	H-cell	45 %	[25]
Au-decorated CU Cu_2O	$KHCO_3$ 0.1 M	-1.3 V Vs RHE	H-cell	24 %	[29]

***Table 3.2**: Comparison between different Cu_2O-based catalysts.*

The electrocatalytic performances for similar materials are reported in Table 3.2. The comparison of the presented examples with literature is not straightforward due to the different experimental conditions and mainly, electrochemical devices. For that reason, pristine materials were used as electrocatalyst toward CO_2RR on H- and flow cells, showing a catalytic behavior dependent on the adopted device. A higher *FE* toward the formation of ethylene was observed for the CU Cu_2O and an increase activity toward HCOOH for RD Cu_2O. The characterizations confirmed a limited selectivity toward the different products of CO_2RR. Post activity characterization highlighted the limited stability of the materials, with a superficial reconstruction of the nanoparticles and a rapid conversion of Cu_2O to metal copper. These two defects are relevant, still poorly investigated and drastically limit the scalability of the material, unless appropriately protected. In the next chapter, the formation of heterostructures is presented as efficient way to improve the dispersion and, at the same time, to tune the overall selectivity towards a particular product. Different composites based on Cu_2O nanoparticles are presented, focusing on their electrochemical characterization and the effects of the formation of a composite on the overall catalytic behavior.

3.5 References

[1] S. Yadav, A. Jain, P. Malhotra, *Green Chem.* 21 (**2019**) 937–955.

[2] Y. Shang, L. Guo, *Adv. Sci.* 2 (**2015**) 1500140.

[3] M.H. Huang, M. Madasu, *Nano Today* 28 (**2019**) 100768.

[4] Y. Xia, Y. Xiong, B. Lim, S.E. Skrabalak, *Angew. Chemie - Int. Ed.* 48 (**2009**) 60-103.

[5] S. Wang, G. Liu, L. Wang, *Chem. Rev.* 119 (**2019**) 5192–5247.

[6] M.D. Susman, Y. Feldman, A. Vaskevich, I. Rubinstein, *ACS Nano* 8 (**2014**) 162–174.

[7] L. Zaza, K. Rossi, R. Buonsanti, *ACS Energy Lett.* 7 (**2022**) 1284–1291.

[8] W. Huang, *Acc. Chem. Res.* 49 (**2016**) 520–527.

[9] S. Chen, F. Xiong, W. Huang, *Surf. Sci. Rep.* 74 (**2019**) 100471.

[10] H. Xu, W. Wang, W. Zhu, *J. Phys. Chem. B* 110 (**2006**) 13829–13834.

[11] J.Y. Ho, M.H. Huang, *J. Phys. Chem. C* 113 (**2009**) 14159–14164.

[12] Y. Sui, W. Fu, H. Yang, Y. Zeng, Y. Zhang, Q. Zhao, Y. Li, X. Zhou, Y. Leng, M. Li, G. Zou, *Cryst. Growth Des.* 10 (**2010**) 99–108.

[13] X. Liang, L. Gao, S. Yang, J. Sun, *Adv. Mater.* 21 (**2009**) 2068–2071.

[14] C. Liu, Y.H. Chang, J. Chen, S.P. Feng, *ACS Appl. Mater. Interfaces* 9 (**2017**) 39027–39033.

[15] K. Self, W. Zhou, *Cryst. Growth Des.* 16 (**2016**) 5377–5384.

[16] L.M. Rossi, J.L. Fiorio, M.A.S. Garcia, C.P. Ferraz, *Dalt. Trans.* 47 (**2018**) 5889–5915.

[17] S. Rej, M. Bisetto, A. Naldoni, P. Fornasiero, *J. Mater. Chem. A* 9 (**2021**) 5915–5951.

[18] Y. Lou, Y. Zhang, L. Cheng, J. Chen, Y. Zhao, *ChemSusChem* 11 (**2018**) 1505–1511.

[19] T. Wei, Y.N. Zhu, X. An, L.M. Liu, X. Cao, H. Liu, J. Qu, *ACS Catal.* 9 (**2019**) 8346–8354.

[20] A.A. Permyakova, J. Herranz, M. El Kazzi, J.S. Diercks, M. Povia, L.R.

Mangani, M. Horisberger, A. Pătru, T.J. Schmidt, *ChemPhysChem* 20 (**2019**) 3120–3127.

[21] S.H. Liu, J.S. Lu, Y.C. Pu, H.C. Fan, *J. CO2 Util.* 33 (**2019**) 171–178.

[22] B. Sun, H. Li, X. Li, X. Liu, C. Zhang, H. Xu, X.S. Zhao, *Ind. Eng. Chem. Res.* 57 (**2018**) 14011–14021.

[23] A. Ajmal, I. Majeed, R.N. Malik, M. Iqbal, M.A. Nadeem, I. Hussain, S. Yousuf, Zeshan, G. Mustafa, M.I. Zafar, M.A. Nadeem, *J. Environ. Chem. Eng.* 4 (**2016**) 2138–2146.

[24] K. Chanda, S. Rej, M.H. Huang, *Nanoscale* 5 (**2013**) 12494–12501.

[25] Y. Gao, S. Yu, P. Zhou, X. Ren, Z. Wang, Z. Zheng, P. Wang, H. Cheng, Y. Liu, W. Wei, Y. Dai, B. Huang, *Small* 18 (**2022**) 2105212.

[26] R. Li, J. Xu, R. Zeng, Q. Pan, T. Tang, W. Luo, *J. Power Sources* 457 (**2020**) 228058.

[27] S. Mohan, B. Honnappa, A. Augustin, M. Shanmugam, C. Chuaicham, K. Sasaki, B. Ramasamy, K. Sekar, *Catalysts* 12 (**2022**) 445.

[28] Y. Gao, Q. Wu, X. Liang, Z. Wang, Z. Zheng, P. Wang, Y. Liu, Y. Dai, M.H. Whangbo, B. Huang, *Adv. Sci.* 7 (**2020**) 1902820.

[29] X. Cao, G. Cao, M. Li, X. Zhu, J. Han, Q. Ge, H. Wang, *Eur. J. Inorg. Chem.* 2021 (**2021**) 2353–2364.

[30] K.P. Kuhl, E.R. Cave, D.N. Abram, T.F. Jaramillo, *Energy Environ. Sci.* 5 (**2012**) 7050–7059.

[31] K.J.P. Schouten, Z. Qin, E.P. Gallent, M.T.M. Koper, *J. Am. Chem. Soc.* 134 (**2012**) 9864–9867.

[32] Y. Hori, I. Takahashi, O. Koga, N. Hoshi, *J. Mol. Catal. A Chem.* 199 (**2003**) 39–47.

[33] G. Vilé, G. Di Liberto, S. Tosoni, A. Sivo, V. Ruta, M. Nachtegaal, A.H. Clark,

S. Agnoli, Y. Zou, A. Savateev, M. Antonietti, G. Pacchioni, *ACS Catal.* 12 (**2022**) 2947–2958.

[34] T.S. Rodrigues, A.G.M. da Silva, L.C. de Oliveira, A.M. da Silva, R.R. Teixeira, P.H.C. Camargo, *Tetrahedron Lett.* 58 (**2017**) 590–595.

[35] W.C. Huang, L.M. Lyu, Y.C. Yang, M.H. Huang, *J. Am. Chem. Soc.* 134 (**2012**) 1261–1267.

[36] H.L. Wu, C.H. Kuo, M.H. Huang, *Langmuir* 26 (**2010**) 12307–12313.

[37] L. Li, C. Nan, Q. Peng, Y. Li, *Chem. - A Eur. J.* 18 (**2012**) 10491–10496.

[38] Y. Petroff, P.Y. Yu, Y.R. Shen, *Phys. Rev. B* 12 (**1975**) 2488–2495.

[39] P.Y. Yu, Y.R. Shen, *Phys. Rev. Lett.* 32 (**1974**) 939–942.

[40] J. Luo, L. Steier, M.K. Son, M. Schreier, M.T. Mayer, M. Grätzel, *Nano Lett.* 16 (**2016**) 1848–1857.

[41] C.Y. Toe, Z. Zheng, H. Wu, J. Scott, R. Amal, Y.H. Ng, *Angew. Chemie - Int. Ed.* 57 (**2018**) 13613–13617.

[42] C. Hou, J. Xie, H. Yang, S. Chen, H. Liu, *RSC Adv.* 9 (**2019**) 37911–37918.

[43] C.K. Wu, M. Yin, S. O'Brien, J.T. Koberstein, *Chem. Mater.* 18 (**2006**) 6054–6058.

[44] K. Chanda, S. Rej, M.H. Huang, *Chem. - A Eur. J.* 19 (**2013**) 16036–16043.

[45] M. Meldal, F. Diness, *Trends Chem.* 2 (**2020**) 569–584.

[46] A.B. Lowe, *Polym. Chem.* 1 (**2010**) 17–36.

[47] V.K. Tiwari, B.B. Mishra, K.B. Mishra, N. Mishra, A.S. Singh, X. Chen, *Chem. Rev.* 116 (**2016**) 3086–3240.

[48] J.E. Hein, V. V. Fokin, *Chem. Soc. Rev.* 39 (**2010**) 1302–1315.

[49] S.P. Shirame, R.B. Bhosale, *Green Chem.* (**2018**).

[50] C. Wei, S. Sun, D. Mandler, X. Wang, S.Z. Qiao, Z.J. Xu, *Chem. Soc. Rev.* 48 (**2019**) 2518–2534.

[51] A. Eilert, F. Cavalca, F.S. Roberts, J. Osterwalder, C. Liu, M. Favaro, E.J. Crumlin, H. Ogasawara, D. Friebel, L.G.M. Pettersson, A. Nilsson, *J. Phys. Chem. Lett.* 8 (**2017**) 285–290.

[52] S. González, M. Pérez, M. Barrera, A.R. González Elipe, R.M. Souto, *J. Phys. Chem. B* 102 (**1998**) 5483–5489.

[53] Y. Lum, J.W. Ager, *Nat. Catal.* 2 (**2019**) 86–93.

[54] Y. Lum, B. Yue, P. Lobaccaro, A.T. Bell, J.W. Ager, *J. Phys. Chem. C* 121 (**2017**) 14191–14203.

[55] F. Dattila, R. Garclá-Muelas, N. López, *ACS Energy Lett.* 5 (**2020**) 3176–3184.

[56] H. Yang, Y. Wu, G. Li, Q. Lin, Q. Hu, Q. Zhang, J. Liu, C. He, *J. Am. Chem. Soc.* 141 (**2019**) 12717–12723.

[57] A. Witkowski, M.S. Freund, A. Brajter-Toth, *Anal. Chem.* 63 (**1991**) 622–626.

[58] M. Liu, Y. Pang, B. Zhang, P. De Luna, O. Voznyy, J. Xu, X. Zheng, C.T. Dinh, F. Fan, C. Cao, F.P.G. De Arquer, T.S. Safaei, A. Mepham, A. Klinkova, E. Kumacheva, T. Filleter, D. Sinton, S.O. Kelley, E.H. Sargent, *Nature* 537 (**2016**) 382–386.

[59] R. Lin, J. Guo, X. Li, P. Patel, A. Seifitokaldani, *Catalyst*, 10 (**2020)** 27-30.

[60] D. Salvatore, C.P. Berlinguette, *ACS Energy Lett.* 5 (**2020**) 215–220.

[61] T. Burdyny, W.A. Smith, *Energy Environ. Sci.* 12 (**2019**) 1442–1453.

[62] M.R. Singh, E.L. Clark, A.T. Bell, *Phys. Chem. Chem. Phys.* 17 (**2015**) 18924–18936.

[63] Q. Si, M. Matsui, T. Horiba, O. Yamamoto, Y. Takeda, N. Seki, N. Imanishi, *J. Power Sources* 241 (**2013**) 744–750.

[64] T. Möller, F. Scholten, T.N. Thanh, I. Sinev, J. Timoshenko, X. Wang, Z.

Jovanov, M. Gliech, B. Roldan Cuenya, A.S. Varela, P. Strasser, *Angew. Chemie - Int. Ed.* 59 (**2020**) 17974–17983.

Chapter 4

Formation of heterostructures to improve selectivity of Cu_2O

4.1 Introduction

Cu_2O shows to possess limitations correlated to its low stability and selectivity in CO_2RR. These aspect has been studied in literature, highlighting the importance of nanostructuring to improve the catalytic behavior of these material [1,2]. The poor stability of these material has been reported in broad fields of applications [3]. The Cu_2O instability in photocatalysis or photo electrocatalysis rises from the high recombination rate of the charge carriers and on their short lifetime [4]. The photogenerated carriers are able to induce a partial self-oxidation or self-reduction of the material, affecting the overall catalytic properties [5]. The most popular approach to limit the photo corrosion is the utilization of sacrificial hole (h^+) scavengers, molecules able to react with the hole, avoiding the oxidation of the active material [6]. Low stability of Cu_2O-based nanostructures has been specifically investigated during eCO_2RR and associated to the easy conversion of the catalyst to metal Cu or CuO [7]. It is also known that strong acid media or high concentration of oxygen cause an oxidation of the material with a rapid conversion to CuO [8]. In the case of eCO_2RR process, the application of a negative voltage partially reduces the material, converting Cu_2O to metal Cu, the most stable chemical phase at those applied voltages or pH (Figure 4.1) [9].

The reduction of Cu_2O during eCO_2RR is typically not complete, with a small fraction of Cu(I) phase still observed even at higher voltages, suggesting a dynamic equilibrium between the application of reductive voltages and the Cu(0) re-oxidation due to oxidative species or local pH [10]. The low stability of Cu_2O-based nanostructures induces a loss of the initial facets, causing a partial deactivation of the material and a variation of the selectivity over the time [11]. Besides recent updates regarding the understanding of the conditions for different CO_2RR pathways, the correlation between chemical state of Cu-based catalysts and selectivity toward a particular product is still under debate [12].

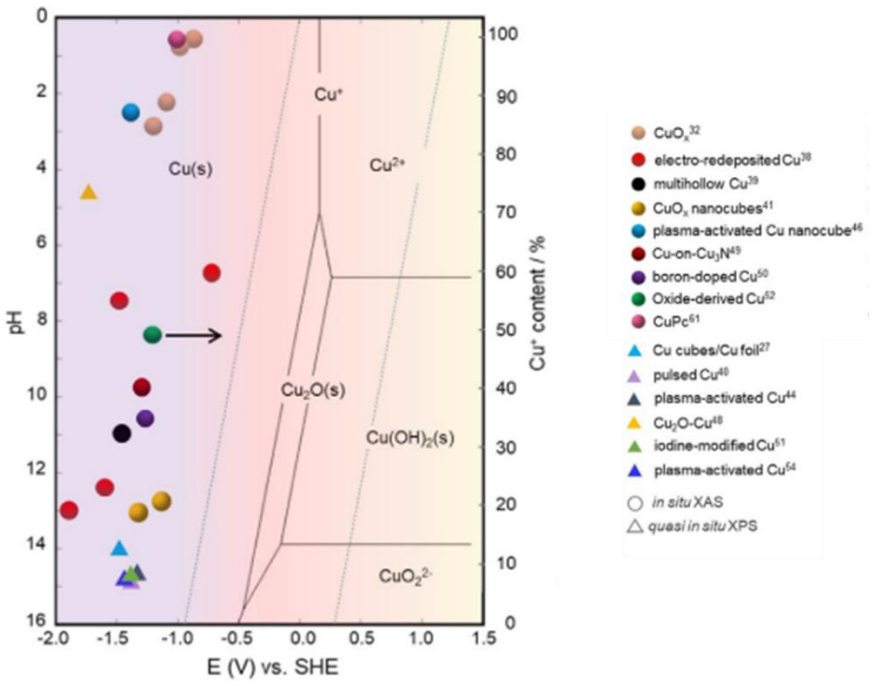

***Figure 4.1**: Purbaix diagram of Cu phases under different electrochemical conditions. From Reference* [9].

Many efforts have been dedicated to find strategies to increase the selectivity towards a specific catalytic product, in particular ethylene. These methods generally involved the improvement of crystallinity, the rational choice of exposed facets or doping elements and surface molecule engineering [13–15], with the final aim of enhance the intermediates stability and promote C-C bond formation [2,16]. The obtainment of heterostructures is one of the most diffuse approaches to improve the stability of a catalyst with a contemporaneous modification of the selectivity toward desired product(s). It has been shown that with a rational design of the support, it is possible to affect the dispersion, the electrochemical surface area and the overall selectivity of Cu_2O nanoparticles [17–19].

Different hybrid Cu_2O-based nanostructures were therefore developed with the aim of enhance the electrocatalytic activity and drive the overall selectivity toward a particular product. The heterostructures were formed coupling Cu_2O with g-C_3N_4, RGO and MoS_2, improving the dispersion of Cu_2O nanoparticles on the support and affecting the overall selectivity of the system. 2D Carbon-based structures are widely used as support due to

their strong efficiency on anchor nanostructures and improve the dispersion. In particular, thanks to the tunable structure and physicochemical properties, graphitic carbon nitride (g-C_3N_4) have got huge interest in several fields of research such as photo- and photoelectrochemical catalysis [20–22]. g-C_3N_4 finds applications in electrochemistry, exploiting the high surface and the good affinity with CO_2 to increase the overall electrochemical active area and influence product selectivity [23,24]. For instance, a recent work of Chen et al, reported the capability of g-C_3N_4 to strongly bind the key intermediates (such as *CO or *CHO) for the formation of hydrocarbon products [25].

Reduced Graphene Oxide (RGO) is another common carbon-based support for electrocatalytic applications thanks to the high surface area and the improved capability of stabilize components [26–28]. In particular, RGO is able to increase the conductivity of the entire composite and optimize the aggregation of catalyst nanoparticles, increasing the number of active sites involved in the catalytic process [29].

Various studies have reported the use of molybdenum disulfide (MoS_2) as support for catalytic applications thanks to its unique layered structure and the opportunity to exploit the interesting functional properties of metal dichalcogenide compounds [30–32]. With the presented procedure, it was possible to prepare nanoflowers of MoS_2 via a facile hydrothermal route and study the effect of the dispersion of Cu_2O nanoparticles on the overall catalytic behavior [33]. DFT calculations have revealed the high electrochemical activity of the edges of nanostructured MoS_2 and the combination of this important feature with the high surface area makes MoS_2 as a potential catalyst toward HER [34]. The coupling of nanostructured MoS_2 with well-defined Cu_2O nanoparticles drives the catalytic activity toward the formation of H_2, improving the overall selectivity toward HER process.

Encouraged by previous published results, Cu_2O nanoparticles were coupled with these different supports with the aim to investigate the role of the heterostructure composition on the electrocatalytic behavior of Cu_2O, in particular regarding stability and selectivity toward a particular product. Each composite has been discussed, focus the attention on the synthetical procedure, the characterization and the electrochemical CO_2RR tests performed using the catalyst as working electrode.

The synthetic procedure allows the formation of heterostructures varying the weight

fraction, an easy control of the final shape of Cu_2O and the decrease of the average sizes of Cu_2O nanoparticles. Moreover, the electrochemical characterization in a gas-tight cell showed an increased productivity of the composites toward the formation of HCOOH, CO and H_2.

4.2 Experimental section

All reagents were of analytical grade and used without further purifications. Melamine was used for the synthesis of graphitic C_3N_4. Graphite, $NaNO_3$, H_2SO_4, $KMnO_4$ and H_2O_2 were utilized for the modified Hummer's method and the preparation of GO while, for the reduction of GO to RGO, it was used NaOH and H_2N_2*$2H_2O$. Na_2MoO_4*$2H_2O$, NH_2CSNH_2 and citric acid were used for the preparation of MoS_2 nanoflakes, while SDS, $CuCl_2$, NH_2OH*HCl and NaOH were used as precursors for the synthesis of Cu_2O nanoparticles on the different supports.

Synthesis of g-C_3N_4

g-C_3N_4 was obtained starting from melamine. In a typical synthesis, 5 g of melamine were calcinated at 550° for three hours, obtaining a pale-yellow powder of g-C_3N_4. After completion of the heating treatment, the dispersion of the material was improved through ball milling and the powder was washed carefully with Milli-Q H_2O and absolute ethanol. g-C_3N_4 was separated by filtration and dried at 50°C overnight.

Synthesis of RGO

RGO was obtained via an adapted two-steps method [35,36]. In the first step graphite was converted to Graphene Oxide (GO) through a modified Hummer's method. In a typical procedure, 0.2 g of Graphite and 0.2 g of $NaNO_3$ were mixed in a round bottom flask with 10 mL of H_2SO_4 (95%). The solution was stirred at 400 rpm and kept in an ice bath for 30 minutes. Potassium Permanganate ($KMnO_4$, 1.2 g) was gradually added to the solution. After five minutes, 16 mL of Milli-Q H_2O were added, and the entire solution was stirred for one hour. The entire setup must be kept in ice bath in order to avoid strong effervescence of the solution during this step. The reaction was concluded adding 40 mL of Milli-Q H_2O and 1.2 mL of H_2O_2 and stirred again for one hour. During this step, the color of the solution changes from violet to brownish. The powder of GO was washed

with a 1:3 HCl solution to remove all the metal traces from the obtained material and it was separated by centrifugation. The obtained material was washed three times with absolute ethanol, separated from the solution by filtration and dried for 12 hours at 45°C. In the second step, GO was reduced to RGO by addition of a strong reducing agent such as Hydrazine. In a typical procedure, 50 mg of GO were mixed with 50 mL of H_2O in a 250 mL round bottom flask. The pH of the mixture was corrected to 10-11 by addition of 0.1 M NaOH solution. 4 mL of $H_2N_2*2H_2O$ were added and the entire solution was heated at 90°C under reflux and stirred for one hour. RGO was filtrated under vacuum using a Millipore filter paper (pore size: 0.2 μm), washed with Milli-Q H_2O and absolute ethanol and dried at 50°C for 12 hrs.

Synthesis of MoS_2

MoS_2 nanoflowers were synthetized via hydrothermal route. In a typical procedure, 179 mg of $Na_2MoO_4*2H_2O$ and 250 mg of NH_2CSNH_2 were mixed with 170 mg of citric acid in 25 mL of Milli-Q water. The solution was stirred for one hour at 500 rpm, placed in a 50 mL Teflon autoclave and kept in an oven at 200°C for 24 hours. The obtained MoS_2 was washed three times with absolute ethanol, separated from the solution by filtration and dried for 12 hours at 45°C.

Preparation of the composites

All the composites were prepared via impregnation, growing Cu_2O nanoparticles on the support. In particular, a proper amount of support (5, 20, 30, 40 and 50 mg respectively for the 2:1, 1:2, 1:3, 1:4 and 1:5 composite) was mixed in the solution of SDS and sonicated for 20 minutes. The synthesis proceeded similarly to the preparation of pure Cu_2O nanoparticles presented on paragraph 3.2.1.

EIS measurements and determination of Mott-Schottky plot

EIS measurements were carried using a Autolab PGSTAT302N workstation in a three-electrode setup where a Pt electrode is the CE and the RE is an Ag/AgCl. Sat electrode. The working electrode was prepared as follow: 5 mg of catalysts were dissolved in 1 mL of 3:1 H_2O:i-propanol ink; 50 μL of Nafion were added and the ink was sonicated for one hour in order to disperse the catalyst. 100 μL of catalyst (two deposition of 50 μL) were

dropcasted on the conductive surface of ITO glass and dried at 45°C for two hours. The deposited area is 1 cm^2.

The EIS measurements were performed in a 0.1 M Na_2SO_4 as electrolyte, in the frequency range of 100000 Hz to 1 Hz under dark conditions. Before each measure, the cell was purged with Ar for 30 minutes in order to keep O_2-free environment. MS analysis was carried out by sweeping voltage from -0.20 V to 0.05 V (vs Ag/AgCl sat.) for Cu_2O and from -0.50 V to 1.00 V (vs Ag/AgCl sat.) for g-C_3N_4.

Electrochemical characterization and CO_2RR tests for the different composites

All the electrochemical characterizations and the CO_2RR tests were performed with the procedures described on chapter 2.8.

4.3 Results and discussion

4.3.1 Composite between CU Cu_2O and g-C_3N_4

4.3.1.1 Synthesis and Characterization of Cu_2O/g-C_3N_4 composites

With the presented method, CU Cu_2O nanoparticles were synthetized on the surface of g-C_3N_4 nanosheets through a two-steps route, where firstly g-C_3N_4 was prepared via calcination of melamine and then it was used as support for the synthesis of Cu_2O nanoparticles (Figure 4.2).

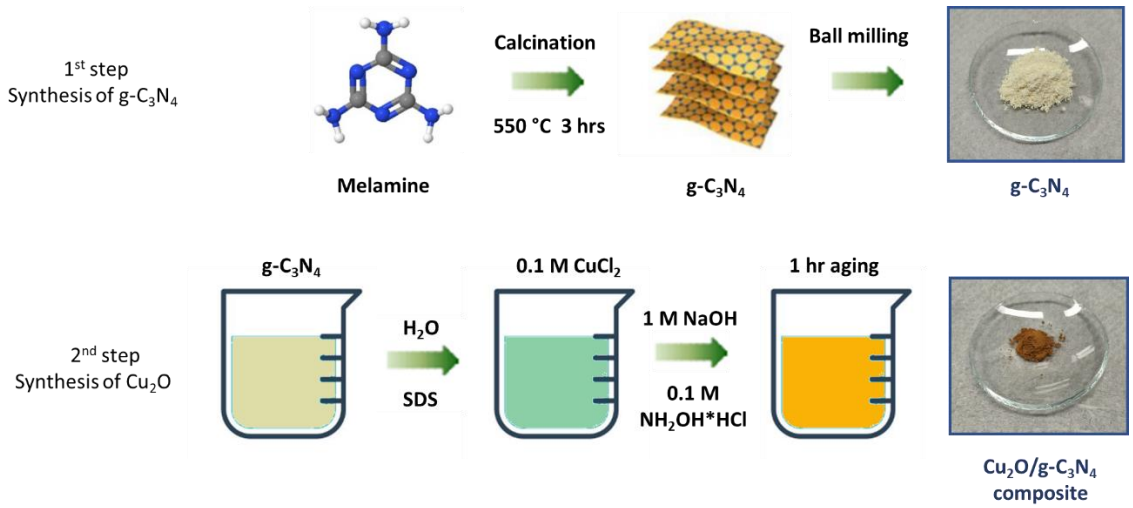

***Figure 4.2**: Synthetic route to obtain pristine g-C_3N_4 and Cu_2O/g-C_3N_4 composites.*

The determination of Cu amount through ICP analysis (Table 4.1) confirmed the weight fraction of the various composites even if a slight difference was observed for the composites with the higher fraction of g-C_3N_4.

Composite CU Cu_2O/C_3N_4		
Cu_2O	C_3N_4 (theorical)	C_3N_4 (Calculated)
1	2	1.9
1	3	2.9
1	4	3.4
1	5	4.2

***Table 4.1**: ICP analysis of CU amount in the different composites with g-C_3N_4.*

XRD diffraction patterns evidenced the typical reflections of crystalline Cu_2O presented on paragraph 3.3.1, with a lattice parameter of 4.27 Å, compatible with similar works (Figure 4.3 A) [37]. Diffraction lines at 13.0° and 27.5° were detected, which can be assigned respectively to (100) and (002) characteristic plane of graphitic carbon nitride and that indicate the formation of a mixed phase between g-C_3N_4 and Cu_2O [38,39]. At the same time, Raman spectra confirmed the formation of the composite by the presence of characteristic vibrations of both the materials (Figure 4.3 B) [40].

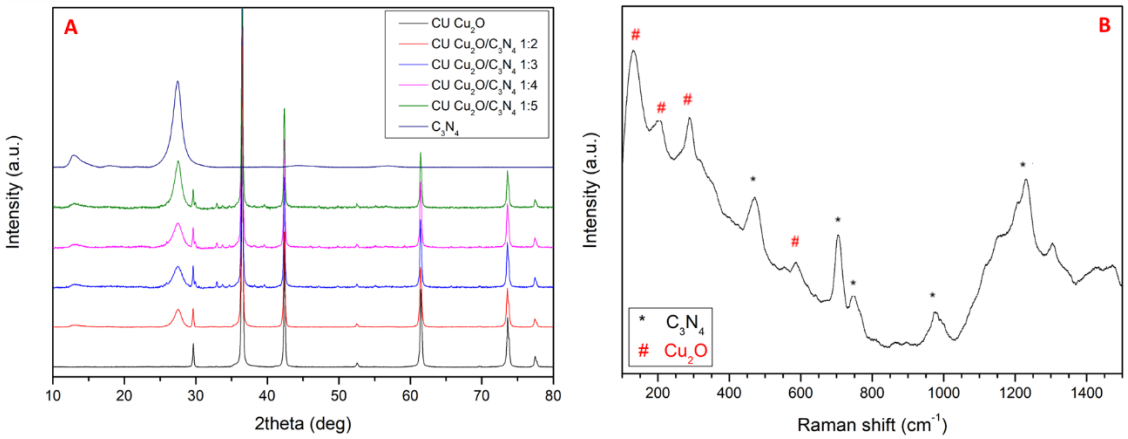

***Figure 4.3**: XRD (A) and Raman spectrum (B) of CU Cu_2O/g-C_3N_4 composite.*

With the proposed synthetical procedure, cubic Cu_2O nanoparticles directly grow on the typical lamellar surface of pristine g-C_3N_4 (Figures 4.4 A and B), as it is possible to observe from SEM and TEM images presented in Figure 4.4.

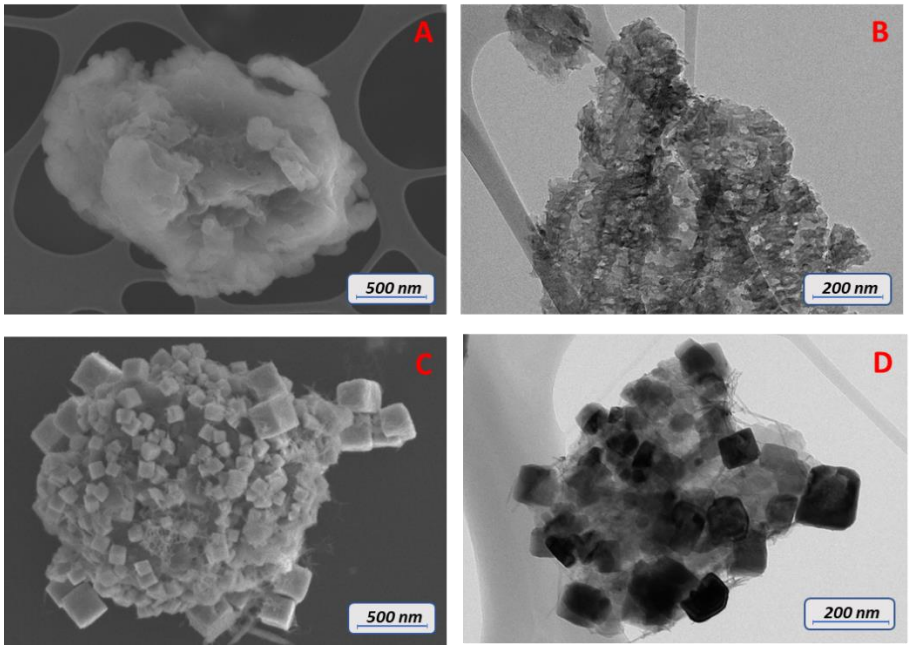

***Figure 4.4**: SEM and TEM images of g-C_3N_4 (A and B) and CU Cu_2O/g-C_3N_4 1:2.*

A decreasing of the average sizes of the nanoparticles occurred when the weight fraction of the support was increased (Figure 4.5). In the case of the composite Cu_2O/g-C_3N_4 1:2, Cu_2O grows both in solution or on the support, resulting in a broader size distribution and the presence of two peaks on the size distribution plot (Figure 4.5 A). When the content of g-C_3N_4 is increased, the distribution become narrowed, indicating a more probable growth of Cu_2O nanoparticles on the support (Figures 4.5 C and D). Under these conditions, average dimension of Cu_2O nanoparticles decreased till the value of 80 nm (σ=20 nm), more than two times lower than those of unsupported materials.

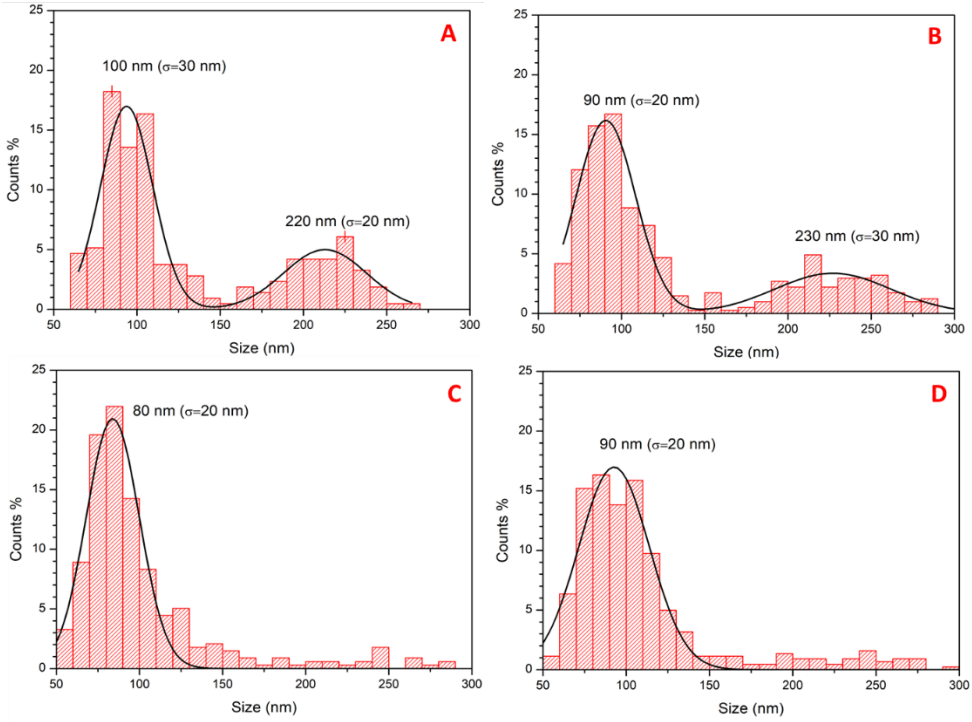

Figure 4.5: *Average sizes of Cu_2O nanoparticles in the composite CU Cu_2O/g-C_3N_4 varying the weight ratio. A) 1:2, B) 1:3, C) 1:4, D) 1:5.*

In addition, the surface distribution of the composite was verified by EDX, confirming the presence of Cu, O and C for the composite CU Cu_2O/g-C_3N_4 1:2 (Figure 4.6).

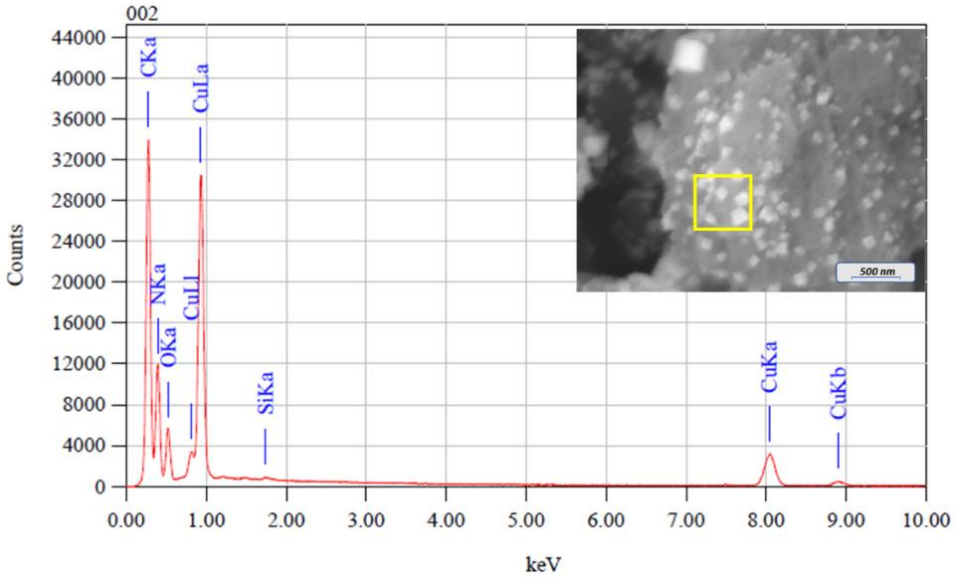

Figure 4.6*: EDS spectrum of CU Cu_2O/g-C_3N_4 1:2 composite. Insert: Selected area for the analysis.*

4.3.1.2 Electrochemical characterization of Cu_2O/g-C_3N_4 composites and CO_2RR tests

The determination of ECSA is essential to evaluate the active surface of the material and to explain possible deviations of the composite from the behaviors observed for the pristine nanoparticles [25]. In particular, following the same procedure presented in paragraph 3.3.3, from the CVs at different scan rates and the determination of capacitive current, it was possible to obtain the value of the capacitance and the subsequent ECSA. The analysis of the capacitive current I_c revealed a general increase of the ECSA value from the value of (2.2±0.2)*10^{-1} cm^2 of CU Cu_2O to the value of (8.5±0.6)*10^{-1} cm^2 of the composite CU Cu_2O/g-C_3N_4 1:3, in line with the decreasing of the average size of Cu_2O nanoparticles (Figure 4.7 A). A decreased ECSA value was observed at higher fraction of support in the composite, even if this variation is still inside the uncertainty of the analysis (Figure 4.7 B). The highest obtained ECSA is related to the composite CU Cu_2O/g-C_3N_4 1:3.

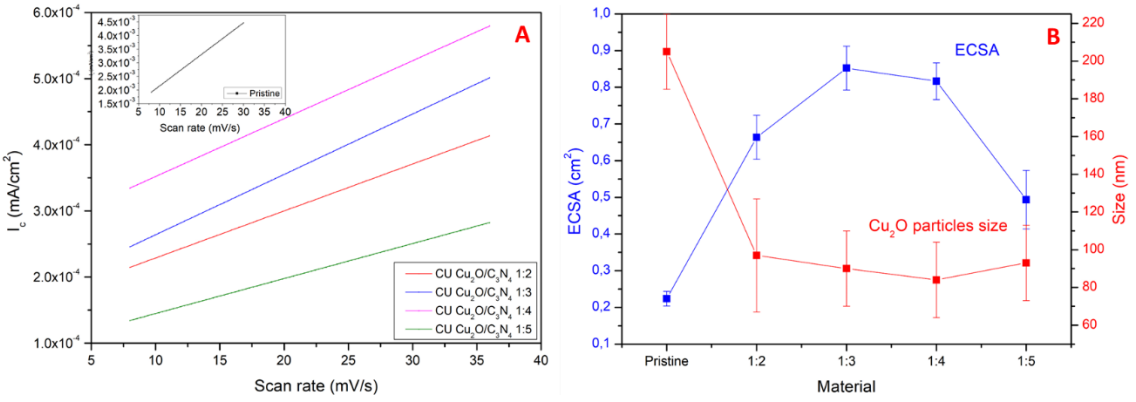

***Figure 4.7**: ECSA for the different CU Cu_2O/g-C_3N_4 composites (A) and obtained trends between the Cu_2O particle size and the relative ECSA (B).*

Higher ECSA values provides more active sites for the catalysis, improving the amount of CO_2 adsorbed molecules and, at the same time, promoting the charge transfer of the species on the catalytic sites of the material, partially confirming a different catalytic behavior of these materials with respect to the pristine Cu_2O [41]. These results suggested improved adsorption and charge properties of these composites respect the pristine materials, involving a different activity compared to CU Cu_2O.

The electrochemical characterization of the composites performed with RDE electrode did not reveal any characteristic behavior different than pristine materials (Figures 4.8 and 4.9): the reduction peak of Cu_2O to metal Cu is observed at -1.0 V (vs SCE), indicating a conversion of the material due to the application of the voltage. Different current values between Ar and CO_2 atmosphere were observed, confirming the dependency of catalytic pathway to the atmosphere of the measurement.

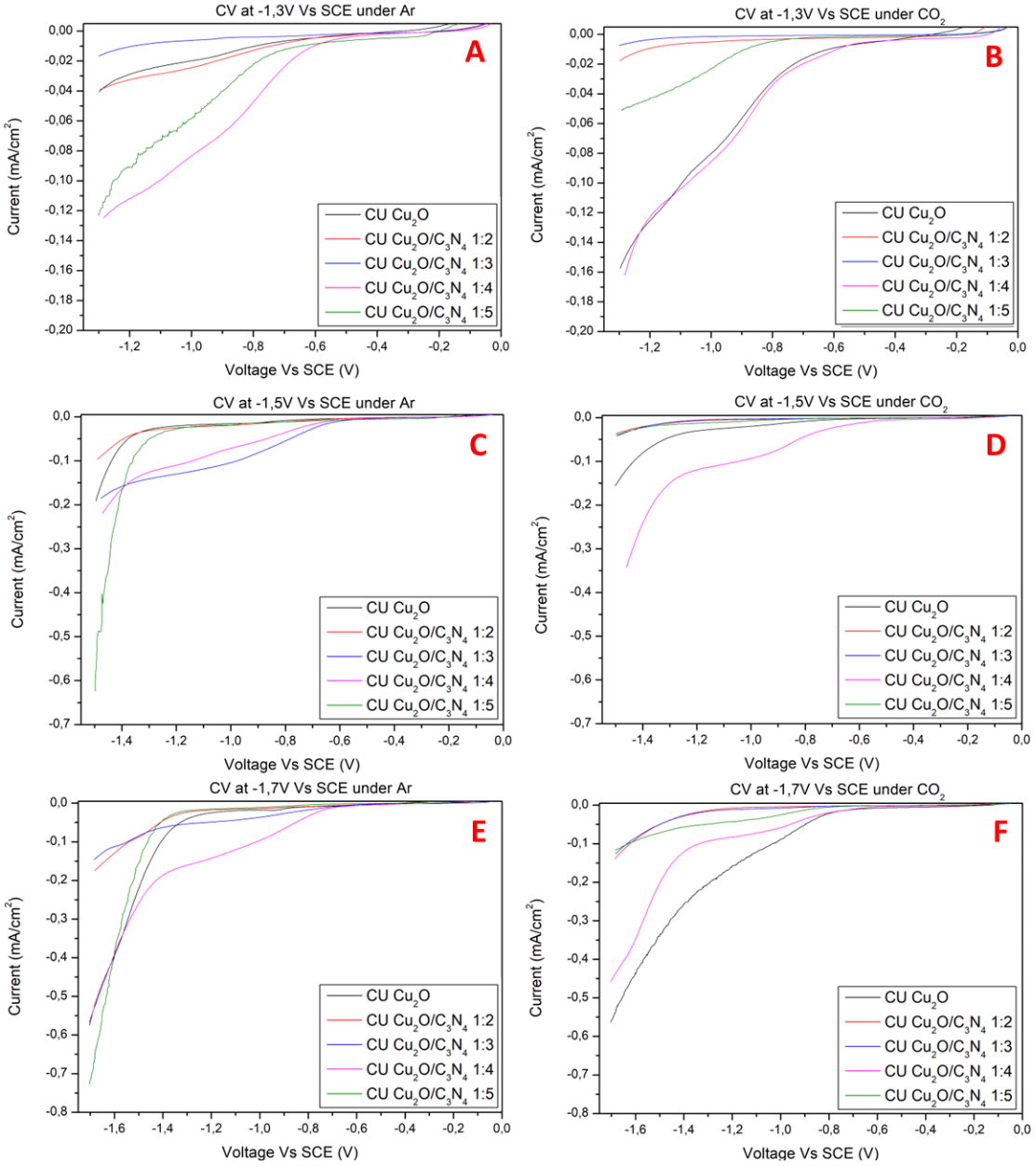

***Figure 4.8**: LSV at -1.3 V (A and B), -1.5 V (C and D) and -1.7 V (E and F) for the different composites CU Cu_2O/g-C_3N_4. All the voltages are vs SCE and corrected with iR compensation.*

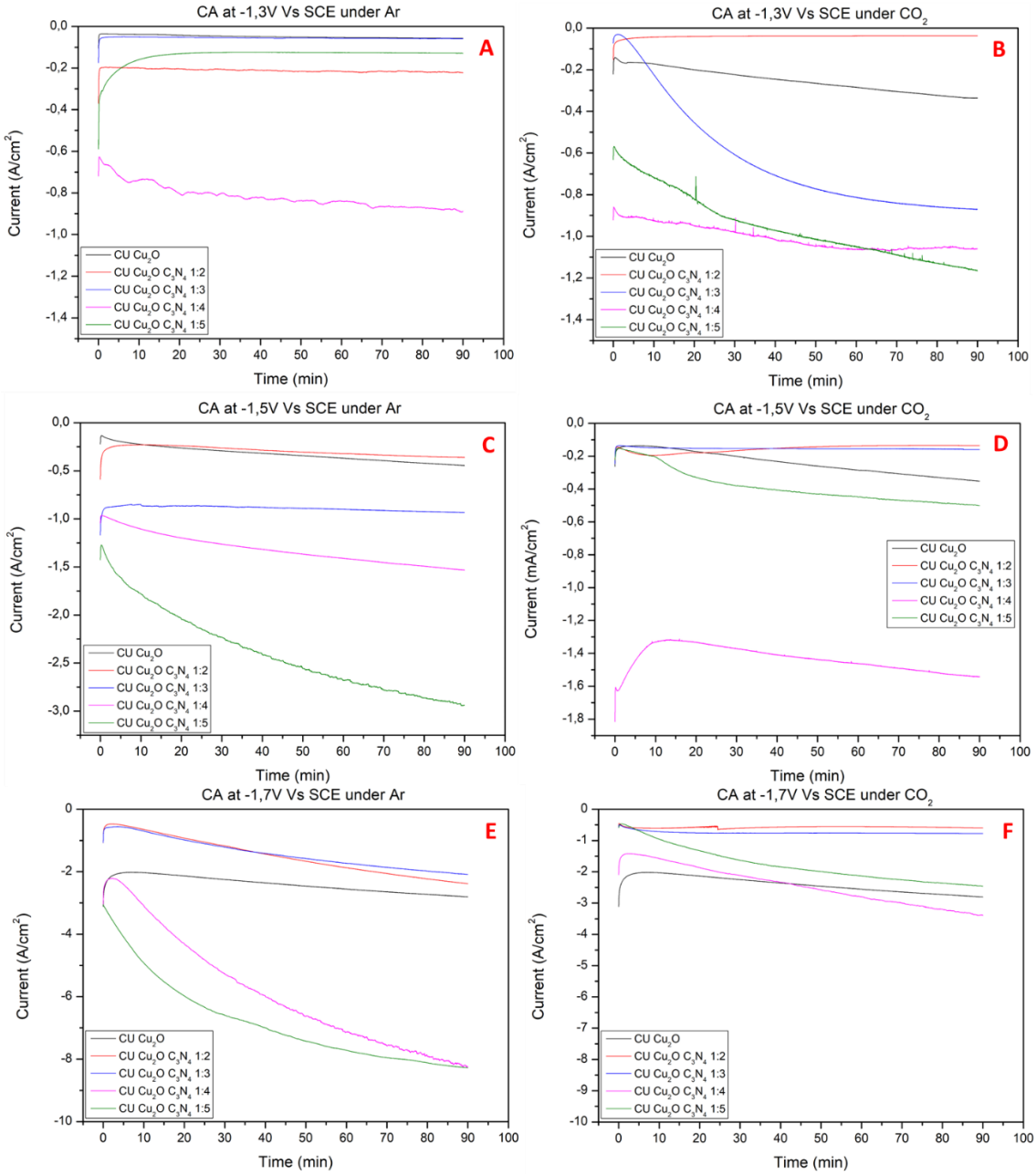

***Figure 4.9**: CAs at -1.3 V (A and B), -1.5 V (C and D) and -1.7 V (E and F) for the different composites CU Cu_2O/g-C_3N_4. All the voltages are vs SCE and corrected with iR compensation.*

More information can be obtained by the analysis of the CO_2RR experiments performed with the gas tight electrochemical cell at the operative voltages (-0.7 V, -0.9 V and -1.1 V vs RHE).

First, the analysis of pristine g-C_3N_4 was reported in order to evaluate the possible contribution of the support on the overall reactivity of the composite. The analysis of pristine g-C_3N_4 at the voltage of -1.1 V vs RHE (Figure 4.10) revealed a low current and a total selectivity toward the formation of H_2, confirming the intrinsic low electrocatalytic behavior of g-C_3N_4 towards CO_2RR process.

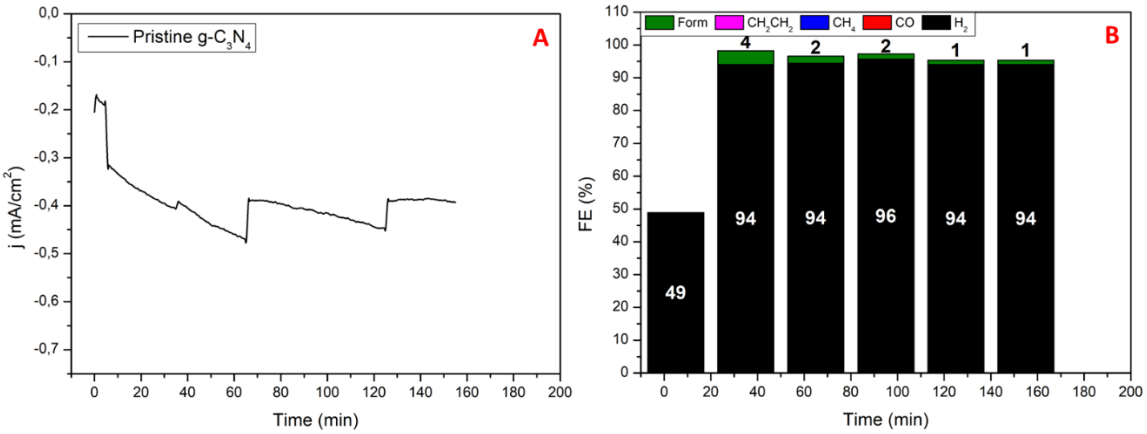

***Figure 4.10**: CA (A) and FEs (B) for g-C_3N_4 at the voltage of -1.1 V vs RHE under CO_2 atmosphere.*

Based on this, it is reasonable to consider that the current of the composites is lower than that of the unsupported Cu_2O and, in general, the FE_{H_2} for the composites was increased with respect to those of the unsupported materials due to the contribution of g-C_3N_4 which is highly selective towards HER. While bare g-C_3N_4 shows poor catalytic CO_2 reduction activity, the formation of the composite and the subsequent improved dispersion of Cu_2O nanoparticles had positive implications on the selectivity of Cu_2O toward the formation of CO_2RR products. Figures 4.11, 4.12 and 4.13 show the electrochemical characterization of the different composites performed at the operative voltages. The voltage of -1.1 V vs RHE is chosen as representative situation for the trend of the reactivity of the composites (Figure 4.11). At this voltage, unsupported CU Cu_2O showed overall FE_{CO} around 40%, high productivity of CO and a quite high productivity of CH_2CH_2. The total FE_{HCOOH} between pure Cu_2O and composites are almost similar (16% for CU Cu_2O and around 22% for the various composites). The composites have an increased productivity towards formic acid, while Cu_2O nanoparticles showed a higher production of CO (Figure 4.11 C). This is evident from the analysis of the ratio between the amount of $HCOO^-$ product and all the CO_2RR products (CO, $HCOO^-$, CH_4 and

ethylene) (Figure 4.11 D). In the case of pure Cu_2O, this ratio drops quickly during the first minute of CA and constantly decrease during the CA due to the contemporaneous increasing of CH_2CH_2 and, mainly, CO productivity. On the other hand, for the composites a general increase of the fraction of $HCOO^-$ is observed, in particular for the composite with the smallest size of Cu_2O nanoparticles (CU Cu_2O/g-C_3N_4 1:3 and 1:5), suggesting a relationship between dispersion of the nanoparticles, dimensions of the nanostructures and different catalytic behavior. The improved $HCOO^-$ formation for the composite is confirmed even observing that, after the three hours of experiments, the fraction of formate for the composite CU Cu_2O/g-C_3N_4 1:3 is almost double (0.57 vs 0.28) respect the pure material.

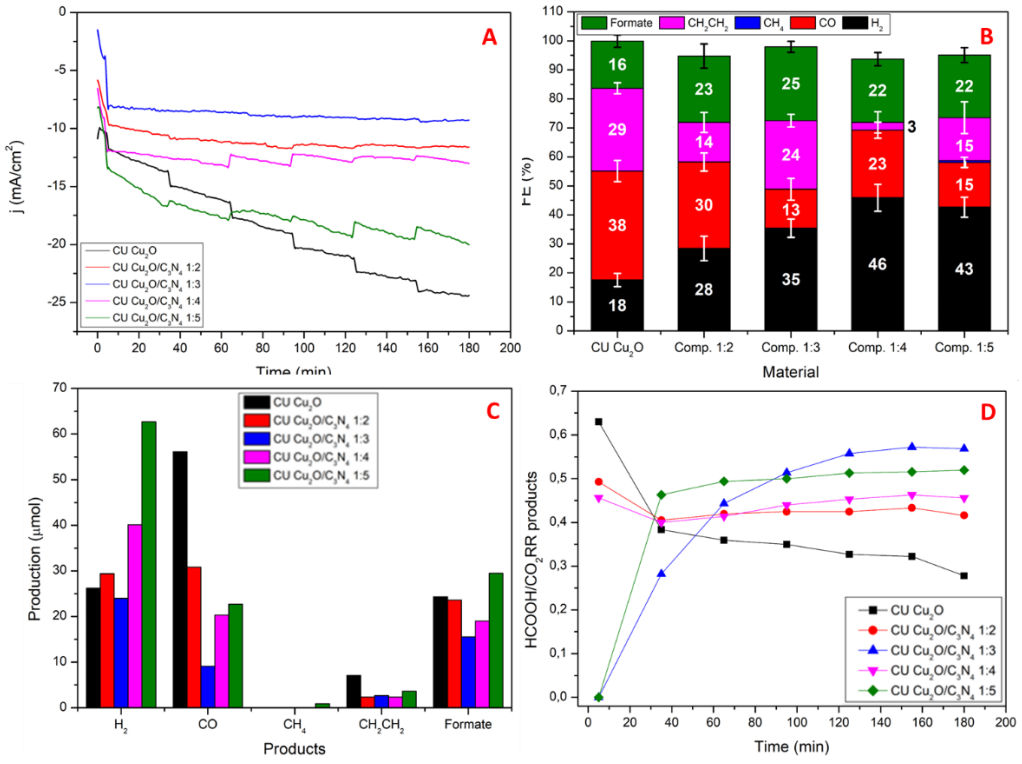

***Figure 4.11**: eCO₂RR tests for composites CU Cu_2O/g-C_3N_4 at the voltage of -1.1 V vs RHE. A) 3-hrs CA under CO_2 atmosphere. B) FEs toward gaseous and liquid products. C) Mol of different products after 3-hrs CA and D) Ratio between HCOOH and the products of CO_2RR for the different composites.*

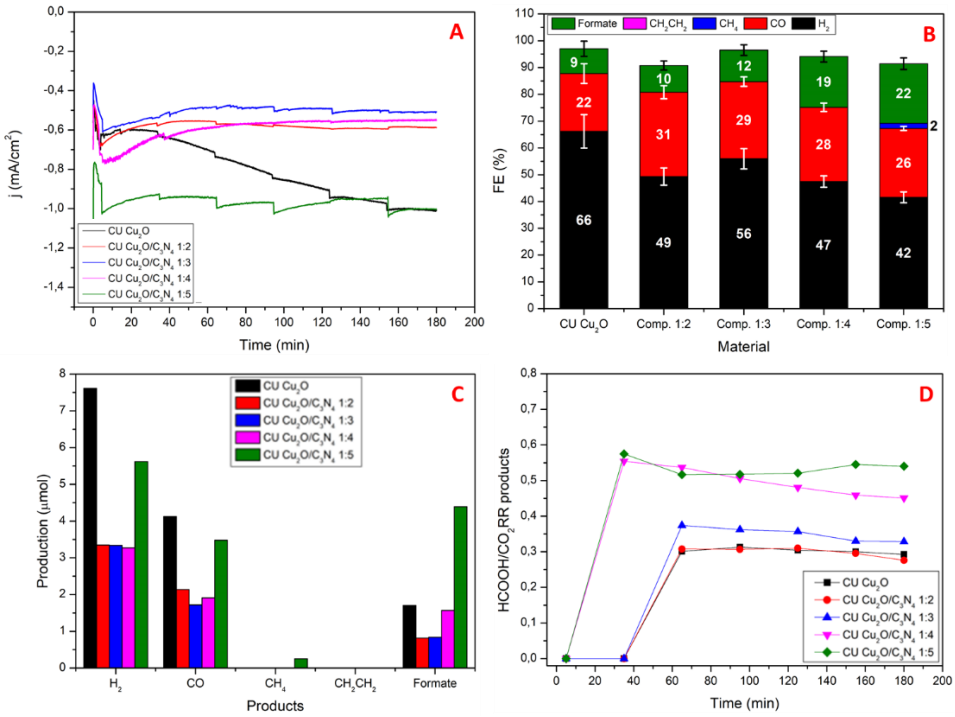

***Figure 4.12**: eCO₂RR tests for composites CU Cu₂O/g-C₃N₄ at the voltage of -0.7 V vs RHE. A) 3-hrs CA under CO₂ atmosphere. B) FEs toward gaseous and liquid products. C) Mol of different products after 3-hrs CA and D) Ratio between HCOOH and the products of CO₂RR for the different composites.*

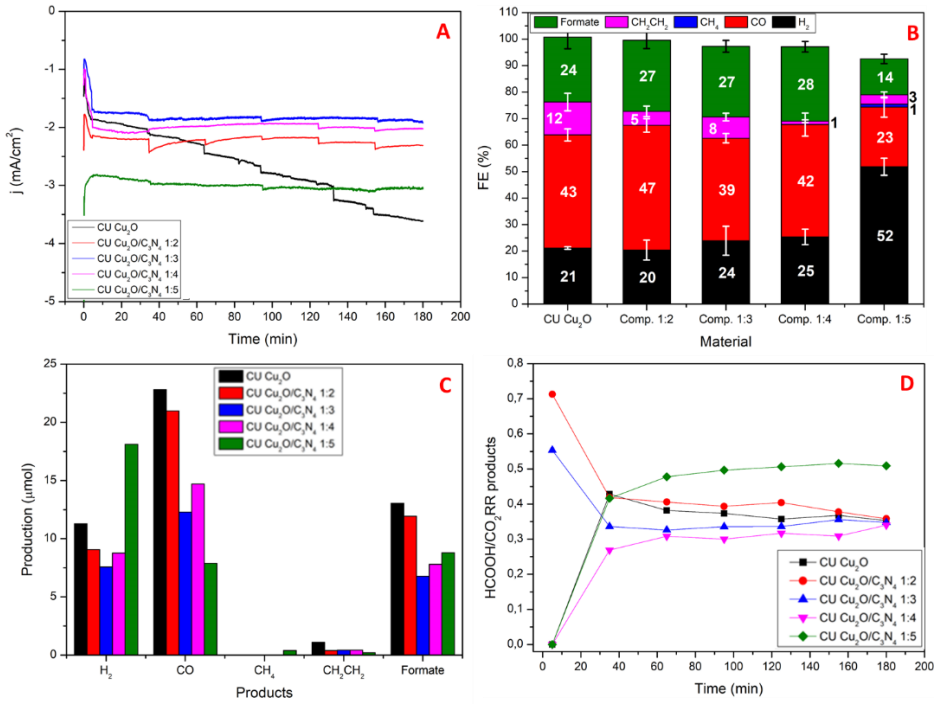

***Figure 4.13**: eCO₂RR tests for composites CU Cu₂O/g-C₃N₄ at the voltage of -0.9 V vs RHE. A) 3-hrs CA under CO₂ atmosphere. B) FEs toward gaseous and liquid products. C) Mol of different products after 3-hrs CA and D) Ratio between HCOOH and the products of CO₂RR for the different composites.*

The analysis of the CO_2RR activity at the other voltages revealed similar trends than the case at -1.1 V vs RHE (Figures 4.12 and 4.13), with a general increased productivity toward $HCOO^-$ for the composites, even at the lowest considered voltage, in particular for those fractions (1:3, 1:4 or 1:5) where Cu_2O nanoparticles are smaller and more homogeneous. Traces of CH_4 were detected during the electrochemical characterization but the contribute to the overall FE is negligible ($FE_{CH_4} < 1\ \%$), meaning that the investigated materials are not active toward the formation of Hydrocarbons.

4.3.1.3 Effects of CO_2RR on the materials

Operando and post characterizations are fundamental to investigate the effects of the catalytic experiments on the heterostructures and to unveil the implications of the improved dispersion of Cu_2O nanoparticles on the stability of the entire structure. In particular, SEM images of the working electrode after electrochemical CO_2RR experiments were collected, revealing that the electrochemical process has implications on the Cu_2O morphology even on the case of the composite (Figure 4.14). Indeed, after electrochemical tests, the morphology of the nanoparticles was altered, showing a rougher surface of the nanostructures and a partial coarsening. The effects of CO_2RR were observed in all the composites and at all the different voltages, confirming the effects of electrochemical characterization on the Cu_2O nanoparticles as observed for pure – unsupported corresponding material.

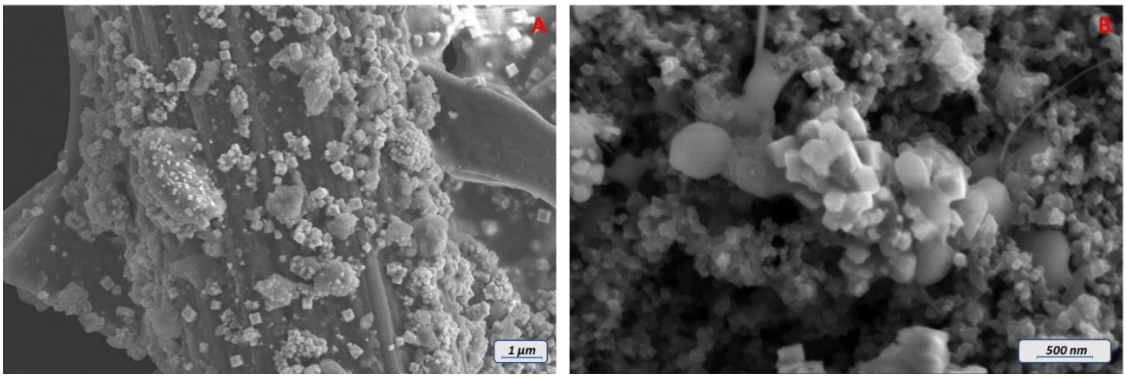

***Figure 4.14**: SEM images of the sample CU Cu_2O/g-C_3N_4 1:2 after electrochemical characterization at the voltage of -1.1 V vs RHE.*

To deeply study the implications of CO_2RR on the chemical state of the catalysts, *operando* XAS experiments were performed during 1hr-CA at the voltage of -0.7 V vs RHE. In Figure 4.15 the collected XAS spectra for the different composition of composite with g-C_3N_4 were presented.

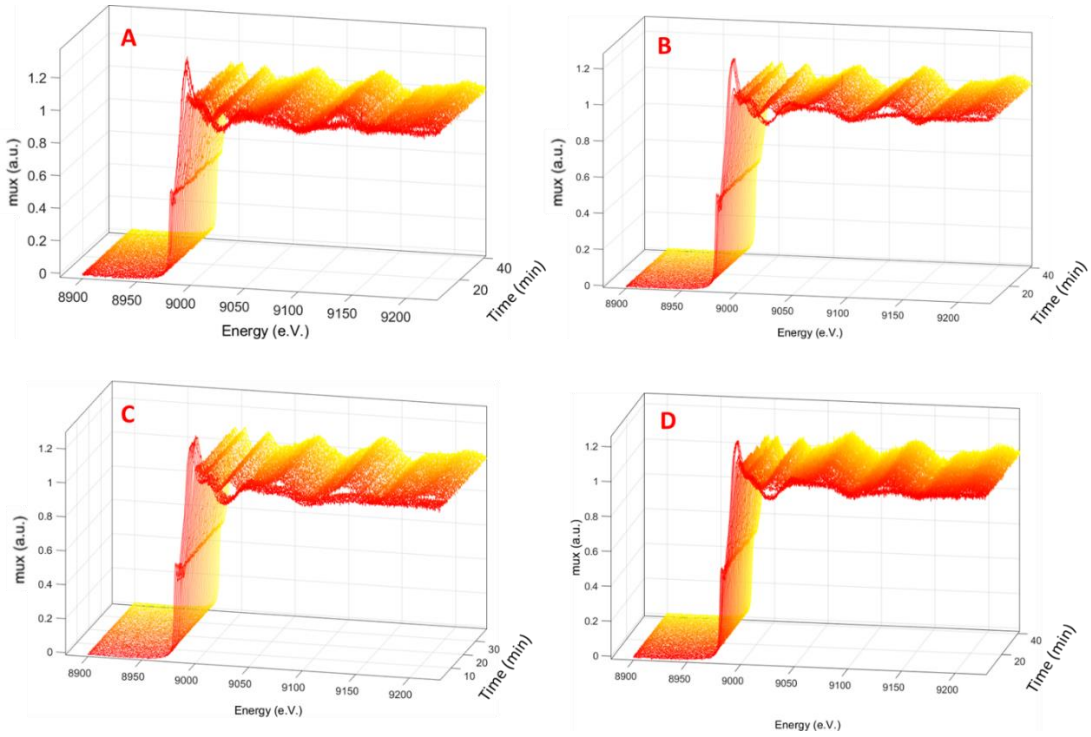

***Figure 4.15**: XAS spectra for the different composites between CU Cu_2O and g-C_3N_4 at the voltage of -0.7 V vs RHE. A) 1:2. B) 1:3. C) 1:4. D) 1:5.*

.

From the comparison of these spectra with the references (i.e. Cu, Cu_2O and CuO), it was possible to quantitatively extrapolate the fraction of the different Cu-based phases under the application of the constant voltage over the time (Figure 4.16). The analysis of the XANES spectra revealed a facile conversion of Cu_2O to metallic Cu while the electrochemical CA is performed. Some traces of CuO were detected during the first minutes of the experiments but they rapidly disappeared to form the reduced species.

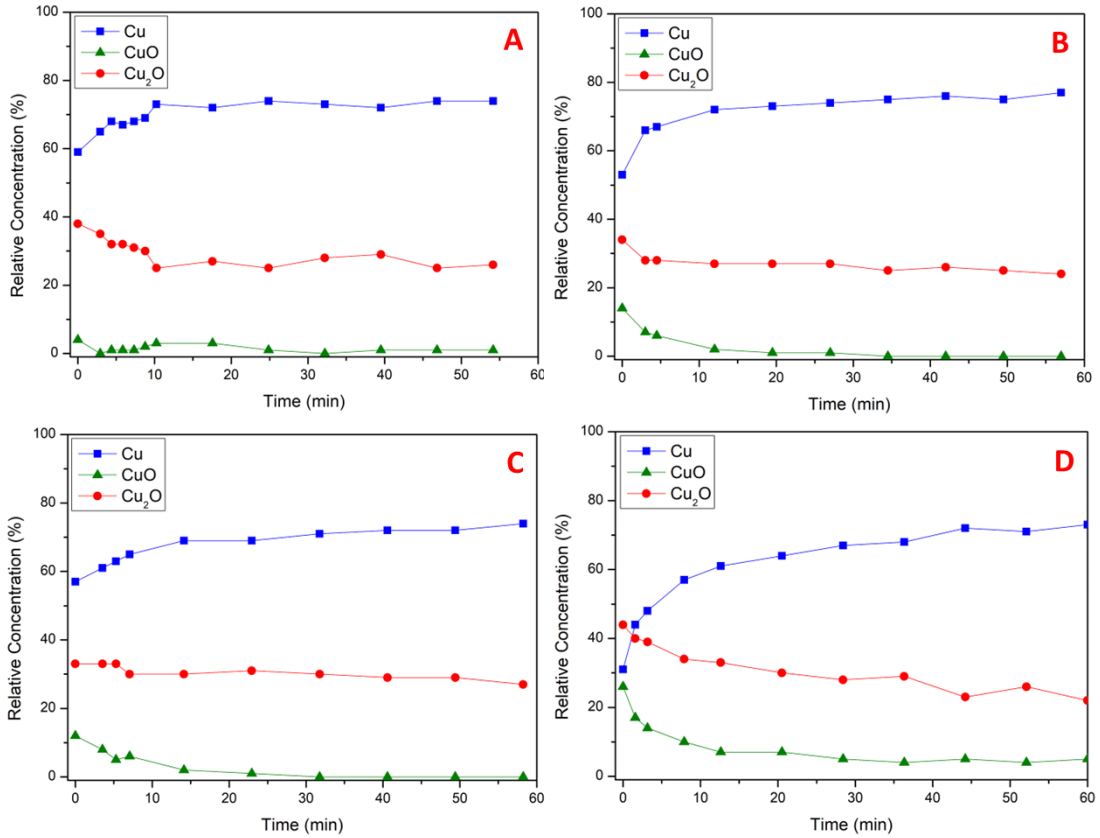

Figure 4.16: *Chemical composition of the different composites under a constant voltage of -0.7 V vs RHE over the time. A) 1:2. B) 1:3. C) 1:4. D) 1:5.*

The percentage of Cu_2O of the composites was compared with the obtained results for the pristine nanoparticles of Cu_2O in order to unveil the role of the fraction of support on the stability of the catalyst (Figure 4.17). As it is possible to observe, there is not evident effect of the different fraction support on the overall stability of the composites. To enhance these differences, the ratio between the fraction of Cu_2O and Cu over the time was calculated (Figure 4.17 B), observing a slightly improved fraction of Cu(I) over the time for the two composites with the higher fraction of C_3N_4, and a partial dependency of the stability of Cu_2O phase with the fraction of support.

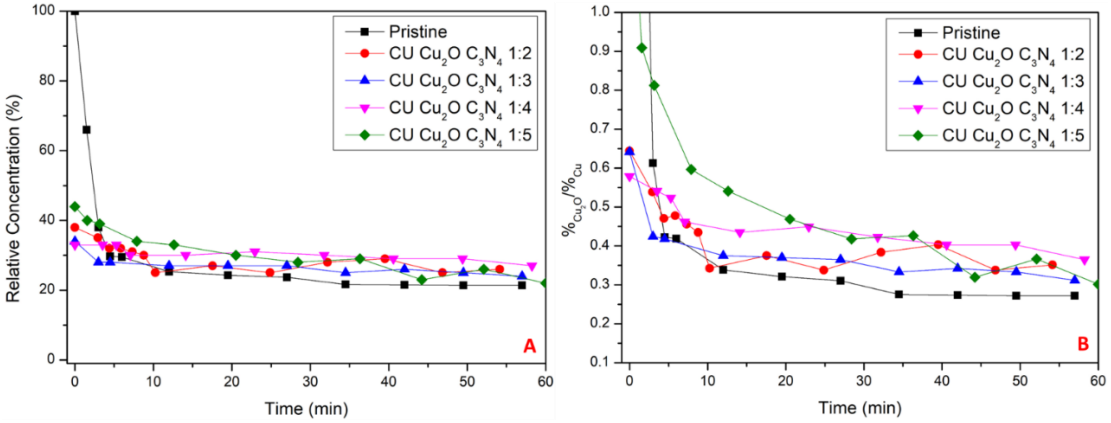

***Figure 4.17**: A) Fraction of Cu_2O under CO_2RR experiments over the time for pristine Cu_2O (black line) and the different composites with g-C_3N_4. B) Ratio between % of Cu_2O and % of Cu over the time for the different materials.*

4.3.1.4 Determination of band structure of Cu_2O/g-C_3N_4

To further explore the properties of the composite, the band structure is determined through Valence band XPS (VB-XPS) and Mott-Schottky (MS) analysis. The coupling of these two analyses allows to investigate the relative position of the two materials and extract interesting information such as the flat band potential (V_{fb}). In particular, Mott Schottky plot determination is one of the most used methods to evaluate the V_{fb} of a catalyst, even if could be complex to work out mainly in the case of composite textures [42]. This analysis is very important to study the phenomena that occur on the semiconductor-electrolyte interface and several publications reported the use of MS analysis to determine the photoelectronical properties of materials [43,44]. The semiconductor capacitance of a material is described by the MS equation (Equation 4.1):

$$\frac{1}{C_{sc}^2} = \frac{2}{\epsilon_0 \epsilon_r e n}\left(V(RE) - V_{FB}(RE) - \frac{k_b T}{e}\right) \qquad (4.1)$$

where ϵ_0 is the free space permittivity, ϵ_r the dielectric constant of the semiconductor, e the elemental charge, n the concentration of donors, $V(RE)$ the electrode potential applied relative to a reference electrode, RE, and $V_{FB}(RE)$ the flat band potential. The different values of capacitance were obtained from EIS measurement at operative voltages, simulating the obtained trend with an equivalent circuit and extracting the desired value (Figure 4.18).

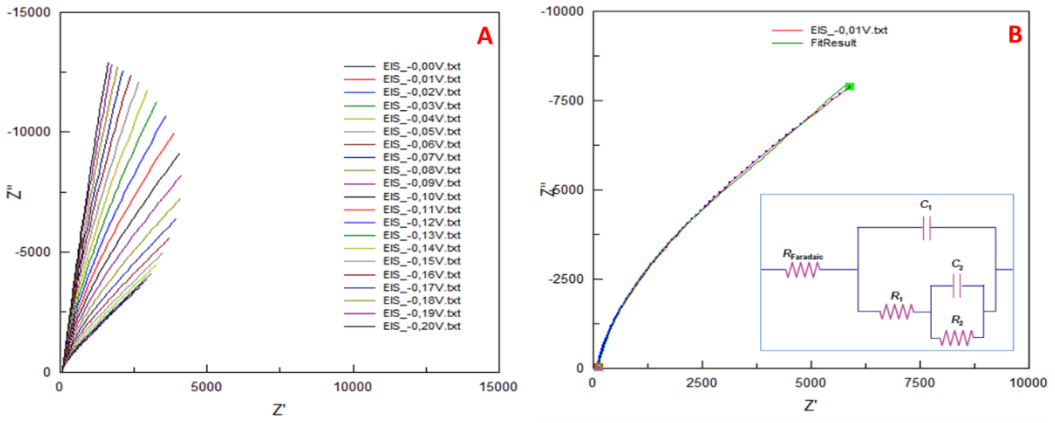

***Figure 4.18**: EIS at different voltages (A) and simulation with the elemental circuit (B) for Cu_2O.*

The reflectance analysis allowed to evaluate the band gap of the synthetized g-C_3N_4, finding a band gap of 2.70 eV (Figure 4.19), in good agreement with literature [45].

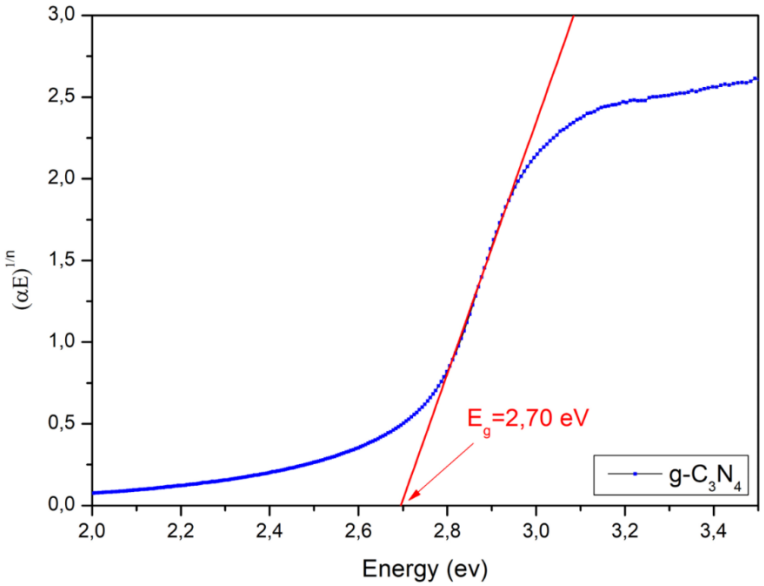

***Figure 4.19**: Tauc Plot for pristine g-C_3N_4.*

MS plot was obtained starting from the equation 4.1, plotting the term $\frac{1}{C_{sc}^2}$ as a function of the voltage of the measure (Figures 4.20 A and B). The obtained plots show similar trend with already published articles, confirming the intrinsic p-type conductivity of Cu_2O and n-type conductivity of g-C_3N_4 [31,46]. In particular, from the intercept of these spectra, it

was possible to have an indication of the V_{FB} of the material, useful to understand the band alignment of the two different structures. The calculated V_{FB} were ≈+0.02 V vs Ag/AgCl sat. (0.54 V vs NHE) for Cu_2O and -0.80 V vs Ag/AgCl sat. (-0.27 V vs NHE) for g-C_3N_4, in agreement with the state of the art [47–49]. The flat band voltage reflect the relative differences between the Fermi level of the catalyst and the potential of the water-reduction semi-reaction of the catalysts [50]. At the same time, VB-XPS spectra (Figure 4.20 C and D) allowed to determine the distance of the VB maximum (VBM) from the E_f, finding respectively, 0.183 eV for Cu_2O and 1.403 eV for g-C_3N_4 [51].

The combination of MS analysis, VB-XPS with E_g calculation determined the approximate band position of different materials of the composites, in which the CB minimum was calculated using the relationship $E_{CB} = E_{VB} - E_g$ (Table 4.2 and Figure 4.20).

	Cu_2O	C_3N_4
MS (V)	0,54	-0,27
VB XPS (eV)	0,183	1,403
E_g (eV)	1,99	2,7

***Table 4.2**: Parameters for the band diagram determination of the composite CU Cu_2O/g-C_3N_4.*

The obtained band structure describes a heterostructure where the charges pass through the material forming the composite and evidencing an efficient flow of the carriers, especially from the point of view of photocatalytic behavior. From this point of view, future applications of this composite can be find in several photo- and photoelectro-catalytic processes, as already reported in literature [52,53].

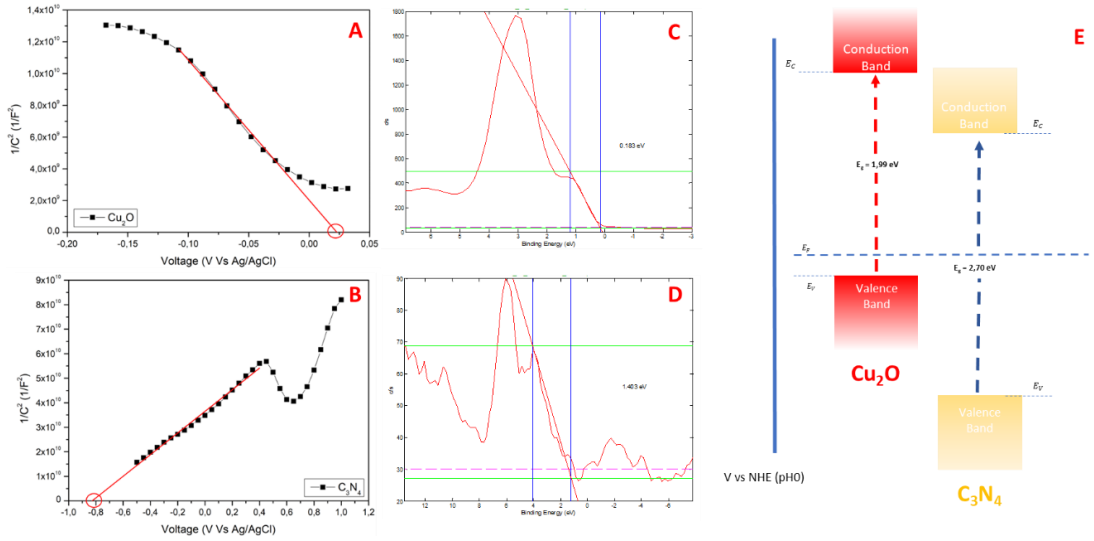

***Figure 4.20**: Mott-Schottky plot and VB XPS spectra of Cu_2O (A and C) and g-C_3N_4 (B and D). E) Band diagram determination for the composite CU Cu_2O/g-C_3N_4.*

4.3.2 Composite between CU Cu_2O and RGO

4.3.2.1 Synthesis and characterization of CU Cu_2O/RGO composite

CU Cu_2O/RGO composite was prepared by growing well-defined Cu_2O nanoparticles directly on sheets of Reduced Graphene Oxide (Figure 4.21). RGO was firstly obtained via a two-step process where graphite was exfoliated and oxidized to form nanosheets of Graphite Oxide and later, the GO was partially reduced by addition of Hydrazine on the solution forming RGO nanosheets. Cu_2O nanoparticles were directly grown on the support by performing the synthetical route showed in paragraph 3.2 with a proper amount of RGO in the solution. In particular, a weight ratio of CU Cu_2O/RGO 2:1 was chosen to optimize the affinity between the two materials.

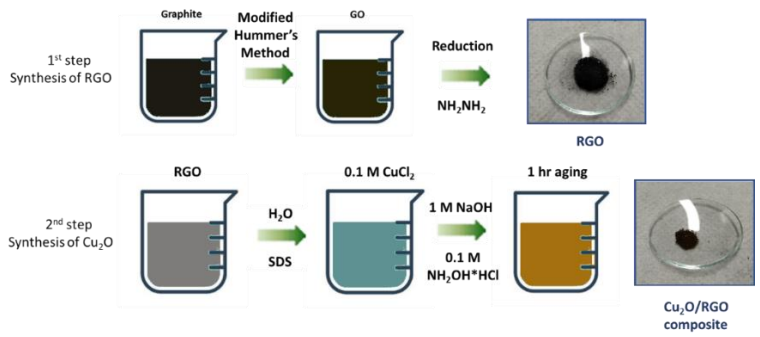

***Figure 4.21**: Synthetic route to obtain pristine RGO and CU Cu_2O/RGO composites.*

The crystalline structure of the as-prepared catalyst was revealed by XRD. The synthesis allowed the formation of crystalline Cu_2O nanoparticles, as it is possible to understand from Figure 4.22, where all the typical feature of Cu_2O XRD diffractograms are revealed. Rietveld analysis allowed to obtain quantitative information regarding the chemical phase of Cu_2O, in particular revealing a lattice parameter of 4.27 Å, in good agreement with previously reported values [37]. On the other hand, no more reflections related to RGO were detected, suggesting that the introduction of RGO has a negligible effects on the crystalline structure of the entire composite [54]. At the same time, Raman spectra (Figure 4.22 B) confirmed the contemporaneous presence of Cu_2O and RGO by detecting the characteristic vibrations of both the phases. D-band and G-band are observed and they can be used to discriminate RGO from GO; indeed, the higher intensity of D-band peak is due to a removal of oxygen moieties from GO after reduction and suggested the presence of RGO instead of GO [55,56].

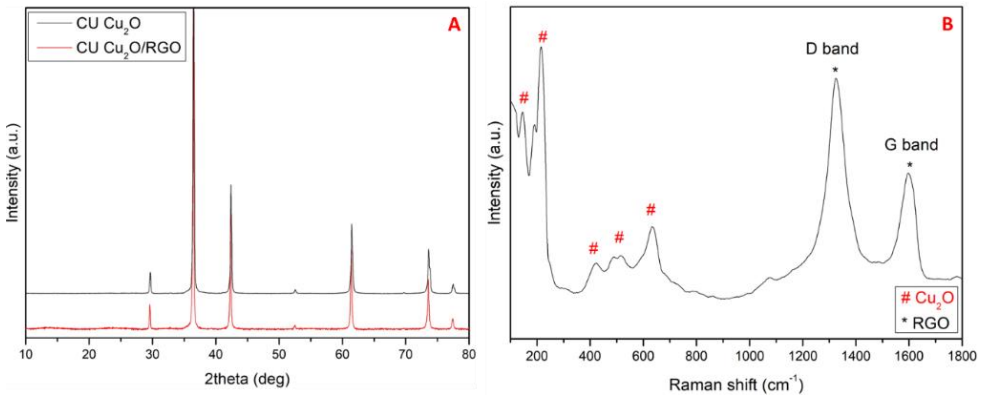

***Figure 4.22**: XRD pattern (A) and Raman spectrum (B) of CU Cu_2O/RGO collected with a 533 nm laser.*

The morphology of the synthetized composite was unveiled by SEM and TEM imaging and the results are presented in Figure 4.23. In particular, SEM images revealed that the synthetized Cu_2O nanoparticles were directly grown on sheets of RGO, thanks to the stabilizing features of the support. On the other hand, TEM images confirmed the intimate contact between the two materials of the composite, with the nanoparticles that are fully bounded by the 3D structure of RGO. Beside the good affinity between nanoparticles and support, the dimensions of Cu_2O nanoparticles are slightly decreased than the

unsupported materials, with an average size of 150 nm (σ=20 nm), smaller than 200 nm obtained for unsupported Cu_2O.

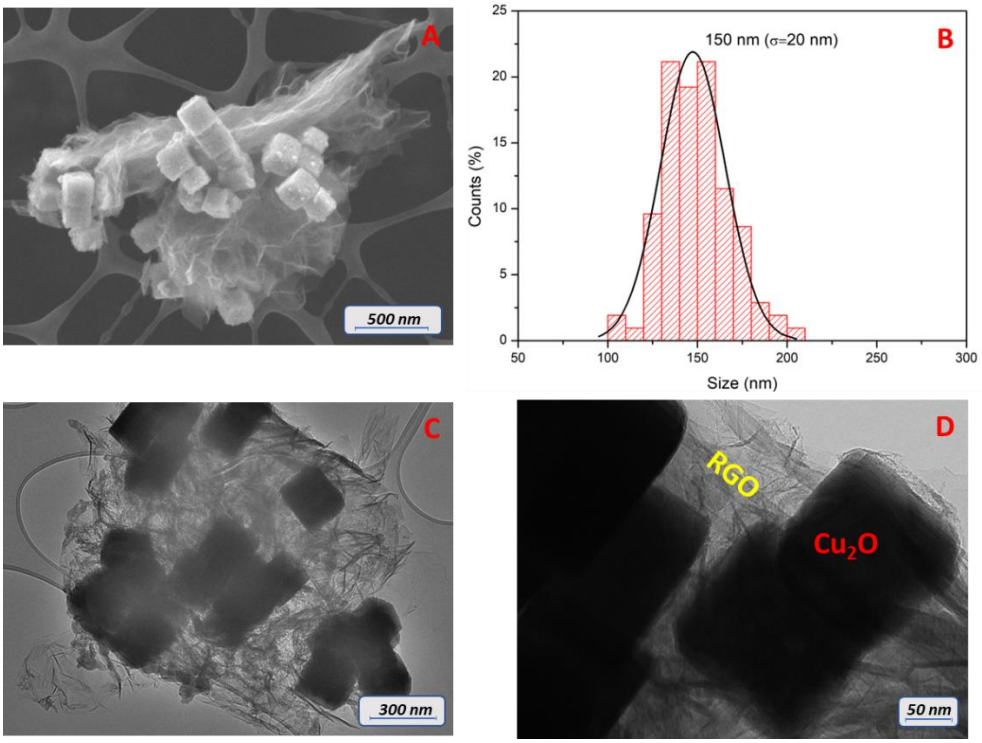

***Figure 4.23**: SEM (A), size distribution (B) and TEM (C and D) for the composite CU Cu_2O/RGO.*

4.3.2.2 Electrochemical characterization of CU Cu_2O/RGO composite and CO_2RR tests

The electrocatalytic behavior of the composite CU Cu_2O/RGO was characterized using the typical three electrode setup and the RDE as working electrode. The CVs and CAs of the pristine materials and the composite under both Ar and CO_2 atmosphere are showed in Figures 4.24 and 4.25. A rational behavior between the different materials is not trivial to obtain, due to the difficult on the distribution of the inks on the WE, but it is possible to observe that generally the current of the composite over the time was more negative than the two pristine materials, indicating a higher activity of the system CU Cu_2O/RGO. Moreover, the obtained current between Ar and CO_2 were different, suggesting a diverse reactivity and catalytic pathway when the atmosphere was changed.

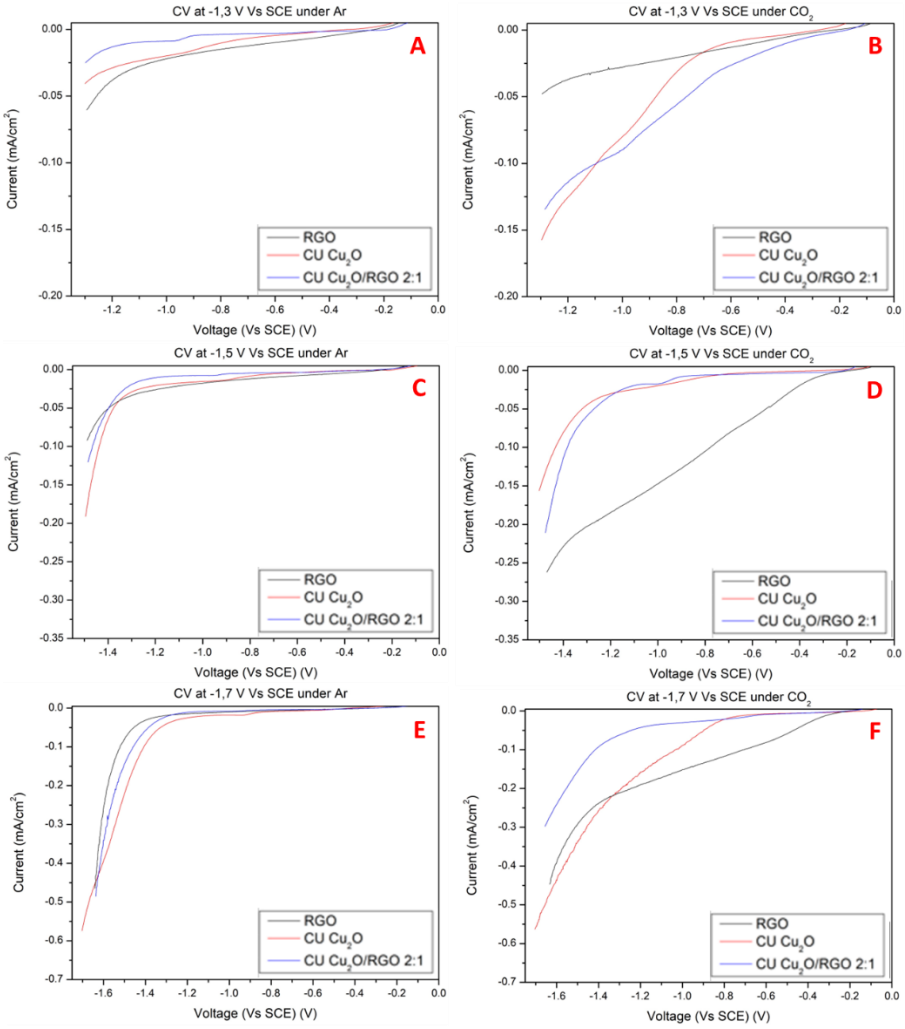

***Figure 4.24**: LSVs at -1.3 V (A and B), -1.5 V (C and D) and -1.7 V (E and F) for the composite CU Cu_2O/RGO. All the voltages are vs SCE and corrected with iR compensation.*

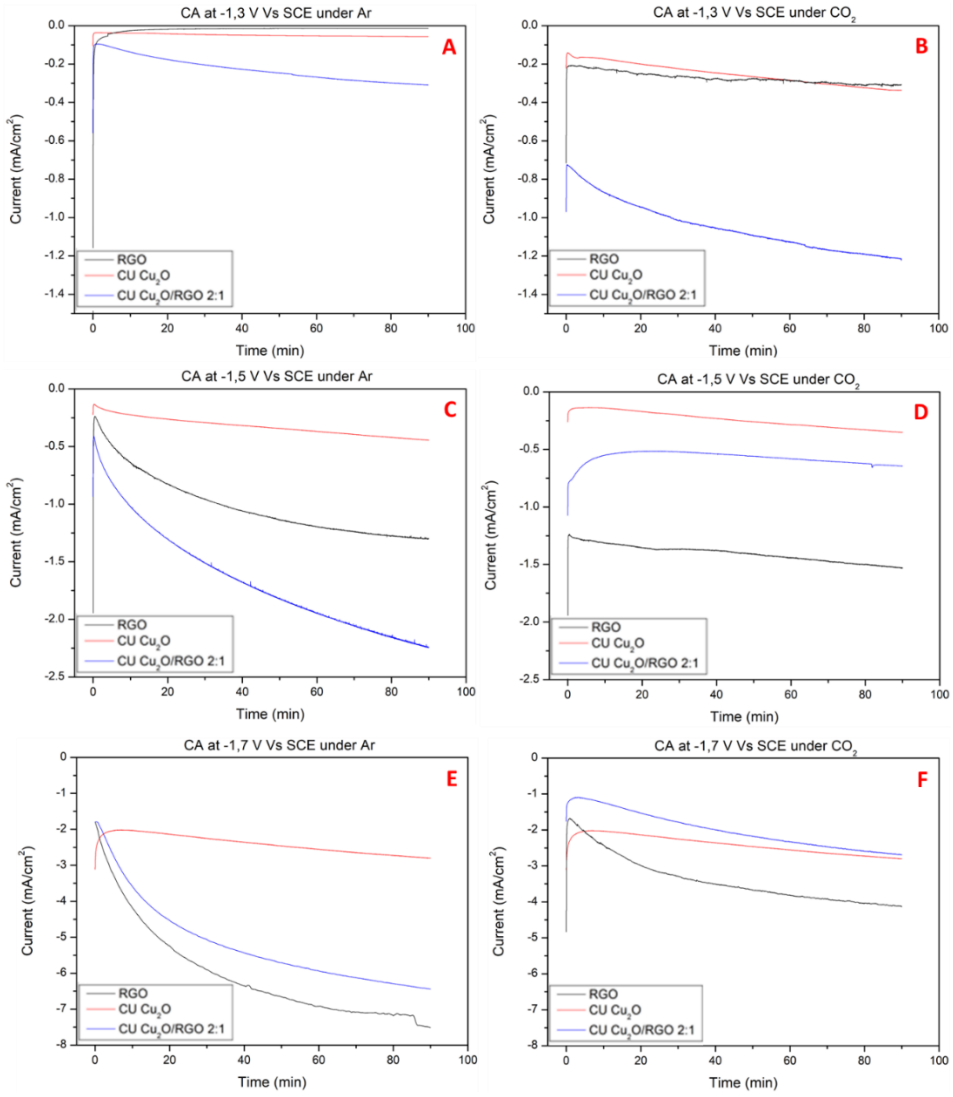

***Figure 4.25**: CAs at -1.3 V (A and B), -1.5 V (C and D) and -1.7 V (E and F) for the composite CU Cu_2O/RGO. All the voltages are vs SCE and corrected with iR compensation.*

Important information regarding the activity of the sample were obtained by electrochemical CO_2RR experiments and the analysis of the obtained products. In particular, In Figures 4.26, 4.27 and 4.28, the results of CO_2RR test at the different voltages were presented. The electrochemical characterization confirmed again the higher current of the composite respect of the pristine materials, in particular at lower voltages.

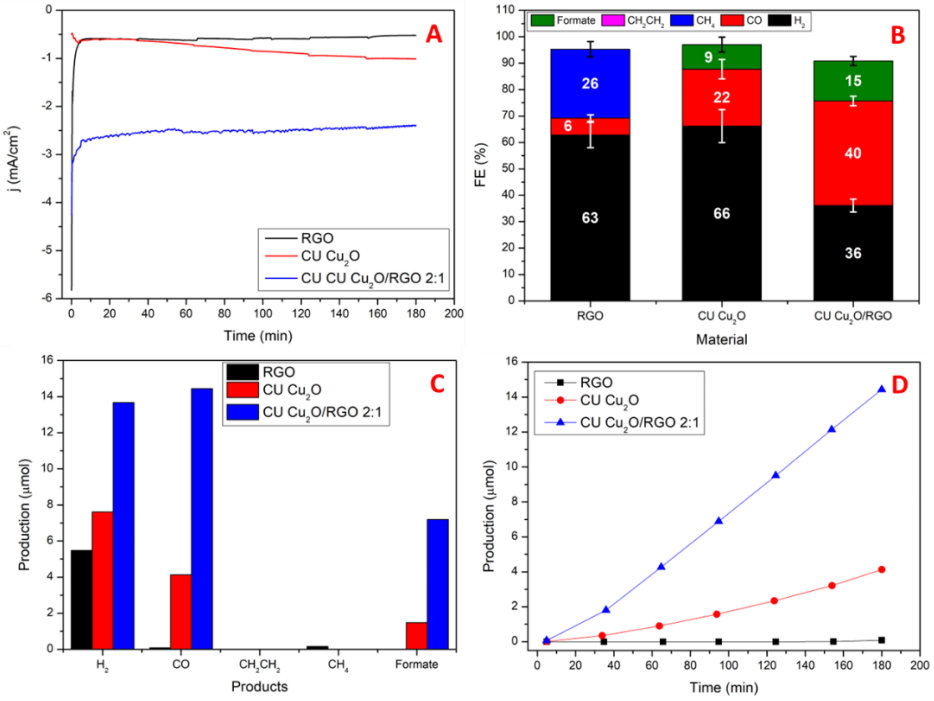

***Figure 4.26**: eCO₂RR tests for composite CU Cu₂O/RGO at the voltage of -0.7 V vs RHE. A) 3-hrs CA under CO₂ atmosphere. B) FEs toward gaseous and liquid products. C) Mol of different products after 3-hrs CA and D) Production of CO during the experiment for the different materials.*

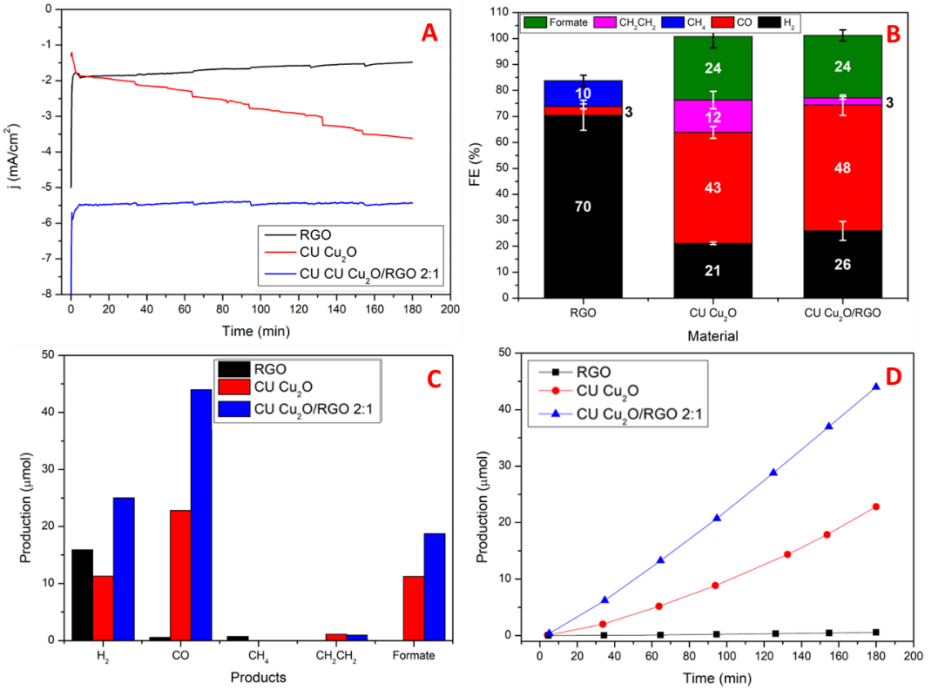

***Figure 4.27**: eCO₂RR tests for composite CU Cu₂O/RGO at the voltage of -0.9 V vs RHE. A) 3-hrs CA under CO₂ atmosphere. B) FEs toward gaseous and liquid products. C) Mol of different products after 3-hrs CA and D) Production of CO during the experiment for the different materials.*

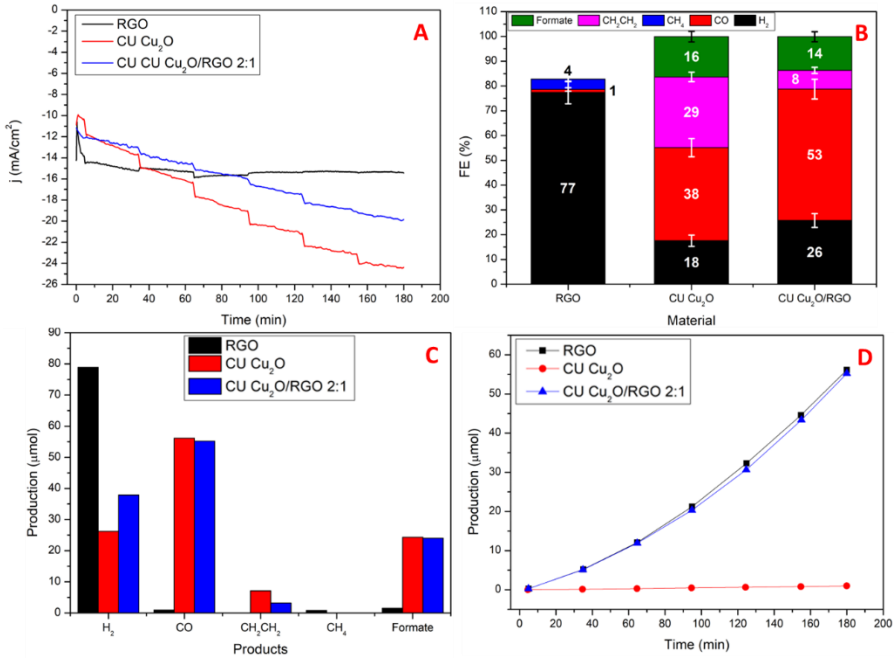

***Figure 4.28**: eCO₂RR tests for composite CU Cu₂O/RGO at the voltage of -1.1 V vs RHE. A) 3-hrs CA under CO₂ atmosphere. B) FEs toward gaseous and liquid products. C) Mol of different products after 3-hrs CA and D) Production of CO during the experiment for the different materials.*

The observed higher current is correlated to the highest conductivity of CU Cu₂O/RGO system, and it had implications on the selectivity and productivity of the different electrocatalytic products. Indeed, beside the quasi-total reactivity of bare RGO toward HER process, the composite showed higher selectivity toward the formation of CO, with a FE_{CO} of 48% instead of 43% of unsupported Cu₂O at the voltage of -0.9 V vs RHE. The obtained selectivity, coupled with the increased current of the composite, provided a higher amount of CO during the experiments, almost double than the experiment with unsupported Cu₂O, indicating a favored pathway toward the formation of CO for the composite CU Cu₂O/RGO, especially at lower voltages. This improved behavior toward CO formation is more evident at the voltage of -0.7 V vs RHE, where the FE_{CO} of the composite is almost the double of the FE_{CO} of unsupported CU Cu₂O (Figure 4.26 B). The formation of CO can act as the first important step to convert CO_2 in high value-added molecules and the use of the composite CU Cu₂O/RGO is an interesting way to drive the overall reactivity of Cu₂O toward this process.

4.3.3 Composite between Cu_2O and MoS_2

4.3.3.1 Synthesis and characterization of Cu_2O/MoS_2 composites

The synthesis of the composite Cu_2O/MoS_2 occurred in an two-steps method, where in the first the bare MoS_2 was prepared and consequently Cu_2O nanoparticles were grown on the support (Figure 4.29).

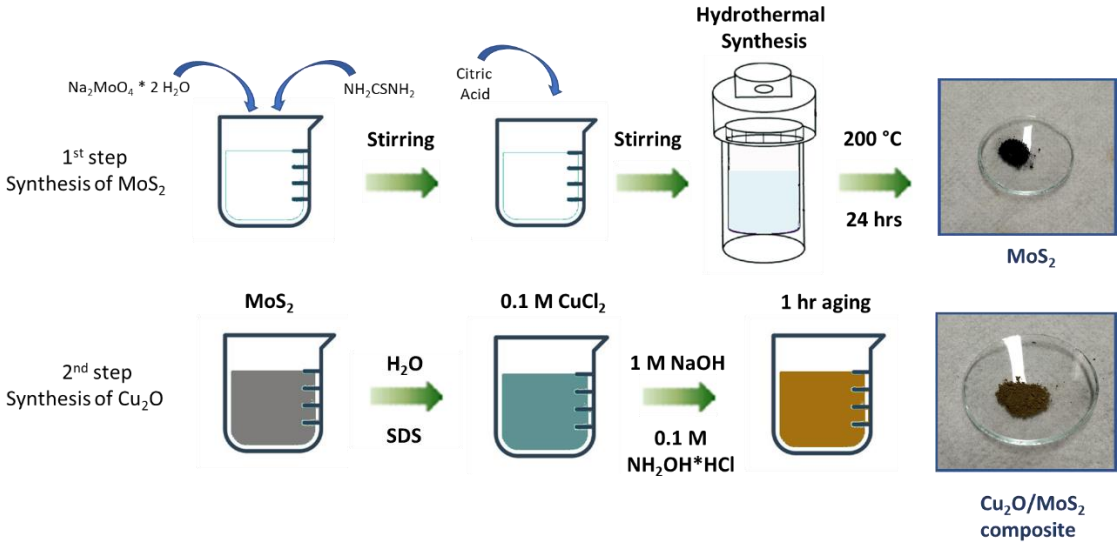

***Figure 4.29**: Synthetic route to obtain pristine nanoflowers of MoS_2 and Cu_2O/MoS_2 composites.*

In particular, in the first step, 3D nanoflowers of MoS_2 were synthetized through a facile approach, by mixing $Na_2MoO_4*2H_2O$ and Thiourea with citric acid as reducing agent and a subsequent heating under hydrothermal conditions. SEM and TEM characterization revealed the formations of a 3D structure based on nanoflowers of pure MoS_2 with an average size of 550 nm (σ=40 nm) (Figure 4.30). Consequently, well-defined Cu_2O nanoparticles were synthetized via the experimental route presented in chapter 3.2 and directly grown on the surface of MoS_2 nanosheets. In order to limit the problem of low affinity between the two materials of the composite and increase the overall dispersion of Cu_2O, the chosen weight ratio of this composite is Cu_2O/MoS_2 2:1 as reported for the composite with RGO.

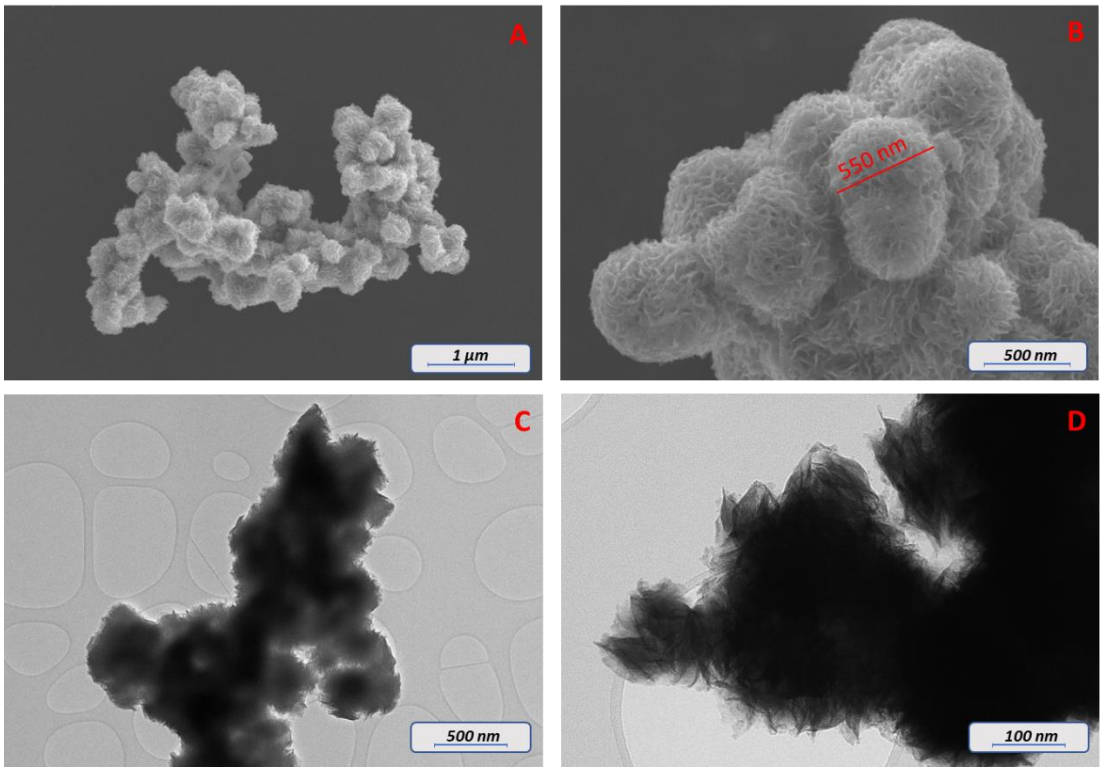

***Figure 4.30**: SEM (A and B) and TEM images (C and D) of pristine nanoflowers of MoS_2.*

XRD was used as technique to investigate the crystallinity and the different chemical phases of the material (Figure 4.31). In particular, the collected diffractogram of the composite is in agree with the typical features of pristine Cu_2O presented in the paragraph 3.3.1, confirming the high degree of crystallinity for the obtain nanoparticles and showing the same lattice parameter of pristine material. On the other hand, no characteristic diffraction peaks related to MoS_2 were observed, indicating a poor crystallinity of the synthetized support and higher intensity of the Cu_2O characteristic reflections, in good agreement with other published works [31,32].

SEM and TEM images revealed the growth of Cu_2O nanoparticles on the nanoflowers of MoS_2, suggesting an intimate interconnection between the two materials of the composite and an immobilization of the nanoparticles on the MoS_2 matrix (Figure 4.32 A, C and D). The coupling between Cu_2O and the rough surface of MoS_2 nanosheets had implication on the average size of the synthetized nanoparticles (Figure 4.32 B), with a decrease of the dimensions from 200 nm (σ=20 nm) of unsupported material to 90 nm (σ=10 nm) for

the composite. EDS elemental analysis confirms the contemporaneous presence of Cu, O, Mo and S with no other impurities (Figure 4.32 E).

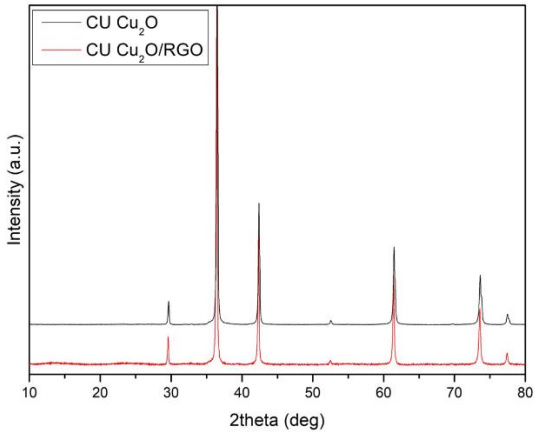

***Figure 4.31**: XRD pattern of CU Cu_2O (black) and CU Cu_2O/MoS_2 composite (red).*

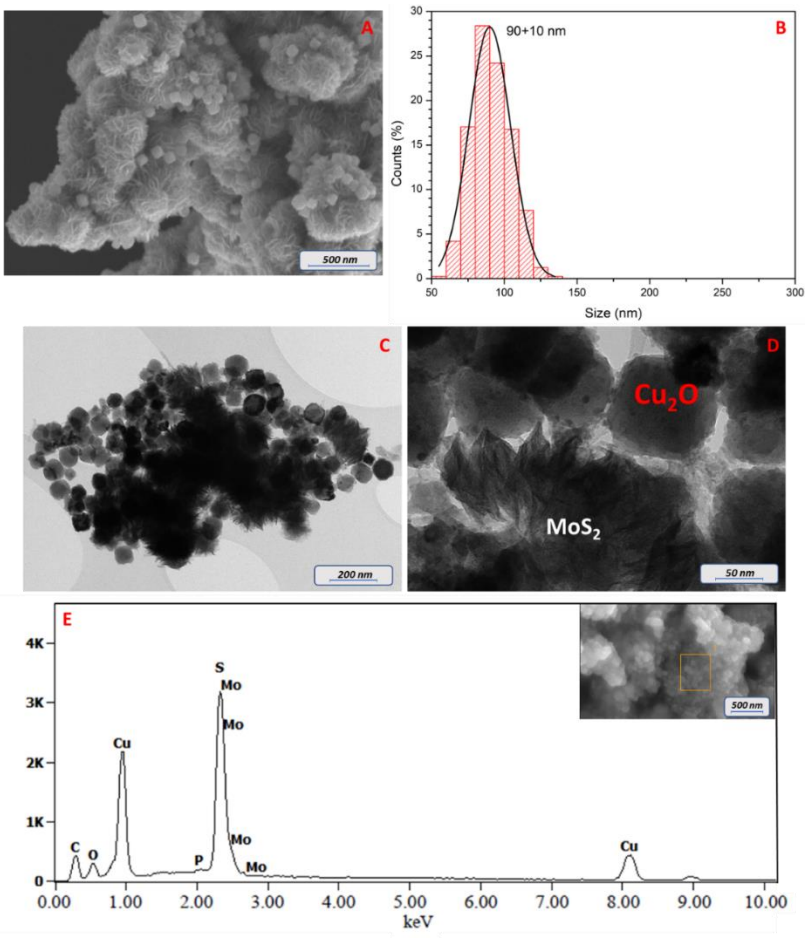

***Figure 4.32**: SEM (A), size distribution (B), TEM (C and D) and EDS spectrum (C) for the composite CU Cu_2O/MoS_2.*

4.3.3.2 Electrochemical characterization of Cu_2O/MoS_2 composites and analysis of FEs

The electrocatalytic characterization of the two synthetized composites (with CU and RD Cu_2O) was performed using the typical RDE setup already presented in the paragraph 3.3.3. The CVs and CAs (both in Ar and CO_2) of the two materials are shown in Figures 4.33 and 4.34.

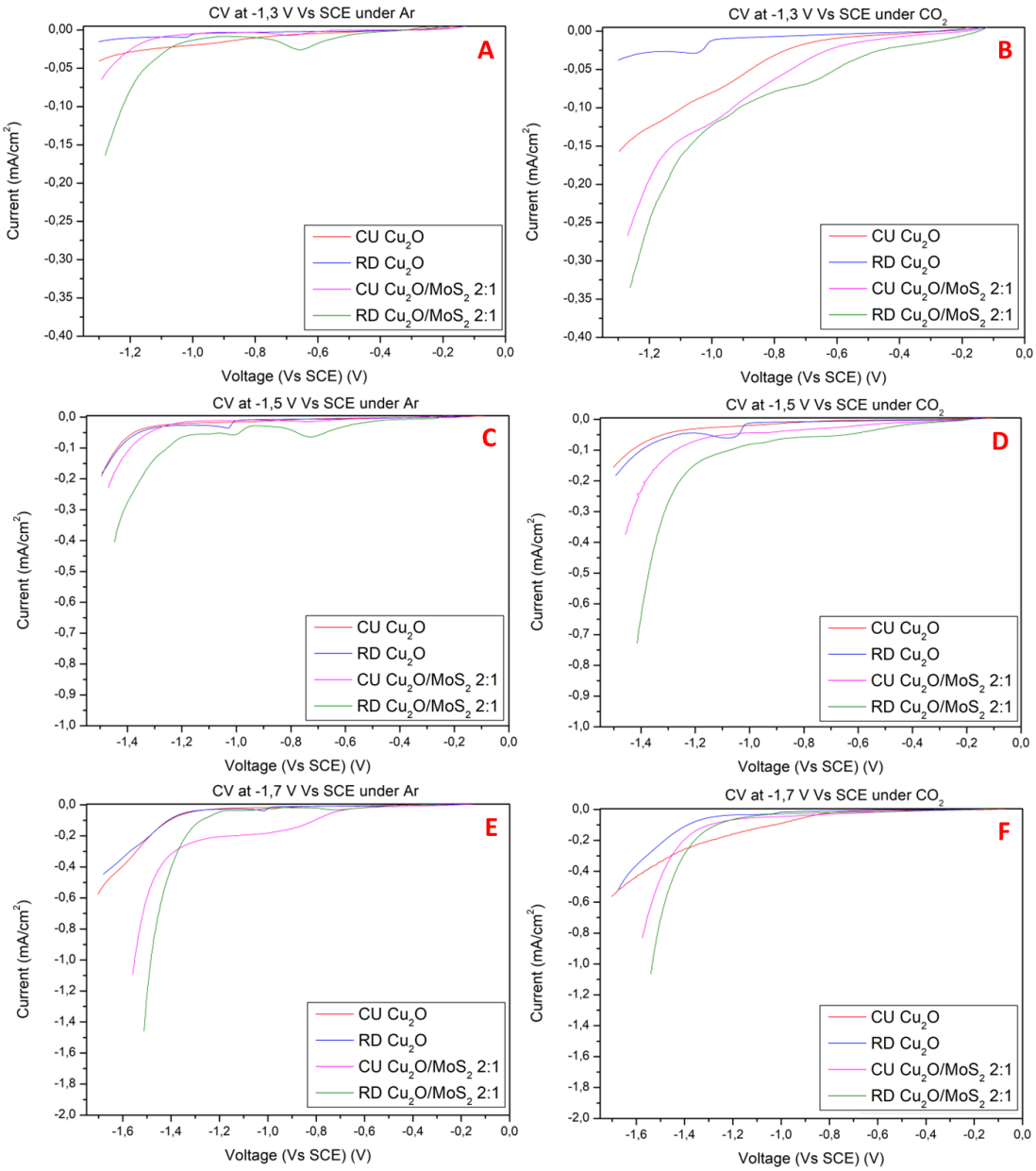

***Figure 4.33**: LSVs at -1.3 V (A and B), -1.5 V (C and D) and -1.7 V (E and F) for the different composites Cu_2O/MoS_2. All the voltages are vs SCE and corrected with iR compensation.*

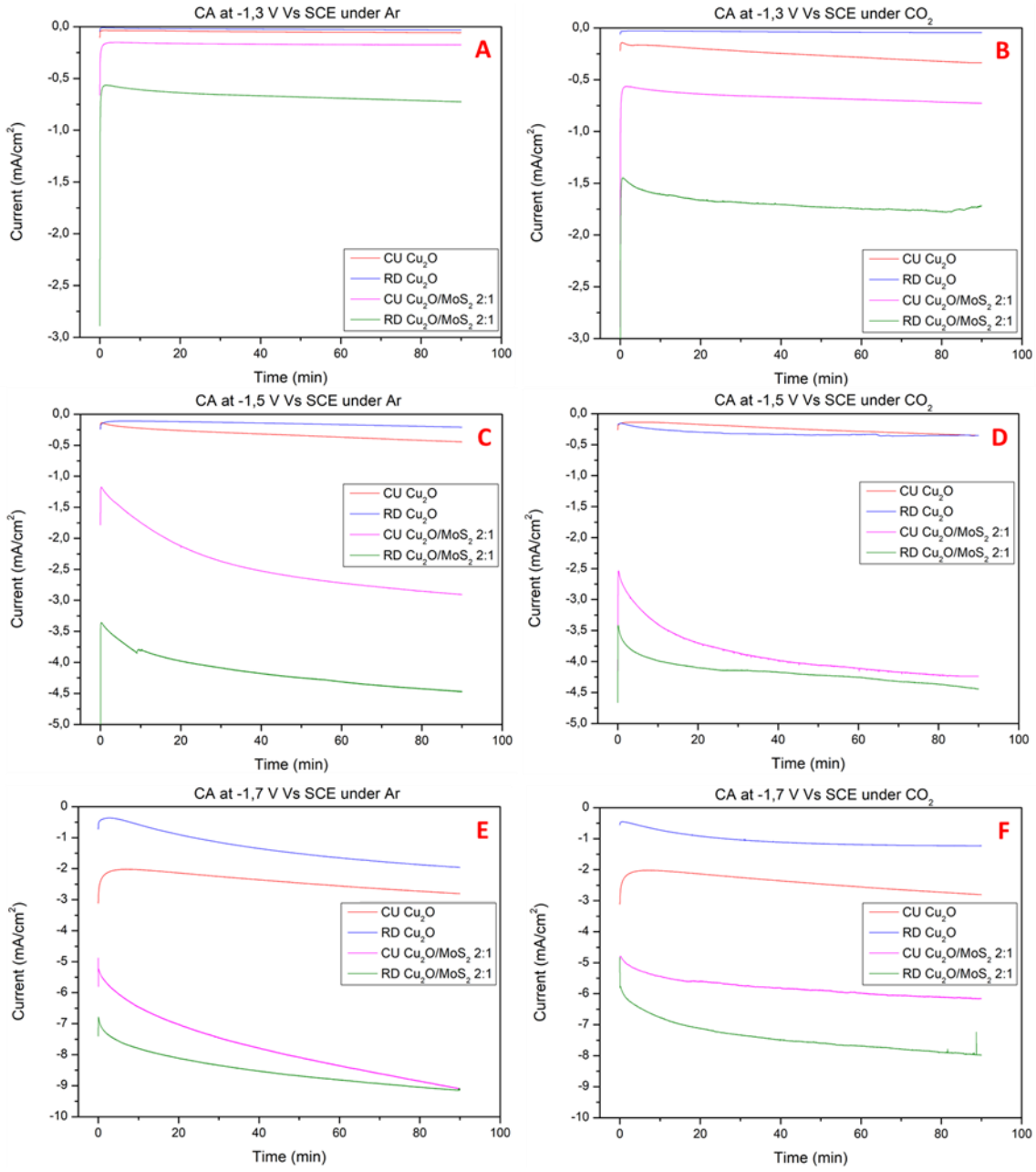

***Figure 4.34**: CAs at -1.3 V (A and B), -1.5 V (C and D) and -1.7 V (E and F) for the different composites Cu_2O/MoS_2. All the voltages are vs SCE and corrected with iR compensation.*

The measured current of the composites was higher than the current of unsupported nanoparticles, in particular at higher voltages, and this increased current was unrelated to the particular environment of the experiment (Ar or CO_2 atmosphere) suggesting the presence of an electrochemical process mostly independent than CO_2. The obtained high currents of the composites had implications even on the measured voltage of the

experiments: indeed, in these cases, the real applied voltage was more reductive due to the iR drop correction. On the other hand, it is noteworthy to note that chronoamperometry tests confirmed the improved catalytic activity of the composites and a good stability up to 90 minutes of the measurement. The increase current of composite materials is attributed to the synergistic effects brought by the intimate interactions and contact between MoS_2 nanosheets and Cu_2O nanoparticles. To understand which processes are involved during the electrocatalytic characterization, CO_2RR tests were performed. The analysis of chronoamperometries, *FEs* and the amount of products at the voltage of -0.7 V and -0.9 V vs RHE is presented in Figures 4.35 and 4.36.

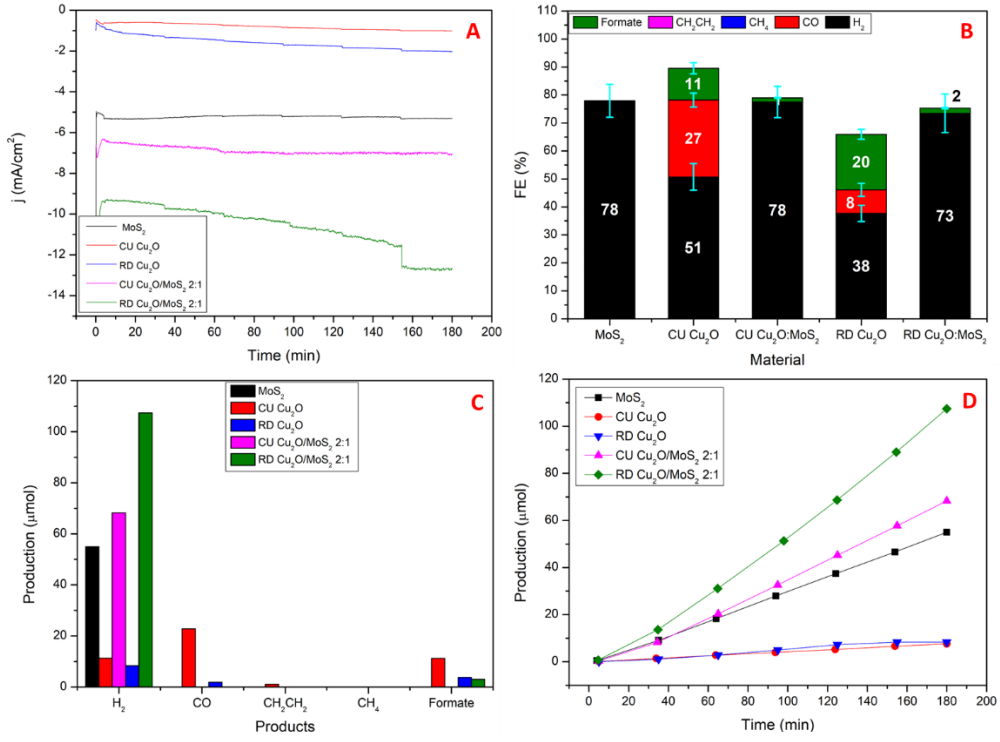

***Figure 4.35**: eCO₂RR tests for composites Cu₂O/MoS₂ at the voltage of -0.7 V vs RHE. A) 3-hrs CA under CO₂ atmosphere. B) FEs toward gaseous and liquid products. C) Mol of different products after 3-hrs CA and D) Production of H₂ during the experiment for the different materials.*

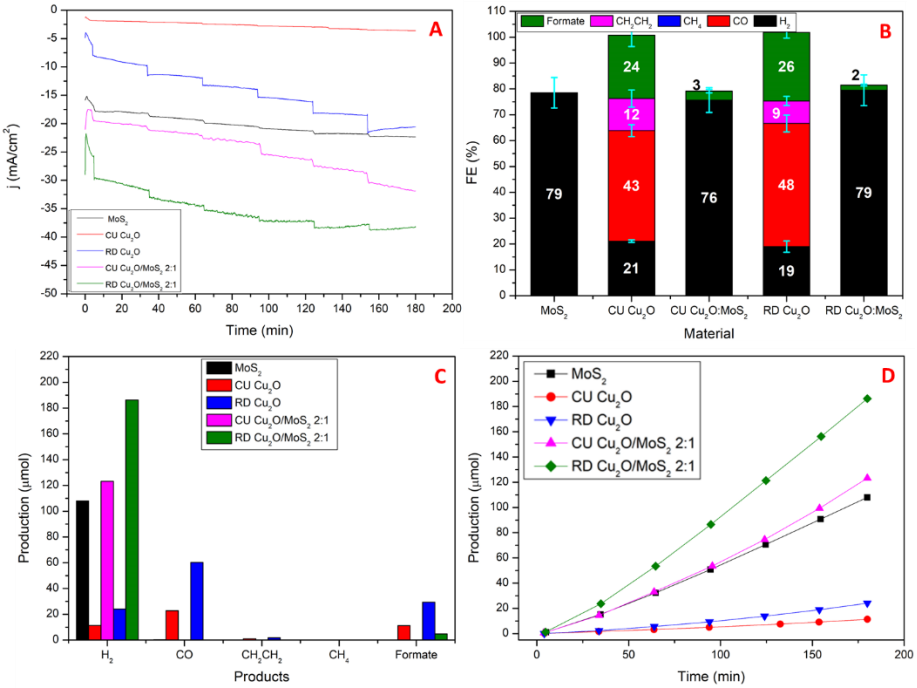

***Figure 4.36**: eCO₂RR tests for composites Cu₂O/MoS₂ at the voltage of -0.9 V vs RHE. A) 3-hrs CA under CO₂ atmosphere. B) FEs toward gaseous and liquid products. C) Mol of different products after 3-hrs CA and D) Production of H₂ during the experiment for the different materials.*

The comparisons between the currents in Figure 4.35 A or 4.36 A, were a useful indication of the conductivity of the materials forming the composite. Indeed, pristine MoS_2 showed higher current than pristine Cu_2O nanoparticles, confirming the overall electrochemical behavior presented in literature [57]. At the same time, the intimate interactions between Cu_2O nanoparticles and MoS_2 nanosheets were suggested by a great increase of the currents for the two composites, in particular with the RD Cu_2O:MoS_2 that showed highest currents (-37.5 mA/cm^2 compared to a maximum of -20 mA/cm^2 collected for RD Cu_2O sample). The analysis of the *FEs* of liquid and gaseous products under CO_2 atmosphere allowed to unveil the different reactivity of the composite. Indeed, pristine MoS_2, CU Cu_2O/MoS_2 and RD Cu_2O/MoS_2 showed higher activity toward the HER process, with an overall *FE* of 76-79% and no other products of CO_2RR detected, except for small traces of HCOOH. The same experiments in Ar atmosphere revealed similar *FEs* toward HER processes but it is interesting to note that all the CO_2RR activity of unsupported Cu_2O nanoparticles is turned into H_2 formation due to the intimate coupling with MoS_2 nanosheets. The high selectivity of composites toward the formation of H_2 is

related to the presence of MoS_2 and the intrinsic HER activity of this material, but it is not the only reason. Indeed, by the analysis of the amount of products after the 3 hours of CA, in particular of H_2 (Figures 4.35 and 4.36, both C and D), it was possible to note that the HER activity of the composites is clearly higher than the unsupported materials (for instance, the H_2 production was 180 μmol for RD CU_2O/MoS_2 vs 100 μmol of pure MoS_2 and 20 μmol of pristine RD Cu_2O), suggesting that the interactions between the Cu_2O nanoparticles and the 3D structure of the Mos_2 nanosheets played a pivotal role to drive the selectivity toward the formation of H_2. The high production rate of these materials open new scenarios regarding possible applications of Cu_2O/MoS_2 composites as electrocatalysts for the in-situ hydrogenations of organic molecules [58].

4.3.3.3 Effects of CO_2RR on the materials

Operando XAS highlighted the effects of CO_2RR process on the stability of the Cu phase on the composite CU Cu_2O/MoS_2 2:1. In Figure 4.37, the evolution of XANES spectra over the time under a voltage of -0.7 V vs RHE is presented.

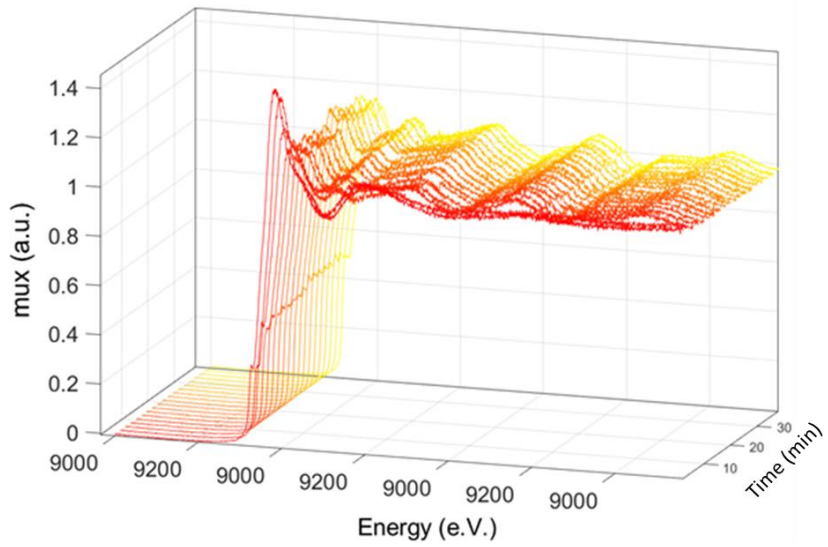

***Figure 4.37**: XAS spectra spectra of CU Cu_2O/MoS_2 at the voltage of -0.7 V vs RHE.*

More quantitative indications were obtained from XANES spectra and the extrapolation of different phases, tracking the evolution of the chemical phase of the catalysts over the time (Figure 4.38 A). Compared to the unsupported materials, lower fractions of Cu_2O and metallic Cu were founded, suggesting the presence of other phases. In particular, the

fraction of Cu_2S that was extrapolated (more than 20%) can be due to a partial reconstruction of the material over the time when the voltage is applied (Figure 4.38 B).

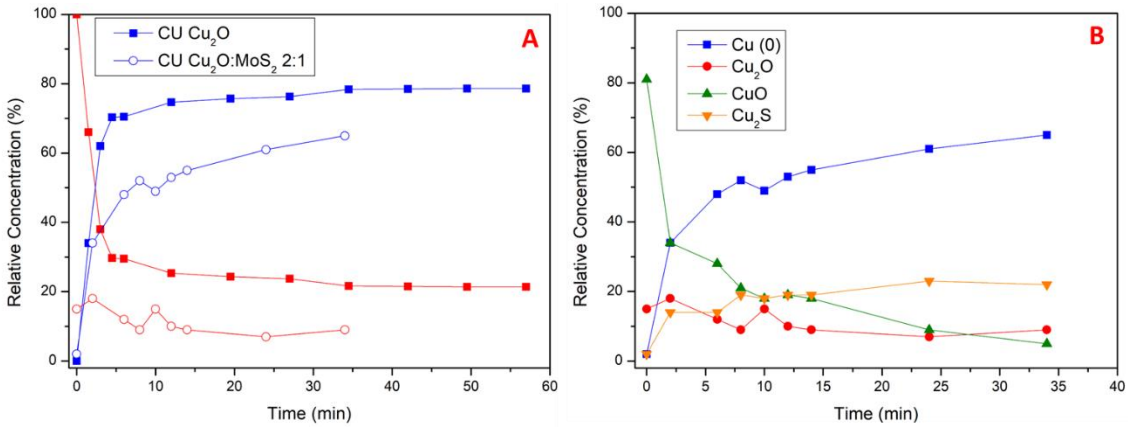

***Figure 4.38**: Chemical phases of CU Cu_2O/MoS_2 2:1 under a constant voltage of -0.7 V vs RHE over the time. A) Compared to pristine Cu_2O. B) Different obtained phases.*

4.4 Conclusions

In the as-presented chapter, the common issues of using Cu_2O nanoparticles as electrocatalysts have been faced. The formation of heterostructures by coupling Cu_2O nanoparticles with supports is one of the most reported ways to improve stability and efficiency, thanks to the good effects on the dispersion of Cu_2O nanoparticles. In particular, several efforts have been dedicated to couple CU Cu_2O with three common supports, such as g-C_3N_4, RGO and MoS_2, forming composites with the main aim to unveil the effects of the improved dispersion on the activity of Cu_2O nanoparticles.

The electrocatalytic performances for similar materials are reported in table 4.3. The comparison of the presented examples with literature is not straightforward due to the different experimental conditions and mainly, studied electrochemical processes.

Catalyst	Electrolyte	Voltage	Main Products	Ref.
Cu_2O (CU)	$KHCO_3$ 0.1 M	-1.1 V Vs RHE	CO (38 %) **CH_2CH_2 (29 %)** HCOOH (16 %)	This work
CU Cu_2O/g-C_3N_4 1:3	$KHCO_3$ 0.1 M	-1.1 V Vs RHE	CO (13 %) CH_2CH_2 (24 %) **HCOOH (25 %)**	This work
CU Cu_2O/RGO 2:1	$KHCO_3$ 0.1 M	-1.1 V Vs RHE	**CO (53 %)** CH_2CH_2 (8 %) HCOOH (14 %)	This work
Cu_2O/C	$KHCO_3$ 0.5 M	-1.1 V Vs RHE	CO (7 %) **CH_2CH_2 (45 %)**	[25] Chapter 3
Cu_2O (CU)	$KHCO_3$ 0.1 M	-0.9 V Vs RHE	**CH_2CH_2 (25 %)** HCOOH (6 %) CH_3CH_2OH (7 %)	[64] Chapter 3
CuO/g-C_3N_4	$NaHCO_3$ 0.1 M	-1.1 V Vs RHE	**CO (7 %)** CH_2CH_2 (2 %) CH_4 (4 %)	[24]
Cu_2O/g-C_3N_4	$KHCO_3$ 0.1 M	-1.1 V Vs RHE	CO (10 %) **CH_2CH_2 (32 %)** HCOOH (10 %)	[41]
Cu_2O/CuS	$KHCO_3$ 0.1 M	-0.9 V Vs RHE	**HCOOH (67 %)**	[59]
Cu_2O/RGO	KOH 1 M	/	Catalyst for HER and OER	[28]
Cu_2SnS_3/RGO	KOH 1 M	/	Catalyst for HER	[29]
Cu_2O/MoS_2	$KHCO_3$ 0.5 M	-1.1 V Vs RHE	**CH_3OH (10%)** CH_3CH_2OH (8 %)	[32]

***Table 4.3**: Comparison between prepared and reported Cu_2O-based catalysts.*

The formation of heterostructure with g-C_3N_4 allowed to directly affect the electrochemical behavior of Cu_2O. Despite the insulator behavior of the g-C_3N_4 and its contribution toward the HER process, composites with CU Cu_2O showed an improved productivity of HCOOH over the time. In particular, a correlation between the decrease average sizes of Cu_2O nanoparticles with the amount of HCOOH during the electrochemical process was observed, with the composite CU Cu_2O/g-C_3N_4 1:3 that showed, at the voltage of -1.1 V vs RHE, a fraction of HCOOH almost double (0.57 vs

0.28) respect the unsupported material. The reasons for the different catalytic behaviour of the composite with g-C_3N_4 compared to pristine nanoparticles, are not easy to understand, but some hypotheses can be proposed. The improved dispersion of Cu_2O nanocubes on the surface of the support allows to expose a higher number of active sites for the CO_2RR process, increasing at the same time the interphase between the two materials and reactivity towards the resulting products. Literature reports the strong capability of g-C_3N_4 to adsorb CO_2 molecules and to locally increase the CO_2 concentration thanks the presence of nitrogen sites on the structure [41]. Moreover, the partial HER activity of the support could facilitate the direct hydrogenation of the CO_2^- radical, the main intermediate in the formation of formats, even if further studies need to be done to support this hypothesis. As a result, the synergetic effect between Cu_2O nanoparticles and g-C_3N_4 support enables the enhanced formation rate of HCOOH and the different reactivity during the electrocatalytic experiments. Despite the improved catalytic behavior, the incorporation of g-C_3N_4 nanosheets had still insufficient effects on the stability of Cu_2O phase, with *operando* XAS analysis that revealed a rapid reduction of Cu_2O phase for the different materials during the first minutes of electrochemical characterization.

The formation of the composite between CU Cu_2O and RGO results in an increased selectivity and productivity toward CO. Indeed, by coupling with RGO, the FE_{CO} rise to almost the double (for instance, at -0.7 V the FE_{CO} of the composite is 40 % vs 22 % of pristine Cu_2O), with an increased amount of CO produced especially at lower voltages.

The presence of a 3D nanostructure of MoS_2 had also implications on the electrochemical behavior of the overall material. Indeed, due to the improved HER activity of pure MoS_2, its coupling with Cu_2O nanoparticles had dramatic effects on the selectivity and productivity of the composite towards H_2, with an important decrease of the selectivity towards all the products of the CO_2RR. The higher HER activity of the composite Cu_2O/MoS_2 was due to the improved dispersion of Cu_2O nanoparticles and the synergistic behavior between the two parts of the composite. This work opens a promising prospect for the utilization of Cu_2O/MoS_2 as catalyst toward the electrochemical hydrogenation of organic molecules.

In the next chapter, a facile sol gel method to form bimetallic particles based on Cu and Sn is presented, with a particular attention on the characterization of the different chemical phases and the study of the activity toward eCO_2RR.

4.5 References

[1] F.A.C. Pastrián, A.G.M. Da Silva, A.H.B. Dourado, A.P. De Lima Batista, A.G.S. De Oliveira-Filho, J. Quiroz, D.C. De Oliveira, P.H.C. Camargo, S.I. Córdoba De Torresi, *ACS Catal.* 8 (**2018**) 6265–6272.

[2] G.O. Larrazábal, A.J. Martín, F. Krumeich, R. Hauert, J. Pérez-Ramírez, *ChemSusChem* 10 (**2017**) 1255–1265.

[3] Q. Hua, D. Shang, W. Zhang, K. Chen, S. Chang, Y. Ma, Z. Jiang, J. Yang, W. Huang, *Langmuir* 27 (**2011**) 665–671.

[4] K.C. Christoforidis, P. Fornasiero, *ChemCatChem* 11 (**2019**) 368–382.

[5] W. Shi, X. Zhang, S. Li, B. Zhang, M. Wang, Y. Shen, *Appl. Surf. Sci.* 358 (**2015**) 404–411.

[6] C.Y. Toe, Z. Zheng, H. Wu, J. Scott, R. Amal, Y.H. Ng, *Angew. Chemie* 130 (**2018**) 13801–13805.

[7] S.C. Lin, C.C. Chang, S.Y. Chiu, H.T. Pai, T.Y. Liao, C.S. Hsu, W.H. Chiang, M.K. Tsai, H.M. Chen, *Nat. Commun.* 11 (**2020**) 3525.

[8] Q. Li, P. Xu, B. Zhang, H. Tsai, S. Zheng, G. Wu, H.L. Wang, *J. Phys. Chem. C* 117 (**2013**) 13872–13878.

[9] J. Wang, H. Tan, Y. Zhu, H. Chu, H.M. Chen, *Angew. Chemie* 133 (**2021**) 17394–17407.

[10] H. Mistry, A.S. Varela, C.S. Bonifacio, I. Zegkinoglou, I. Sinev, Y.W. Choi, K. Kisslinger, E.A. Stach, J.C. Yang, P. Strasser, B.R. Cuenya, *Nat. Commun.* 7 (**2016**) 12123.

[11] P. Grosse, D. Gao, F. Scholten, I. Sinev, H. Mistry, B. Roldan Cuenya, *Angew. Chemie - Int. Ed.* 57 (**2018**) 6192–6197.

[12] S. Popović, M. Smiljanić, P. Jovanovič, J. Vavra, R. Buonsanti, N. Hodnik, *Angew. Chemie - Int. Ed.* 59 (**2020**) 14736–14746.

[13] C. Hahn, T. Hatsukade, Y.G. Kim, A. Vailionis, J.H. Baricuatro, D.C. Higgins, S.A. Nitopi, M.P. Soriaga, T.F. Jaramillo, *Proc. Natl. Acad. Sci. U. S. A.* 114 (**2017**) 5918–5923.

[14] A. Verdaguer-Casadevall, C.W. Li, T.P. Johansson, S.B. Scott, J.T. McKeown, M. Kumar, I.E.L. Stephens, M.W. Kanan, I. Chorkendorff, *J. Am. Chem. Soc.* 137 (**2015**) 9808–9811.

[15] X. Feng, K. Jiang, S. Fan, M.W. Kanan, *ACS Cent. Sci.* 2 (**2016**) 169–174.

[16] Y. Zhang, X.Y. Zhang, K. Chen, W.Y. Sun, *ChemSusChem* 14 (**2021**) 1847–1852.

[17] Z.A. Shaikh, N. Moiseev, A. Mikhaylov, *Appl. Sci.* 11 (**2021**) 9974.

[18] S. Fodor, L. Baia, K. Baán, G. Kovács, Z. Pap, K. Hernadi, *Molecules* 26 (**2021**) 1149.

[19] H. Xie, T. Wang, J. Liang, Q. Li, S. Sun, *Nano Today* 21 (**2018**) 41–54.

[20] P.Y. Chang, I.H. Tseng, *J. CO2 Util.* 26 (**2018**) 511–521.

[21] A. Verma, S. Kumar, W.K. Chang, Y.P. Fu, *Dalt. Trans.* 49 (**2020**) 625–637.

[22] Z. Xiang, X. Wang, L. Xu, Z. Wang, J. Meng, J. Zhang, J. Zhao, H. Wang, *J. Mater. Sci.* 57 (**2022**) 2424–2435.

[23] C. Hu, M.T. Liu, A. Sakai, M. Yoshida, K.Y.A. Lin, C.C. Huang, *J. Ind. Eng. Chem.* 115 (**2022**) 329–338.

[24] C.L. Sung, R.H. Wang, Y.C. Shih, Z.Y. Wu, S.R. Alvarado, Y.H. Chang, C.C. Lin, *ACS Omega* 8 (**2023**) 7368–7377.

[25] Z. Chen, M.R. Gao, Y.Q. Zhang, N. Duan, T. Fan, J. Xiao, J. Zhang, Y. Dong, J.

Li, X. Yi, J.L. Luo, *Nano Energy* 73 (**2020**) 104833.

[26] M. Mirza-Aghayan, M. Saeedi, R. Boukherroub, *Appl. Organomet. Chem.* 34 (**2020**) 1–13.

[27] X. An, K. Li, J. Tang, *ChemSusChem* 7 (**2014**) 1086–1093.

[28] M. Nallal, K.H. Park, S. Park, J. Kim, S. Shenoy, C. Chuaicham, K. Sasaki, K. Sekar, *ACS Appl. Nano Mater.* 5 (**2022**) 17271–17280.

[29] J. Xu, R. Wang, X. Chen, R. Zhou, J. Zhang, *Mater. Today Energy* 17 (**2020**) 100435.

[30] S. Khaja Hussain, B.N. Vamsi Krishna, G. Nagaraju, S. Chandra Sekhar, D. Narsimulu, J.S. Yu, *Chem. Eng. J.* 403 (**2021**) 126319.

[31] X. Zhang, M. Xia, F. Wang, W. Lei, *Ionics (Kiel).* 26 (**2020**) 6359–6369.

[32] N. Hussain, M.A. Abdelkareem, H. Alawadhi, A.H. Alami, K. Elsaid, *Appl. Phys. A Mater. Sci. Process.* 128 (**2022**) 131.

[33] X. Zhang, X. Huang, M. Xue, X. Ye, W. Lei, H. Tang, C. Li, *Mater. Lett.* 148 (**2015**) 67–70.

[34] B. Hinnemann, P.G. Moses, J. Bonde, K.P. Jørgensen, J.H. Nielsen, S. Horch, I. Chorkendorff, J.K. Nørskov, *J. Am. Chem. Soc.* 127 (**2005**) 5308–5309.

[35] M.C. Ramakrishnan, R.R. Thangavelu, *Adv. Mater. Res.* 678 (**2013**) 56–60.

[36] K. Bansal, J. Singh, A.S. Dhaliwal, *IOP Conf. Ser. Mater. Sci. Eng.* 1225 (**2022**) 012050.

[37] M.D. Susman, Y. Feldman, A. Vaskevich, I. Rubinstein, *ACS Nano* 8 (**2014**) 162–174.

[38] Y. Li, S. Wu, L. Huang, J. Wang, H. Xu, H. Li, *Mater. Lett.* 137 (**2014**) 281–284.

[39] B. Shen, Z. Hong, Y. Chen, B. Lin, B. Gao, *Mater. Lett.* 118 (**2014**) 208–211.

[40] T. Suter, V. Brázdová, K. McColl, T.S. Miller, H. Nagashima, E. Salvadori, A. Sella, C.A. Howard, C.W.M. Kay, F. Corà, P.F. McMillan, *J. Phys. Chem. C* 122 (**2018**) 25183–25194.

[41] J. Zhang, Y. Guo, B. Shang, T. Fan, X. Lian, P. Huang, Y. Dong, Z. Chen, X. Yi, *ChemSusChem* 14 (**2021**) 929–937.

[42] C. V. Niveditha, M.J.J. Fatima, S. Sindhu, *J. Electrochem. Soc.* 163 (**2016**) H426–H433.

[43] J. Liu, J. Ke, D. Li, H. Sun, P. Liang, X. Duan, W. Tian, M.O. Tadé, S. Liu, S. Wang, *ACS Appl. Mater. Interfaces* 9 (**2017**) 11678–11688.

[44] L. Wang, C.S. Tsang, W. Liu, X. Zhang, K. Zhang, E. Ha, W.M. Kwok, J.H. Park, L.Y. Suk Lee, K.Y. Wong, *J. Mater. Chem. A* 7 (**2019**) 221–227.

[45] J. Yan, Z. Song, X. Wang, Y. Xu, W. Pu, H. Xu, S. Yuan, H. Li, *Appl. Surf. Sci.* 466 (**2019**) 70–77.

[46] Y. Liu, X. Xu, H. Li, Z. Si, X. Wu, R. Ran, D. Weng, *Catal. Letters* 152 (**2022**) 972–979.

[47] Q. Huang, F. Kang, H. Liu, Q. Li, X. Xiao, *J. Mater. Chem. A* 1 (**2013**) 2418–2425.

[48] Y. Yang, D. Xu, Q. Wu, P. Diao, *Sci. Rep.* 6 (**2016**) 35158.

[49] B. Qian, X. Yang, X. Li, Z. Song, *J. Solid State Electrochem.* 24 (**2020**) 1669–1678.

[50] L. Liao, Q. Zhang, Z. Su, Z. Zhao, Y. Wang, Y. Li, X. Lu, D. Wei, G. Feng, Q. Yu, X. Cai, J. Zhao, Z. Ren, H. Fang, F. Robles-Hernandez, S. Baldelli, J. Bao, *Nat. Nanotechnol.* 9 (**2014**) 69–73.

[51] W. Ou, Y. Zou, K. Wang, W. Gong, R. Pei, L. Chen, Z. Pan, D. Fu, X. Huang, Y. Zhao, W. Lu, J. Jiang, *J. Phys. Chem. Lett.* 9 (**2018**) 274–280.

[52] Z. Sun, W. Fang, L. Zhao, H. Chen, X. He, W. Li, P. Tian, Z. Huang, *Environ. Int.* 130 (**2019**) 104898.

[53] S. Han, X. Hu, W. Yang, Q. Qian, X. Fang, Y. Zhu, *ACS Appl. Energy Mater.* 2 (**2019**) 1803–1811.

[54] X. An, K. Li, J. Tang, *ChemSusChem* 7 (**2014**) 1086–1093.

[55] Y. Wang, Z.X. Shi, J. Yin, *ACS Appl. Mater. Interfaces* 3 (**2011**) 1127–1133.

[56] P. Cui, J. Lee, E. Hwang, H. Lee, *Chem. Commun.* 47 (**2011**) 12370–12372.

[57] T. Manyepedza, J.M. Courtney, A. Snowden, C.R. Jones, N. V. Rees, *J. Phys. Chem. C* 126 (**2022**) 17942–17951.

[58] S. Jung, A.N. Karaiskakis, E.J. Biddinger, *Catal. Today* 323 (**2019**) 26–34.

[59] S. Wang, T. Kou, J.B. Varley, S.A. Akhade, S.E. Weitzner, S.E. Baker, E.B. Duoss, Y. Li, *ACS Mater. Lett.* 3 (**2021**) 100–109.

Chapter 5

Bimetallic electrocatalysts for CO_2 conversion

from: Wangchao Yuan, Nivetha Jeyachandran, Tingke Rao, Azeem Ghulam Nabi, Matteo Bisetto, Devis Di Tommaso, Tiziano Montini, Cristina Giordano, Study on the Structure vs Activity of Designed Non-Precious Metal electrocatalysts for CO_2 Conversion, Materials Letters 341 (2023) 134167

5.1 Introduction

Cu-based catalysts are promising nonprecious metal alternatives thanks to the possibility to catalyse the formation of multi-carbon products and the relatively high availability of Cu supply [1]. Besides these important features, Cu-based catalysts show different drawbacks, in particular related to the high overpotential of the process, the low stability and poor selectivity [2]. In the previous chapters, the problems of selectivity and stability were tackled by exploiting different exposed facets and by coupling Cu_2O with opportune supports, in order to improve the dispersion of the nanoparticles. Even if the presence of a support affected the overall selectivity or productivity, the problem of the low stability of the catalyst is still unsolved. A possible solution could rise by utilization of metal Cu nanoparticles as catalyst for the eCO_2RR, in order to exploit the metal behaviour to perform eCO_2RR with high current densities. For this reason, several researches are now focusing in optimizing metal Cu-based catalysts for CO_2RR, to make this process practically but also economically feasible [3–5]. Different methods can be adopted to increase the overall catalytic behavior of Cu-based materials, including the optimization of the specific surface area or the number of active sites through surface modification, doping with metal materials or alloying [6–9]. Many recent publications focus the attention on the tailored synthesis of Cu particles in order to finely control the porosity, sizes and crystallinity of the obtained materials [10–12]. The synthetic methodology to prepare Cu nanoparticles is, therefore, critical to maximize catalytic activity and selectivity of eCO_2RR. It is surprising that not much attention has been devoted to optimizing such a key step. Cu nanoparticles have been prepared for different

applications, using selected pathways, e.g. via microwave or electron beam irradiation, bio-synthesis and laser ablation [13–15]. Since Cu is easily aggregated and oxidized, many researchers synthesize Cu nanoparticles capped with polymers, such as PVP (poly vinyl pyrrolidone) and gelatine [16,17]. However, polymers cannot be decomposed easily, leaving a polymeric residue that might affect the catalytic performances. Strong reducing agents, such as hydrazine and sodium borohydride, have been widely used to synthesize Cu nanoparticles with surfactants; however, hydrazine is extremely toxic and dangerous, and sodium borohydride will produce impurities, such as boron and sodium salts, which are difficult to remove by solvent washing. Kim et al. managed to synthesize monodispersed copper nanoparticles without the use of strong reducing agents by thermal decomposition of Cu-oleate complex, which was prepared by the reaction of $CuCl_2$ with aqueous sodium oleate. However, this method required very low pressure (0.3 torr) [18].

In the present chapter, an alternative non-toxic methodology to prepare monometallic Cu and Sn or bimetallic Cu-Sn materials with a fixed composition and morphology is presented. In particular, this method is based on a sol-gel procedure called urea glass route (UGR) [19,20]. The as-prepared particles were tested for the electrochemical CO_2 reduction reaction (CO_2RR). The monometallic samples, both Cu and Sn, showed a high selectivity in the production of H_2. On the other hand, bimetallic Cu-Sn electrocatalysts showed an improved ability towards the formation of the products of CO_2 reduction, mainly CO and HCOOH at the investigated potentials. The results clearly show that bimetallic materials possess active sites with an increased specific activity toward activation and reduction of CO_2.

5.2 Experimental section

Copper(II) nitrate trihydrate (CAS Number 13778-31-9, 99.999% purity), Tin (IV) chloride (CAS Number 7646-78-8, 98%) and urea (CAS 57-13-6, ACS, Reag. Ph Eur) were purchased from Sigma-Aldrich. Ethanol (Puriss p.a Absolute ≥99.8%). All reagents were of analytical grade and used without further purifications.

Synthesis of Cu and Sn monometallic Nanoparticles

Cu(0) and Sn(0) nanoparticles were synthesized by a modified urea glass route methodology, starting from copper(II) nitrate trihydrate, tin (IV) chloride and urea as precursors [20].

In a typical synthesis of Cu(0), $Cu(NO_3)_2$ and fixed amount of urea (depending on the desired final ratio) were dissolved in ethanol to form light blue mixture. The prepared mixture was then heated under a N_2 atmosphere at 350 °C for 4 hours with a rate of 3.5 °C/min, in order to form a pure metallic Cu phase. At the end of the thermal treatment, a brown-red powder of Cu(0) was obtained. Similarly, for the synthesis of Sn(0) nanoparticles, $SnCl_2$ and an appropriate amount of urea were dissolved in 10 mL of ethanol. The mixture was firstly sonicated for 30 minutes and then annealed under a N_2 atmosphere at 550°C for 4 hours with a rate of 3.5 °C/min. At the end of the process a silver-grey powder of metal Sn(0) was obtained. Samples with different urea/metal salt molar ratio (R) were prepared to investigate the influence of the urea amount over nanoparticles crystallinity and/or size. In particular, we prepared samples with ratio R=3 (labelled as Cu R3 and Sn R3) and samples with R=5 (labelled as Cu R5 and Sn R5).

Synthesis of CuSn bimetallic Nanoparticles

CuSn alloys (strategy A)

CuSn alloys were prepared with the strategy A by simple mixing the two solutions of precursors used for the synthesis of monometallic Cu and Sn. The amount of urea depends on the chosen value of R=urea/metal salt; even in this case the material was prepared with two different molar ratio R (labelled as CuSn R3 and CuSn R5). After the two precursors were mixed together, the obtained solution was sonicated for one hour, obtaining a green Cu-Sn solution. The resulting suspension was then transferred in a crucible and heated up to 350 °C for 4 hours, using a rate of 3.5 °C/min under an atmosphere of N_2. At the end of the thermal treatment, a black powder was obtained.

Cu@Sn core/shell (strategy B)

A core@shell nanostructructure, where Cu is the core and Sn the thin shell, was obtained by a two-step method. In the first step, Cu-R5 nanoparticles were prepared following the

procedure presented for the monometallic materials. In the second step, a proper amount of Cu(0) nanoparticles was added in the Sn precursor solution, in order to achieve a Cu:Sn molar ratio of 1:1. The obtained dispersion was then sonicated for 30 minutes, transferred into a crucible and heated at 550°C for 4 hours using a rate of 3.5 °C/min under a N_2 atmosphere.

Sn@Cu core/shell (strategy C)

Sn@Cu nanoparticles were prepared starting from Sn(0) nanoparticles and the solution of precursors for the synthesis of monometallic Cu. In particular, Sn(0) nanoparticles with R=5 were prepared and mixed with the solution of $Cu(NO_3)_2$ and urea in ethanol, in order to obtain a Cu:Sn molar ratio of 1:1. The obtained suspension was sonicated for 30 minutes, transferred into a crucible and heat treated heated up to 350 °C for 4 hours, using a rate of 3.5 °C/min under an atmosphere of N_2.

Preparation of Electrocatalysts, electrochemical setup and measurements

The electrochemical experiments were performed in the typical 3-electrodes system and using the same procedure already mentioned in chapter 2.8 except for the chrono amperometry that last for one hour instead of 3 hours.

5.3 Results and discussion

5.3.1 Characterization of monometallic and bimetallic particles

The synthesis allows to prepare monometallic and bimetallic nanoparticles based on metal Cu and Sn through a facile urea glass method. In particular, Figure 5.1 summarizes the different experimental strategies to obtain bimetallic alloy of Cu and Sn and the two different core/shell nanoparticles. The preparation of all the materials had been performed by the research group of Pr. Cristina Giordano of the Queen Mary University of London.

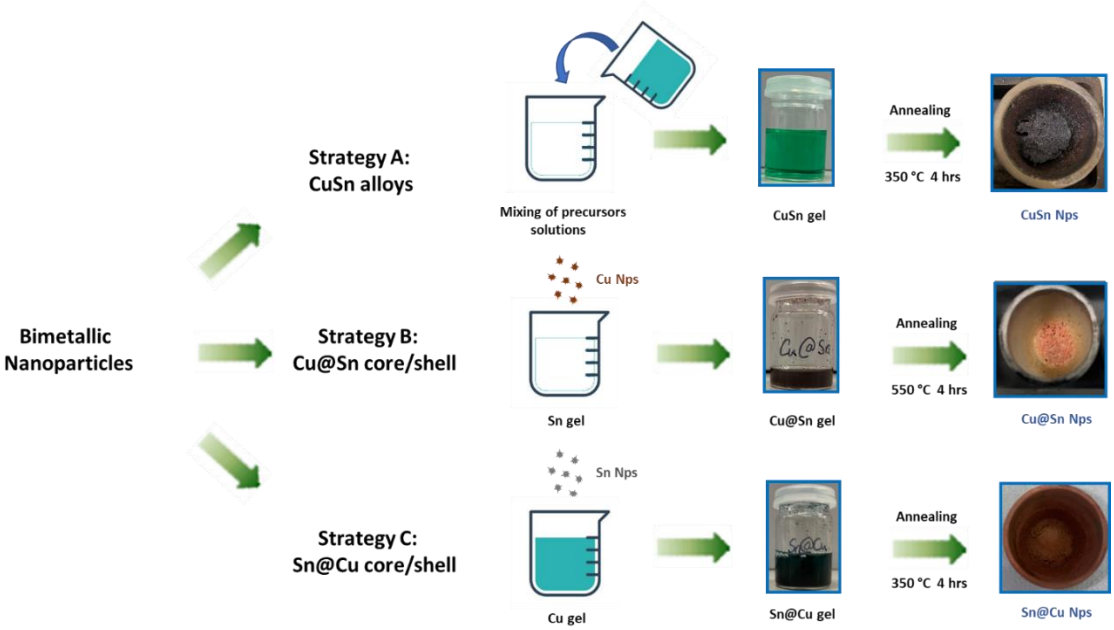

***Figure 5.1**: Synthetic approaches for the synthesis of bimetallic nanoparticles.*

Phase attribution of as-prepared materials was done through XRD characterization. For both Cu R3 and R5, the expected crystal structure of pure metallic (cubic) Cu was achieved around 350 °C; on the other hand, a temperature of 550°C is required to obtain pure Sn(0) phases. Figure 5.2 shows the XRD patterns of CuSn samples prepared via different strategies; the XRD pattern of monometallic Cu and Sn, and the physical mixture (PM) are also included for comparison. The XRD pattern for the CuSn physical mixture shows two distinct phases that are in good agreement with the expected patterns of the pristine Cu(0) and Sn(0), confirming that grinding the as-prepared materials does not induce the formation of alloyed phases. To investigate the structural properties of the synthesized samples, the XRD pattern was fitted by the Rietveld method. The results are summarized in Table 5.1.

Figure 5.2 A presents the pattern of the CuSn R5 sample obtained from the strategy A, revealing the simultaneous presence of three different crystalline phases: Cu(0), SnO_2 and intermetallic Cu_3Sn. The incorporation of Sn into the Cu structure was suggested by a slight increase in the cell parameter (correspondent to the shift at lower angles of the typical Cu(0) peaks). The presence of an alloyed Cu:Sn phase was indicated by the difference with the CuSn-PM.

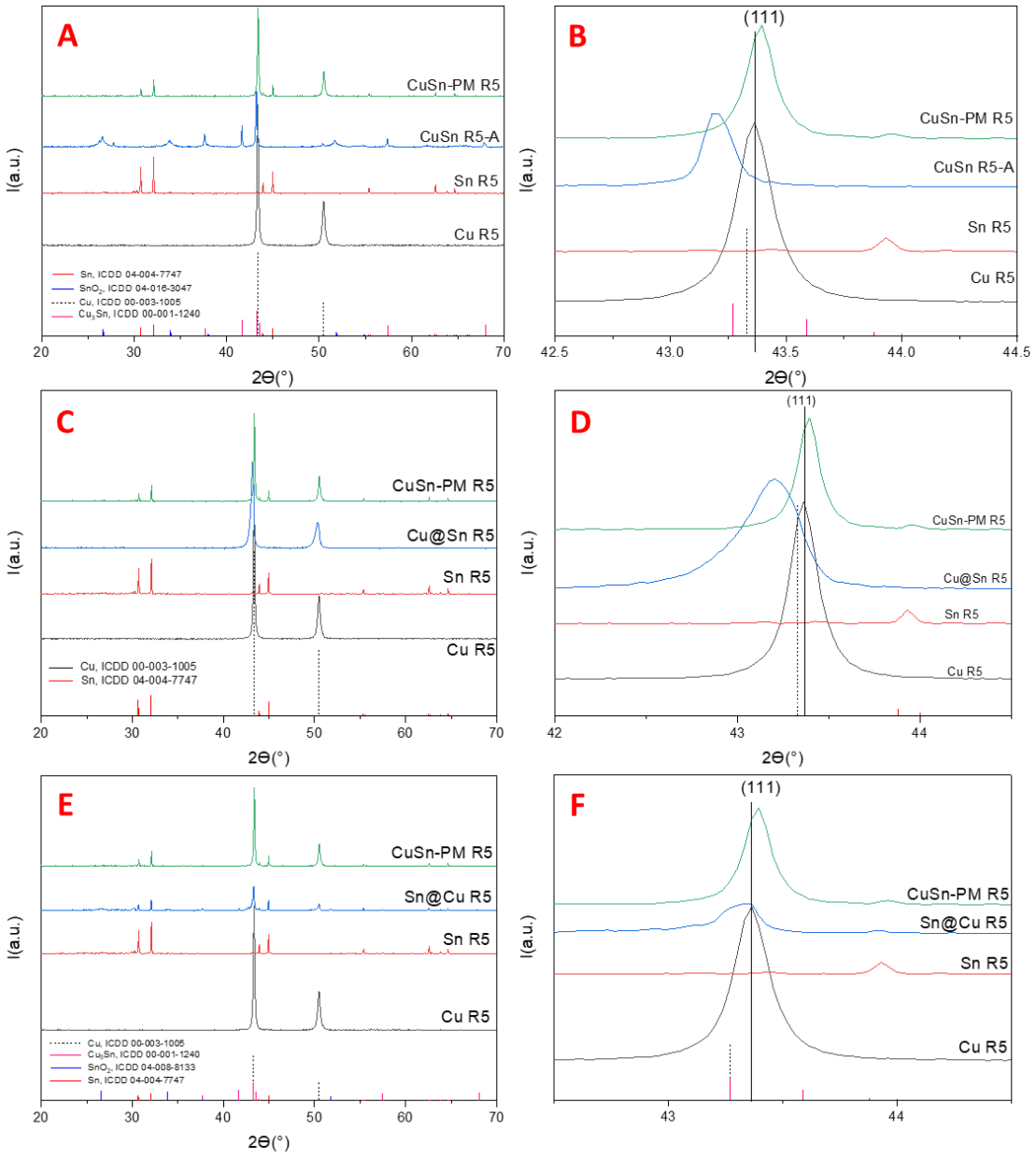

***Figure 5.2**: XRD patterns of bimetallic samples prepared with different strategies (A: CuSn R5 alloy, C: Cu@Sn R5, E: Sn@Cu R5) compared with the patterns of pure Cu (ICDD 00-003-1005), Sn (ICDD 04-004-7747) and corresponding CuSn physical mixture. XRD patterns were enlarged between 42-44° around the Cu (111) peak (Figures B, D and F).*

Sample	Phase	Weight fraction (wt %)	Mean Crystallite Size (nm)	Cell parameters (nm)
Cu R3	Cu	100%	65	a = 0.3611
Cu R5	Cu	100%	55	a = 0.3621
Sn R3	Sn	100%	180	a = 0.5836 c = 0.3184
Sn R5	Sn	100%	194	a = 0.5835 c = 0.3184
CuSn-PM	Cu	94%	75	a = 0.3610
	Sn	6%	167	a = 0.5821 c = 0.3175
CuSn R3	Cu	50%	139	a = 0.3617
	Cu_3Sn	5%	100	a = 0.5509 c = 0.4333
	SnO_2	45%	15	a = 0.4750 c = 0.3192
CuSn R5	Cu	39%	134	a = 0.3619
	Cu_3Sn	18%	104	a = 0.5518 c = 0.4334
	SnO_2	43%	30	a = 0.4745 c = 0.3191
Cu@Sn-B	Cu	100%	95	a = 0.3625
Sn@Cu-C	Cu	54%	75	a = 0.3615
	Cu_3Sn	14%	27	a = 0.5524 c = 0.4326
	Sn	13%	230	a = 0.5827 c = 0.3178
	SnO_2	19%	57	a = 0.4733 c = 0.3182

***Table 5.1**: Results from Rietveld analysis of the investigated samples.*

The comparison of samples prepared at lower urea:metal ratio (Figure 5.3) suggested that increasing the urea:metal ratio improve the Cu-Sn contact, as indicated by the content of the intermetallic Cu_3Sn and by the shift of the Cu cell parameter to higher values. Despite the complexity of the observed patterns, we can safely assume the formation of a CuSn intermetallic phase via the UGR. Regarding the Cu@Sn R5 material synthetised via strategy B (Figure 5.2 C), the XRD pattern showed the reflections typical of Cu, with an asymmetric shape of the Cu peaks, a shift toward lower angles compare to the pattern of pure Cu, and the absence of Sn peaks, suggesting the formation of a core-shell nanostructure. Finally, Figure 5.2 E showed the pattern of the sample prepared via strategy C, observing different features of the synthetised Sn@Cu system compared to the pattern of pure metals. The Sn@Cu sample led to the formation of Cu, Cu_3Sn, Sn and

SnO_2 phases, very similar to what observed for the bimetallic samples prepared via strategy A. By comparison of the three strategies, despite the chosen Cu:Sn molar ratio was always 1:1, the presence of a Cu(0) phase in all the diffractogram suggested that metallic Cu is the main phase of the materials.

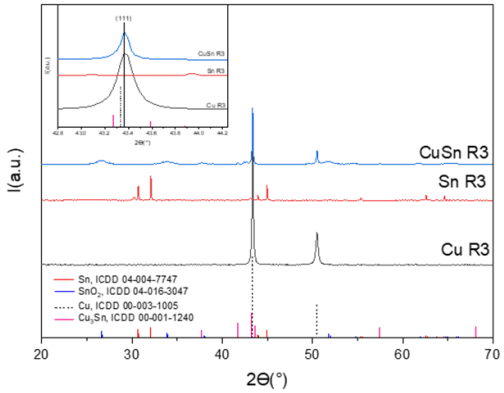

***Figure 5.3**: XRD patterns of CuSn R3 prepared via strategy A compared to pure Cu (ICDD 00-003-1005) and Sn (ICDD 04-004-7747). Inset: XRD patterns in the range 42-44° focus on the Cu_{111} peak.*

To gain information on the morphology and homogeneity of the different materials, all samples were analysed through SEM (Figure 5.4). Cu R3 and Cu R5 samples are composed by highly interconnected polycrystalline particles (Figures 5.4 A and B). On the other hand, Sn R3 and Sn R5 samples are composed by polycrystalline spherical particles, with an improved homogeneity of the sample Sn R3 respect than Sn R5 (Figures 5.4 C and D).

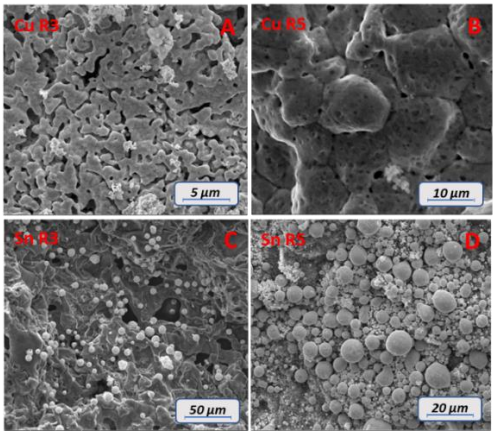

***Figure 5.4**: SEM images of Cu R3 (A), Cu R5 (B), Sn R3 (C) and Sn R5 (D).*

SEM images of bimetallic materials were difficult to interpret due to the homogeneous and bulky structure of the obtained materials. From this point of view, SEM-EDS was a useful tool to confirm the intimate contact between Cu and Sn on all the bimetallic materials (Figures 5.5, 5.6 and 5.7).

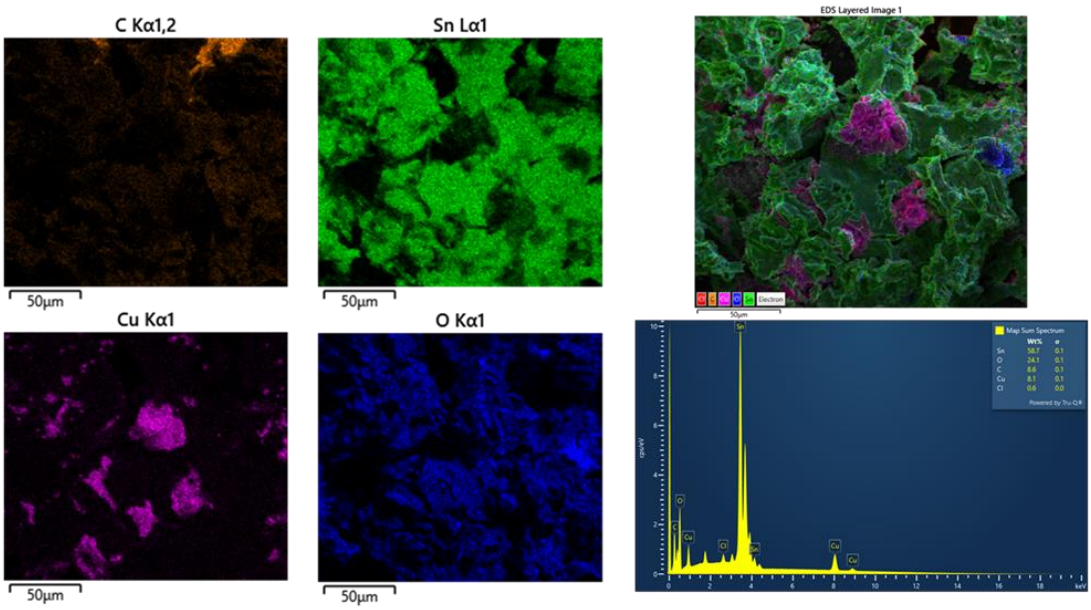

***Figure 5.5**: SEM-EDS mapping and spectrum of CuSn R3-A at low magnification.*

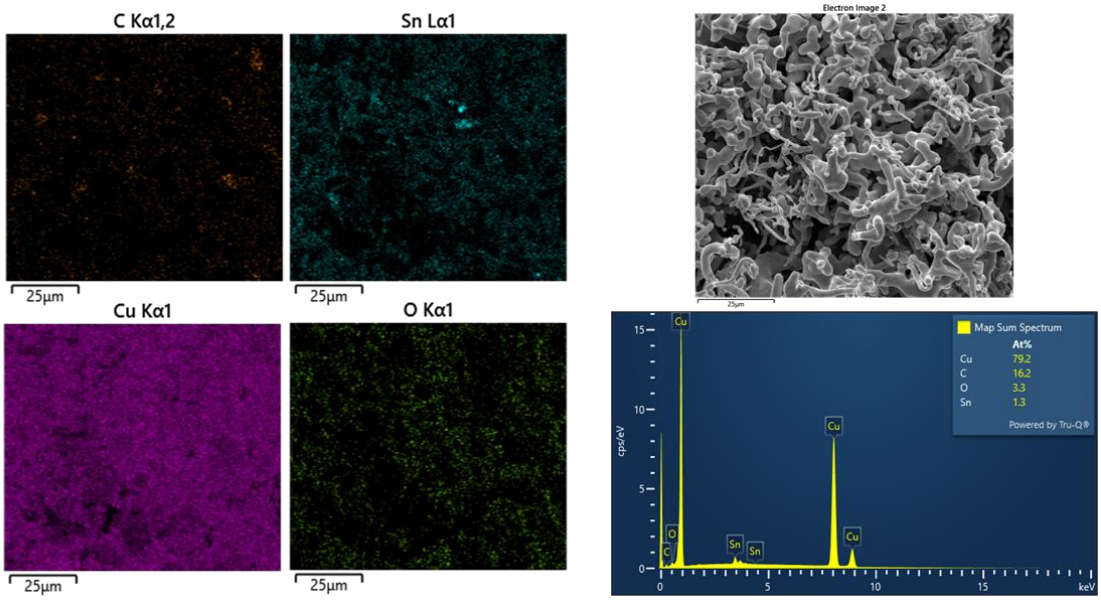

***Figure 5.6**: SEM-EDS mapping and spectrum of Cu@Sn R5-B.*

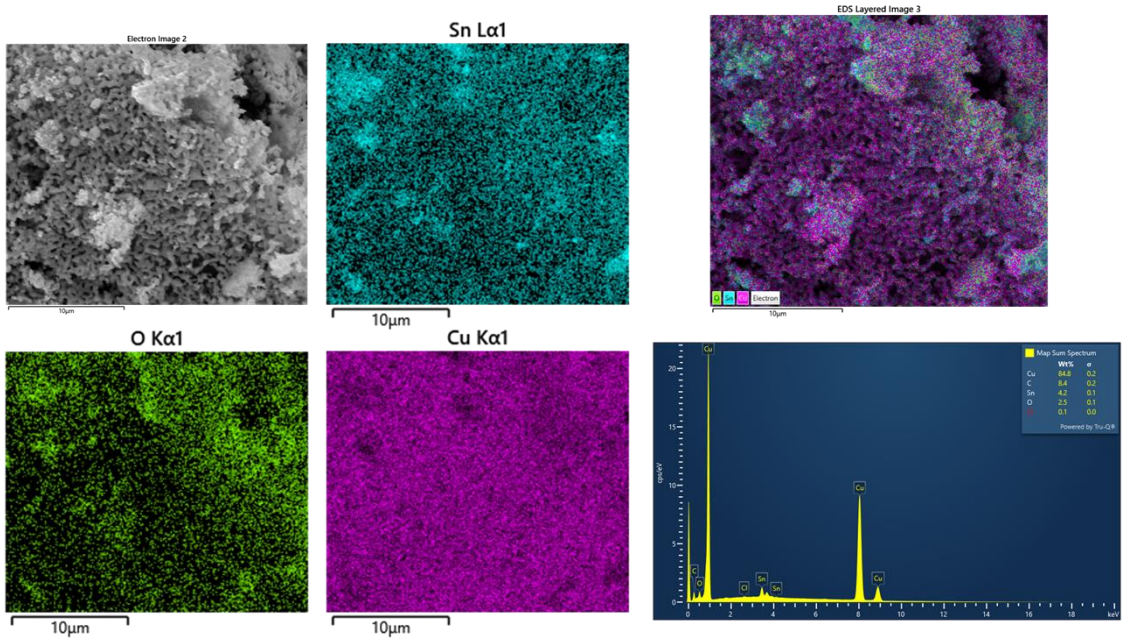

***Figure 5.7**: SEM-EDS mapping and spectrum of Sn@Cu R5-C at high magnification.*

To conclude, the Cu@Sn material prepared through strategy B showed clusters with elongated structures, as confirmed from TEM measurements (Figure 5.8).

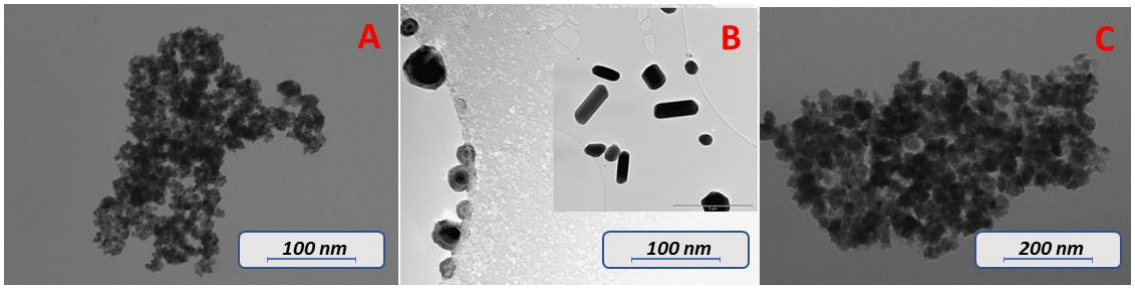

***Figure 5.8**: Representative TEM images of CuSn R3 (A), Cu@Sn R5 (B) and Sn@Cu R5 (C).*

5.3.2 Electrocatalytic CO_2 reduction reaction experiments

In this section, the electrochemical investigation of the catalytic activity of Cu/Sn bimetallic systems toward CO_2RR is reported. Cyclic voltammetries (CVs) were used to release adsorbed species from the surface of the electrode and obtain a preliminary evaluation of the electrocatalytic behavior. CVs were performed under CO_2 atmosphere reaching various negative potentials (−1.3 V, −1.5 V and −1.7 V vs Ag/AgCl sat.

corresponding respectively to −0.7 V, −0.9 V and −1.1 V vs RHE) and showing similar trends (Figure 5.9): the monometallic materials presented enhanced current densities compare to the bimetallic samples, suggesting an improved tendency to exploit electrons for the electrocatalytic reaction. To evaluate the contribution of CO_2 reduction on electrochemical process, preliminary CVs and CAs performed under CO_2 were compared with blank experiments under inert Ar atmosphere (Figure 5.10) for representative samples. These comparisons highlighted a limited increase of the current under CO_2 for the sample Cu R3, with the bimetallic species Cu@Sn-B and Sn@Cu-C that showed larger improvements in current densities under CO_2 atmosphere.

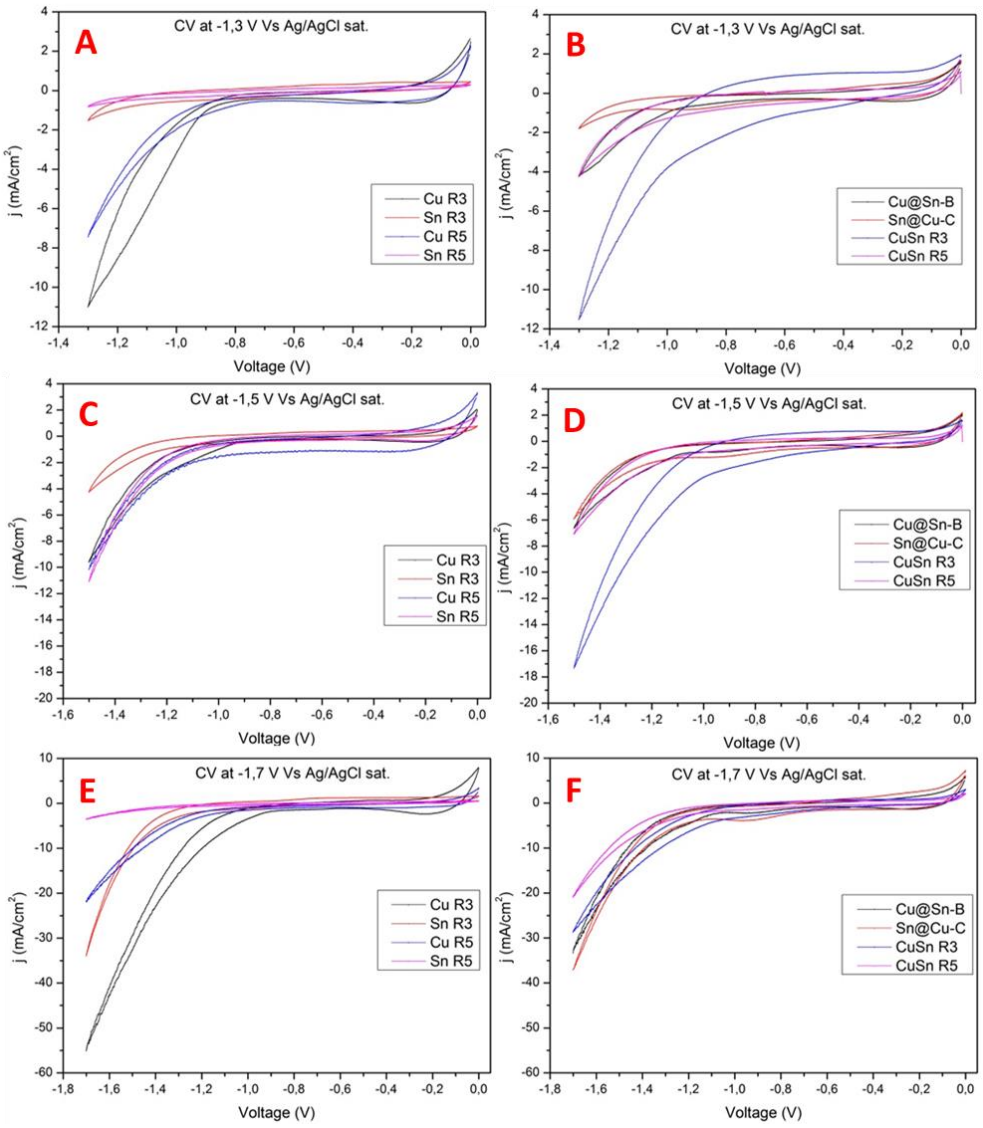

***Figure 5.9**: CVs of monometallic (left) and bimetallic (right) catalysts under CO_2 atmosphere at different potentials (A and B: −0.7 V, C and D: −0.9 V, E and F: −1.1 V vs RHE).*

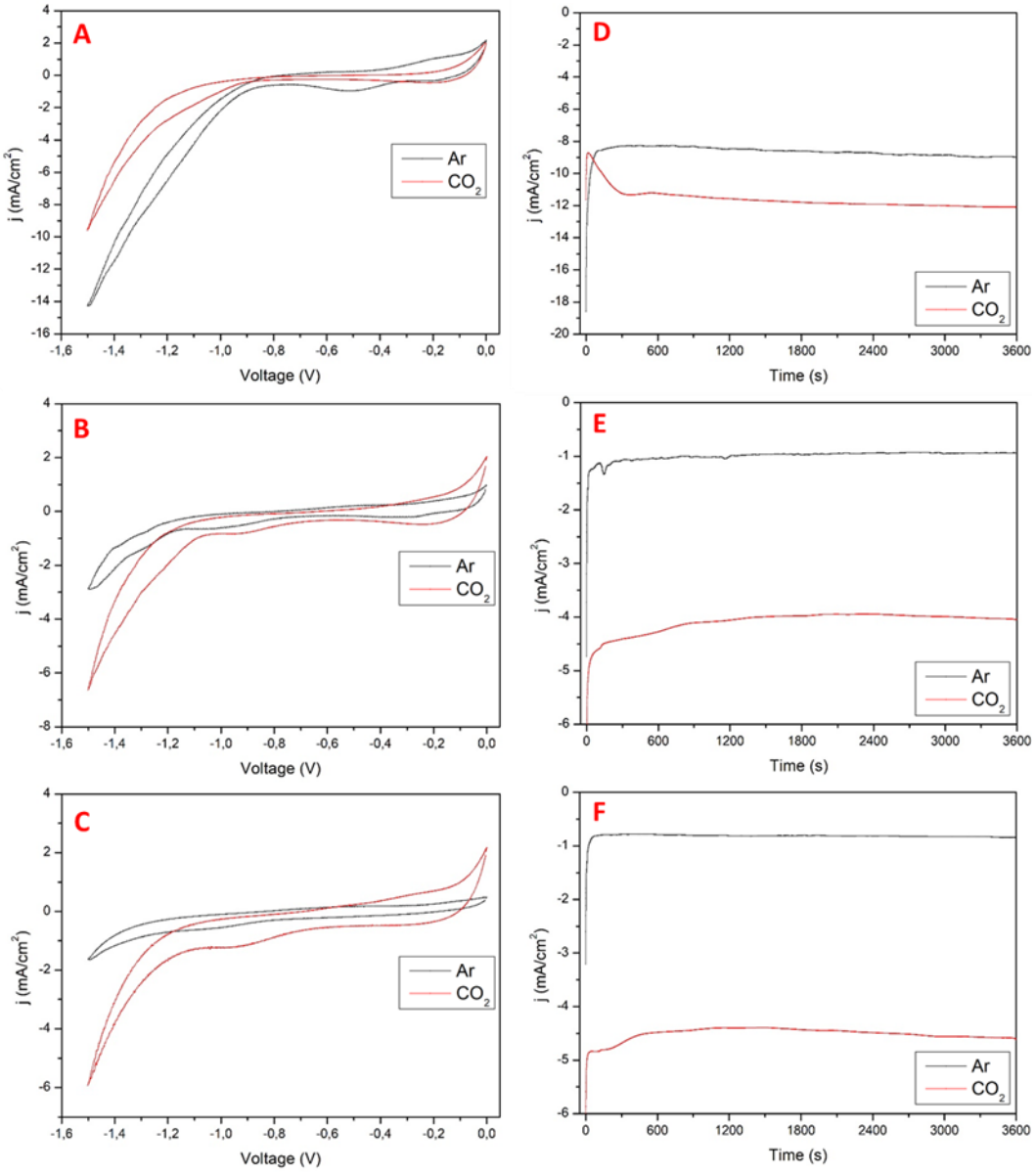

***Figure 5.10**: CVs (left) and CAs (right) under Ar and CO_2 atmosphere at the potentials of −0.9 V vs RHE for Cu R3 (A, D), Cu@Sn B (B, E) and Sn@Cu C (C, F).*

The electrocatalytic behavior of different materials towards CO_2RR was investigated performing chrono amperometries, applying the chosen voltage for one hour and tracking the composition of gaseous and liquid products. Figures 5.11, 5.12 and 5.13 show the results of the electrocatalytic experiments obtained at the different experimental voltages (−0.7 V, −0.9 V vs RHE and −1.1 V vs RHE). In agreement with preliminary CVs experiments, the measured current densities increased as the potential applied moves to more negative values. Monometallic Cu materials showed the highest currents compare

to all the bimetallic materials: at the voltage of −0.9 V vs RHE, Cu R3 and Cu R5 samples showed an average current density of −11.6 mA/cm^2 and −8.8 mA/cm^2, respectively. These intense current densities are mainly due to the formation of gaseous H_2 from H_2O (Figures 5.11 C, 5.12 C and 5.13 C). Similarly, Sn R3 and Sn R5 were mainly selective toward HER process, even if producing lower amount of H_2, in agreement with the lower current densities. All the monometallic compounds had showed a FE_{H_2} around 60 – 70 % (Figures 5.11 E, 5.12 E and 5.13 E), confirming the metallic behavior to promote HER process. Consequently, very low productivities toward the formation of CO_2RR-derived products were observed.

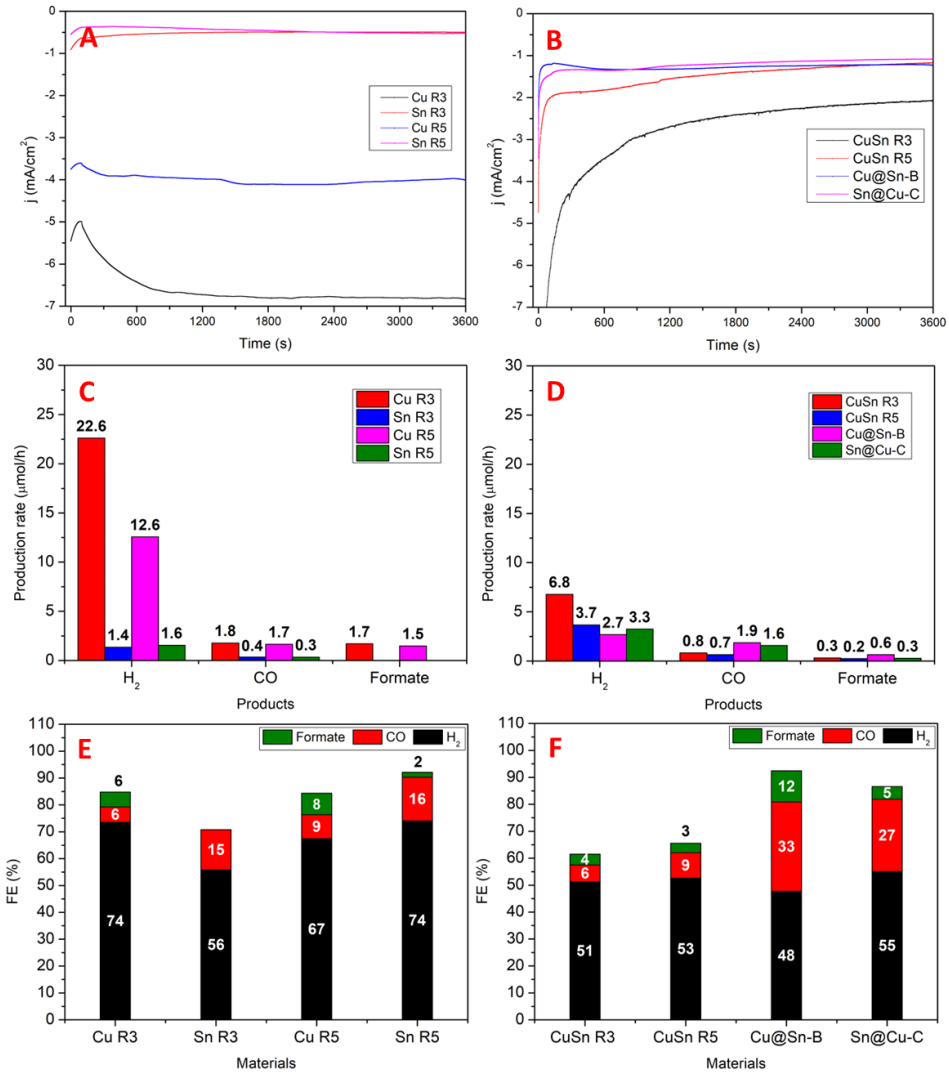

Figure 5.11: *eCO$_2$RR experiments at the voltage of −1.3V vs Ag/AgCl sat. (−0.7 V vs RHE) of monometallic (left) and bimetallic (right) materials. (A, B) CAs; (C, D) Production rate of the detected products; (E, F) Faradaic Efficiencies (FE) toward the detected products.*

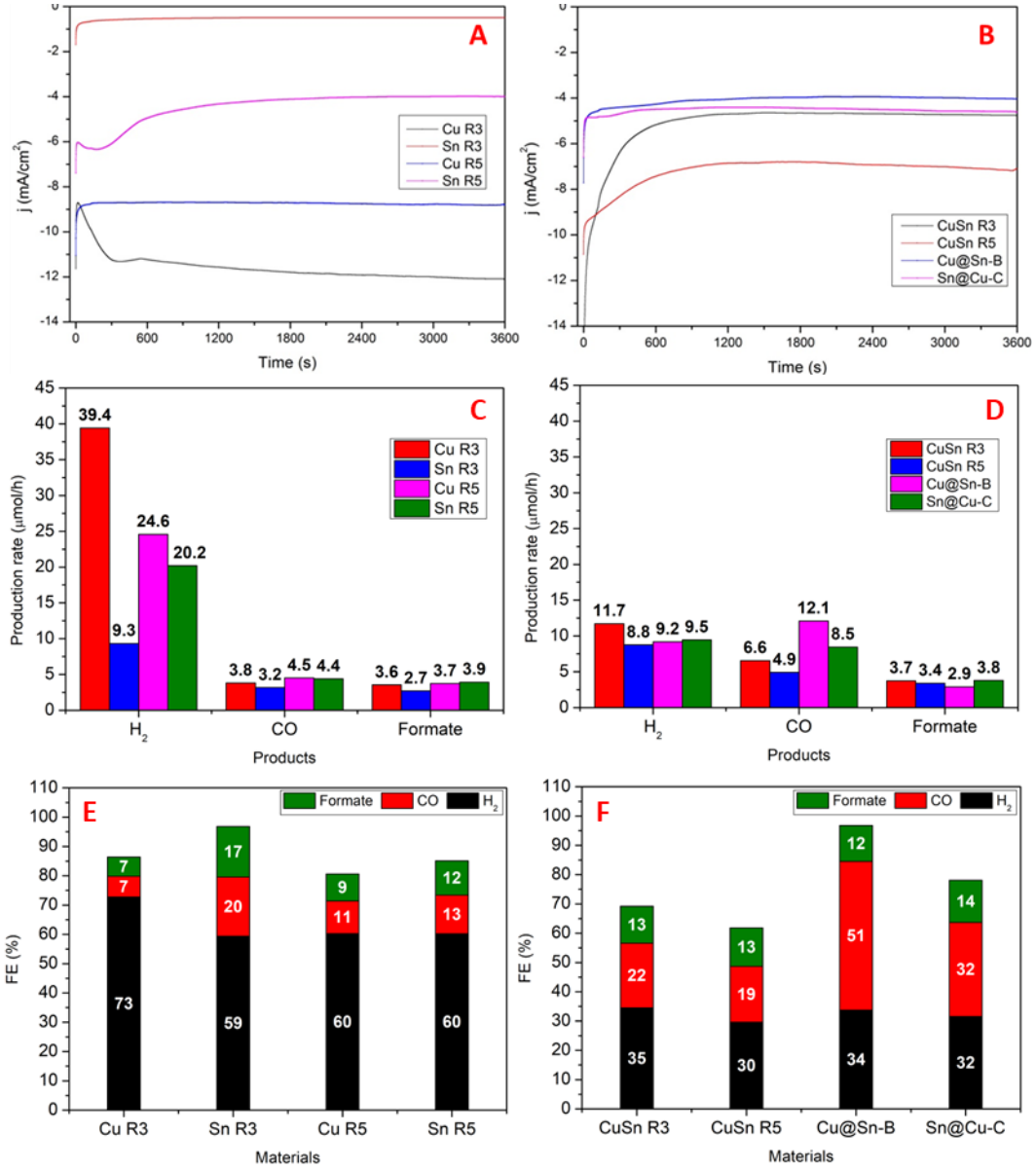

***Figure 5.12**: eCO₂RR experiments at the voltage of −1.5 V vs Ag/AgCl sat. (−0.9 V vs RHE) of monometallic (left) and bimetallic (right) materials. (A, B) CAs; (C, D) Production rate of the detected products; (E, F) Faradaic Efficiencies (FE) toward the detected products.*

On the other hand, bimetallic materials showed an improved selectivity towards CO_2RR products, in particular at the voltage of −0.9 V vs RHE. Indeed, despite lower current densities with respect to the monometallic Cu R3 and Cu R5 (Figure 5.12 B), bimetallic materials presented increased FEs toward the formation of carbon-based species such as CO or HCOOH (Figures 5.12 D and 5.12 F). Similar effects were observed even at the other voltages, with a general increasing of HER activity for monometallic Cu and Sn and

improved Faradic efficiencies towards CO_2RR products for bimetallic compounds (Figures 5.11 and 5.13). In particular, the sample Cu@Sn-B presented the best catalytic performances, with FE_{CO} higher than 50% and the formation of significant amounts of Ethylene at the voltage of −1.1 V vs RHE (Figure 5.13 F). Notably, the FEs of different materials differ from 100% due to the presence of secondary and parasitic reactions that reduced the overall fraction of electrons available for the reduction of CO_2. Considering that these materials contain relevant amounts of SnO_2, it is reasonable to consider that part of the electrons are consumed for reduction of SnO_x species.

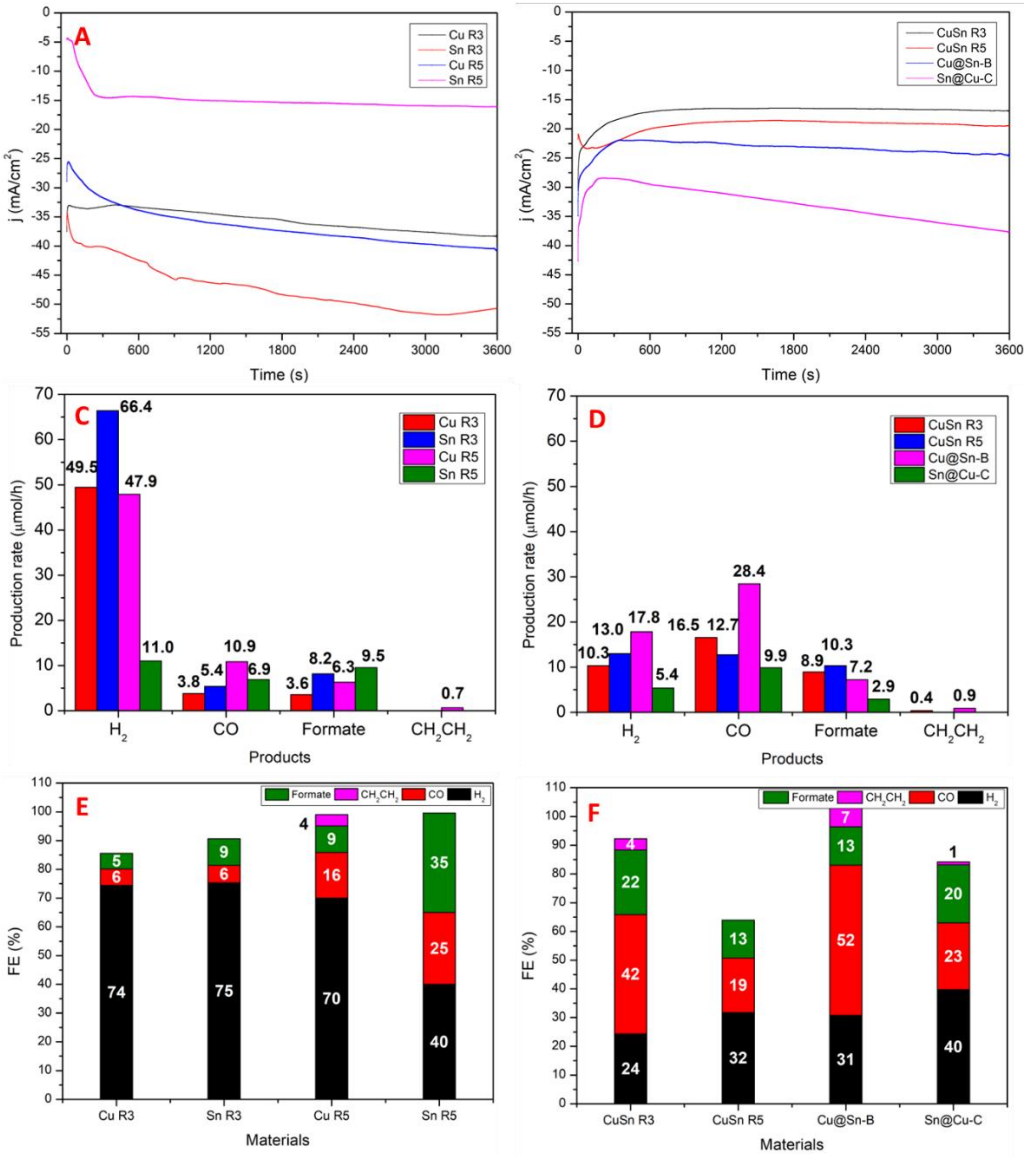

Figure 5.13: *e CO_2RR experiments at the voltage of −1.7 V vs Ag/AgCl sat. (−1.1 V vs RHE) of monometallic (left) and bimetallic (right) materials. (A, B) CAs; (C, D) Production rate of the detected products; (E, F) Faradaic Efficiencies (FE) toward the detected products.*

To further prove the effect of bimetallic composition on the selectivity, the molar ratio between the electrons employed in the production of CO_2RR-products (HCOOH and CO as C_1 products while Ethylene is the most important C_2 product) and those consumed for the HER process has been calculated using the equation:

$$\frac{C_1+C_2}{H2} = \frac{2\ mol_{CO}+2\ mol_{HCOOH}+8\ mol_{CH_2CH_2}}{2\ mol_{H_2}}$$

Figure 5.14 highlights these differences for the chosen voltages, showing a general increase ratio for bimetallic materials and confirming a most selectively catalytic behavior toward CO_2RR. As an example, at the voltage of −0.9 V vs RHE, a maximum ratio $(C_1+C_2)/H_2$ for the most selective Cu@Sn-B was obtained, ratio 8 times higher than that observed for the less selective Cu R3. These results confirmed the higher selectivity of bimetallic CuSn materials toward CO_2RR process: in comparison with the results obtained from monometallic catalysts, bimetallic materials direct electrons toward CO_2 reduction reaction, strongly limiting the production of molecular H_2. This effect suggests that a modification of the reaction pathway takes place in bimetallic materials with respect to the monometallic ones.

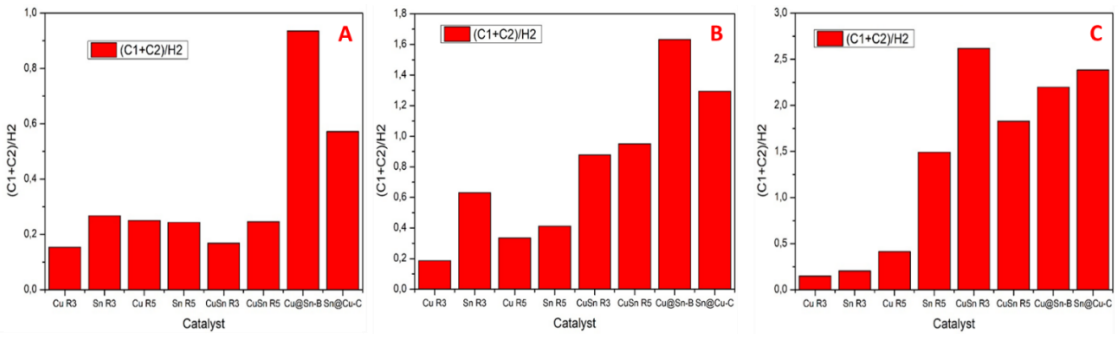

***Figure 5.14**: Ratio between electrons employed for CO_2RR and for H_2 for the different catalysts at the potential of -0.7 V (A), – 0.9 V (B) and -1.1 V (C) vs RHE.*

To rationalize the preference towards HER or CO_2RR, the adsorption energies of H_2O, CO_2 and the products of their reduction reaction on the Cu (100), (110), and (111) surfaces were calculated through DFT calculations by the research group of Prof. Devis Di Tommaso from the Queen Mary University of London. H_2 has an adsorption energy of approximately −0.1 eV, which corresponds to a significantly weaker surface binding than

*COOH and *CO, the first two intermediates in the CO_2RR reaction pathway. Therefore, on all Cu surfaces H_2 desorbs more easily than HCOOH and CO, leading to the observed high FE for the HER. On the other hand, calculation of Gibbs free energy profiles for CO_2RR and HER on different surfaces suggested that both Cu (100), and CuSn (100) surfaces have low overpotential towards CO production. However, HER is competitive with CO formation especially for Cu (100), confirming the higher activity of Cu surfaces toward the H_2 formation and the improved conversion of CO for the mixed CuSn surfaces.

5.4 Conclusions

In this work, monometallic and bimetallic particles based on Cu and Sn were synthetized for the first time by an easy and scalable sol-gel process called urea glass route (UGR). In particular, the presented procedure allowed to synthetize bimetallic Cu/Sn particles exploiting different approaches. With the first approach, bimetallic alloys were prepared by mixing the urea-based solutions used as precursor for the synthesis of monometallic materials. The other two strategies allowed to form core-shell nanoparticles based on the two considered metals: Cu@Sn-B and Sn@Cu-C. All the prepared materials were tested towards CO_2RR at different voltages revealing peculiar catalytic behaviors for bimetallic materials. In particular, monometallic materials showed higher current densities, mainly due to favorable activity towards the formation of H_2. On the other hand, bimetallic materials presented interesting increase in selectivity toward the formation of products of CO_2RR, in particular to HCOOH and CO. The sample Cu@Sn-B presented the best catalytic performances, with FE_{CO} higher than 50% and the presence of Ethylene at -1.1 V vs RHE. The improved selectivity of bimetallic materials towards CO_2RR was suggested even by the analysis of the molar ratio between CO_2-based products and H_2. This work opens a promising prospect for the utilization of easy and scalable experimental procedures to obtain efficient metal electrocatalysts toward CO_2RR.

5.5 References

[1] J.M. Hammarstrom, M.L. Zientek, H.L. Parks, C.L. Dicken, Assessment of Undiscovered Copper Resources of the World, 2015, **2019**.

[2] D.D. Zhu, J.L. Liu, S.Z. Qiao, *Adv. Mater.* 28 (**2016**) 3423–3452.

[3] K.D. Yang, W.R. Ko, J.H. Lee, S.J. Kim, H. Lee, M.H. Lee, K.T. Nam, *Angew. Chemie - Int. Ed.* 56 (**2017**) 796–800.

[4] Y. Li, F. Cui, M.B. Ross, D. Kim, Y. Sun, P. Yang, *Nano Lett.* 17 (**2017**) 1312–1317.

[5] H. Mistry, A.S. Varela, C.S. Bonifacio, I. Zegkinoglou, I. Sinev, Y.W. Choi, K. Kisslinger, E.A. Stach, J.C. Yang, P. Strasser, B.R. Cuenya, *Nat. Commun.* 7 (**2016**) 12123.

[6] S. Shen, J. He, X. Peng, W. Xi, L. Zhang, D. Xi, L. Wang, X. Liu, J. Luo, *J. Mater. Chem. A* 6 (**2018**) 18960–18966.

[7] L. Liu, H. Yao, Z. Jiang, T. Fang, *Appl. Surf. Sci.* 451 (**2018**) 333–345.

[8] J. Dean, Y. Yang, N. Austin, G. Veser, G. Mpourmpakis, *ChemSusChem* 11 (**2018**) 1169–1178.

[9] W. Xiong, J. Yang, L. Shuai, Y. Hou, M. Qiu, X. Li, M.K.H. Leung, *ChemElectroChem* 6 (**2019**) 5951–5957.

[10] R. Reske, H. Mistry, F. Behafarid, B. Roldan Cuenya, P. Strasser, *J. Am. Chem. Soc.* 136 (**2014**) 6978–6986.

[11] G. Mangione, J. Huang, R. Buonsanti, C. Corminboeuf, *J. Phys. Chem. Lett.* 10 (**2019**) 4259–4265.

[12] B. Yang, C. Liu, A. Halder, E.C. Tyo, A.B.F. Martinson, S. Seifert, P. Zapol, L.A. Curtiss, S. Vajda, *J. Phys. Chem. C* 121 (**2017**) 10406–10412.

[13] R. Zhou, X. Wu, X. Hao, F. Zhou, H. Li, W. Rao, *Nucl. Instruments Methods Phys. Res. Sect. B Beam Interact. with Mater. Atoms* 266 (**2008**) 599–603.

[14] M. Nasrollahzadeh, S.M. Sajadi, M. Khalaj, *RSC Adv.* 4 (**2014**) 47313–47318.

[15] M. Muniz-Miranda, C. Gellini, E. Giorgetti, *J. Phys. Chem. C* 115 (**2011**) 5021–5027.

[16] Y. Jianfeng, Z. Guisheng, H. Anming, Y.N. Zhou, *J. Mater. Chem.* 21 (**2011**) 15981–15986.

[17] S. Jeong, K. Woo, D. Kim, S. Lim, J.S. Kim, H. Shin, Y. Xia, J. Moon, *Adv. Funct. Mater.* 18 (**2008**) 679–686.

[18] Y.H. Kim, Y.S. Kang, W.J. Lee, B.G. Jo, J.H. Jeong, *Mol. Cryst. Liq. Cryst.* 445 (**2006**) 231/[521]-238/[528].

[19] C. Schliehe, J. Yuan, S. Glatzel, K. Siemensmeyer, K. Kiefer, C. Giordano, *Chem. Mater.* 24 (**2012**) 2716–2721.

[20] L. Ma, L.R.L. Ting, V. Molinari, C. Giordano, B.S. Yeo, *J. Mater. Chem. A* 3 (**2015**) 8361–8368.

Chapter 6

TiN nanotubes as catalyst for gas-phase photothermal CO_2 reduction

6.1 Introduction

In the last years, many efforts have been done to develop metamaterials with advanced and innovative performance, in particular related to their optical, thermal and catalytic properties [1–3]. Generally based on noble metal nanoparticles, these materials provide enhanced light absorption behavior thanks to the opportunity to exploit Localized Surface Plasmon Resonance (LSPR) [4,5]. Through an adequate control of the nanostructure of the materials, plasmon resonance can be exploited to induce an enhance of the light absorption or to increase the reflectivity of a particular surface. Plasmon resonance in metamaterials can relax via two different pathways (Figure 6.1): a radiative pathway with release of energy by a re-emission of a photon or a non-radiatively way through Landau damping, with the generation a hot electron-hole pair [6].

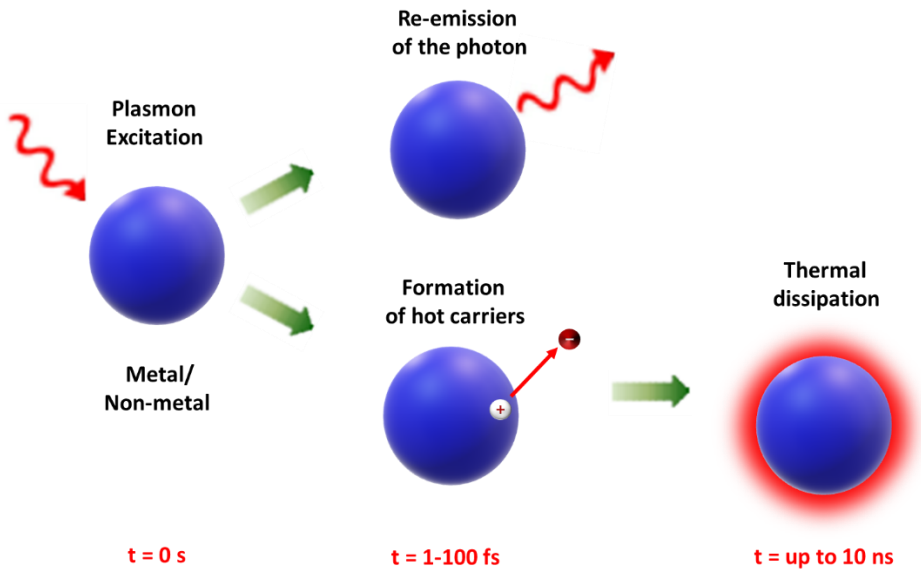

***Figure 6.1**: Relaxation of a plasmon resonance via radiative and non radiative pathway.*

Metamaterials are able to exploit LSPR and its relaxation to produce hot electrons that can be used in many applications or devices, in particular in catalytic processes. Indeed, due to their transient high energy, hot electrons activate electronic or vibrational transitions directly on molecules adsorbed on the material surfaces being able to catalyze chemical reactions, increasing the overall activity of the system. The presence of these hot electrons is drastically limited on extended metal surfaces due to the low lifetime and mobility of the carriers [7]. These factors can be improved with control of nanostructure of the system and the optimization of the electron confinement, increasing the density of states and reducing the electron-electron interactions in order to enhance the overall lifetime of the produced hot electrons [8].

Generally, LSPR is exploited using noble metals nanoparticles. The use of Au or Ag nanoparticles is diffuse for these applications but, on the other hand, the utilization of noble-metal nanoparticles introduces some issues related to the metal response that increase the overall reflectivity at non-resonant frequencies and the low melting point of the materials, inducing modifications on the nanostructure and on the overall catalytic behavior [9]. In addition, the high cost of these critical raw materials urges researcher to find new materials to exploit plasmonic features. Common transition metals such as nickel or aluminum are still able to exploit plasmonic excitation, but their optical properties are generally limited and their stability is still low to exploit them as solar absorber for catalytic properties [10]. On the other hand, transition metal nitrides bear different properties such as the presence of LSPR, good absorption and emission properties and, mainly, a mechanical stability that rise especially at very high temperatures. Titanium Nitride (TiN) is one of the most promising refractory materials used for solar thermal technologies, thanks to the high melting point, the improved chemical and thermal stability and durability [11,12]. Compare to typical metals, TiN shows an improved behavior to locally increase the temperature and a work function lower than mostly of noble metals ($\phi_M \approx 4$ eV), indicating its important role on the development of different metal nano-optics devices [13]. Moreover, thanks to its flexibility, it is possible to tailor the optical properties by a rational choice of the stoichiometry or the nanostructure of the final material, exhibiting a tunable absorption spectra that can be extended toward Near-infrared region without particular optical losses [14]. Different approaches had been used to synthetize nanostructured TiN in order to

enhance the absorption properties of the entire system, optimizing the LSPRs and promoting the light trapping effects through nanostructuration [15–17]. In particular, high aspect-ratio nanostructures are able to significantly optimize the photo-thermal behavior thanks to the high anisotropic effects on the system [18].

Hence, control of nanostructure is exploited to improve the catalytic properties of TiN. In particular, TiN nanotubes are synthetized via a three-steps method and used as catalysts toward the gas-phase photothermal reduction of CO_2. Different metals were used to decorate TiN nanotubes in order to study the effects on the overall catalytic behavior: briefly, TiN with Ru nanoparticles is mostly active toward CO_2 methanation (through Sabatier reaction) while TiN decorated with Pt nanoparticles catalyzes the reverse Water Gas Shift reaction (rWGS). To unveil the role of hot electrons on the overall catalytic process, a layer of Al_2O_3 with different thickness was deposited on TiN samples, resulting in a drop of the CO production rate as the thickness of the interlayer increases.

This work opens promising perspectives focus on the use of LSPR to locally increase the temperature of a sample, enabling catalytic processes and limiting the overall energy consumption.

6.2 Experimental section

All reagents were of analytical grade and used without further purifications.

Synthesis of TiN nanotubes

The synthesis of TiN nanotubes was performed in a three-steps process, with TiO_2 nanotubes were grown on a Ti foil via anodization and annealing and finally converted to TiN via heat treatment under NH_3 atmosphere. In a typical procedure, a Ti foil was firstly cleaned in a multistep procedure by washing with acetone, ethanol and deionized H_2O under sonication. Then, the polished Ti foils were used as working electrode in a two-electrode electrochemical cell, facet with a Pt foil as counter electrode and connected to DC power supply. The anodization was performed by applying 60 V for 3 hours in a solution of diethylene glycol (DEG) containing 0.5 wt. % of NH_4HF_2 and 3.6 wt. % of H_2O [19]. The entire electrochemical setup was kept at 40 °C. The anodization allows the formation of TiO_2 nanotubes on the Ti foil. At the end of the electrochemical process, the

foil was annealed in air at 450 °C for 2 hours in order to improve the crystallinity of the obtained TiO_2 nanotubes. In the last step of the synthesis, TiO_2 nanotubes were undergo to nitridation, by annealing at 900 °C for 1 hr under ammonia atmosphere. The heating and cooling ramp was set at 5 °C/min.

Deposition of metal nanoparticles or Al_2O_3 layer

Different metal nanoparticles were deposited on the top of TiN nanotubes array through Direct Current (DC) sputtering, using different targets and setting a nominal thickness of 2 nm. Pt nanoparticles were deposited even via chemical impregnation in order to compare the two methods. In particular, Pt nanoparticles were deposited via impregnation following an adapted procedure from the reference [20]. In a typical procedure, TiN foils were immerged in a solution containing 87 mg of $H_2PtCl_6*2H_2O$ in 0.7 mL of HCl (37 %) and 100 μL of ethylene glycol in 60 mL of H_2O for 30 s. Pt nanoparticles were synthetized by reduction of Pt precursor through immersion of the sample in a solution containing 1 g of $NaBH_4$ in 50 mL of H_2O and repeating the procedure for 10 times. The different metals used in this work and the relative experimental method are presented in the Table 6.1.

Metal	Method
Cu	DC Sputtering
Ni	DC Sputtering
Au	DC Sputtering
Ag	DC Sputtering
Pd	DC Sputtering
Ru	DC Sputtering
Pt	DC Sputtering
Pt	Wet impregnation

***Table 6.1**: Different metal deposited on TiN nanotubes.*

TiN nanotubes were also covered with a thin layer (nominal thickness 2, 4, 7, 10 and 20 nm) of Al_2O_3 via Atomic Layer Deposition (ALD) using $Al(CH_3)_3$ as precursor and performing the deposition at 100 °C with a rate of 10 cycles/nm.

Catalytic tests

The catalytic tests were performed using a home-made gas tight cell assembled with a front viewport in order to transmit a wide range of the light. The reactive mixture (25

mL/min) was flown in the cell by controlling the flow rate with a digital mass flow controller. Before each catalytic experiment, the cell was tightly closed, and the air was removed flowing the reactive mixture for 20 minutes at 100 mL/min. The sample was illuminated from the top using a 1000 W solar simulator (Sciencetech) equipped with a Xe lamp and an AM 1.5G filter. Gas-phase catalytic CO_2 reduction was performed illuminating the sample with different light intensities (from 3.19 to 5.53 mW/cm^2, that correspond to light ranging from 8.6 to 15 Suns) and analyzing the composition of the gaseous mixture through GC analysis. Stability tests were performed illuminating the sample at 15 Suns for 50 hours, controlling the stability of the light intensity every 6 hours. All the catalytic measurements were normalized for the light spot area of the system (1.13 cm^2).

6.3 Results and discussion

6.3.1 Preparation and characterization of TiN nanotubes array

TiN nanotubes were prepared via a facile and scalable three-steps method, where TiO_2 nanotubes were firstly directly grown on a Ti foil by anodization and then converted to TiN nanotubes via nitridation under NH_3 atmosphere (Figure 6.2). The synthesis and characterization of TiN samples were performed by the research group of Prof. Alberto Naldoni from RCPTM of Olomouc (Czech Republic).

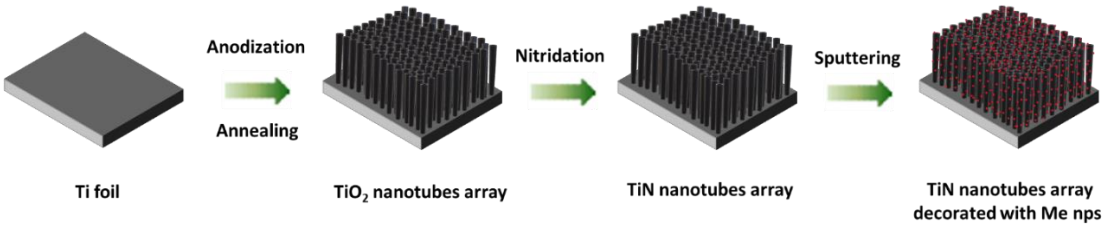

***Figure 6.2**: Steps involved on the preparation of TiN nanotubes.*

The experimental procedure allowed to prepare TiN nanotubes with good grade of purity (Figure 6.3). In the first step of anodization, amorphous TiO_2 was grown on Ti foil: the diffraction pattern shows the subsequent typical reflection of pristine Ti (◊) while reflection related to TiO_2 (anatase: △ triangle) can be detected. The annealing in air had the direct implication of increasing the crystallinity of TiO_2 nanotubes, as indicated by

the arising of reflections related to anatase polymorph of TiO_2. At the same time, the thermal treatment under NH_3 atmosphere converted TiO_2 phase into titanium nitrides: XRD pattern clearly shows the formation of TiN, with minor amounts of Ti_2N (TiN: □, Ti_2N: ■).

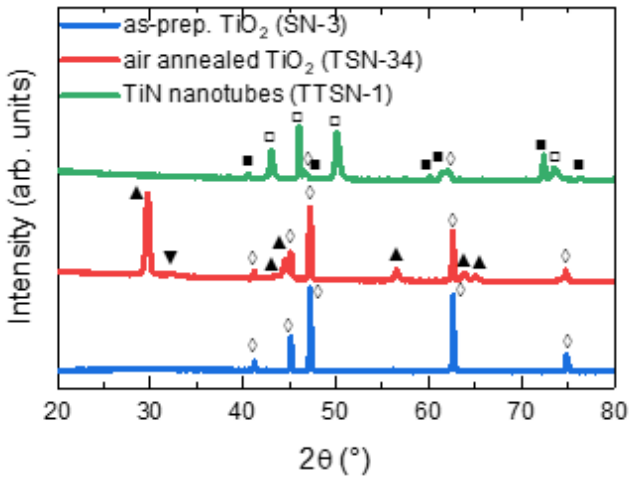

***Figure 6.3**: XRD of the sample after each step of the preparation (Ti: ◊, TiO_2: △, TiN: □, Ti_2N: ■).*

The nitridation treatment affects also the morphology of the obtained nanotubes (Figure 6.4). Indeed, after the initial annealing in air, separated TiO_2 nanotubes are obtained, with an average length of 5 μm and an average diameter of 250 nm (Figure 6.4 A, B and C). Upon nitridation, the nanotubes shrink to an average length of 3 μm and become more porous (Figure 6.4 D and E). TEM images (Figure 6.4F) give more information regarding the sizes of the obtained nanostructures, revealing TiN nanotubes with an average diameter of 225 nm and a thickness of 20 nm.

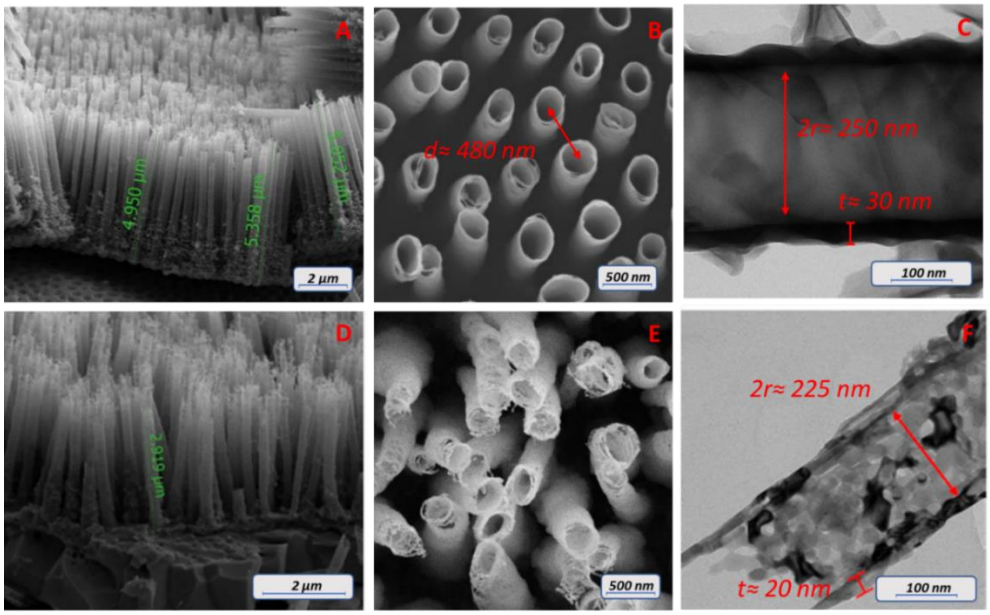

***Figure 6.4**: SEM and TEM images of TiO_2 (A, B and C) and TiN nanotubes (D, E and F).*

The analysis of optical properties revealed a superior absorption of the obtained TiN nanotube array respect the TiO_2 nanotubes (Figure 6.5 A: UV-Vis spectrum, Figure 6.5 B: FTIR spectrum). Indeed, the determination of absorption spectrum indicates an absorbance of almost 99% in the visible range, higher than the absorbance of TiO_2 nanotubes, both pre- and post-annealing. Moreover, TiN shows a broad absorption even in the IR region (up to 25000 nm), suggesting the ability of these materials to absorb part of the IR region of the solar light.

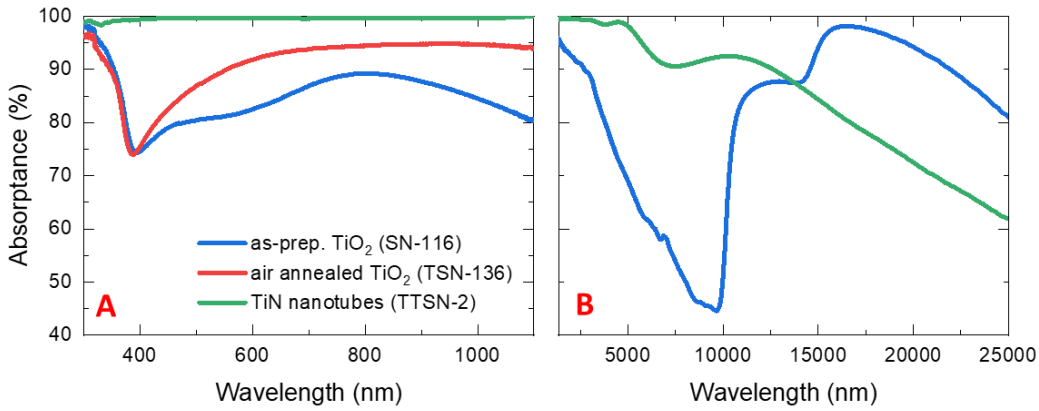

***Figure 6.5**: Optical properties of the as-prepared TiN nanotubes. A) UV-Vis spectrum, B) FT-IR spectrum.*

6.3.2. Optimization of the conditions for catalytic experiments

The photothermal experiments were performed in a home-made gas tight cell where TiN samples are directly illuminated from the top using a solar simulator (Figure 6.6).

The particular cell presents a front viewport transparent to UV-vis light; the light produced by the solar simulator was directly focused on the surface of TiN sample through an optical lens with an adequate focal length. The reactor, designed with a minimal dead volume to maximize the contact of the catalyst as thin film with the reactive gases, was directly fed with the reaction mixture and the outlet gases were analyzed on-line by a GC.

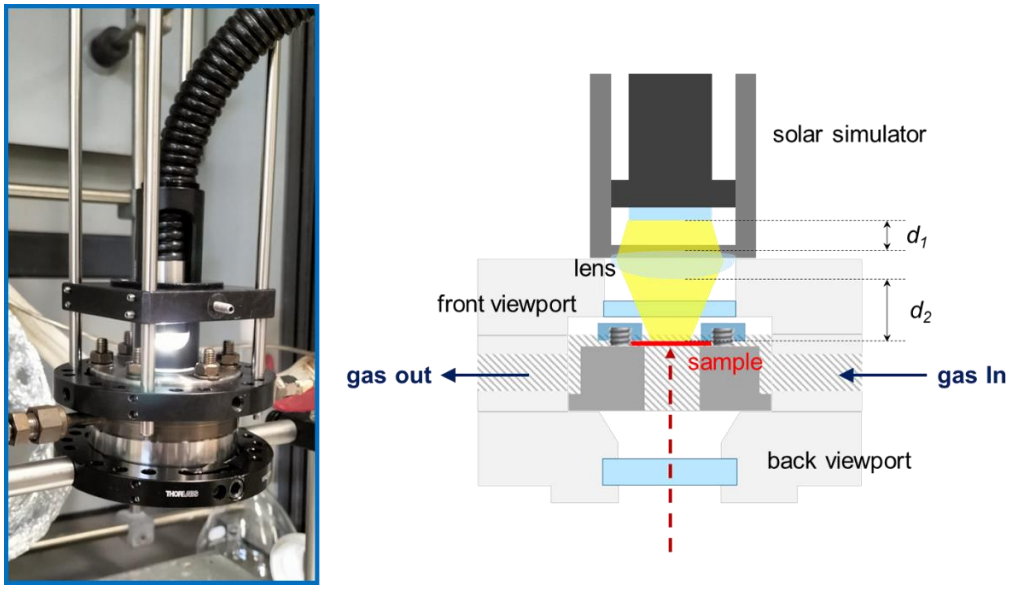

***Figure 6.6**: Cell for photothermal experiments using TiN samples.*

In order to study the catalytic behavior of the different prepared systems, it is fundamental to identify the optimal experimental condition in terms of composition of gaseous reaction mixture, temperature on the surface of the sample and pressure inside the cell, due to the dependency of thermal processes from those parameters [21]. To do this, TiN decorated with Pt nanoparticles (TiN/Pt) was chosen as standard material for catalytic experiments. With a constant total gas flow of 25 mL/min, the composition of reaction mixture was optimized using a molar fraction of CO_2 of 3.0% and changing the H_2 molar fraction in the range from 3.0% to 30%. Under these experimental conditions, the samples were

active toward the rWGS, partially converting CO_2 to CO without any further secondary product, such as methane (Figure 6.7).

From the analysis of the CO production rates, it is possible to understand that the catalytic activity of the sample toward rWGS is drastically dependent from the H_2 content in the reaction mixture. Indeed, it is well known that the activity toward this process is strictly correlated to the fraction between the two reactive gas in the mixture [22].

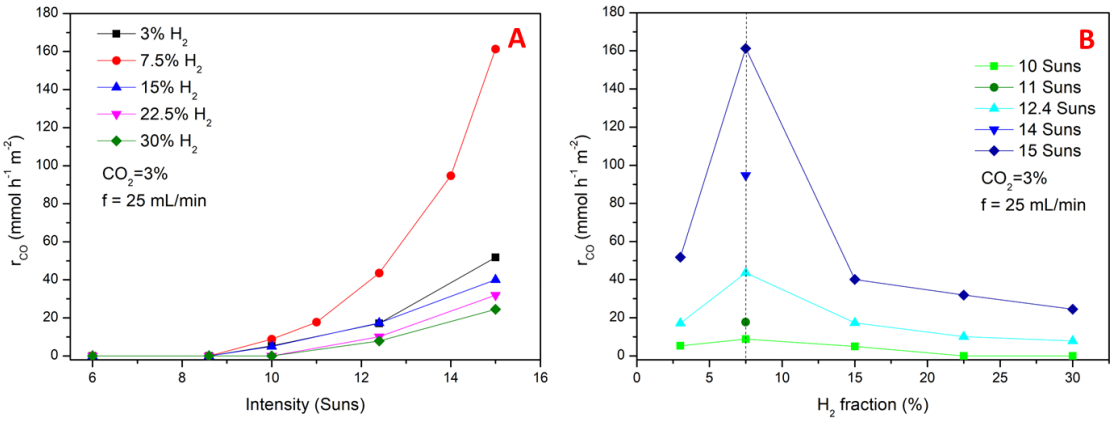

***Figure 6.7**: Dependency of H_2 fraction on the catalytic behaviour of TiN/Pt sample. A) With the increasing of light intensity; B) With the increasing of H_2 content.*

The highest CO production rate is observed for the composition CO_2 (3%) + H_2 (7.5%), with a r_{CO} of 160 mmol m^{-2} h^{-1} under an illumination of 15 Suns (Figure 6.7 A). Considering that the rWGS is an equilibrium reaction, it is expected a general increase of the CO productivity as the H_2 concentration increases. The experimental results reported in Figure 6.7 show a different scenario. This is due to the variation of the catalyst temperature on the amount of H_2, with a decrease of the temperature when the H_2 concentration increases.

To understand the relationship between the composition of the gas and the actual temperature of the catalytic film upon illumination, thermal analysis using both IR thermal sensor and thermal camera were performed. The two devices provide different information regarding the observed temperature: thermal camera was able to evaluate point by point the superficial temperature of TiN sample under different experimental conditions, showing the maximum temperature (T_{max}) reached during the process, while the IR sensor gives indication regarding the average temperature of the overall surface. It

must be underlined that the measure with IR sensor is very easy and using a cheap equipment while the use of the thermal camera is much more complicated and the instrumentation is more expensive. Assuming that the overall reactivity is mostly related to the zone of the sample at highest temperature T_{max}, a procedure for estimation of the T_{max} was developed on the basis of the comparison of temperature measurements using the two sensors. Firstly, the average temperature of the catalytic thin film was measured using the IR sensor under H_2/Ar mixtures with different composition as a function of the irradiation power. These analyses show that the average temperature of the film decreases as the H_2 concentration increases (Figure 6.8 A): as a result of the higher thermal conductivity of H_2 with respect to Ar, the gaseous mixture is able to dissipate more heat when the H_2 concentration is higher [23]. From these measurements, a scaling factor between the temperature in the case of a particular fraction of H_2 and in absence of H_2 was calculated. Using the thermal camera, selected and dedicated experiments were performed to reveal the temperature distribution on the film and to estimate the real T_{max} while flowing Ar in the cell. Assuming that the scaling factor can be applied to T_{max} as well, it was possible to calculate the value of T_{max} on the sample with the increasing of H_2 concentration (Figure 6.8 B). For example, under 15 Suns of illumination the maximum temperature of the sample ranges from 393 °C for 0% of H_2 to 284 °C with 30% of H_2 in the gaseous mixture. These experiments allowed to directly correlate the intensity of the light and the obtained r_{CO} with the temperature of the experiment (Figure 6.8 C and D). Indeed, experimental measurements performed under different concentration of CO_2 or Ar did not reveal any important variation of the overall temperature of the system since the thermal conductivity of Ar and CO_2 are comparable. This fact indicates that the fraction of H_2 is the most important parameter that affect the real temperature of the system upon illumination. Due to the endothermic nature of rWGS reaction, higher temperatures affect the equilibrium of the process, increasing the overall catalytic conversion [21]. Considering the results of these experiments, the reaction mixture with composition CO_2 (3%) + H_2 (7.5%) in Ar was chosen as reactive mixture for all the performed experiments.

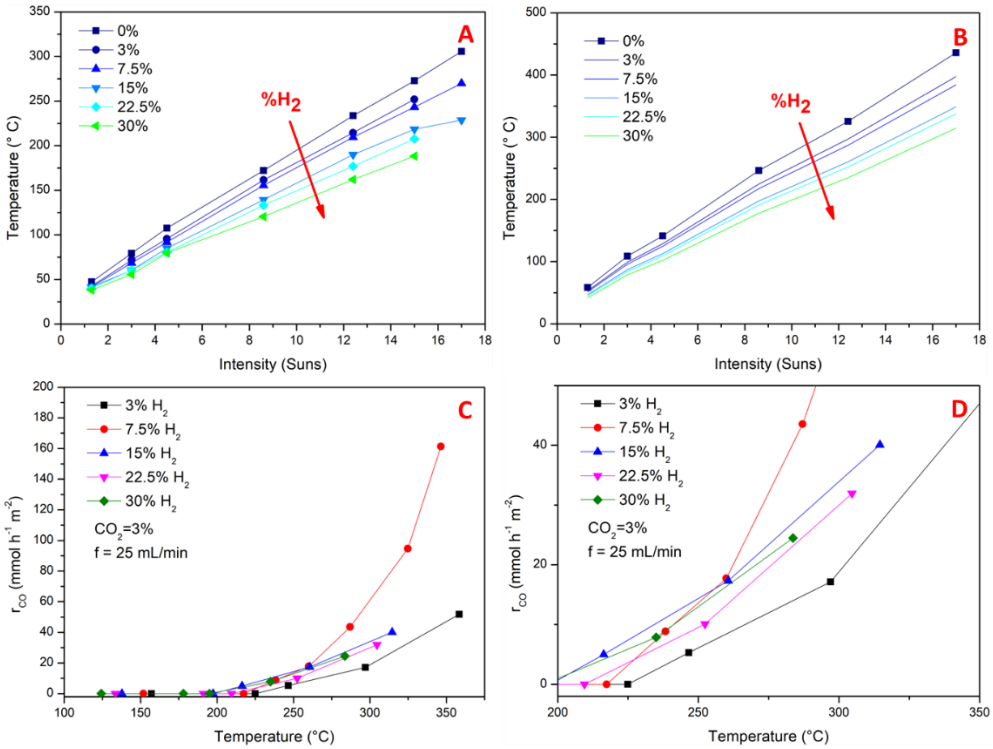

Figure 6.8: *A) Decreasing of average temperatures with the H_2 fraction (measures performed with IR sensor). B) Determination of T_{max} of TiN/Pt sample with 0% of H_2 using thermal camera and calculation of T_{max} for the other compositions. C) Catalytic experiments corrected with the real T_{max} of the process. D) Magnification of the zone 200-350 °C.*

6.3.3. Screening of catalytic behavior: Pt-based catalysts

Once that the best catalytic conditions were found, it was possible to measure the activity of the different samples. In particular, the case of the sample with Pt nanoparticles (labelled as TiN/Pt) is peculiar because this sample was used as reference for the analysis to find the best experimental conditions.

Pt nanoparticles were deposited via DC Sputtering or chemical impregnation (see experimental method, paragraph 6.2). At the end of the deposition, Pt nanoparticles with size of 1−2 nm were homogeneously distributed over the surface of the TiN nanotubes array, as confirmed by TEM images (Figure 6.9 A and B). For both the methods (sputtering or chemical impregnation) the deposition was regular and the size of the nanoparticles uniform. It is noteworthy to note that the low contrast of metal nanoparticles does not allow a precise quantification of the average sizes.

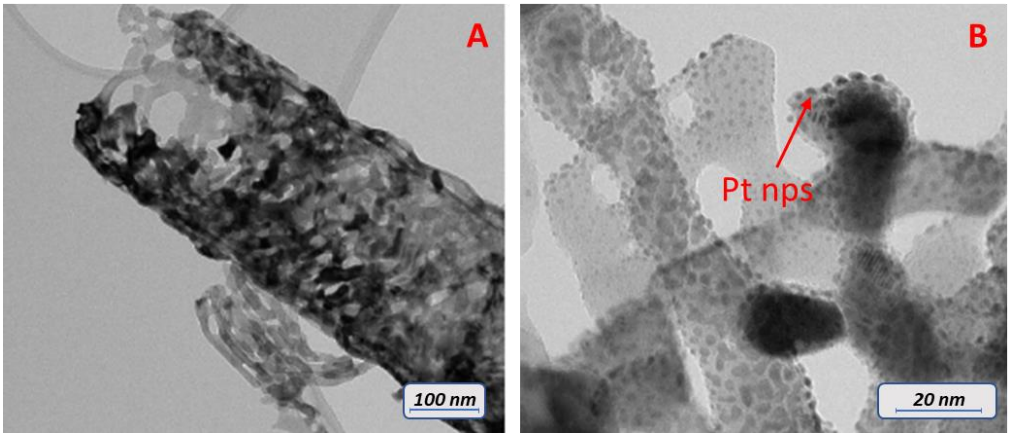

***Figure 6.9**: TEM images of TiN/Pt sample prepared via DC sputtering.*

The samples were tested for the photothermal CO_2 reduction, finding an overall activity toward the formation of CO through rWGS (Figure 6.10). In particular, the r_{CO} increase with the increasing of the intensity of illumination, starting from a power of 10 Suns (3.69 W) and reaching a maximum r_{CO} of 164.8 mmol m^{-2} h^{-1} at 15 Suns (5.53 W). The catalytic behaviors of the system TiN/Pt prepared with the two different methods are very similar, confirming the homogeneity of the dimensions irrespectively from the preparation methodology of the Pt nanoparticles.

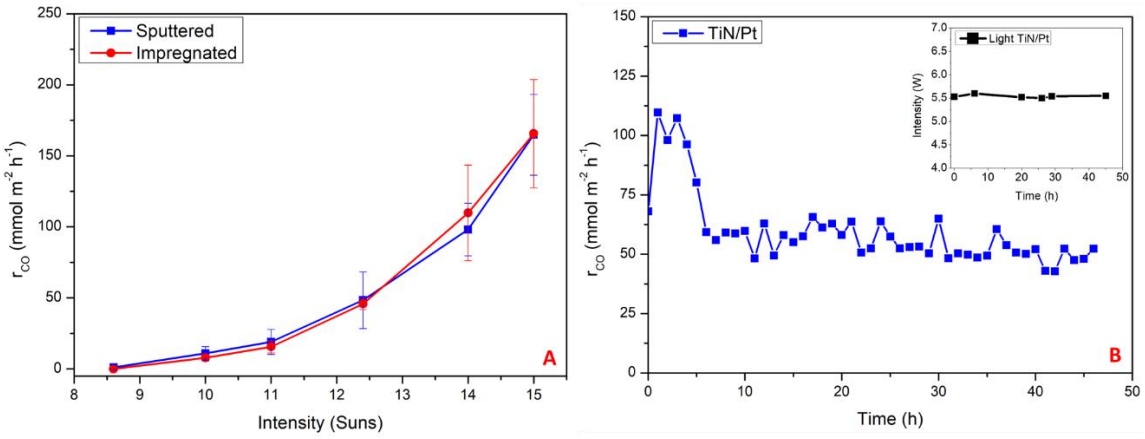

***Figure 6.10**: Catalytic activity varying the intensity (A) and Stability test under 15 Suns (B) for the sample TiN/Pt prepared by DC Sputtering.*

Stability tests were performed in order to evaluate the stability of TiN/Pt prepared by DC Sputtering upon illumination over the time. Here, different tests were done by

illuminating the samples at 15 Suns for 46 hours and checking the stability of the intensity at determined intervals. Figure 6.10 B shows a representative example of the performed stability test. The analysis revealed a decreasing of the activity during the initial 5 – 6 hours of illumination followed by a stabilization of the catalytic performance. The partial lost of catalytic activity of the sample during stability test is justified by post characterization TEM, revealing slightly modifications of the nanoparticles after the test and an increasing of the average sizes from 2-3 nm to 3-5 nm (Figure 6.11).

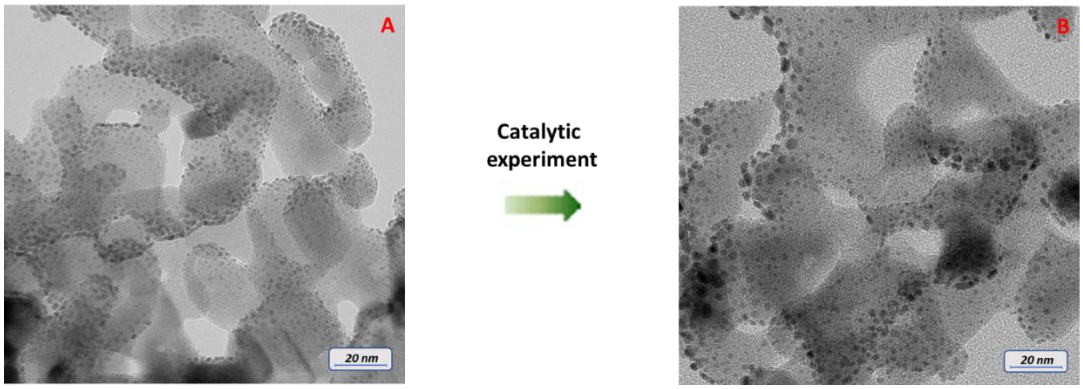

***Figure 6.11**: effects of catalytic experiments on Pt nanoparticles.*

The catalytic experiments revealed that TiN/Pt samples are able to catalyze the conversion of CO_2 through rWGS reaction, but no information are obtained regarding the mechanism of the catalytic process. In particular, it is not clarified the role of LSPR of TiN on the entire process and, at the same time, its contribution on the catalytic pathway, discriminating through purely photocatalytic, purely thermal or photothermal process. To gain information about this, different layers of Al_2O_3 were deposited on the sample of TiN (as already reported in the experimental section) and decorated with Pt nanoparticles. Al_2O_3 interlayer had different thickness, from 2 nm to 20 nm and the catalytic activity of these samples were compared with the case of pristine TiN/Pt (here labelled as TiN/Pt 0 nm) (Figure 6.12).

The thickness of Al_2O_3 interlayer is important to discriminate the mechanism of the entire catalytic process. Indeed, the overall mechanism is a combination of intrinsic thermal effects due to the LSPR and light-induced energy transfers. These phenomena are not trivial to deeply understand but have tremendous implication on the catalytic response of

the material. Different non-radiative mechanisms can theoretically be involved on the light-induced contribution to the catalytic activity (direct injections of hot electrons, PIRET [24]), generating charge separation phenomena in the metal nanoparticles or resulting in electron transfer to the active sites. Further studied are still ongoing in order to unveil the intrinsic mechanisms that rules the process, but a simple and general model can be depicted from some general considerations. When the thickness of Al_2O_3 is low, TiN LSPR can easily affect the electronical properties of metal nanoparticles and the overall activity, resulting in a catalytic behavior that is a combination of thermal effects of plasmonic resonance and light-induced effects. On the other hand, when the thickness of the interlayer is high, TiN cannot affect Pt nanoparticles, involving a purely thermal contribution to the overall catalytic process.

The analysis of the rates presented in Figure 6.12 A and B revealed that the catalytic activity decreases with the increasing of the Al_2O_3 thickness, indicating a lower reaction rate of catalytic process when an interlayer of an insulating material isolates the TiN nanostructure. In the attempt to discriminate the contribution of the electronic effects of the plasmonic material from its purely thermal heating of Pt nanoparticles, the activity of sample with Al_2O_3 interlayer of 20 nm could be considered as resulting from the purely thermal effect. On the other hand, as a first approximation, the photothermal catalytic activity of the samples with thinner Al_2O_3 layer can be considered as the sum of this purely thermal contribution and of the "photocatalytic" contribution deriving from electronic influence of the plasmonic TiN. Therefore, the purely photocatalytic contribution can be extrapolated as (equation 6.1):

$$Rate_{photocatalytic} = Rate_{photothermal} - Rate_{thermal} \quad (6.1)$$

The extrapolation of the photocatalytic rate is presented in Figure 6.12 C. For the sample without Al_2O_3 layer; as it is possible to observe, the contribution of the thermal catalysis is low, suggesting that CO_2 reduction on TiN/Pt derives almost completely from a photocatalytic mechanism. In particular, the purely thermal reaction is substantially slower than the photothermal one and its contribution is considerable only at higher temperature (higher irradiation powers).

The activation energies E_A for the different mechanisms have been determined through the Arrhenius plots (Figure 6.12 D), by the analysis of conversion rates as a function of

the sample temperature (T_{max}). The obtained activation energies are presented in Table 6.2. Again, the values obtained for E_A suggests that the overall photothermal reaction is dominated by the photocatalytic contribution, being the E_A of the extrapolated photocatalytic contribution very close to the overall E_A.

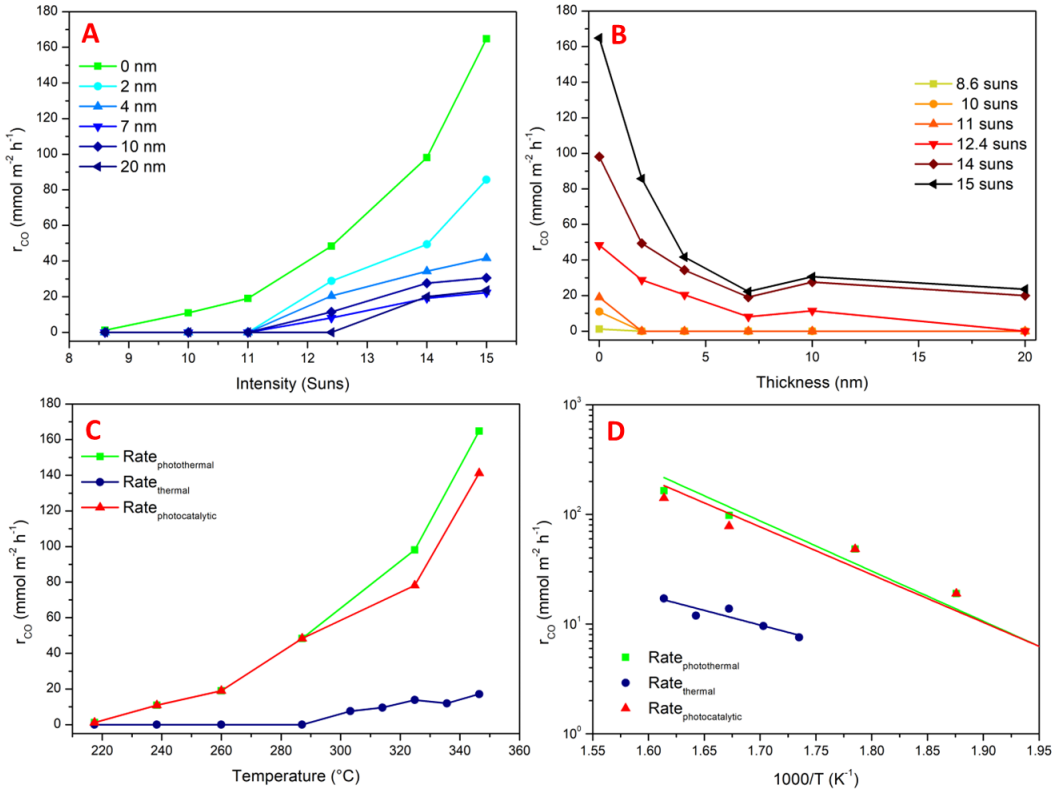

***Figure 6.12**: Experiments with TiN/Al_2O_3/Pt samples in order to unveil the mechanism of the catalytic process. A) r_{CO} for different Al_2O_3 layers with the increasing of the light intensity. B) r_{CO} at different intensities increasing the thickness of Al_2O_3 layer. C) Discrimination between rate of photothermal (green), purely thermal (Blue) and purely photocatalytic process (Red). D) Arrhenius plot for the three different catalytic mechanisms.*

$E_{A,\ photothermal}$	**30.1 kJ mol^{-1}**
$E_{A,\ thermal}$	**18.8 kJ mol^{-1}**
$E_{A,\ photocatalytic}$	**27.5 kJ mol^{-1}**

***Table 6.2**: Activation energies of the different mechanisms for CO formation with TiN/Pt sample.*

6.3.4. Screening of catalytic behavior: Ru-based samples

Another sample with a peculiar behavior is obtained with TiN decorated with Ru nanoparticles (labelled as TiN/Ru). DC sputtering of this metal allowed to deposit ultra small Ru nanoparticles on the TiN nanotube array with an average size of 1 nm (Figure 6.13 A). Due to the very low dimensions of the nanoparticles and the low contrast of the TEM images, Ru nanoparticles are difficult to detect, and other techniques are necessary to evaluate the presence of Ru on TiN nanostructure. In particular, XPS confirm the deposition of metal Ru through the presence of the typical peaks of Ru (IV) and Ru (III) [25].

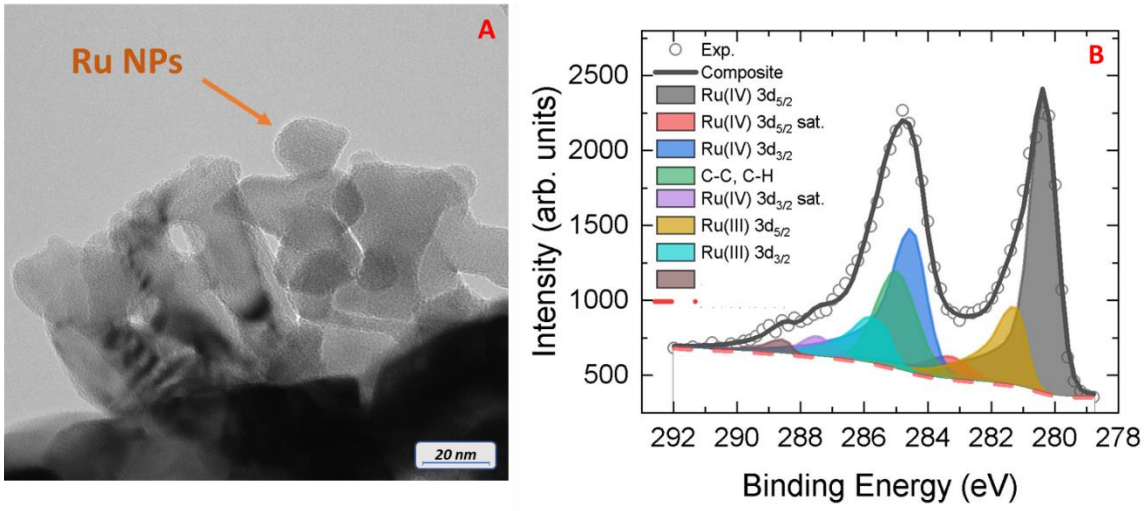

***Figure 6.13**: TEM image (A) and XPS of Ru region (B) for as-deposited the sample TiN/Ru.*

Even TiN/Ru samples were tested toward the gas phase photocatalytic reduction of CO_2 with the typical experimental conditions (25 mL/min, 3% CO_2 + 7.5% H_2 in Ar) but in this case the reactivity is different than TiN/Pt samples. In particular, by increasing the intensity of the light (and the temperature of the process), a mixture of CO and CH_4 was detected, suggesting that the material is able to catalyze both the rWGS and Sabatier reactions (Figure 6.14 A). The reduction to form CH_4 is favored at lower intensities, with almost 100% selectivity till 10 Suns of illumination (≈238 °C); when the intensity increase, the CO starts to be formed, affecting the overall selectivity of the process. At the end of experiment, under 15 Suns of illumination and at the temperature of ≈345 °C,

the rates toward the formation of different products are respectively 157 mmol m^{-2} h^{-1} for CH_4 and 90 mmol m^{-2} h^{-1} for CO, with a selectivity of 60% for CH_4 and 40% of CO (Figure 6.14 B).

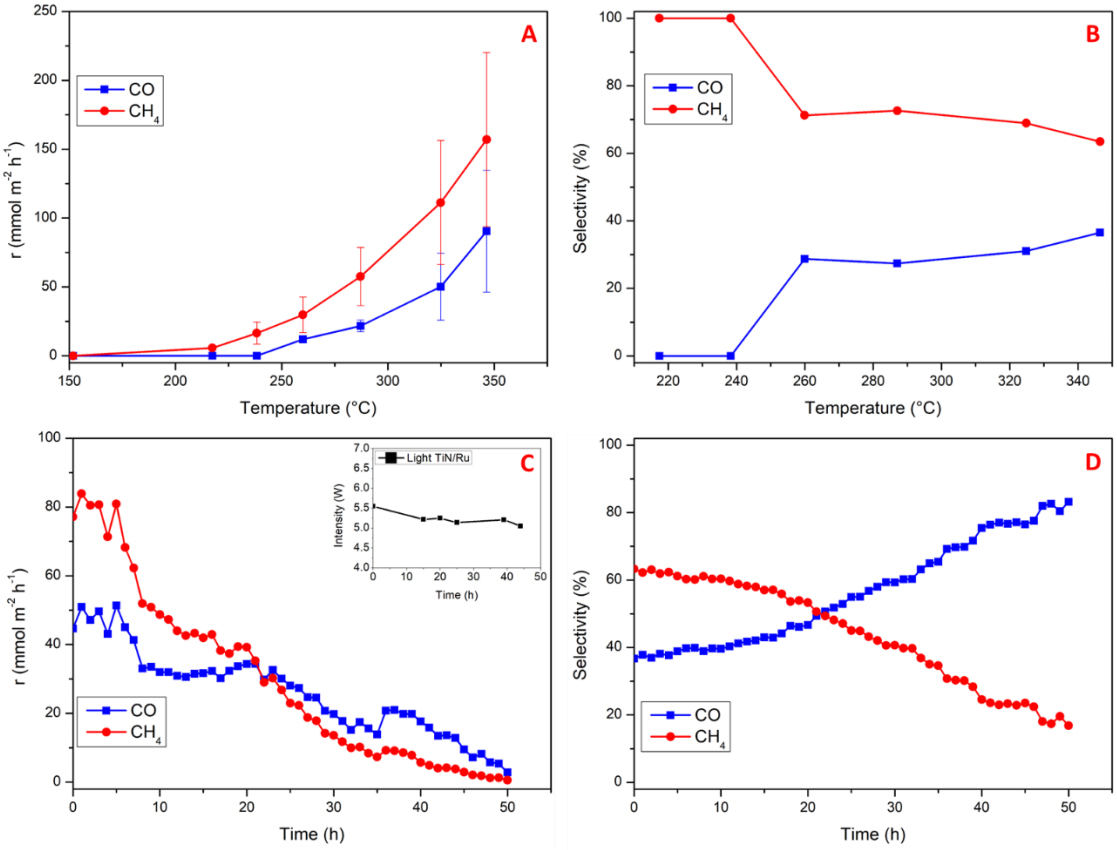

***Figure 6.14**: Catalytic experiments for the TiN/Ru sample. A) Rates towards the formation of CO and CH_4 upon different illumination. B) Selectivity of the two products with the increasing of the temperature of the experiment. C) Stability test for TiN/Ru under 15 Suns (insert: light intensity over the time). D) Trend of the selectivity during the stability test.*

Stability tests were performed even in the case of TiN/Ru sample with the aim to understand the stability of the material and how the selectivity changes over the time upon illumination at 15 Suns. From the analysis of the CO and CH_4 productions rates in Figure 6.14 C, it is possible to observe that the catalytic behavior of the sample decreases upon the 50 hours of illumination for both the products, even if with a different rate over the time. Indeed, the selectivity at 15 Suns vary over the time, with a gradual decreasing of the selectivity toward the formation of CH_4, suggesting that the two products are related to different mechanisms (Figure 6.14 D). The very low activity at the end of the

experiment in mainly related to a slightly coarsening of the Ru nanoparticles, with an average increasing of the size up to 3-4 nm (Figure 6.15).

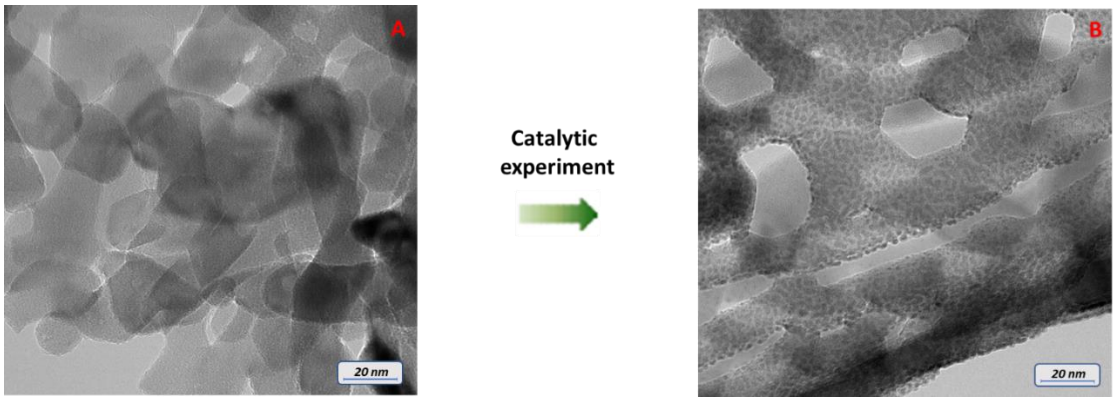

Figure 6.15*: Effects of the catalytic experiments on Ru nanoparticles for TiN/Ru sample.*

The reaction mechanism (photocatalytic or photothermal) leading to CO or CH_4 was studied also in the case of TiN/Ru, depositing an interlayer of Al_2O_3 with the thickness of 20 nm on the TiN and decorated with Ru nanoparticles. Also in this case, it is reasonable to assume that the catalytic behavior of the TiN/Ru sample with the interlayer of 20 nm of Al_2O_3 is purely due to the thermal behavior. Considering that, it is possible to apply equation 6.1 and evaluate the contribution of the purely photocatalytic process. The comparison of the rates for the two processes reveals interesting catalytic pattern (Figure 6.16 A for the formation of CO and Figure 6.16 C for CH_4). In particular, in the case of CO formation, it is possible to observe that the rate of the sample TiN/Ru pristine is similar with the sample of TiN/Al_2O_3 (20 nm)/Ru, indicating that the thermal contribution is dominant on the overall photothermal rWGS process. The mechanism of formation of CH_4 is the opposite: the r_{CH_4} for the sample TiN/Al_2O_3 (20 nm)/Ru is drastically lower compared to the case of the sample without alumina (Figure 6.16 C). Due to this low activity toward the thermal reduction, it is possible to assume that the purely photocatalytic pathway is dominant in the photothermal Sabatier process, especially at lower temperatures.

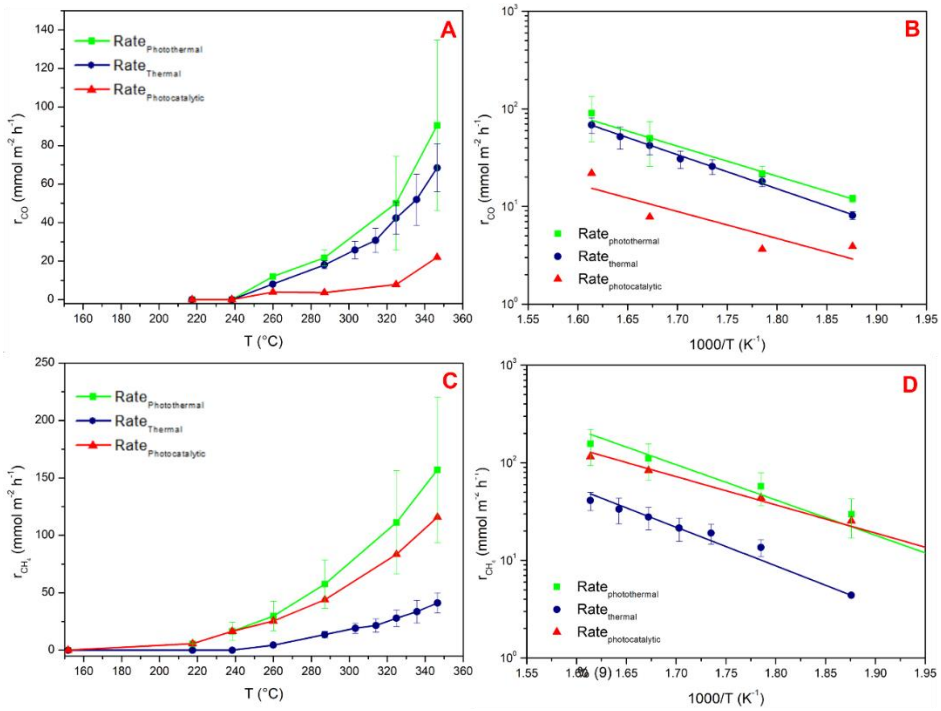

***Figure 6.16**: Experiments with TiN/Al_2O_3/Ru sample to unveil the mechanism of the catalytic process (green: photothermal; blue: thermal; red: photocatalytic). A) Discrimination between different processes for the formation of CO. B) Arrhenius plot for the three different catalytic mechanisms of CO formation. C) CH_4 Rates for the different mechanisms and D) Relatives Arrhenius plot for the formation of CH_4.*

At the same time, from the obtained conversion rates it was possible to calculate the Arrhenius plot of the different processes, having an indication of the activation energies E_A of the catalytic processes involved into the experiments (Figure 6.16 B and D). The obtained activation energies E_A, presented in the Table 6.3, again support the indication that CO production on TiN/Ru is controlled by a thermal process while the photocatalytic route is dominant in the production of CH_4.

	CO	***CH_4***
$E_{A,\ photothermal}$	***25.6 kJ mol^{-1}***	***30.1 kJ mol^{-1}***
$E_{A,\ thermal}$	***29.1 kJ mol^{-1}***	***33.0 kJ mol^{-1}***
$E_{A,\ photocatalytic}$	***23.0 kJ mol^{-1}***	***24.1 kJ mol^{-1}***

***Table 6.3**: Activation energies of the different mechanisms for CO and CH_4 formation with TiN/Ru sample.*

6.3.5. Comparison between different metals

Beside the already presented case of TiN/Pt and TiN/Ru, other metals were tested toward the photothermal reduction of CO_2. Catalytic experiments performed under different illuminations revealed that mostly of them were not active under the chosen experimental conditions: TiN/Cu, TiN/Ni, TiN/Ag and TiN/Au had showed no catalytic activities toward the conversion of CO_2. Only with the use of TiN/Pd sample a low activity toward the conversion of CO_2 to CO through rWGS reaction is obtained, even if its catalytic behavior is lower than the rates obtained for TiN/Pt and TiN/Ru (Figure 6.17).

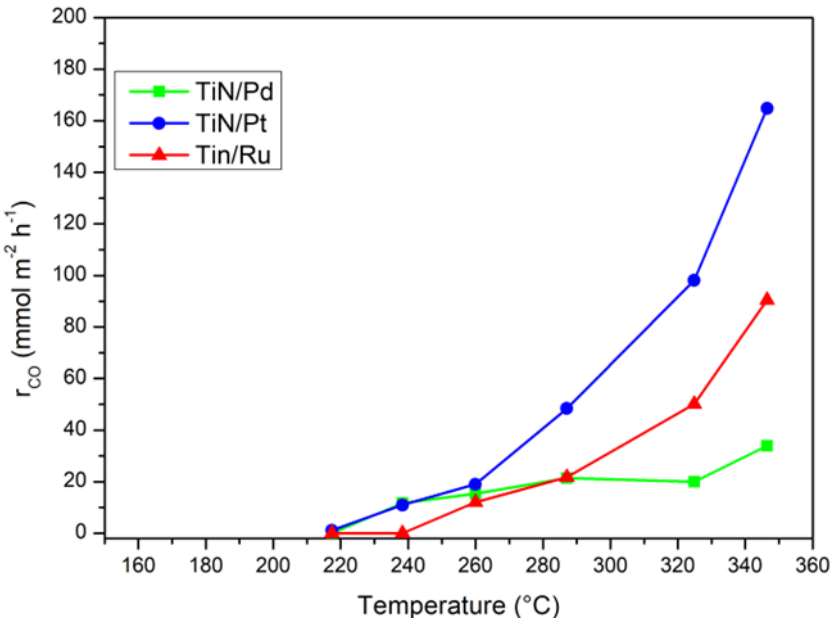

***Figure 6.14**: r_{CO} of the sample TiN/Pd compared withTiN/Pt and TiN/Ru.*

6.4 Conclusions

In this chapter, TiN nanotubes arrays were synthetized and studied toward the photothermal reduction of CO_2. The presented experimental procedure allowed to form high-aspect ratio nanostructure of TiN nanotubes via a three steps method where a Ti foil was firstly converted to TiO_2 nanotubes through anodization and then to TiN by nitridation. The system was decorated with different metals through DC sputtering or chemical impregnation, with the aim to understand the effects of the different metals on

the catalytic behavior of TiN. Indeed, the different samples can act as catalyst toward the photothermal reduction of CO_2, due to the possibility of exploit the LSP to locally increase the temperature and the overall catalytic behavior toward the considered process. Firstly, temperature measurements using UV sensor and thermal camera had allowed to find the dependency of the temperature to the amount of H_2 and find the best experimental conditions to perform the catalytic process. The photocatalytic experiments revealed that only TiN/Pd, TiN/Ru and TiN/Pt are active toward the photothermal reduction of CO_2. In particular, all these three samples revealed a catalytic activity toward the formation of CO through rWGS process, with the different activity presented in Figure 6.17: TiN/Pt was the most active sample, followed by TiN/Ru and TiN/Pd. The case of TiN/Ru was peculiar due to the different reactivity showed by this sample; indeed, beside the activity toward the rWGS, this material showed even a high activity toward the formation of CH_4 through Sabatier reaction, especially at low temperature. The selectivity between the different products changed by the increasing of the temperature (at 15 Suns selectivity was 60% toward the formation of CH_4) and over the time, suggesting a different catalytic pathway for the formation of the two products. To unveil the mechanism of the catalytic process, a layer of 20 nm of Al_2O_3 was deposited on top of TiN nanostructure through ALD, acting as barrier to the flow of the charge carriers and the photocatalytic reaction and allowing to discriminate between the contribution of the light-induced catalysis and thermal process. On TiN/Pt, samples with different thickness of the Al_2O_3 interlayer allow to conclude that CO production is dominated by a photocatalytic process. On the other hand, the measurements performed with TiN/Ru sample revealed that the CH_4 is mainly formed at low temperatures through photocatalytic process, while rWGS is mostly activated at higher intensities due to the intrinsic thermal behavior. Different experiments need to be done in order to fully understand the contribution of the two mechanisms on the overall processes taking place on this kind of materials. Besides this, the presented work focuses the attention on the importance of nanostructure control of TiN to exploit this material as efficient solar absorber, with the aim of using as scalable and cost-efficient catalyst towards thermophotocatalytic processes.

6.5 References

[1] K.L. Tsakmakidis, A.D. Boardman, O. Hess, *Nature* 450 (**2007**) 397–401.

[2] W. Luo, H. Ma, F. Mou, M. Zhu, J. Yan, J. Guan, *Adv. Mater.* 26 (**2014**) 1058–1064.

[3] X. Ni, N.K. Emani, A. V. Kildishev, A. Boltasseva, V.M. Shalaev, *Science* 335 (**2012**) 427.

[4] K. Aydin, V.E. Ferry, R.M. Briggs, H.A. Atwater, *Nat. Commun.* 2 (**2011**) 1–7.

[5] Y.Y. Cai, Y.C. Choi, C.R. Kagan, *Adv. Mater.* (**2022**) 2108104.

[6] M.L. Brongersma, N.J. Halas, P. Nordlander, *Nat. Nanotechnol.* 10 (**2015**) 25–34.

[7] J. Gavnholt, A. Rubio, T. Olsen, K.S. Thygesen, J. Schiøtz, *Phys. Rev. B - Condens. Matter Mater. Phys.* 79 (**2009**) 195405.

[8] K. Watanabe, D. Menzel, N. Nilius, H.J. Freund, *Chem. Rev.* 106 (**2006**) 4301–4320.

[9] G. V. Naik, V.M. Shalaev, A. Boltasseva, *Adv. Mater.* 25 (**2013**) 3264–3294.

[10] D.F. Swearer, H. Zhao, L. Zhou, C. Zhang, H. Robatjazi, J.M.P. Martirez, C.M. Krauter, S. Yazdi, M.J. McClain, E. Ringe, E.A. Carter, P. Nordlander, N.J. Halas, *Proc. Natl. Acad. Sci. U. S. A.* 113 (**2016**) 8916–8920.

[11] S. Ishii, R.P. Sugavaneshwar, T. Nagao, *J. Phys. Chem. C* 120 (**2016**) 2343–2348.

[12] W. Li, U. Guler, N. Kinsey, G. V. Naik, A. Boltasseva, J. Guan, V.M. Shalaev, A. V. Kildishev, *Adv. Mater.* 26 (**2014**) 7959–7965.

[13] A. Naldoni, U. Guler, Z. Wang, M. Marelli, F. Malara, X. Meng, L. V. Besteiro, A.O. Govorov, A. V. Kildishev, A. Boltasseva, V.M. Shalaev, *Adv. Opt. Mater.* 5 (**2017**) 1601031.

[14] S. Ishii, S.L. Shinde, T. Nagao, *Adv. Opt. Mater.* 7 (**2019**).

[15] A. Naldoni, Z.A. Kudyshev, L. Mascaretti, S.P. Sarmah, S. Rej, J.P. Froning, O.

Tomanec, J.E. Yoo, D. Wang, Š. Kment, T. Montini, P. Fornasiero, V.M. Shalaev, P. Schmuki, A. Boltasseva, R. Zbořil, *Nano Lett.* 20 (**2020**) 3663–3672.

[16] L. Zhou, J.M.P. Martirez, J. Finzel, C. Zhang, D.F. Swearer, S. Tian, H. Robatjazi, M. Lou, L. Dong, L. Henderson, P. Christopher, E.A. Carter, P. Nordlander, N.J. Halas, *Nat. Energy* 5 (**2020**) 61–70.

[17] T.L. Thi Le, L. Tan Nguyen, H.H. Nguyen, N. Van Nghia, N. Minh Vuong, H. Nhat Hieu, N. Van Thang, V. Thong Le, V. Huong Nguyen, P.C. Lin, A. Yadav, I. Madarevic, E. Janssens, H. Van Bui, L. Le Thi Ngoc, *Nanomaterials* 11 (**2021**) 1–11.

[18] S. Ishii, M. Higashino, S. Goya, K. Tanaka, S. Murai, E. Shkondin, T. Nagao, O. Takayama, *Nanophotonics* 10 (**2021**) 1487–1494.

[19] D. Kowalski, J. Mallet, S. Thomas, J. Rysz, B. Bercu, J. Michel, M. Molinari, *Electrochim. Acta* 204 (**2016**) 287–293.

[20] Y.X. Chen, V. Gombac, T. Montini, A. Lavacchi, J. Filippi, H.A. Miller, P. Fornasiero, F. Vizza, *Green Chem.* 20 (**2018**) 2299–2307.

[21] K. Oshima, T. Shinagawa, Y. Nogami, R. Manabe, S. Ogo, Y. Sekine, *Catal. Today* 232 (**2014**) 27–32.

[22] J.E. Whitlow, *AIP Conf. Proc.* 1123 (**2003**) 1116–1123.

[23] L. Mascaretti, A. Schirato, T. Montini, A. Alabastri, A. Naldoni, P. Fornasiero, *Joule* 6 (**2022**) 1727–1732.

[24] L. Mascaretti, A. Dutta, Š. Kment, V.M. Shalaev, A. Boltasseva, R. Zbořil, A. Naldoni, *Adv. Mater.* 31 (**2019**) 1805513.

[25] A. Lewera, W.P. Zhou, C. Vericat, J.H. Chung, R. Haasch, A. Wieckowski, P.S. Bagus, *Electrochim. Acta* 51 (**2006**) 3950–3956.

Chapter 7

Conclusions and perspectives

In recent years, CO_2 emissions resulting from anthropogenic factors have raised significant issues due to their implications on the delicate equilibrium of the biosphere. To mitigate the effects of CO_2 on our environment, it is necessary to find different strategies, developing efficient renewable energies and processes. In particular, many processes have been proposed to recycle CO_2 and reuse it as a starting point for the production of fuels or chemicals. Electrocatalytic CO_2 Reduction Reaction is a very promising way to use CO_2, thanks to the possibility to work under mild conditions or relatively simple management operations. On the other hand, this approach still suffers a mismatch between the lab and the industrial scales, due to the low efficiency and stability of the catalysts, the low selectivity and the consequent difficulties in separating the resulting products. Current research is focused on developing efficient electrocatalysts, exploring the intrinsic relationships between the nanoscale phenomena and their macroscopic behavior. The role of nanostructuring is fundamental to tailor the overall performance of a material. With a rational choice of exposed facets in a crystal or a particular nanostructure, it is possible to significantly improve the catalytic behavior of a material by limiting bulk recombination and promoting charge transfer.

The main objective of this Ph.D. thesis was the development of nanostructured materials able to exhibit peculiar and distinct features, studying the catalytic behavior and the effects of electrochemical characterization on the stability of the prepared materials. In particular, the synthesis of different Cu-based nanostructured electrodes was investigated, exploiting the possibility of copper to catalyze the formation of C_+ species via electrocatalytic CO_2RR.

The thesis first discusses the synthetic procedures to obtain Cu_2O nanoparticles with particular shapes. The method presented in Chapter 3 allows to prepare cubic and rhombo dodecahedral nanoparticles of Cu_2O, with a narrow size distribution. XRD, Raman and TEM characterizations confirmed the purity of the chemical phase and the typical structural features of crystalline Cu_2O. The electrochemical characterization confirmed the interesting catalytic properties of the material towards the eCO_2RR and a low stability

of the obtained nanoparticles, due to their easy conversion to metallic Cu. The different exposed facets of Cu_2O nanoparticles affects the overall catalytic behavior of the materials, with higher *FE* toward the formation of CH_2CH_2 for CU Cu_2O and an increase activity toward HCOOH for RD Cu_2O. For example, at the voltage of -1.1 V vs RHE, $FE_{CH_2CH_2}$ was 30% for CU Cu_2O respect to a $FE_{CH_2CH_2}$ of 15% for RD Cu_2O. The catalytic behavior of pristine Cu_2O was exhaustively studied using other electrochemical setups such as H-cell or electrolyzers, highlighting a scarce selectivity toward eCO_2RR products. Moreover, *operando* and post characterizations confirmed the poor stability of the material, with a rapid reduction of Cu_2O nanoparticles to Cu(0) and a superficial reconstruction that has implications on the exposed facets of the material. These two drawbacks need to be faced, finding solutions to increase selectivity and stability, enhancing at the same time the overall catalytic behavior of the material.

One possible solution to address the stability and selectivity of this material is the formation of heterostructures, exploiting the affinity of Cu_2O with typical 2D materials to improve the dispersion and sizes of the nanoparticles. In Chapter 4, pristine nanoparticles of CU Cu_2O were coupled with three common support materials, such as g-C_3N_4, RGO and MoS_2, with the aim to understand the effects of reduced dimensions and improved dispersion on the catalytic behavior of the material. The formation of the composite between Cu_2O and g-C_3N_4 affected the overall catalytic activity of the material, resulting in improved HCOOH productivity over the time, with a correlation between the average sizes of Cu_2O nanoparticles and the formate produced during the catalytic process. For example, considering -1.1 V vs RHE, the composite CU Cu_2O/g-C_3N_4 1:3 showed an almost double fraction of HCOOH (0.57 vs 0.28) respect pristine Cu_2O, despite similar FE_{HCOOH} between the different materials. On the other hand, *operando* XAS experiments, showed similar results to pristine Cu_2O, evidencing no significant implications on the stability of Cu_2O for the different composites. Cu_2O was coupled also with Reduced Graphene Oxide, a 2D carbon-based support able to affect the overall catalytic behavior of the composite thanks to its intrinsic conductive properties. The formation of CU Cu_2O/RGO composite directly affected the selectivity and productivity toward CO, with an almost double FE_{CO} (40% for composite vs 22% of pristine Cu_2O at -0.7 V vs RHE) and improved production of CO, especially at lower voltages. MoS_2 nanoflakes were able to improve both the dispersion and size of Cu_2O

nanoparticles, greatly enhancing the faradaic efficiency and the productivity of pristine Cu_2O toward the HER process. The improved dispersion and synergistic effects between Cu_2O nanoparticles and MoS_2 nanoflakes had significant impact on the overall selectivity of the composite toward the formation of hydrogen, resulting in high currents and productivity toward H_2. This work opens a promising prospect for the utilization of Cu_2O/MoS_2 as catalyst toward the in-situ electrochemical hydrogenation of organic molecules such as furfural. The formation of heterostructures is surely one efficient way to opportunely drive the catalytic behavior of Cu-based catalysts but much work still needs to be done in order to rationally improve the overall efficiency toward high-value added products such as ethylene or alcohols.

In Chapter 5, monometallic and bimetallic particles based on Cu and Sn were synthetized through a facile and scalable urea glass route (UGR). Different experimental approaches allowed to explore the preparation of CuSn alloy and core-shell particles based on these metals. Electrochemical characterization revealed a particular activity of monometallic materials toward HER process due to their strong metallic behavior. On the other hand, bimetallic compounds demonstrated an improved activity toward CO_2RR process, forming mainly HCOOH, CO and traces of ethylene. The sample Cu@Sn-B exhibited the best catalytic performances, with FE_{CO} higher than 50% and the presences of ethylene at the voltage of -1.1 V vs RHE. The improve activity of bimetallic materials towards CO_2RR was further supported by the analysis of the molar ratio between CO_2RR products and H_2. These findings suggest that metallic Cu with incorporation of Sn in the bimetallic system can lead to improved catalytic performance for CO_2RR, with the potential for selective production of high-value products.

Refractive metamaterials are able to exploit the nanostructuration and the presence of a localized surface plasmon resonance to improve their activity towards the targeted process. In Chapter 6, nanostructured TiN was used as perfect solar absorber and catalyst toward the photothermal reduction of CO_2. The presented experimental method consisted in the formation of TiN nanotubes array through anodization of a Ti foil and a following nitridation. The obtained nanostructures were decorated with different metal nanoparticles, investigating the role of the metal on the overall catalytic behavior. The LSPR is able to locally increase the temperature of the sample and catalyze the reduction of CO_2 through the photothermal process. The photocatalytic experiments revealed that

TiN/Pd, TiN/Ru and TiN/Pt were active toward the photothermal conversion of CO_2 to CO via rWGS, with the TiN/Pt sample exhibiting the best catalytic behavior. Additionally, TiN/Ru presented a peculiar reactivity toward the formation of CH_4 through Sabatier process, particularly at lower temperatures. The variation of the activity and selectivity with temperature and time suggested different catalytic pathways for CO and CH_4 formation. A layer of Al_2O_3 with the thickness of 20 nm was deposited over the TiN array to obtain more information about the mechanism of the catalytic process. The performed experiments revealed that CH_4 is mainly formed at low temperatures through photocatalytic reduction while, rWGS is mostly active at high intensities and temperatures due to the intrinsic thermal behavior of the process. The presented method holds promise for exploiting the peculiar intrinsic features of nanostructured TiN in the photothermal reduction of CO_2, but further work still needs to be done in order to have scalable and cost-efficient catalysts for these thermophotovoltaic applications.

Despite significant advancements in CO_2 reduction research, industrial applications still suffer of problems that drastically limits this process in a large-scale economy. Many efforts still need to be done, in particular in terms of optimization of the costs, from the preparation of highly efficient catalysts to the separation and purification of the different products, highlighting the carbon neutral impact of the process. The issues related to the low selectivity of the catalysts and the separation of the different products of CO_2 reduction processes are fundamental and greatly impact the overall viability of industrially available methods. Moreover, the understanding of the underlying mechanisms of CO_2 reduction is essential to rationally suggest the more efficient ways to catalyze the considered process. In conclusion, the collaboration and rational contributions of all stakeholders involved are necessary for the development of an efficient and successful mechanism to convert excess CO_2 into valuable chemicals and fuels. Only by addressing the described challenges, it will be possible to overcome these limitations and achieve significant progress in the field of CO_2 reduction.

List of pubblications

- "Well-defined Cu_2O photocatalysts for solar fuels and chemicals". S. Rej, M. Bisetto, A. Naldoni, P. Fornasiero, *J. Mater. Chem. A*, **2021**, *9*, 5915-5951
- "Engineering Cu_2O nanowire surfaces for photoelectrochemical hydrogen evolution reaction". G. Solomon, M. Lecca, M. Bisetto, M. K. Gilzad, I. Concina, M. M. Natile, A. Vomiero. ACS Appl. Energy Mater. **2023**, 6, 2, 832–840.
- "Study on the Structure vs Activity of Designed Non-Precious Metal electrocatalysts for CO_2 Conversion". W. Yuan, N. Jeyachandran, T. Rao, A. Ghulam Nabi, M. Bisetto, D. Di Tommaso, T. Montini, C. Giordano. Materials Letters, **2023**, 341, 134167.

Acknowledgments

Firstly, I would like to express my sincere gratitude to my supervisors, Professor Paolo Fornasiero and Professor Tiziano Montini for their supervision and their suggestions throughout the duration of this three-years project. Paolo is an exceptional supervisor and a fantastic researcher. He allowed me the freedom to explore and learn from both successes and failures, while offering invaluable insights and solutions to overcome challenging research problems. His expertise and mentorship have been instrumental in shaping the direction and success of my research. I am sincerely thankful for his involvement and contribution to my academic journey. I am also deeply thankful to Tiziano for his profound insights, supports, patience (in particular during the beamtime at Soleil Synchrotron and the intensive months of writing). I am truly grateful for the knowledge and guidance they imparted during my Ph.D. journey.

I would to thanks Dr. Manuela Bevilacqua for her constant supports on these years, in particular numerous insights regarding the development of electrochemical setups and procedures exploited during all this Ph.D.

Special thanks to all my colleagues of Mee group, past and present: Pr. Michele Melchionna, Dr. Valentina Gombac, Dr. Francesco Longobardo, Dr. Marcello Ferrara, Dr. Mario Daka, Dr. Luka Suhadolnik, Dr. Patricjia Bostjančič, Mrs Smritirekha Talukdar, Mrs. Miriam Marchi, Mr. Giuseppe Sportelli, Mrs. Gaia Castellani and Mrs. Gaia Grando. Thank you all for providing me suggestions in both research and daily life. I will also thanks to Dr. Greta Camilla Magnano, Mr. Andrea Bogo, Mrs. Giovanna Marussi and Mrs. Anastasia Gaetano for all the fruitful time that we spent together in these years.

I would like to thank all the members of Professor Maurizio Prato's research group for their generous support and allowing me access to their laboratories and facilities. Their assistance and collaboration have been instrumental in the successful completion of my research. Additionally, I extend my thanks to the research group of Professors Gianpiero Adami and Matteo Crosera for their assistance with the ICP measurements.

I would like to extend my thanks to Mr. Elvio Merlach for his contribution to the development of the H-cell for electrochemical measurements. His extensive experience and expertise were crucial in creating and optimizing this important experimental setup.

I would also to thank the department of Chemical and Pharmaceutical Science, the PhD course of Nanotechnology, the University of Trieste and Regione Friuli Venezia Giulia for the opportunity to join the PhD program and this incredible experience.

I would like to express my appreciation to all the members of the Regional Centre of Advanced Technologies and Materials (RCPTM) in Olomouc, Czech Republic. I am incredibly grateful for the opportunity they provided me to spend a period in their laboratories and utilize their state-of-the-art facilities in 2020 and all the characterizations performed during these three years of project. I would like to extend a special thanks to Professor Alberto Naldoni for his exceptional enthusiasm and unwavering support throughout our research endeavours. His passion and dedication towards every experiment and measurement conducted were truly inspiring. I am grateful for his valuable suggestions, insightful guidance, and his willingness to listen and provide feedback on the progress of our projects. I would like to pass my sincere thanks to Dr. Luca Mascaretti for his support on these years and his helpful presence, especially during all the long experiments performed together. I will also thank Mr. Mahdi Shahrezaei and Mr. Morteza Afshrar for their participation on the project related to the study of catalytic activity of TiN nanostructures and their constant help to perform the experiments; Dr. Sourav Rej and Dr. Zhang Yu for their kindly supervisions at RCPTM, especially related to the synthesis of pristine Cu_2O nanoparticles.

I will thank the research group of Pr. Cristina Giordano for the fruitful collaboration focus on the synthesis and electrochemical characterization presented in chapter 5, in particular Pr. Devis Di Tommaso for DFT calculations.

Furthermore, all the members of SAMBA beamline from Soleil Synchrotron, especially Dr. Emiliano Fonda, are gratefully acknowledged for all the XAS measurements performed during our Beamtimes in September/October 2022.

To conclude, a big thanks to my family, in particular my parents and my siblings, for their constant and unconditioned love and support. I would also thank all my friends (from Pezzan and Padova) and all those who have been supportive throughout this long

journey, in particular Natalia, for the patient and careful support during these intense months. Without them, I won't be able to achieve what I have achieved so far.